EXPERIMENTAL INVESTIGATION OF THE AERODYNAMIC INTERACTIONS OF VEHICLES IN CLOSE-FOLLOWING AND PASSING SITUATIONS

A THESIS SUBMITTED TO
THE GRADUATE SCHOOL OF NATURAL AND APPLIED SCIENCES
OF
MIDDLE EAST TECHNICAL UNIVERSITY

BY

ÜNSAL GÜMÜŞLÜOL

IN PARTIAL FULFILLMENT OF THE REQUIREMENTS
FOR
THE DEGREE OF MASTER OF SCIENCE
IN
MECHANICAL ENGINEERING

JUNE 2006

Approval of the Graduate School of Natural and Applied Sciences

Prof. Dr. Canan ÖZGEN
Director

I certify that this thesis satisfies all the requirements as a thesis for the degree of Master of Science.

Prof. Dr. Kemal İDER
Head of Department

This is to certify that we have read this thesis and that in our opinion it is fully adequate, in scope and quality, as a thesis for the degree of Master of Science.

Prof. Dr. Kahraman ALBAYRAK
Co-Supervisor

Instr. Dr. A. Tahsin ÇETİNKAYA
Supervisor

Examining Committee Members

Prof. Dr. O. Cahit ERALP (METU,ME)

Instr. Dr. A.Tahsin ÇETİNKAYA (METU,ME)

Prof. Dr. Kahraman ALBAYRAK (METU,ME)

Prof. Dr. Mehmet ÇALIŞKAN (METU,ME)

Prof. Dr. Nafiz ALEMDAROĞLU (METU,AEE)

I hereby declare that all information in this document has been obtained and presented in accordance with academic rules and ethical conduct. I also declare that, as required by these rules and conduct, I have fully cited and referenced all material and results that are not original to this work.

Name, Last Name : Ünsal GÜMÜŞLÜOL
Signature :

ABSTRACT

EXPERIMENTAL INVESTIGATION OF THE AERODYNAMIC INTERACTIONS OF VEHICLES IN CLOSE-FOLLOWING AND PASSING SITUATIONS

Gümüşlüol, Ünsal
M.S., Department of Mechanical Engineering
Supervisor: Instr. Dr. A. Tahsin Çetinkaya
Co-supervisor: Prof. Dr. Kahraman Albayrak

June 2006, 184 pages

In this thesis study, aerodynamic interactions of vehicle models in close-following and passing situations were investigated experimentally. Effects of the inter-vehicle spacing and lateral distance on drag coefficients of two close-following vehicles were observed.

Two different types of vehicle models were used in order to investigate the shape effect on aerodynamic vehicle interactions. Drag forces and surface pressures of the models at each situation were measured. Two different blockage correction methods on the basis of drag coefficient results were applied.

Linear increments of drag coefficients were observed on leading and trailing MIRA models. Because of their blunter shapes and sharp edges, the leading and trailing

Ahmed Body models feel the presence of the aerodynamic interactions substantially. The most important reduction in drag force occurs at the least vehicle spacing for both vehicle types. The greatest reduction in drag force occurs at the least vehicle spacing for both vehicle types.

In the passing situations, it was observed that drag coefficient of MIRA models did not change considerably. However, big amount of changes were observed at all positions for Ahmed Body. Maximum values of drag coefficients were reached when the models were at side by side position for both vehicle types.

In conclusion, it is possible to obtain more drag reductions with more numbers of vehicles in close-following. The lower drag coefficients in close-following operations cause to increase fuel savings and to reduce air pollution.

Keywords: Aerodynamics of road vehicles, drag, close-following, passing

ÖZ

YAKIN TAKİP VE GEÇİŞ DURUMUNDAKİ TAŞITLARIN AERODİNAMİK ETKİLEŞİMLERİNİN DENEYSEL İNCELENMESİ

Gümüşlüol, Ünsal
Yüksek Lisans, Makina Mühendisliği Bölümü
Tez Yöneticisi: Öğr. Gör. Dr. A. Tahsin Çetinkaya
Yardımcı Tez Yöneticisi: Prof. Dr. Kahraman Albayrak

Haziran 2006, 184 sayfa

Bu tez çalışmasında, yakın takip ve geçiş durumundaki taşıtların aerodinamik etkileşimleri deneysel olarak incelenmiştir. Taşıt aralığı ve yanal uzaklığın, yakın takipteki iki taşıtın sürüklenme katsayısına olan etkileri araştırılmıştır.

Aerodinamik taşıt etkileşimi üzerindeki şekil etkisinin incelenmesi için iki farklı tip taşıt modeli kullanılmıştır. Modellerin her durumdaki sürüklenme kuvvetleri ve yüzey basınçları ölçülmüştür. Sürüklenme katsayıları sonuçlarını temel alan iki ayrı blokaj düzeltme metodu uygulanmıştır.

Öndeki ve arkadaki MIRA modellerinde sürüklenme katsayılarının doğrusal artışı gözlemlenmiştir. Daha kaba biçimleri ve keskin kenarları nedeniyle, öndeki ve arkadaki Ahmed Body modelleri aerodinamik etkileşimleri büyük oranda hissetmektedir. Her iki taşıt tipi için, sürüklenme kuvvetindeki en büyük düşüş, en küçük taşıt aralığında gerçekleşmektedir.

Geçiş durumlarında, MIRA modellerinin sürüklenme katsayılarının çok değişmediği gözlemlenmiştir. Buna karşın, Ahmed Body için bütün durumlarda büyük miktarlarda değişiklikler gözlemlenmiştir. Her iki taşıt tipi için, sürüklenme katsayılarının en büyük değerlerine modeller yan yana durumdayken ulaşılmıştır.

Sonuç olarak, yakın takipteki daha çok sayıda taşıtlarla, sürüklenme kuvvetinde daha fazla düşüşler mümkündür. Yakın takip çalışmalarındaki düşük sürüklenme katsayıları, yakıt tasarruflarının artmasına ve hava kirliliğinin azalmasına sebep olur.

Anahtar kelimeler: Yol taşıtlarının aerodinamiği, sürüklenme, yakın takip, geçiş

To My Family

ACKNOWLEDGMENTS

The author wishes to express his appreciation to his supervisor Instr. Dr. A. Tahsin Çetinkaya and co-supervisor Prof. Dr. Kahraman Albayrak for their guidance, advice, criticism, encouragements and insight throughout the study.

The author would like to thank Prof. Dr. O. Cahit Eralp for his guidance, suggestions and comments during the tests in the Fluid Mechanics Laboratory.

The technical aids of Fluid Mechanics Laboratory technicians Mehmet Özçiftçi and Rahmi Ercan in the construction and maintenance of the experimental set-ups are gratefully acknowledged.

The author would also like to thank Assistant Serkan Kayılı and Mr. Erdem Örselli for their helps throughout the study.

The help and encouragement of all friends and relatives throughout the research are particularly appreciated.

The author would like to thank Nadiye Gür, his nearest and dearest, for her love, faith and understanding.

Finally, the author would like to thank and dedicate this thesis to his family for their endless support and love.

TABLE OF CONTENTS

LIST OF TABLES

TABLES

LIST OF FIGURES

FIGURES

LIST OF SYMBOLS

A_{model}	Frontal area of the model [m^2]
$A_{wind\ tunnel}$	Cross-sectional area of the test section, [m^2]
C	Cross-sectional area of the duplex test section, [m^2]
C_D	Drag coefficient
$C_{Dcorrected}$	Corrected drag coefficient
C_{Dovm}	Drag coefficient of the model in the overtaking maneuver situation
$C_{Dplatoon}$	Drag coefficient of the model in the platoon
C_{Dref}	Uncorrected drag coefficient determined with using the reference dynamic pressure
$C_{Dsingle}$	Drag coefficient of the model in the single vehicle situation
C_P	Pressure coefficient
$(C_{Dp})_{avg}$	Average drag coefficient of the models in the platoon
C_S^*	Slant part pressure drag coefficient
C_B^*	Base pressure drag coefficient
C_K^*	Forebody pressure drag coefficient
C_R^*	Friction drag coefficient
C_W^*	Total drag coefficient
C_{Dlocal}*	Corrected drag coefficient found with continuity correction method
C_{Dlocal}^{**}	Corrected drag coefficient found with pressure signature method
D	Drag force, [N]
D_p	Pressure drag, [N]
D_f	Skin friction drag, [N]
E	Bridge output voltage, [V]
E_a	Strain experienced by pair of strain gauge A
E_b	Strain experienced by pair of strain gauge B
E_c	Strain experienced by pair of strain gauge C
H	Height of the rear base, [m]
L	Length of the vehicle, [m]

N	Steady state normal force, [N]
P_{empty}	Static pressure at the ceiling when the test section is empty, [Pa]
$P_{with\ model}$	Static pressure at the ceiling when the test section contains the model, [Pa]
P_{local}	Local dynamic pressure, [Pa]
P_{∞}	Static pressure at the reference, [Pa]
Re	Reynolds number
$Re_{x\ crit}$	Reynolds number at the position of completed transition, [m]
S	Cross-sectional area of the model plus its mirror image, [m^2]
St	Strouhal number
S_d	Inter-vehicle spacing, [m]
T	Steady state tangential or axial force , [N]
U_{eff}	Effective fluid velocity, [m/s]
U_{local}	Local velocity, [m/s]
U_{∞}	Free stream velocity, [m/s]
V	Velocity of the vehicle, [m/s]
V_C	Corrected velocity, [m/s]
X_r	Recirculation length, [m]
d	Lateral spacing between models, [m]
f_v	Characteristic frequency of vortex shedding, [Hz]
k	Roughness height, [m]
l	Length of the model, [m]
q	Uncorrected dynamic pressure, [Pa]
q_c	Corrected dynamic pressure, [Pa]
t_d	lane change duration, [s]
u'	Turbulence intensity level, [m/s]
w	Width of the model, [m]
x	Distance from rear end of the leading model to front end of the trailing model, [m]
x_k	Position of the roughness element, [m]
x_{crit}	Position of the completed transition, [m]

α	Yaw angle, [Degree]
β	Rear slant (Backlight) angle, [degree]
δ	Boundary layer thickness, [m]
δ^*	Displacement thickness, [m]
$\delta_{l\ crit}$	displacement thickness at the position of transition, [m]
$\delta_{l\ k}$	displacement thickness at the position of the roughness element, [m]
ε	Equivalent roughness height, [m]
μ	Absolute viscosity, [N.s/m^2]
ρ	Fluid density, [kg/m^3]
τ	Shear stress, [N/m^2]
ΔCp	Differential pressure coefficient
ΔR	Change in electrical resistance, [ohm]
Δv	Change in voltage, [V]

CHAPTER 1

INTRODUCTION

In the early stages, the aerodynamic development was done by individuals mostly coming outside the car industry. What they tried to do was to carry over the aerodynamic principles of the aerospace and naval industry to cars. However it soon turned out to be the wrong approach and new concepts were introduced. As the years passed, the studies on aerodynamic effects on cars increased and the designs were developed to accommodate for the increasing needs and for economic reasons. Nowadays, what the designers are trying to develop is the concept of the car which is influenced by many factors [1]. (Figure 1.1)

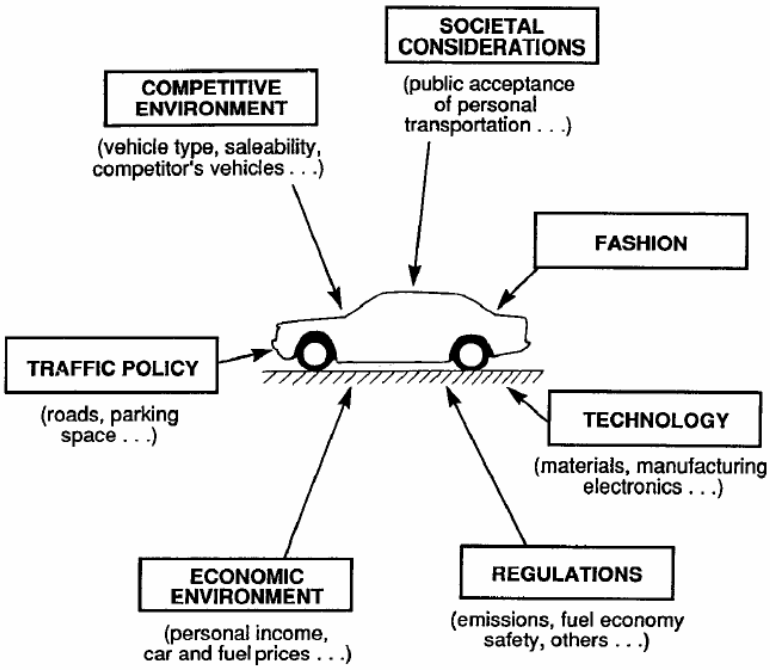

Figure 1.1 The concept of a car [1]

In Fluid Mechanical terms, a road vehicle is essentially a bluff body in very close ground proximity. The geometry of the vehicle is complex, the flow around it is fully three-dimensional, the boundary layers are turbulent, flow separation is common and there are large turbulent wakes in which longitudinal trailing vortices are common. As it is typical for bluff bodies, the principal contribution to drag experienced by a road vehicle is pressure drag and a major objective of vehicle aerodynamic design is the avoidance, reduction or control of flow separation. The prime considerations in road-vehicle design are function, economics and aesthetics. Hence, the characteristics of a particular road vehicle are often not intentional but a consequence of the vehicle's shape. Vehicle attributes which are affected by the aerodynamic characteristics include performance, fuel economy, handling, crosswind sensitivity and “Functionals”. [1]

It is a common experience among drivers that one feels a severe aerodynamic effects when his car passes or is passed by a large truck. Several studies have discovered that a passed car experiences a significant change of drag, side force and yaw moment induced by an overtaking vehicle, which may cause the disturbed car lose control. In recent years, the situation of simultaneous driving on the expressway of various sizes of vehicles has been increasing. From this situation, the aerodynamic interference problem has become more serious. [2]

In the current study, aerodynamic interactions of vehicle models in close-following and passing situations are investigated experimentally. The main aim of this experimental work is to examine the effects of the aerodynamic interaction parameters on the behavior of vehicle drag. In the direction of this aim, in chapter 2, various studies about reference models and aerodynamic interactions are reported extensively. In chapter 3, theoretical considerations about aerodynamics of road vehicles are summarized. In Chapter 4, the experimental equipments and instrumentation used in the experiments are explained. Required calibrations and preparations of the experiments and experimental procedures are mentioned in Chapter 5. Test results and discussions are given in Chapter 6. Finally, in Chapter 7, conclusions and future work recommendations are made.

CHAPTER 2

REVIEW OF PREVIOUS WORKS

Road Vehicle Aerodynamics is important as it can affect many areas of a ground vehicle's performance. Aerodynamics can significantly influence the fuel efficiency, stability, handling and noise levels of a vehicle. Designers have gained their understanding of the air flow around a vehicle through extensive wind tunnel testing.

Wake structure is an important factor that affects aerodynamic characteristic of a vehicle. The flow region which presents the major contribution to a car's drag, is the wake flow behind the car. The location at which the flow separates determines the size of the separation zone,and consequently the drag force. In this study, it is aimed to investigate the effects of gap and position with a lateral distance on drag coefficients of two close-following vehicles. For all measurements, the effect of shapes of the models is also aimed to be investigated. In the direction of these aims, firstly, previous studies about MIRA and Ahmed Body reference models are presented. Finally, aerodynamic interaction studies in the Literature are mentioned.

Ahmed et al [3] defined a simplified vehicle-like body to conduct a detailed study of the surface pressure distribution, wake structure and how the wake structure is modified by varying rear-slant angle (Figure 2.1). An investigation of the relative contributions to drag from pressure on the nose, base and slant was done at $\beta = 5°$, 12.5°, 30° (high drag) and 30° (low drag). A vertical splitter plate in the symmetry plane was used in the wake of the 30° slant to encourage the low-drag flow. Visualization techniques were employed to examine the structure of the wake and time-averaged velocity measurements were made on the centerline plane and at transverse planes in the wake. Measurements of the total drag were made at 5° intervals for slant angles from $\beta = 0°$ to 40°.

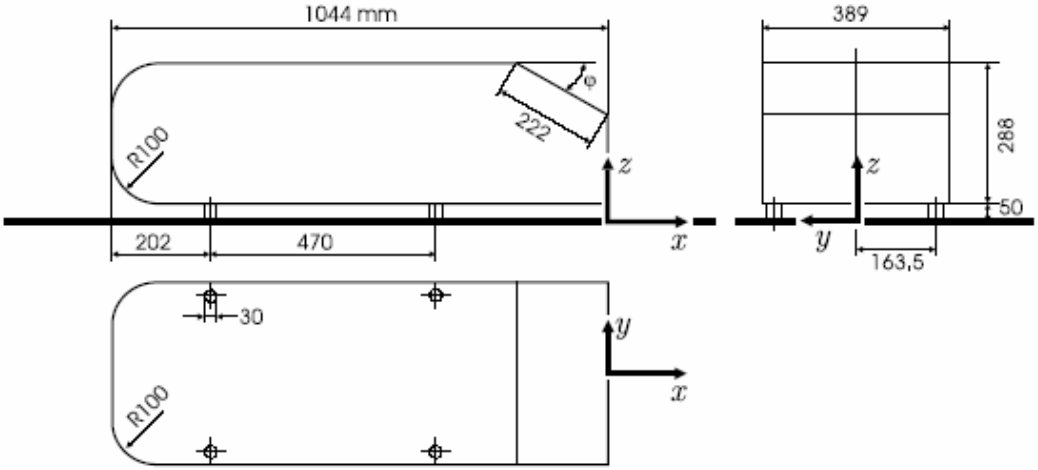

Figure 2.1 Ahmed Body

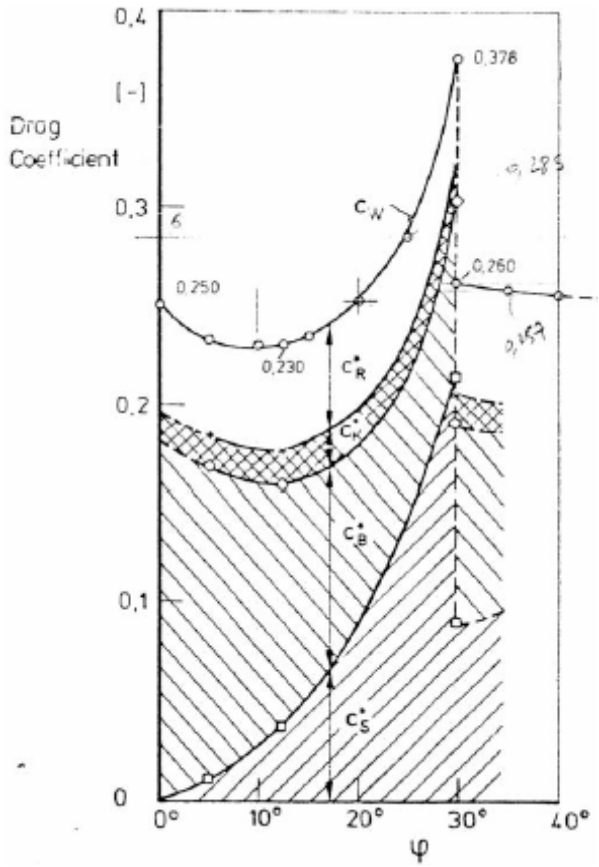

Figure 2.2 Variation of Drag with Base Slant Angle

where, C_S^* is the slant part pressure drag coefficient ; C_R^* is the friction drag coefficient ; C_B^* is the base pressure drag coefficient ; C_K^* is the forebody pressure drag coefficient and C_W^* is the total drag coefficient.

Figure 2.3 show sketches of the time-averaged wake structure for the low drag $\beta \approx 20°$ and high drag $\beta \approx 30°$ configurations [3]. It was observed that the flow over the 20° slant was fully attached. Downstream of the base of the Ahmed Body, there were two horseshoe vortices (marked as *A* and *B* in Figure 2.3) which interacted with the flow leaving the slant, the side-edge vortices and the flow from the underside of the body. As the slant angle was increased from 20° to 30°, the strength of the side-edge vortices increased and a separation bubble appeared at the leading edge of the slant (where the slant meets the top surface of the Ahmed Body).

a) **b)**

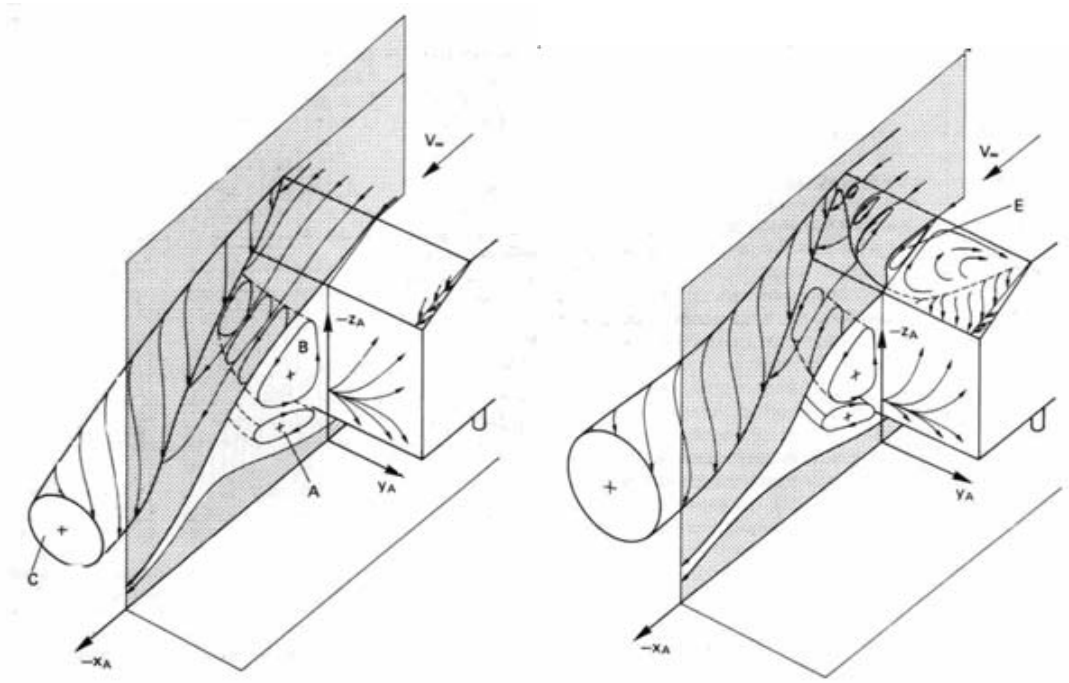

Figure 2.3 Time-averaged wake structure of the Ahmed Body [3]:
a) Low Drag Flow (20°), b) High Drag Flow (30°)

Using the same geometry, Sims-Williams [4] conducted a detailed study on the time-averaged and unsteady flow structures associated with the critical geometry. Using a smoke flow visualization technique, Sims-Williams demonstrated the sensitivity of the flow pattern near the critical backlight angle. They observed that when the tunnel was started up from rest, the flow would be in the low drag state, and then it would switch to the high drag state after several minutes and persist indefinitely. The lower the freestream speed, the longer that the low drag flow state would exist. Figure 2.4 shows the two flow states existing at the same backlight angle.

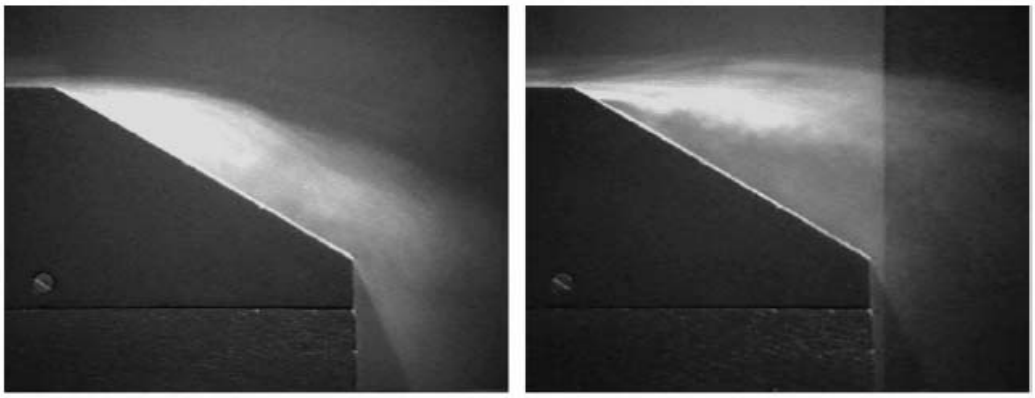

(a) High-Drag (b) Low-Drag

Figure 2.4 High and Low Drag Structures at the Same Backlight Angle of 30° [4]

Duell and George [5] and Berger et al [6] proposed a link between the shedding from the base and the pumping at the free stagnation point through repeated vortex pairing in the shear layers. In their work, Duell and George [5] reported that the shear layer vortices were first shed uniformly on one side, then obliquely from the top of the model. One half periods after that process started, the vortex was shed uniformly from the opposite side, then obliquely from the bottom of the model, which was connected to the next vortex shed uniformly from the original side. That formed a pseudo-helical vortex structure. Vortex pairing occurred as vortices were convected downstream in the shear layer. Vortex pairing reduced the characteristic frequency of

the resulting vortices by about on-half and increased their size. Pairing continued until the shear layer closed at the free stagnation point. They define a mean circulation length which is an important characteristic feature of the near wake circulation region. The recirculation length, X_r, was defined as the distance between the model base and the mean location of the free stagnation point. They demonstrated how the characteristic frequency in the shear layer decreased as the distance from the separation point on the body increased. The distinct peak of the power spectral density of the velocity measured at $0.266X_r$. Figure 2.5 shows the schematic view of the model and mean near wake along X-Z plane at Y = 0. Also, the growth of eddies in the shear layer and eventual vortex shedding, resulting in free stagnation point fluctuation is shown in this figure.

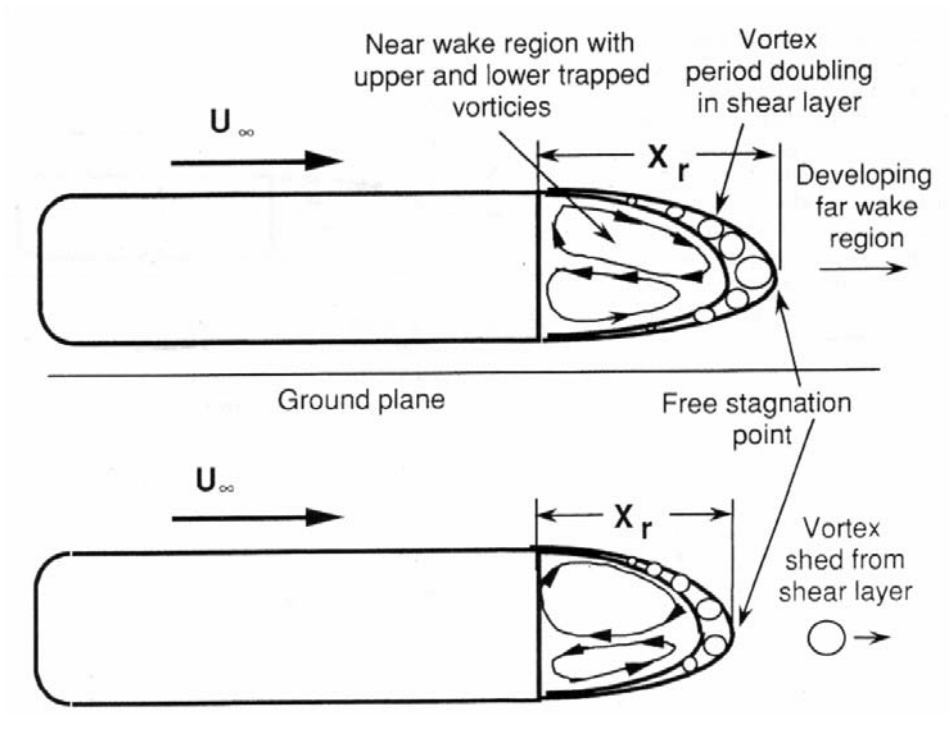

Figure 2.5 Schematic View of the Model and Mean near Wake along X-Z Plane at Y= 0 at Two Successive Times

Templin and Raimando [7] used a pressure signature method for 0.2, 0.25 and 0.3 scale MIRA Notchback models in DSMA closed test section wind tunnel. In that

study, wall interference was experimentally investigated in one solid and two open-area ratios (OAR) slotted wall test sections. The blockage interference was studied using surface pressures from three scales of MIRA Notchback reference models, representing 8.3%, 13.0% and 18.7% area blockage. This method was used to determine the wall-induced interference velocity at the model location for the solid-wall test-section. Comparison was made between the predicted "free-air" pressures and those measured in the 30% slotted wall test sections. It was shown that a slotted wall test section can provide a virtually interference-free testing environment. Basic dimensions of the vehicle are shown in Figure 2.6

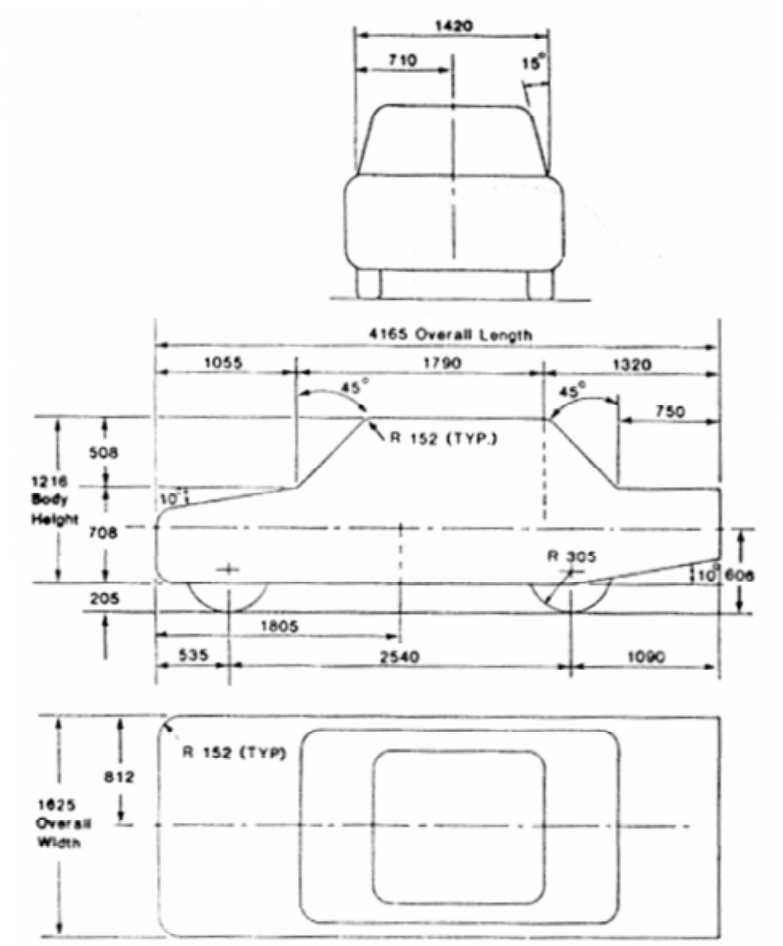

Figure 2.6 MIRA Notchback Car Model (dimensions are in mm) [7]

Jack Williams et al [8] used different scale MIRA models for the comparison of relative aerodynamic simulation quality obtained with two test section configurations: semi-open jet and slotted wall in Ford/Sverdrup drivability test facility (DTF). In their study, MIRA and CoA closed wall test sections extrapolated to zero blockage values were also used. Four automobile shapes (MIRA models) and six sport utility vehicle (SUV) shapes representing blockages from 7% to 25% were used (7%, 11%, 15%, 20%, 25%). Six component force and moment measurements were made with an external strain gage balance. Strain gage output was amplified using a signal conditioning unit and all models were tested at a single Reynolds number 1×10^6 to arrive the largest Reynolds number that could be achieved for all of the models; the smallest model was tested at the highest possible tunnel speed. In order to match Reynolds number for each model, the velocity was changed to compensate for the various model lengths. This change in velocity altered the boundary layer displacement thickness. When the ground effects were compared, the largest models were found to be best. The drag coefficient results for MIRA Notchback configurations are presented as a function of blockage ratio in Figure 2.7

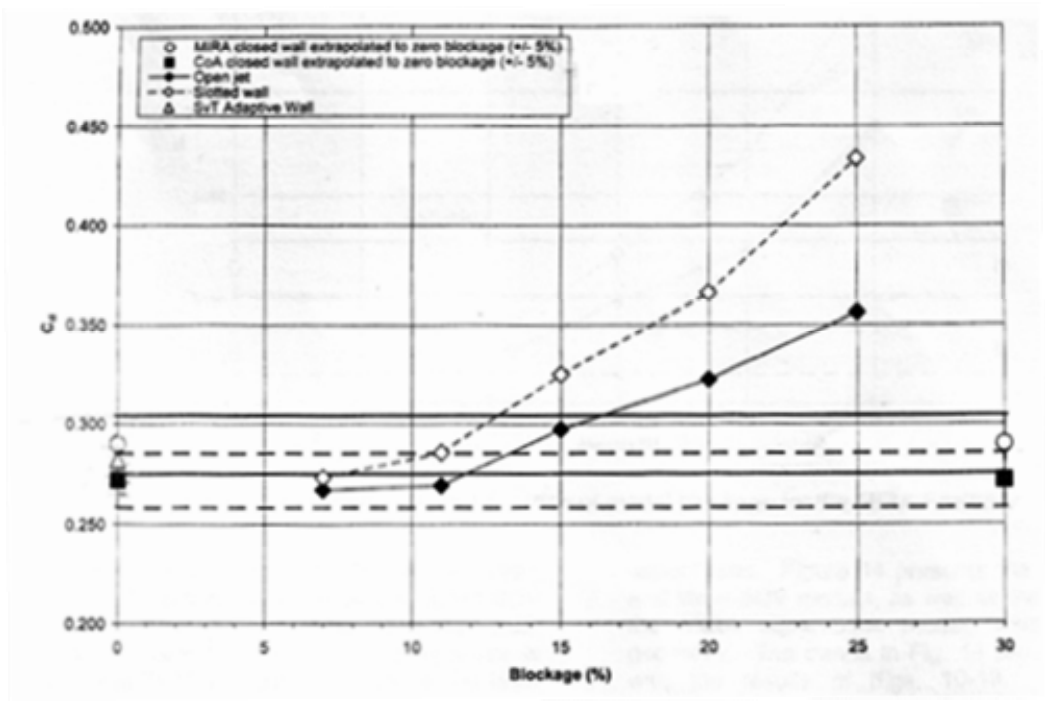

Figure 2.7 C_D as a Function of Model Blockage for MIRA Notchback Model [8]

According to the results, it was concluded that the open jet test section had better agreement than the slotted wall test section. It was especially pronounced at the higher blockage ratios.

Mercker E. [9] described his method which was about corrections of blockage effects on passenger cars tested in a closed test section of a wind tunnel normal to the flow and in a cross wind flow up to 30°. Full scale of MIRA Notchback model was tested in German-Dutch Wind Tunnel (DNW) with three differently closed test sections (6×6, 8×6, 9.5×9.5 m²). C_D value of full-scale MIRA Notchback model was found 0.28 for 8×6 m² and 0.278 for 6×6 m² test section configurations.

Zabat et al [10], [11] determined the aerodynamic characteristics for a platoon* of vehicles under steady conditions. Their study gives detailed information about the design and implementation of wind tunnel tests to evaluate the aerodynamic performance of individual members of 2, 3 and 4-vehicle platoons. l/8th scale General Motor's Chevrolet Lumina All-Purpose Vehicle models were used (Figure 2.8).

Figure 2.8 1/8 Scale of 1991 GM Lumina APV Model

* Two or more vehicles as a unit when they are traveling at the same speed with relatively small inter-vehicle spacing.

Experiments were conducted at Reynolds numbers in the range 3.2-4.1×10^5 corresponding to air speeds of 20-25 m/s in the USC Dryden Wind Tunnel. Its test section had an octagonal shape 1.37 m wide and 7.4 m long. The ground plane was installed in the test section. Interior of the ground plane was equipped with an optical rail secured to the center line of the bottom plate. Four movable carriages slide along the optical rail were used to support the vehicle models above the porous surface. The wind-tunnel test section was equipped with a traverse mechanism which could be moved in three directions by means of stepper motors. Pitot tubes or hot-wire sensors were mounted on this traverse to measure local values of pressure or velocity at any location in the test section. For the boundary layer, a Pitot tube with an outer diameter of approximately 1 mm was used. The models were placed either on the porous ground plane or on a portion of the ground plane which was covered with a thin sheet of Mylar, referred to as a *footprint.* A simpler procedure, but one which also makes use of the static pressure distribution along the wind tunnel ceiling was used for blockage correction.

Drag was measured on each of 2, 3 and 4 models in tandem in the wind tunnel. The spacing between models was uniform and measured from the trailing edge of the forward vehicle to the leading edge of the rear vehicle. The distance was normalized by the model length, so that spacing 1 is a distance of 1 car-length. The data presented was averaged over at least three sets of independent measurements.

According to the results, the average drag coefficient was measured 0.361 with a standard deviation of 3.5%. The Blockage-corrected estimate was 0.332 with a standard deviation of 2.6%. Figure 2.9 presents the data for a 2-vehicle platoon as a function of spacing between vehicles. C_D of each platoon member was divided by C_D for the same model in isolation at the identical position in the wind tunnel. Spacing was measured on the centerline from the rear bumper of the lead model to the front bumper of the trail model and normalized with model length.

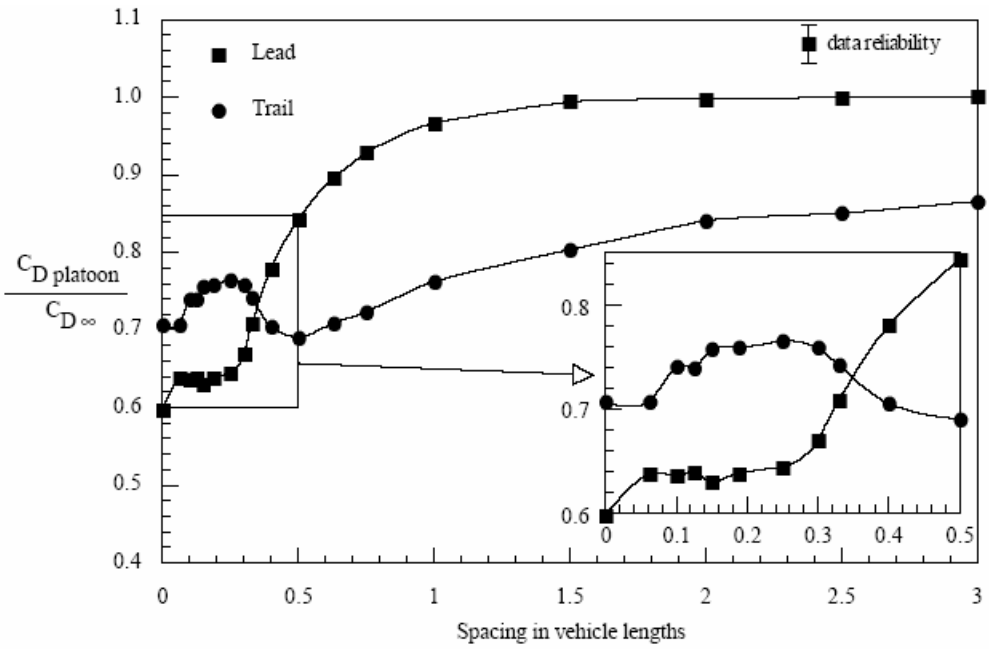

Figure 2.9 Drag Reduction for a 2-Car Platoon

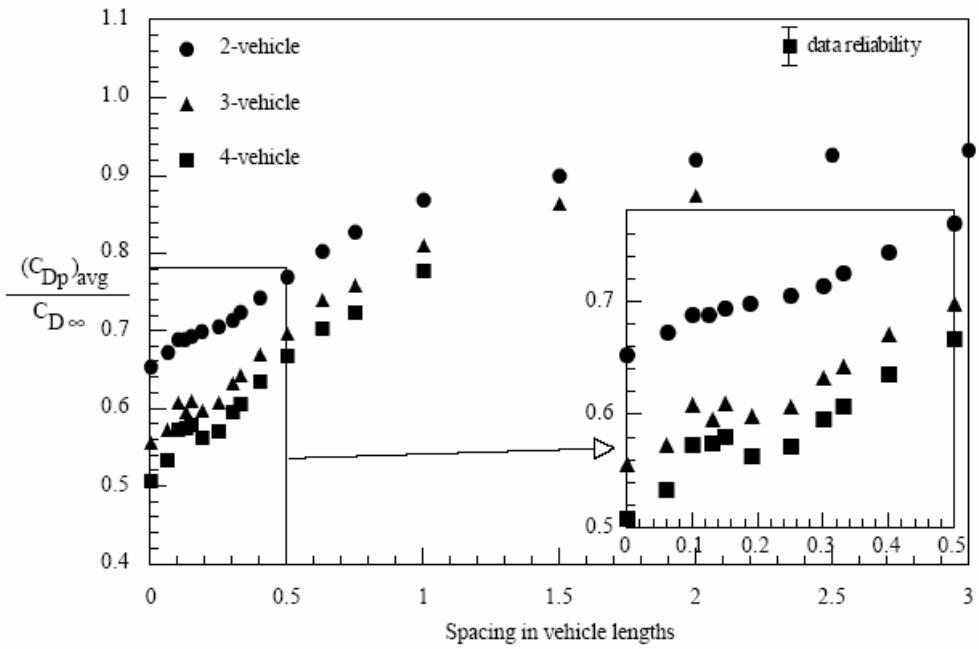

Figure 2.10 Average Drag Coefficient Ratios for 2, 3 and 4 Vehicle Platoons

Chen et al. [12] investigated the transient aerodynamic forces on automotive vehicles traveling in close proximity to each other. In that study, drag force, side force and yawing moment on each of the 4 vehicles was measured for various configurations of the platoon. 1/20 scale models of the 1997 Buick LeSabre were used (Figure 2.11).

Figure 2.11 1/20 Scale Model of the 1997 Buick LeSabre [12]

Experiments were conducted at Fluid Mechanics Laboratory of the University of California at Berkeley. All measurements were made at Re= 3.4×10^5 corresponding a wind tunnel speed of 20 m/s. Since the frontal area of the model was too small when compared with the wind tunnel test section area, A_{model} / $A_{wind\ tunnel}$ < 0.01, blockage corrections were not needed to be applied. With the inter-vehicle spacing of S_d = 0.41 and lane change duration of t_d= 0.5 seconds, three inter-vehicle spacings were tested**:** 0.21, 0.41**,** 1. Any one of the four models could be arranged as the mobile car. For each location of the mobile vehicle and each vehicle separation, the mobile car was moved at six different accelerations. Three experimental runs were made for each configuration of the platoon. For each experimental run, the mobile car was moved out of the platoon 2.5w**,** paused, and returned back into the platoon. Measurements were also made on a single vehicle model for comparison with the measurements for vehicles in a platoon configuration. In addition, measurements

were made at the design separation S_d using a platoon of rectangular boxes, simpler shapes than the cars for comparison.

According to the results, single vehicle drag coefficient was measured 0.297. The ratio of the drag coefficient for vehicles in a platoon to that of a single vehicle versus the vehicle location in the platoon and the vehicle separation is shown in Figure 2.12, respectively. The data of this study are shown as lines, while those of Zabat et al [10] are shown as symbols.

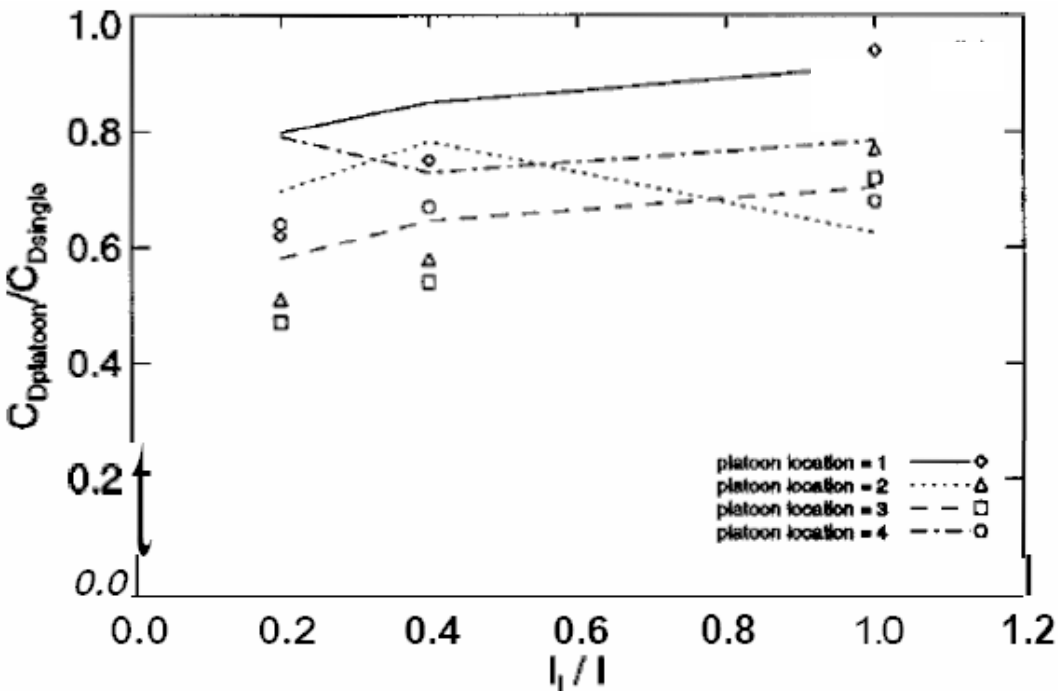

Figure 2.12 Drag Coefficient of Vehicles vs. Vehicle Location in The Platoon [12]

Browand F. et al. [13] conducted an experimental study that aimed to document the drag reduction for a two vehicle platoon. An extensive set of full scale experiments were conducted on El Mirage dry lakebed, using two Ford Windstar minivans. (Figure 2.13)

Figure 2.13 Two Vehicles Close-Following at El-Mirage Dry Lakebed. [13]

The drag forces were measured with the aid of a tow bar. Three series of experiments were carried out: i) coast-down experiments for a single vehicle with transmission set to "Neutral" position; ii) coast-down experiments for a single vehicle with "Free-wheeling" hubs mounted on the drive wheels (to eliminate transmission/engine influences); iii) two-vehicle close-following experiments consisting of an acceleration phase and a deceleration phase. The acceleration phase allowed estimation of the drag of the trail vehicle, and the deceleration phase provides an estimate for the drag of the lead vehicle. Two separate sets of tow bar data were analyzed. Estimation of the drag of both vehicles in the platoon as a fraction of the drag of a vehicle in isolation was obtained for spacing between 0.23 vehicle lengths to 1.0 vehicle lengths.

It was stated by the authors that the drag ratio curves displayed a dependency on vehicle spacing similar to the wind tunnel results obtained using 1/8 scale models (Figure 2.14). The lead vehicle experiences less drag than the trailing vehicle at close spacings. The reversal occurs at a spacing of about 0.43 vehicle lengths, compared to the wind tunnel prediction of 0.38 lengths. The drag reductions observed for the full scale vehicles are 5-10% greater than the results obtained in the wind tunnel.

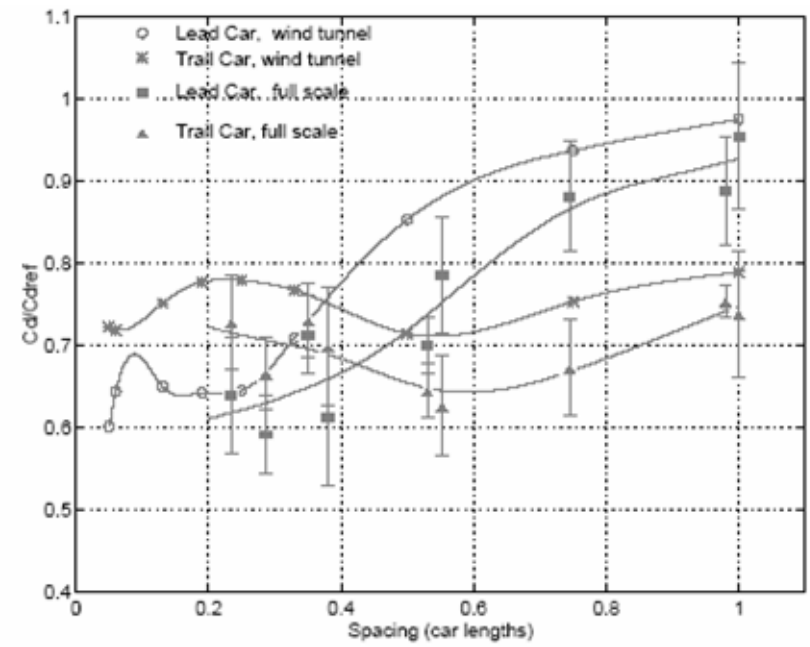

Figure 2.14 Drag Coefficient Ratios for a Full Scale Two-Car Platoon: A Comparison to the Wind Tunnel 1/8 Scale Results. [13]

In the study carried out by Browand F. and Michaelian M. [14], on-road test results involved 2, 3 and 4 car platoon operations under fully automatic longitudinal and lateral control were given. They demonstrated that the fuel injector pulse width, in combination with engine Rpm and forward speed could be used to determine accurate estimates of instantaneous fuel consumption. Platoons of two, three and four cars were formed and operated at spacings of 3m, 4m, 5m, and 6m. In terms of the length of the Buick LeSabre, 5.1 meters, the spacings became 0.59, 0.78, 0.98, and 1.18 vehicle lengths. Specifically, the two-car platoon and the three-car platoon were tested at all four spacings; the four-car platoon was tested at 0.78, 0.98, and 1.18 vehicle lengths. On-Road platoon configurations are illustrated in Figure 2.15. All of the configurations were first run south-to-north and then returned north-to-south. They called each of these tests as a round trip and during three test days, twenty two separate round trips were recorded.

Figure 2.15 Two Vehicles Close-Following in the HOV Lane [14]

The authors mentioned that south-to-north travel had 2.4 km distance since there was more uphill travel in this direction. They tried to take out the effects of non-zero road slope. Additional fuel expenditure would be used to compensate the power dissipated in the braking process. In order to assess this effect, a second test circuit was formed. This second test circuit was referred to as the 1.8 km abridged round trip.

The Buick LeSabre cars were designed for close-following employ radar sensors to monitor spacing and magnetometer sensors for lane keeping. These inputs were accompanied by the appropriate computer algorithms to allow autonomous steering, throttling, and braking. A variety of engine parameters were recorded digitally during normal platoon operations. Of particular use in this study were engine rpm, forward velocity, absolute position on the roadway (magnetic marker position), intake manifold pressure, brake pressure, and longitudinal acceleration. The last three were not used directly, but prove useful in evaluating the quality of the individual trips. These data, sampled continuously at 100 Hz, were stored in a laptop computer installed next to the driver. To obtain estimates of instantaneous fuel consumption for each car, the engine fuel injector signals were measured. The engine Power Control Module (computer) generated a pulse train that was output to the fuel injectors to

establish the timing and duration of fuel injector openings and closings. The major fuel consumption results for close-following are displayed in Figure 2.16 for two car platoon state. The upper numbers are for the full 2.4 kilometer section, the lower numbers are for the 1.8 kilometer portion.

According to the results, it was obtained that fuel consumption savings resulting from close following did not depend upon the round-trip paths. Fuel savings for individual vehicles within a platoon were strongly correlated with position within the platoon for all the spacings tested (3m - 6m). Interior vehicles experienced fuel savings of the order of 10%. Trail vehicles experienced approximately 7% savings, and forward vehicles (lead vehicles) showed a gain of 3-4%. Regarding the platoon as a whole, the average fuel savings for 2, 3, 4 vehicle platoons at a spacing of 3 meters were 5.5%, 7.5%, and 8.5 %, respectively.

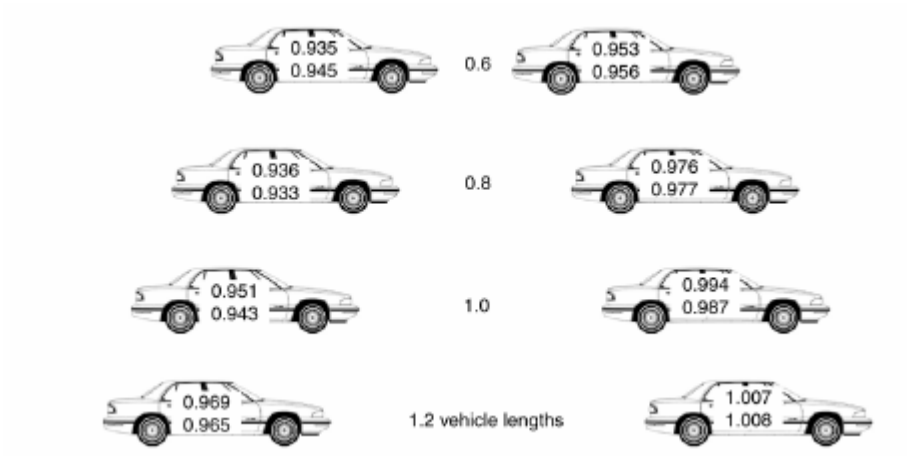

Figure 2.16 Fuel Consumptions for Vehicles in Two-Car Platoon Relative to Fuel Consumption for the Identical Trip[1] [14]

[1] Top numbers are for the 2.4 km round trip; bottom numbers for 1.8 km portion.

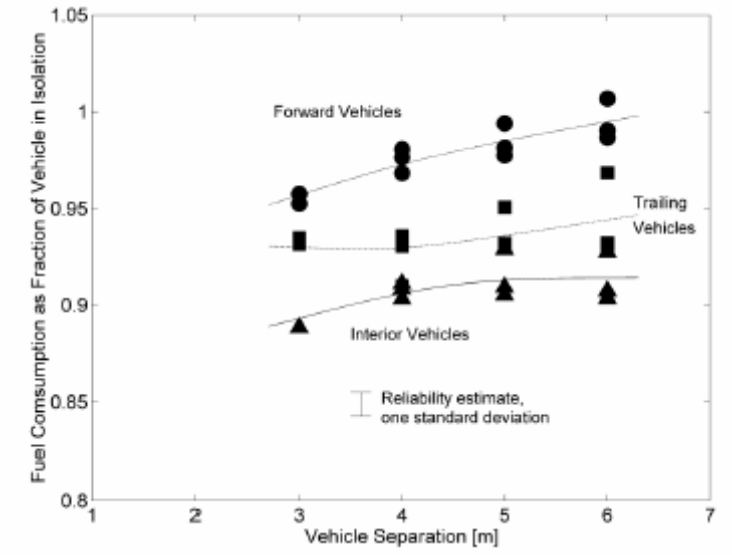

Figure 2.17 Fuel Consumption for Close Following Relative to Fuel Consumption for a Single Vehicle over the 2.4 km Round Trip. [14]

Another Coast-Down experimental study about close-following operations was conducted by Browand et al. [15]. In that study, the fuel consumption of two tandem trucks was recorded for truck spacings of 3, 4, 6, 8, and 10 meters.

Figure 2.18 Two Freightliner Trucks in Close-following [15]

The trucks were linked by means of an electronic control system, and were operated on an unused runway at Crows Landing, California (Figure 2.18). The trucks had automatic transmissions. The engine controls were modified to allow throttle and braking to take place under programmed computer control. The control algorithm included input from a laser ranging device mounted on the front of the following truck. As a result, it was found that the average fuel consumption saving to be achieved by tandem operation varies from about 11% at 3-4 meters spacing to about 8% at 8-10 meters spacing.

A few studies were conducted on the passing of a smaller vehicle by a larger vehicle [16], [17]. According to the results of these studies, it was obtained that when a large vehicle passed a smaller one, the larger vehicle induced a side force and yawing moment on the smaller vehicle, which could result in loss of control. Other studies had attempted to simulate a passing maneuver with static measurements. In these studies, a large vehicle was placed at different longitudinal and lateral spacings with respect to a smaller vehicle [18], [19]. According to the results, certain configurations resulted in large aerodynamic forces induced on the smaller vehicle, although they were not able to capture any transients.

The aerodynamics of road vehicles is essentially flow around bluff bodies. The majority of the studies had focused on the steady aerodynamic characteristics of bluff bodies in tandem, including various combinations of cylinders [20], [21], disks [22], boxes [23], and scale vehicle models [24]. Koenig and Roshko [25] performed experiments on a disk and cylinder in tandem. A review of data about two cylinders in tandem, lateral alignment, and staggered arrangements was performed by Zdravkovich [26]. The results of these studies showed that drag could be minimized for certain optimal configurations, while other configurations resulted in high values of drag and side forces.

CHAPTER 3

THEORETICAL CONSIDERATIONS

In characterizing the aerodynamic behavior of road vehicles in close-following and passing situations, drag is the most important factor from the viewpoint of the fuel economy. In this chapter, firstly, aerodynamic drag of road vehicles and its components are considered. From the dimensional analysis, the relevant flow parameters are identified. Then, the basis of similarity is discussed. Finally, the wall interference effects and blockage correction methods are mentioned briefly

3.1 Aerodynamic Drag

A body in motion is affected by aerodynamic forces. The aerodynamic force acts externally on the body of a vehicle. The component of the resultant aerodynamic force which opposes the forward motion is called the aerodynamic drag. Aerodynamic drag affects the performance of a car in both speed and fuel economy as it is the power required to overcome the opposing force. The other component, directed vertically, is called the aerodynamic lift. It reduces the frictional forces between the tires and the road thus changing dramatically the handling characteristics of the vehicle. The aerodynamic force is the net result of all the changing distributed pressures which airstreams exert on the car surface.

There are two different perspectives to examining the aerodynamic force: (1) from that of the body, and (2) from that of the fluid flow. According to Newton's third law, the force on the body due to the fluid flow is opposite to the force imposed by the body on the fluid flow. The force on the body in the direction of the free stream is called *Drag, D.* The Drag that a fluid stream exerts on a vehicle is the integral of the normal (pressure) and the tangential (skin friction) surface forces, i.e. $D = D_p + D_f$.

In order to explain the Aerodynamic Drag, two forces skin friction and pressure drags have to be analyzed.

3.1.1 Skin Friction Drag

If a velocity gradient *du / dy* is present in a viscous fluid at the wall, due to the molecular friction a shear stress τ acts everywhere on the surface. (Figure 3.1) The integration of the corresponding force components in the free stream direction according to $D_f = \oint \tau \sin\theta dA$ leads to *skin friction drag, D_f* [27].

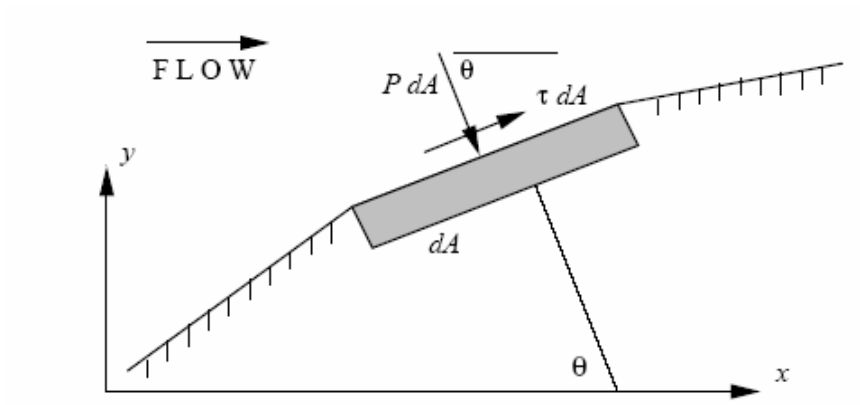

Figure 3.1 Pressure and shear forces on a differential element of a moving body

3.1.2 Pressure Drag

Integrating the force components in the free stream direction resulting from pressure distribution $D_p = \oint P \cos\theta dA$ gives *pressure drag* or *form drag, D_p*.

The flow separations that lead to a pressure drag can be divided into two different types. In the first type, the separation line is located perpendicular to the flow direction. In this case, vortices are generated, the axes of which are also

perpendicular to the outer flow. Velocity components parallel to the vortex axes are very small. For small Re, symmetrical flow in the separated region exits. For larger Re, periodic vortex shedding occurs and the flow in the separated region is basically unsteady. The kinetic energy of the vortex field is rapidly dissipated by turbulent mixing and irreversibly converted into frictional heat. This leads to a considerable total pressure loss in the region behind the body and corresponding deficit in kinetic energy is equal to the work which is necessary to overcome pressure drag. Behind the body, a wake is formed in which time averaged, relatively uniform suction and very low flow velocities are present.

Second type of flow separation is characterized by a separation line inclined with respect to the oncoming flow. In this case, vortices are shed, the axes of which are roughly parallel to the separation lines. A considerable velocity component, parallel to the separation line and therefore in the direction of the vortex axes, is present. Thus, a well-ordered, steady three dimensional flow separation is found. On the rearward surface of the body, this separated flow induces suction which leads to a pressure drag. On the inclined base of the body, the flow is attached. In the vicinity of vortices, the pressure distribution is characterized by suction peaks. Behind the body, only relatively small total pressure losses are observed. The flow field of the concentrated vortices contains a lot of kinetic energy which corresponds to the work necessary to overcome the pressure drag [28].

3.2 Dimensional Analysis and Similarity

3.2.1 Dimensional Analysis of the Flow on a Road Vehicle

Considering the effect of each parameter on the drag experimentally is time consuming and expensive. Instead of these works, the meaningful results can be obtained with significantly less effort through the use of dimensional analysis. By making a dimensional analysis, dimensionless groups are obtained. Then, these groups are utilized in preparation and testing of the large and small scale configurations.

The Buckingham Π theorem is a statement of the relation between a function expressed in terms of dimensional parameters and a related function expressed in terms of nondimensional parameters. Use of the Buckingham Π theorem allows the important nondimensional parameters to be developed. According to the theorem, the parameters that affect the drag of a Road vehicle can be written in functional form as:

$$D = g\left(L, V, \rho, \mu, \varepsilon, \alpha\right) \tag{3.1}$$

where, L is the length of the vehicle (m); V is the velocity of the vehicle (m/s); ρ is density of air (kg/m^3); μ is the absolute viscosity of air (N.s/m^2); ε is the equivalent roughness height (m) and α is the yaw angle. The angle α does not have a dimension, so it can be taken out of the function. Then, a set of primary dimensions are selected, and the dimensions of all parameters are written in terms of the primary dimensions. If "M, L, t" is selected as primary dimensions, the dimensions of all parameters in Equation 4.17 are listed as

$$\begin{array}{lcccccc} D = g\left(\right. & L, & V, & \rho, & \mu, & \varepsilon\left.\right) & \text{n=6 parameters} \\ \downarrow & \downarrow & \downarrow & \downarrow & \downarrow & \downarrow & \\ \dfrac{M.L}{t^2} = & L & \dfrac{L}{t} & \dfrac{M}{L^3} & \dfrac{M}{L.t} & L & \text{r=3 primary dimension} \end{array} \tag{3.2}$$

Now, repeating parameters are selected. The number of repeating parameters is generally equal to the number of primary dimensions. They must include all the primary dimensions. If ρ, V, and L are selected as repeating parameters, then n-r=3 dimensionless groups will result. By setting up dimensional equations, the nondimensional Π parameters are obtained.

$$\Pi_1 = G\left(\Pi_2, \Pi_3\right) \tag{3.3}$$

The first parameter Π_1 is obtained as:

$$\Pi_1 = \rho^a.V^b.L^c.D = \left[\left(\frac{M}{L^3}\right)^a.\left(\frac{L}{t}\right)^b.(L)^c.\left(\frac{M.L}{t^2}\right)\right] = \left[M^0.L^0.t^0\right] \tag{3.4}$$

Equating the exponents of M, L, t results in

$$\begin{array}{lll} M: & a+1=0 & a=-1 \\ t: & -b-2=0 & b=-2 \\ L: & -3a+b+c+1=0 & c=-2 \end{array}$$

Therefore,

$$\Pi_1 = \frac{D}{\rho.V^2.L^2} \tag{3.5}$$

Equation (3.5) can be expressed in a form that the *projected frontal area of the vehicle, A,* can be written instead of L^2. And dividing this parameter with 1/2 results in;

$$\Pi_1 = \frac{D}{\frac{1}{2}\rho.V^2.A} \tag{3.6}$$

where, $1/2\rho V^2$ is the free stream dynamic pressure on largest cross-section of the body and A is the frontal area exposed to the oncoming flow. Thus, this parameter is expressed as the ratio of drag force with the dynamic head and called as *drag coefficient.*

In a similar way, the other nondimensional parameters can be determined.

$$\Pi_2 = \rho^d.V^e.L^f.\mu = \left[\left(\frac{M}{L^3}\right)^d.\left(\frac{L}{t}\right)^e.(L)^f.\left(\frac{M.}{L.t}\right)\right] = \left[M^0.L^0.t^0\right] \tag{3.7}$$

Equating the exponents of M, L, t results in

$$\begin{array}{lll} M: & d+1=0 & d=-1 \\ t: & -e-1=0 & e=-1 \\ L: & -3d+e+f+1=0 & f=-2 \end{array}$$

Therefore,

$$\Pi_2 = \frac{\mu}{\rho.V.L} \tag{3.8}$$

$$\Pi_3 = \rho^x.V^y.L^z.\varepsilon = \left[\left(\frac{M}{L^3}\right)^x.\left(\frac{L}{t}\right)^y.(L)^z.(L)\right] = \left[M^0.L^0.t^0\right] \tag{3.9}$$

After equating the exponents of M, L, and t; x and y are determined as 0 and z is -1. The third Π number is obtained as;

$$\Pi_3 = \frac{\varepsilon}{L} \tag{3.10}$$

Thus, this functional relationship is obtained;

$$\frac{D}{\frac{1}{2}\rho.V^2.A} = G\left(\frac{\rho.V.L}{\mu}, \frac{\varepsilon}{L}\right) \tag{3.11}$$

The Π group at the left hand side of the above equation is the force coefficient, and the others at right hand side have special names, which are important parameters in Fluid Mechanics. When Equation 3.11 is written in terms of these numbers (also including the angle α), this function is obtained:

$$C_D = G\left(Re, \frac{\varepsilon}{L}, \alpha\right) \tag{3.12}$$

where, C_D is the Drag Coefficient; Re is the Reynolds number; ε / L is the Surface Roughness and α is the yaw angle.

The effect of *surface roughness, ε / L,* is to cause transition from laminar to turbulent boundary layer flow to occur at a lower Reynolds number than if the surface is smooth. In practice, surface roughness varies from one body to another and depends on material texture, surface finish, extent of corrosion and the build up of deposits. For the purposes of estimating drag forces it is convenient to define an equivalent surface roughness height, ε. The equivalent roughness height of a rough body refers to the size of uniform particles evenly distributed over the smooth surface of a geometrically identical body which gives the same resistance to motion under identical flow conditions. It is usually assumed that the equivalent roughness height is independent of Reynolds number so that the ratio is a non-dimensional parameter influencing the value of the drag coefficient. As the model become smaller, the surface smoothness becomes worse and that affects the skin friction. However, the most part of the drag arises from the pressure differences. Thus, surface roughness is the secondary important parameter for road vehicle aerodynamics.

Yaw angle, α, is the angle of inclination of free-stream direction to body longitudinal axis. Generally, road vehicles operate at nonzero angle of yaw. It is the aerodynamic component along the direction of travel that resists vehicle motion, so this is the relevant drag. In this study, all experiments were conducted at zero angle of yaw. Since it was taken at a constant value, yaw angle was not considered for the drag coefficient.

3.2.2 Similarity

When experimental testing of a full size prototype is either impossible or too expensive, the only feasible way of attacking the problem is through model testing in the laboratory. A model test must yield data that can be scaled to obtain the forces, moments and dynamic loads that would exist on the full scale prototype. There are three types of similarity conditions that must be met to ensure the similarity of model and prototype flows. These are;

a) Geometric Similarity
b) Kinematic Similarity
c) Dynamic Similarity

3.2.2.1 Geometric Similarity

The first requirement is that the model and prototype must be *geometrically similar.* It requires that the model and prototype be the same shape and that all linear dimensions of the model be related to corresponding dimensions of the prototype by a constant scale factor. In the present study, 1/4 scale Ahmed Body model with 0° rear slant angle and 1/18 scale MIRA Notchback models were used.

3.2.2.2 Kinematic Similarity

A second requirement is that the model and prototype flows must be *kinematically similar*. Two flows are kinematically similar when the velocities at corresponding points are in the same direction and are related in magnitude by a constant scale factor. Thus, two flows that are kinematically similar also have streamline patterns related by a constant scale factor. Since the boundaries from the bounding streamlines, flows that are kinematically similar must be geometrically similar.

In principle, kinematic similarity would require that a wind tunnel of infinite cross-section be used to obtain data for drag on an object, in order to model correctly the performance in an infinite flow field. But in practice, wind tunnel walls restrict the expansion of the streamlines around the body and its wake. This effect is termed as *blockage* and results in increased velocities around the model and its wake. *Blockage area ratio* is the ratio of model cross-sectional area to wind tunnel cross-sectional area [29]. In this study, the blockage ratios for the models used in the experiments are much lower than the accepted limit of 5% for the aerodynamic testing of cars. However, two different blockage correction methods were applied in order to obtain more accurate results from the experiments.

3.2.2.3 Dynamic Similarity

When the two flows have force distributions such that identical types of forces are parallel and are related in magnitude by a constant scale factor at all corresponding points, the flows are *dynamically similar.* To establish the conditions required for complete dynamic similarity, all forces that are important in the flow situation must be considered.

Reynolds number, Re, is the ratio of inertia forces to viscous forces. For complete dynamic similarity, in addition to geometric similarity, the Reynolds number in the experiments must be the same as that of the full scale flow. However, this is often not achievable in the laboratory. In this case, the experiments are conducted at Re = $0(10^5)$ while the full scale flow is at Re = $0(10^7)$, two orders of magnitude higher. Despite the mismatch, the Reynolds numbers in both cases are sufficiently high that the inertia forces dominate the viscous forces, except in boundary layers. Since the models are bluff bodies, the flow separates over them; hence, the forces are mostly due to pressure differences over various parts of the bodies. Thus, to achieve similarity between the dynamic variables, the separation patterns on both the model and the actual object must be the same. Separation of the flow is determined by the behavior of the boundary layers. Laminar boundary layers, which occur at low Reynolds number, are more susceptible to early separation along a wall than a turbulent boundary layer, which has more energy to overcome an adverse pressure gradient, over the same wall at higher Reynolds numbers. The boundary layers over the models are expected to be laminar due to the low Reynolds numbers in the experiments. To overcome this problem, the boundary layers are tripped and made turbulent by using tripping wires. Thus, these experiments are conducted in the *incomplete Reynolds number similarity* regime. Since the forces are mostly due to pressure differences, which are relatively insensitive to changes in the Reynolds number at high Reynolds number, the wind tunnel results should realistically simulate the actual flow. Tripping insures a turbulent boundary layer more nearly in character with a boundary layer at higher Reynolds number. Details of the tripping method are given in Appendix E.

3.3 Wall Interference Effects in Closed Wind Tunnel Test Sections

One of the several sources of inaccuracy in the interpretation of wind tunnel data is the constraint imposed by wind tunnel walls on the flow around the model, *the wall interference.* There are two general effects of confinement due to the solid wind tunnel walls. Firstly, the walls restrict the expansion of the streamlines around the body and its wake and secondly, the inclination of the streamlines downstream of the body is modified to become parallel to the wall. The first effect is termed as *blockage* and results in increased velocities around the model and its wake. The second effect is termed as *lift interference* and influences primarily the lift force.

Blockage is divided into two parts; solid blockage and wake blockage. Solid blockage contribution is associated with the volume and shape of the body resulting in increased velocities near the body compared to the unconfined flow. The Velocity around the model must be increased in order to satisfy continuity of mass flow through the reduced cross section area around the model [29].

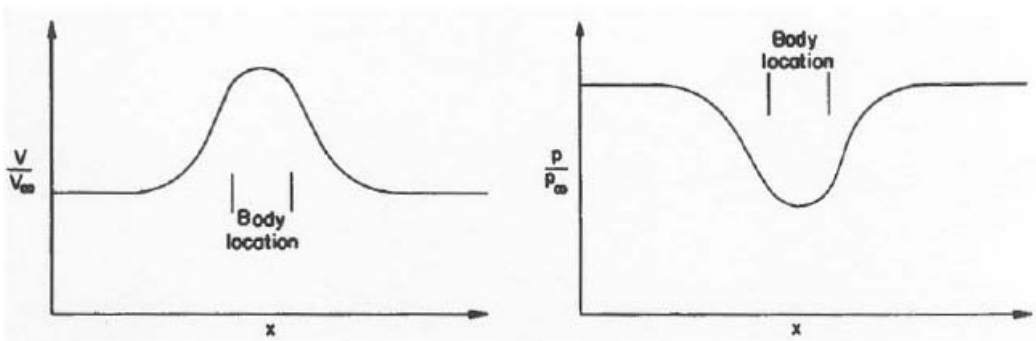

Figure 3.2 Solid Blockage Effect

Downstream of the body, there is an expanding low velocity region, a wake, around which the flow velocity is increased. This increase causes the effective velocity around the model being increased as well, which is illustrated in Figure 3.3. This wake blockage term is related to the viscous displacement effect of the wake in the

presence of test section walls. As a result it produces a wind-axis pressure drag increment on the model, termed either wake-induced drag or longitudinal-buoyancy drag [29].

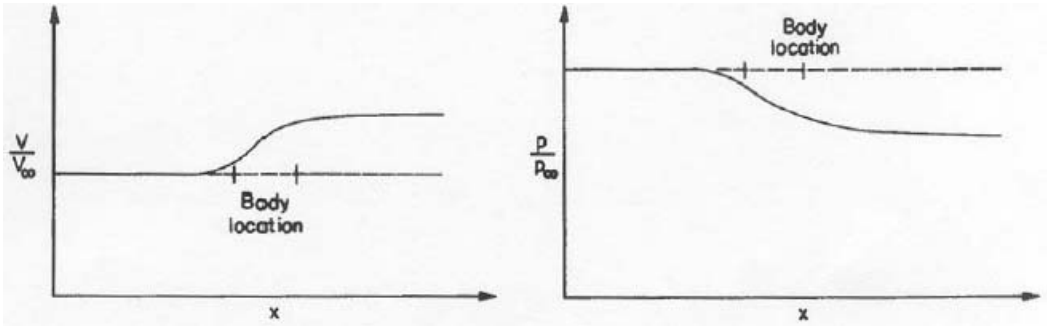

Figure 3.3 Wake Blockage Effect

The total blockage effect, when the solid blockage and wake blockage contributions are superimposed, produces velocity and pressure variations, which are shown in Figure 3.4.

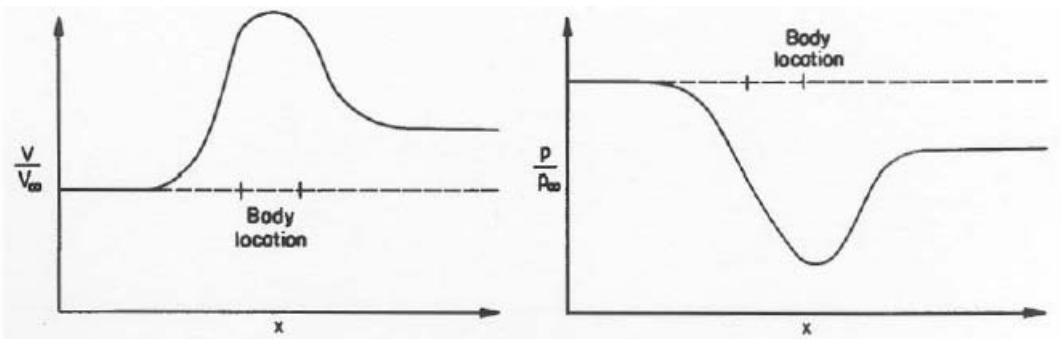

Figure 3.4 Total Blockage Effect

3.4 Blockage Correction Methods

The flow around the model in the wind tunnel is constrained by the bounding walls and the velocities in the proximity of the model are higher than if the walls were not present. Since the velocity is increased, the drag is also increased above the value obtained in the absence of the walls. The blockage correction methods are used for basing the drag coefficient upon a realistic estimate of the higher velocity surrounding the model.

Most of the correction methods are based on a mathematical approach assuming symmetry and represented by doublets, i.e. a combination of sources and sinks. The mathematical model assumes that the wind tunnel model, which as a default has usually been an airplane, is situated symmetrically in the centre of the wind tunnel test section. For automotive testing, however, the model is placed on the wind tunnel floor, thus violating this principle. The duplex test section approach is used in the correction formulae. Symmetry is achieved by assuming, that the floor is actually a wind tunnel symmetry line and the test section and the model are reflected about it to create a mirror image. Thus, the situation corresponds to an aircraft placed in the wind tunnel at 90° roll angle, the height of the duplex test section being the width of the actual test section and the width of the duplex test section being twice the height of the actual test section [29].

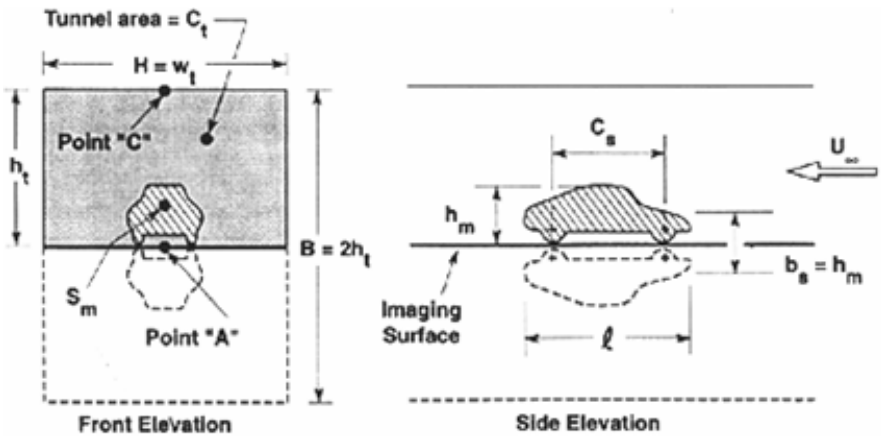

Figure 3.5 Duplex Test Section [29]

3.4.1 Continuity Method

Continuity based correction method is the simplest of all the methods. The effective velocity of the airflow at the model is assumed to be increased according to the ratio of the cross-sectional areas of the model and the test-section

$$\frac{V_C}{V} = \frac{C}{C - S} \tag{3.13}$$

where, V_C is the corrected velocity and V is the measured value. C and S are the cross-sectional areas of the duplex test section and the model plus its mirror image, respectively. The ratio of the corrected and uncorrected dynamic pressures is then:

$$\frac{q_c}{q} = \left(\frac{V_C}{V}\right)^2 = \left(\frac{C}{C-S}\right)^2 = \left(1 - \frac{S}{C}\right)^{-2} \tag{3.14}$$

The correction for the drag coefficients can then be calculated by dividing the uncorrected values by the dynamic pressure increment:

$$C_{Dcorrected} = \frac{C_D}{q_c / q} \tag{3.15}$$

As it can be seen, this blockage correction algorithm does not take into account the wake blockage. The use of this model is justified in test conditions, where the model does not have a wake wider than the body.

3.4.2 Pressure Signature Method

The pressure signature method is based on the pressure measurements at number of locations along the centerline of the tunnel ceiling. The correction method accounts for solid and wake blockage and for the wake induced drag increment. No assumptions are made concerning vehicle geometry, its alignment in the tunnel or the distribution of drag components. The pressure measurements along the centerline of the test section ceiling are taken with and without the model in place. According to

these measurements, the incremental velocities due to the model are calculated at each location.

The velocity increment is made up of two components, the first one being due to the normal velocity increase around the model, which would occur in free air as well. The second component is due to the constraining effect of the test section walls and must be identified by the correction procedure. This is obtained by subtracting the pressure coefficient values that were measured with the model in place from those with the empty tunnel.

Three line singularities are used to represent the body and its wake. A source-sink pair represents the body and a source positioned between the body source-sink pair represents the wake. The singularities are positioned along the duplex test section centre line, i.e. on the floor of the actual test section. The velocity signature is divided into two parts; the symmetric part, which is the signature due to the solid blockage and the anti-symmetric part, which carries the information of the wake blockage.

Using an iterative method, the location and the sizes of the singularities are determined, the computed effects matching the symmetric and anti-symmetric parts of the velocity signature. This process requires a computer program to carry out the iterations. In the process the anti-symmetric part of the signature is extracted first. Three empirical constants must be determined from pre-calculated tables, the values depending on the shape of the test section.

The symmetric part is obtained by subtracting the anti-symmetric part from the measured signature. At this point the results are checked. The position of the velocity peak of the symmetric signature along the tunnel centre line is compared with the assumed location of the wake source. If the locations differ, the singularity parameters are changed and the velocity distributions are reiterated until the result is satisfactory [29].

As this method is too complex to apply Zabat et al [10], [11] resorted to a simpler procedure, but one which also makes use of the static pressure distribution along the wind tunnel ceiling. First, the difference in pressure between the tunnel empty and the tunnel containing the model is determined. The pressure difference ΔCp is defined as:

$$\Delta C_P = \frac{(P_{empty} - P_{with\ model})}{\frac{1}{2}\rho U_\infty^2} \tag{3.16}$$

ΔC_P is positive when the velocity in the model cross-section is greater than in the empty tunnel. The presence of the model creates a characteristic signature which is independent of the position of the model. There is an increase in velocity (positive ΔC_P) to a local maximum in the cross-section just downstream of the plane containing the center of the model. Behind the model, the difference pressure coefficient decreases to a smaller non-zero value which represents the blockage effect of the vehicle wake. Their correction for blockage consists of taking the velocity corresponding to the maximum ΔC_P as representative of the velocity in the plane of the model. This value of velocity is used to determine the local dynamic pressure as the basis of the drag coefficient. This local dynamic pressure is determined at the maximum of ΔC_P.

According to this, Bernoulli principle is used between the reference place and the local place.

$$P_{local} + (1/2\rho U_{local}^2) = P_\infty + (1/2\rho U_\infty^2) \tag{3.17}$$

Writing P_{local} in the right hand side of the equation (3.17);

$$(1/2\rho U_{local}^2) = P_\infty - P_{local} + (1/2\rho U_\infty^2) \tag{3.18}$$

Dividing the both sides of the equation (3.18) with $(1/2\rho U_\infty^2)$;

$$\frac{(P\infty - Plocal)}{1/2\rho U_\infty^2} + 1 = \frac{1/2U_{local}^2}{1/2U_\infty^2} \tag{3.19}$$

Rearranging the equation (3.19);

$$\frac{U_{local}^2}{U_\infty^2} = \frac{(P_\infty - P_{local})}{1/2\rho U_\infty^2} + 1 \tag{3.20}$$

Defining the pressure coefficient

$$C_P = \frac{(P_{local} - P_\infty)}{(1/2\rho U_\infty^2)} \tag{3.21}$$

and substituting it into equation (3.20);

$$\frac{U_{local}^2}{U_\infty^2} = 1 - C_P \tag{3.22}$$

Using the equation (3.14), substituting q_c/q instead of U_{local}^2 / U_∞^2 into the equation (3.21);

$$\frac{q_c}{q} = 1 - C_P \tag{3.23}$$

Finally, substituting the equation (3.23) into the equation (3.15);

$$C_{Dcorrected} = C_D /(1 - C_p) \tag{3.24}$$

According to the determined C_P values from each static tap, the graph of C_P vs. position of the static taps are drawn and at the value of C_P at the location of maximum ΔC_P is used for correction Formula; $C_{Dcorrected} = C_D / (1- C_P)$.

Carr and Stapleford [30] compared results obtained with car shaped bluff bodies in different wind tunnels around Europe. The objective of the tests was to assess three different blockage correction methods on the basis of drag coefficient results: The MIRA continuity based method, the Mercker-method and the Pressure-signature method. In their study, they reported that "For blockage ratios 3.5 – 10 %, the area-ratio correction method (continuity) appears to provide better overall correction, judged mainly by the collapse of corrected drag coefficient data from the MIRA small-scale model tunnel" than either the Mercker or pressure-signature methods. The Mercker and pressure-signature methods were reported to give substantially smaller blockage corrections than the continuity method for the model and tunnel combinations that were tested.

It was concluded that the simple continuity based method used and developed at MIRA gives corrections, which are too large for streamlined bodies and too small for very bluff shapes, but that it may well constitute an adequate, simple correction for bluff vehicle bodies between these two extremes.

CHAPTER 4

EXPERIMENTAL SET-UPS AND INSTRUMENTATIONS

In order to investigate the aerodynamic interactions of vehicles in close-following and passing situations; an experimental procedure was planned. The main equipment and instrumentation for the measurements are a wind tunnel, the scale vehicle models, a set-up for force measurements and a set-up for surface pressure measurements. In addition to these, a set-up and a data acquisition system for turbulence intensity measurements are required. The design considerations and the other parts of the experimental apparatus are described in the following sections.

4.1 The Vehicle Models

Two different ground vehicle type models were used to investigate the shape effect on aerodynamic vehicle interactions of vehicles in close following and passing situations. First type is 1/18 scale MIRA (Motor Industry Research Association) reference test car model with the notchback configuration. It was chosen as the test vehicle because of its simplicity of shape and close resemblance to actual cars. Other ground vehicle type model is the 1/4 scale Ahmed Body with 0° rear slant angle. The shape of it looks like a bus or a minivan. Also, it generates the essential features of flow around a car, namely: flow impingement and displacement around the nose, relatively uniform flow around the middle and flow separation and wake generation at the rear. The principal aim of studying such a simplified car body is to understand the flow processes involved in drag production.

Scaling the MIRA model down to 1/18 allows more accurate drag measurements for the models in close-following spaced at one vehicle length apart to place in the wind

tunnel test section. This arrangement also allows a lateral separation of 0.5 vehicle widths between two vehicles to measure drag force accurately. The finished 1/18 scale model of MIRA weighs 367 g, and 1/4 Ahmed Body scale model weighs 890 g. The models were made of wood and they were varnished two times for high surface smoothness. The completed MIRA and Ahmed Body models are shown in Figure 4.1 and Figure 4.2, respectively. Specifications appear in Table 4.1 for the MIRA Notchback and in Table 4.2 for the Ahmed Body.

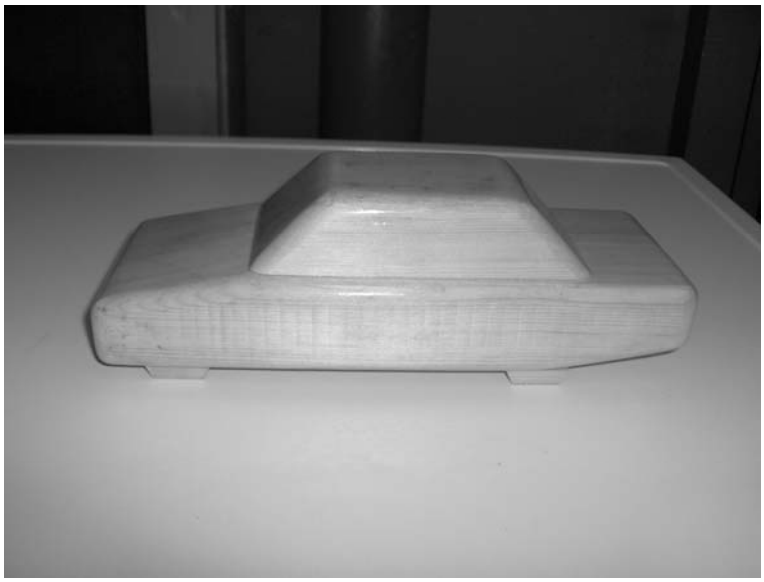

Figure 4.1 The MIRA Notchback Model

Table 4.1 Dimensions of the MIRA Notchback

Dimensions (mm)	**Prototype**	**Model**
Vehicle length	4133	229
Vehicle width	1612	89
Vehicle height	1206	67

Figure 4.2 The Ahmed Body Model

Table 4.2 Dimensions of the Ahmed Body

Dimensions (mm)	Prototype	Model
Vehicle length	1044	261
Vehicle width	389	97
Vehicle height	288	72

4.2 Open Circuit Low Speed Wind Tunnel

Experiments were conducted in an Open Circuit Low Speed Wind Tunnel (Figure 4.3). The Wind Tunnel is driven by an axial - flow fan. The motor drive turns the six bladed, axial flow fan that drives the flow. This motor drive can be turned on by the switch on the control panel. Fine adjustments to velocity are made using a potentiometer (Figure 4.4). The diffuser is the gradually-expanding passage following the test section in which the flow speed decreases and the pressure rises. The recovery of pressure from kinetic energy reduces the power needed to drive the tunnel: in the case of open-circuit tunnels the diffuser also reduces drafts in the laboratory. The pressure rise is less than that given by Bernoulli's equation, because

of losses due to skin friction and resulting growth of boundary-layer displacement thickness. Dimensions of the test section are; 300×750×2400 mm. It is covered with Plexiglas. The entrance cone or nozzle accelerates the flow into the test section.

Figure 4.3 Open Circuit Low Speed Wind Tunnel

Figure 4.4 Control Panel of the Wind Tunnel

A ground plane and an upper plane were installed into the test section as shown in Figure 4.5. The ground plane was 1000 mm in length, 730 mm in wide and 6 mm in thick. Two legs that have dimensions of 1000 mm length, 60 mm height and 6 mm wide were attached to underside of the ground plane. Both ground plane and the legs were made of Plexiglas. Dimensions of the upper plane were 950 mm in length, 500 mm in wide and 6 mm in thick. It was used for the blockage corrections. 18 static pressure taps were placed in the centreline of the plane with a uniform spacing of 50 mm.

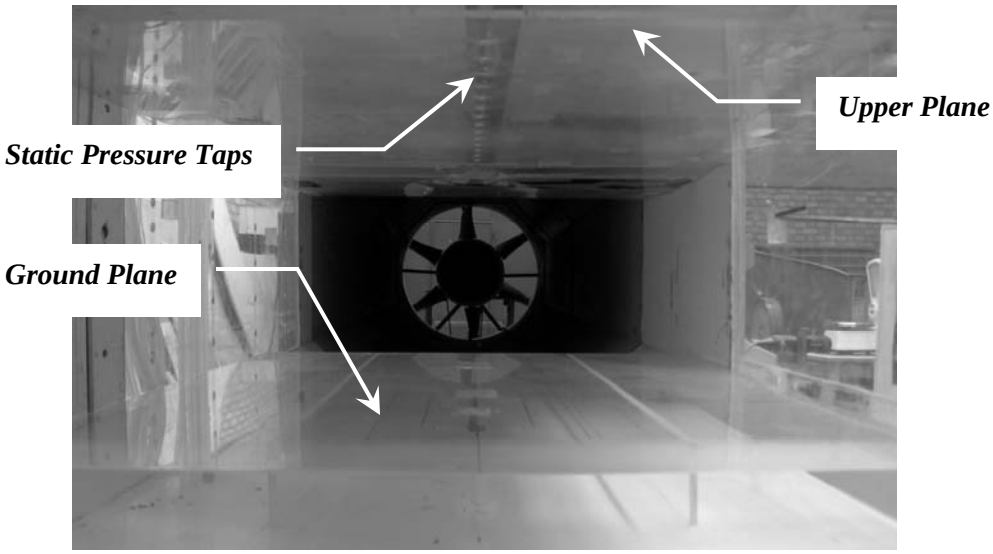

Figure 4.5 Ground Plane and Upper Plane in the Test Section

4.3 Drag Force Measurement Set-up

Drag Force Measurement Set-up consists of an iron structure on which some parts can be installed; a three component balance, an amplifier and an oscilloscope. Figure 4.6 illustrates the photograph of the test set-up which was used in force measurement tests. In the figure, the iron structure carries a strut that it is a three component balance. This balance supports the vehicle models and measures the steady state drag force acting on the models (Figure 4.7). The vehicle model is attached to three

component balance with a T-connection. It consists of a rectangular part and two legs. The parts of T-connection and their dimensions are given in Figure 4.8

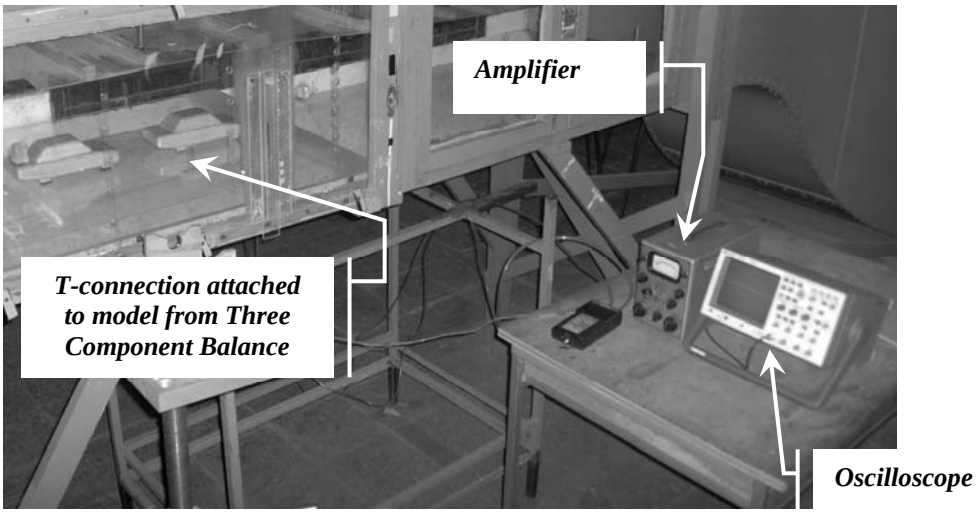

Figure 4.6 Drag Force Measurement Set-up

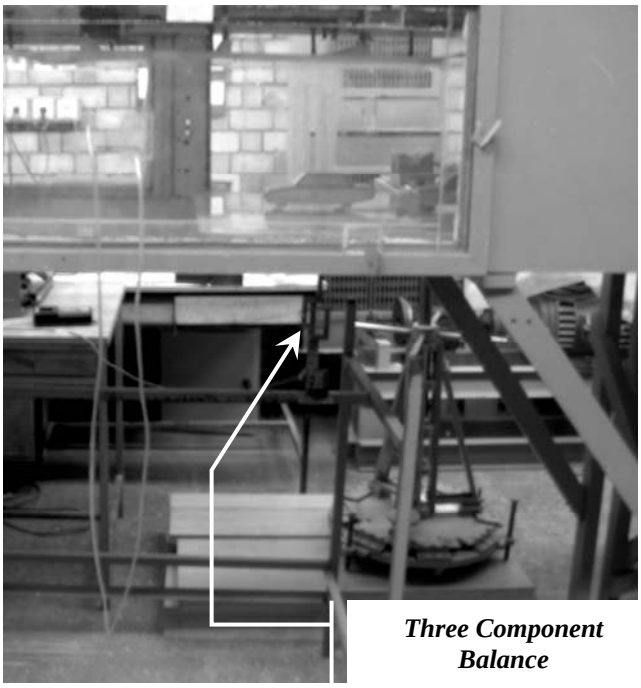

Figure 4.7 MIRA Model Attached to the Test Set-up

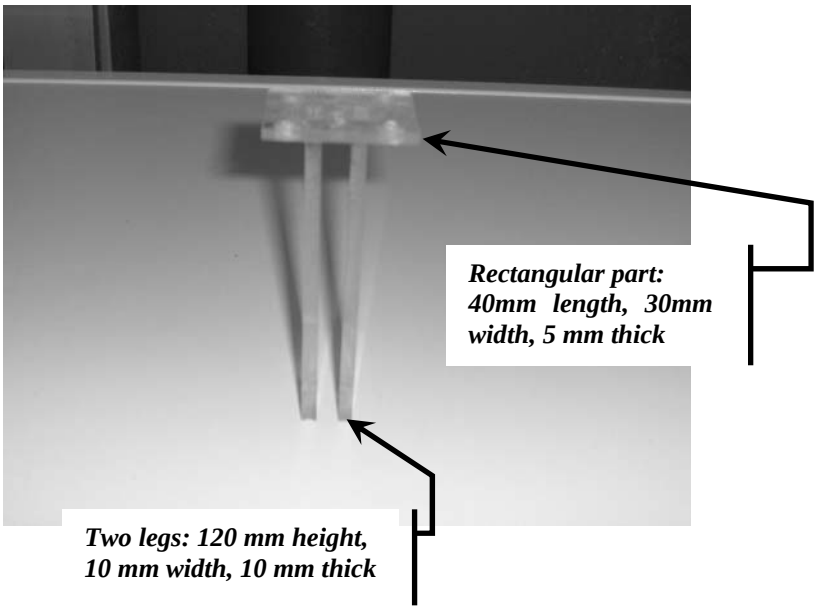

Figure 4.8 T-connection

The three component balance was designed to measure pitching moment, lift and drag forces on small aerodynamic models. It is suitable for use in small subsonic wind tunnels. Figure 4.9 illustrates the schematic view of the balance. The points A, B, and C in the figure indicate the strain gauges attached to the steel structure. There are three pairs of strain gauges on the balance. They are bonded resistance type strain gauges [31]. The moment and force components in the figure are denoted by M, N, and T, respectively. One end of the balance is to attach the model to be tested, and the other end is to fix the balance to a supporting stand.

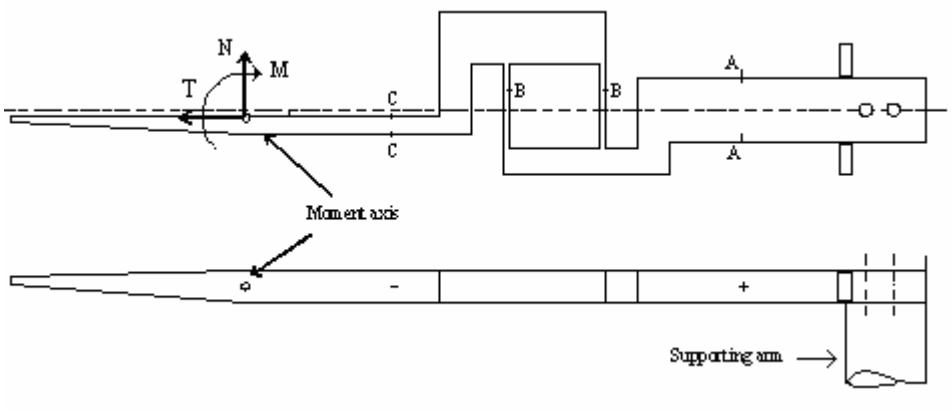

Figure 4.9 Schematic View of the Three Component Balance [31]

Being a transducer, each pair of strain gauge converts a change in strain $\Delta\varepsilon$ in the specimen to a change in electrical resistance ΔR in the gauge. The change in resistance ΔR can then be converted to a change in voltage Δv by a signal conditioning circuit. The Wheatstone bridge is a signal conditioning circuit used with a strain gauge. In the design of the three component balance, a half Wheatstone bridge was used with each pair of gauge on it. In order to see or use the voltage output from the transducer-signal conditioning circuit combination, a suitable amplifier was necessary. One channel Hottinger Amplifier was used with each pair of gauge one by one (Figure 4.10). To display the measurement from the amplifier, a recorder was necessary. As a recorder, a Hewlett Packard Oscilloscope was used (Figure 4.11). The block diagram representing the electronic instrumentation system is given in Figure 4.12.

Figure 4.10 One Channel Hottinger Amplifier

Figure 4.11 Four Channel Hewlett Packard Oscilloscope

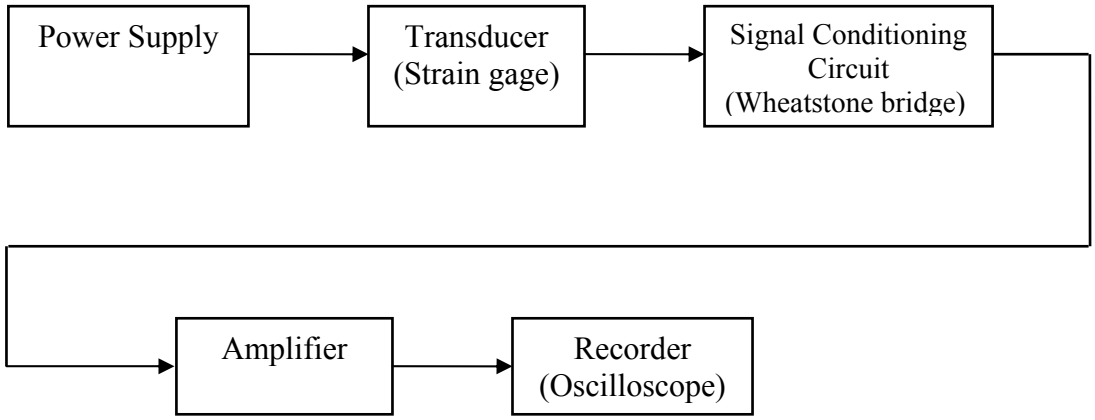

Figure 4.12 Block Diagram Representing the Electronic Instrumentation

4.4 Micromanometer

All pressure measurements were done with using the Micromanometer (Figure 4.13). This instrument was chosen for pressure measurements because of its accuracy and facility in working. It consists of a transducer that read the pressures coming from two separate pressure ports. The pressures applied from these positive and negative ports can be read from the digital screen. Micromanometer was also used to measure the free-stream velocity. The hose connected to the static hole at the wall of the Wind Tunnel was attached to the negative port of the Micromanometer. Likewise, the hose connected to a total Pitot tube that was fixed to the wall of the Wind Tunnel was attached to the positive port of the Micromanometer. Technical details of the Micromanometer are given in Table 4.3.

Figure 4.13 Micromanometer

Table 4.3 Specifications of the Micromanometer [32]

Model	ALNOR / AXD 540
Velocity Measurement Range	1.27 to 78.7 m/s
Pressure Measurement Range	-1245 to 3735 Pa
Resolution (velocity)	0.1 m/s
Resolution (pressure)	1 Pa
Accuracy	± 1 % f.M*

4.5 Hot-wire Anemometer

Thermal anemometry is a method for measuring fluid velocities by sensing the changes in heat transfer from a small, electrically heated sensor exposed to the fluid motion. The most common thermal anemometer is the hot-wire anemometer. Normally, the property being measured is the velocity. Since these elements are

* % f.M (from measurement) is relative error in percantage from measurement value.

sensitive to heat transfer between the element and its environment, temperature and composition changes can also be sensed.

Dantec Hot–wire anemometer set up was used to observe frequency of velocity peaks (Figure 4.14). It is a Constant Temperature Anemometer (CTA). It works based on the fact that the probe's resistance is proportional to the temperature of the hot wire. The bridge circuit shown in Figure 4.15 is set up by setting the adjustable resistor to the resistance that is required during operation. (The other two legs of the bridge have identical resistance.) The servo amplifier tries to keep the error voltage zero (meaning the resistances of the two lower legs of the bridge match). It adjusts the bridge voltage such that the current through the probe heats it to the temperature, which gives the selected resistance. When the probe is put into the flow, the air (or water) is tried to be cooled. In order to maintain the temperature (resistance) constant, the bridge voltage has to be increased.

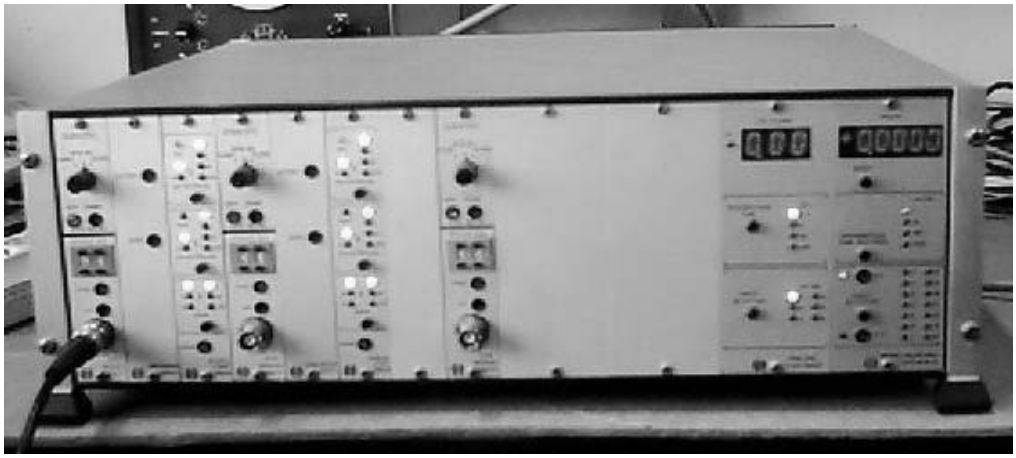

Figure 4.14 Hot-wire Anemometer

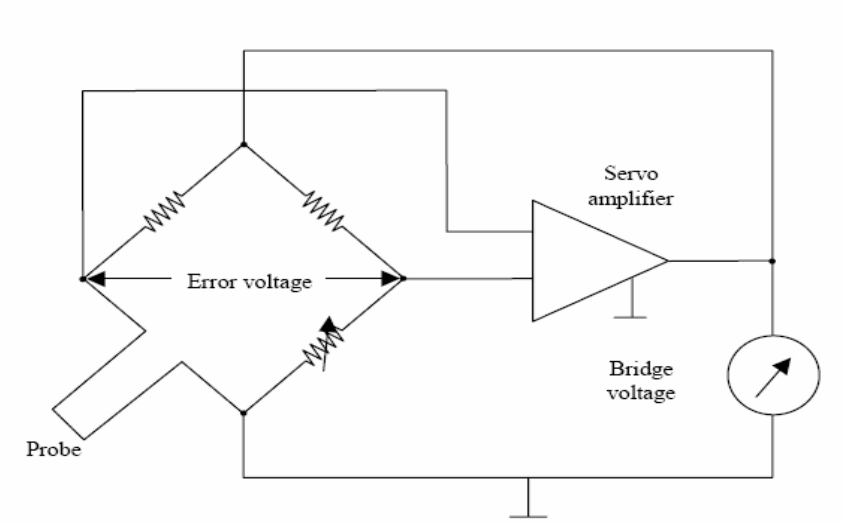

Figure 4.15 CTA Bridge Circuit

4.6 Traverse Mechanism

The wind tunnel test section was equipped with a traverse mechanism which can be moved in three directions (Figure 4.16). This mechanism designed and constructed by Prof. Dr. Cahit ÇIRAY in Aeronautical Engineering Department. It was also used in Fluid Mechanics Laboratory of Mechanical Engineering Department for another Master Thesis study which was about Three Dimensional Velocity Measurements with Hot-wire probe [33]. Hot-wire probe was mounted on this mechanism to measure the turbulence level and obtaining the frequencies of vortices behind the Ahmed Body model. The probe was attached to the mechanism by a cylindrical bar (Figure 4.17). This bar has diameter of 10 mm and a length of 300 mm. The probe support was attached to this bar with tight passage. A hole with 20 mm diameter was drilled on this bar in order to put out the end of the cable of probe. The probe was located into the relevant points according to the two marked rulers. One of the rulers was attached at the traverse mechanism and the other was on the side wall of the test section. The probe was moved from up to down by the vertical micrometer of the traverse. When the arms were rotated one period, the probe moved 5 mm vertically. In order to move it in horizontal direction, another micrometer on the flat surface of the Traverse was used. When it was rotated one period, the probe moved 3 mm in horizontal direction.

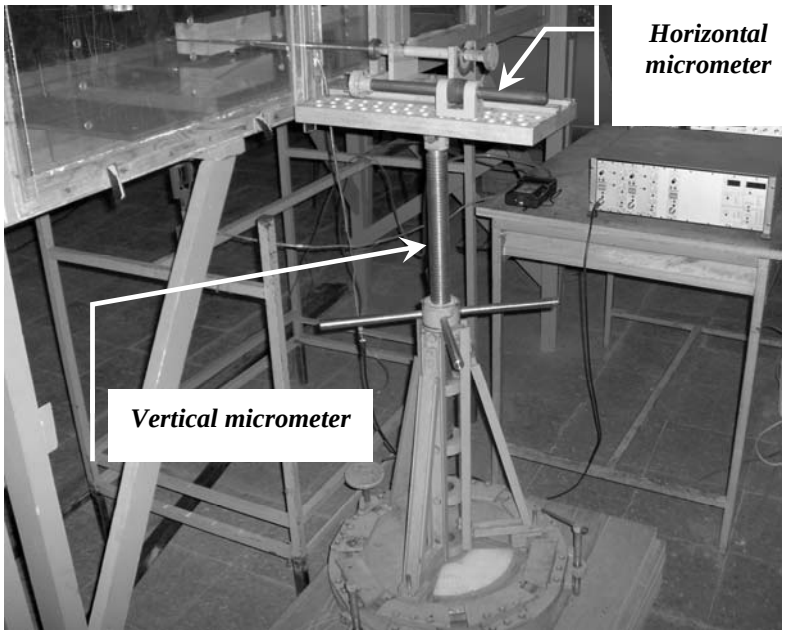

Figure 4.16 Traverse Mechanism

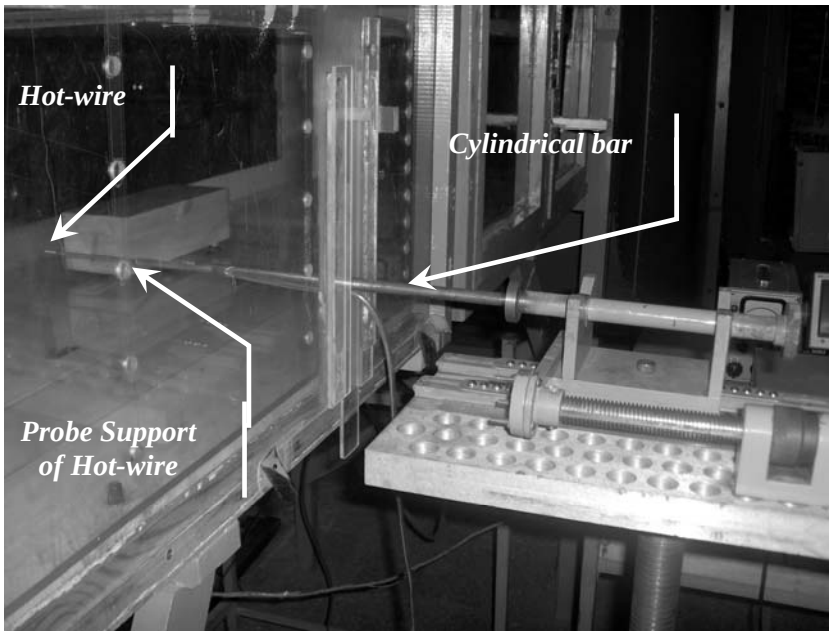

Figure 4.17 Cylindrical Bar and Hot-wire Probe Attached to the Traverse Mechanism

4.7 Data Acquisition System

Data Acquisition System was used to measure the turbulence level in the test section and flow induced vibrations of Ahmed Body model. It consists of an Advantech data acquisition card and a PC with MATLAB software installed. This system was used for previous works in Fluid Mechanics Laboratory of Mechanical Engineering Department. In the scope of the course "ME 483 Experimental Techniques in Fluid Mechanics" by Prof. Dr. O. Cahit ERALP in Mechanical Engineering Department, two undergraduate students, Ceyhun ŞAHİN and Sertan SUKAŞ, prepared and used the system for the aerodynamic studies of flow induced vibrations [34]. It was also used for another project of the same course [35].

This system works based on the fact that Advantech data acquisition card 1710 (Figure 4.18) was used to collect data and, Matlab was used to observe data. Simulink operations took external data and control loop (Figure 4.19), set on the screen resulted in the graph of voltage values in the time interval. Open loop control system was designed on Matlab Simulink. External mode runs with sampling rate 1/1000. Displayed voltage was simultaneously plotted on the scope. Basic features of Data Acquisition are given in Table 4.4.

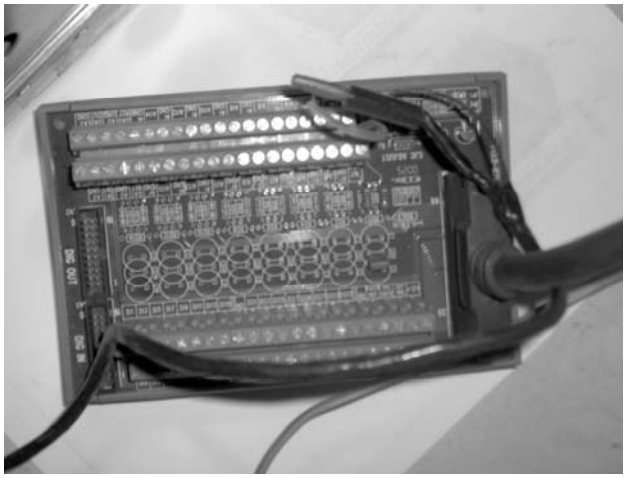

Figure 4.18 Data Acquisition Card

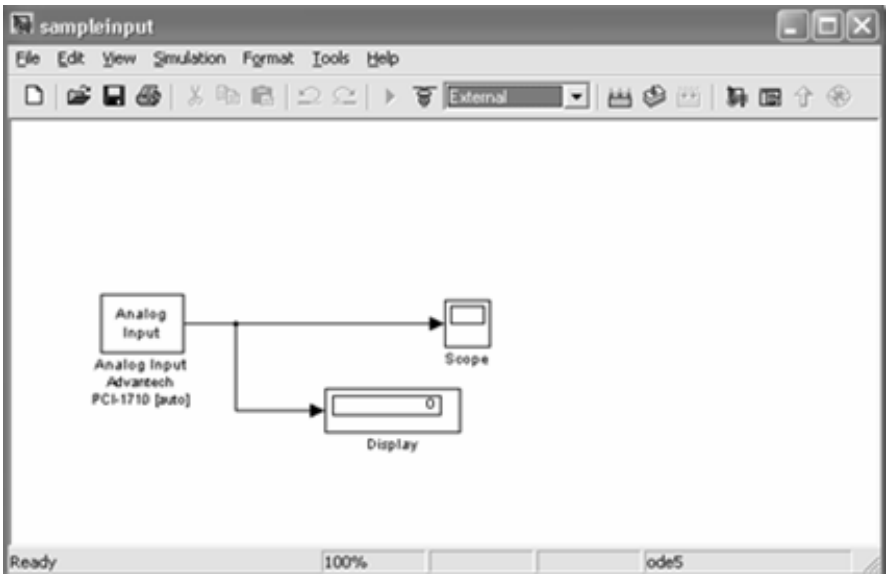

Figure 4.19 Data Acquisition with Matlab

Table 4.4 Basic Features of Data Acquisition

Maximum frequency of interest	500 Hz
Sampling frequency	1000 Hz
Sampling Interval	0.001 s
Accuracy figure	1
Effective bandwidth	1
Required Record length	1
Number of Data Points	1000
Number of Ensemble Averaged Data	9

CHAPTER 5

EXPERIMENTAL PROCEDURE

Before the experiments are carried out, instruments have to be calibrated and/or prepared. In this chapter, firstly, calibrations and some preparations made for the experiments, determinations of the turbulence level and velocity profiles are explained. Then, procedures and parameters used to measure the aerodynamic interactions are described.

5.1 Calibrations and Preparations of the Experiments

In order to conduct experiments, some of the instruments were calibrated and some measurements were done. The three component balance was calibrated. Then, the wind tunnel calibration was done. Velocity profiles at different four distinct planes were measured and finally turbulence level of the free stream velocity was obtained.

5.1.1 Calibration of the Three-Component Balance

Calibration of the balance was made by considering the approach explained in Reference [31]. Calibration approach with matrix solution is used. A 3x3 matrix is considered to find some coefficients for balancing. By assuming a linear relationship between the strains and the loads, three equations for each pair of gauges are written.

$$E_A = a_1.N + b_1.M + c_1.T \tag{5.1}$$

$$E_B = a_2.N + b_2.M + c_2.T \tag{5.2}$$

$$E_C = a_3.N + b_3.M + c_3.T \tag{5.3}$$

Here, N, M, and T denote normal force, moment, and axial or tangential force, respectively. E_A, E_B, E_C are the strains experienced by the pairs of gauges A, B, and C, respectively. The remaining small letters in the equations are balance coefficients. For the solution of these equations, the Cramer's Rule is used (Equation 5.4-5.6).

$$T = \frac{\begin{vmatrix} E_A & b_1 & c_1 \\ E_B & b_2 & c_2 \\ E_C & b_3 & c_3 \end{vmatrix}}{\begin{vmatrix} a_1 & b_1 & c_1 \\ a_2 & b_2 & c_2 \\ a_3 & b_3 & c_3 \end{vmatrix}} \tag{5.4}$$

$$M = \frac{\begin{vmatrix} a_1 & E_A & c_1 \\ a_2 & E_B & c_2 \\ a_3 & E_C & c_3 \end{vmatrix}}{\begin{vmatrix} a_1 & b_1 & c_1 \\ a_2 & b_2 & c_2 \\ a_3 & b_3 & c_3 \end{vmatrix}} \tag{5.5}$$

$$A = \frac{\begin{vmatrix} a_1 & b_1 & E_A \\ a_2 & b_2 & E_B \\ a_3 & b_3 & E_C \end{vmatrix}}{\begin{vmatrix} a_1 & b_1 & c_1 \\ a_2 & b_2 & c_2 \\ a_3 & b_3 & c_3 \end{vmatrix}} \tag{5.6}$$

Small letters in Equations 5.4-5.6 are balance coefficients. They are found from the calibration. During the tests, the strains E_A, E_B, E_C are measured and than they are substituted in to Equations 5.4-5.6.

The balance coefficients were calculated in three steps. First step was to find coefficients a_1, a_2, a_3. To do this, Equations 5.1-5.3 were taken into consideration. Provided the value of the moment and the axial force are made equal to zero in these

equations, and only a normal force is applied, strains experienced in each pair of gauge give these coefficients. In Figure 4.9, the point at which the forces are shown is called as "Moment axis" in Reference [31]. If the balance is rigidly fixed from its supporting stand in a horizontal position, any dead weight hung from this moment axis gives N=W, T=0, and M=0 (Figure 5.1). Thus, output data, E_A, E_B and E_C, from each pair of gauge corresponding to this weight can be used in calculation of these coefficients (Equations 5.7-5.9). First step calibration results are submitted in Table 5.1.Their corresponding calibration curves are presented in Figure 5.2.

$$a_1 = \frac{E_A}{W} \tag{5.7}$$

$$a_2 = \frac{E_B}{W} \tag{5.8}$$

$$a_3 = \frac{E_C}{W} \tag{5.9}$$

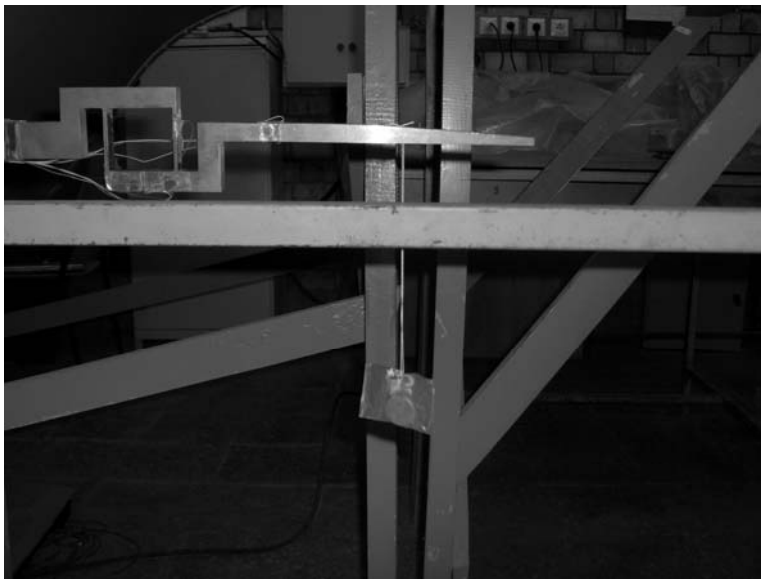

Figure 5.1 Calculation of Balance Coefficients a_1, a_2, a_3

Table 5.1 First Step of the Balance Calibration

Normal Force			
mass (g)	**E_A (mV)**	**E_B (mV)**	**E_C (mV)**
10	3.9	1.9	6.3
20	7.9	4.2	12.2
30	12.1	6.5	18.5
40	16	8.8	24.4
50	20.2	10.9	30.4
60	23.7	13.3	36.3
70	27.8	15.7	42.5
80	32.1	17.7	48.6
90	35.6	20.1	54.6
100	39.9	22.3	60.6

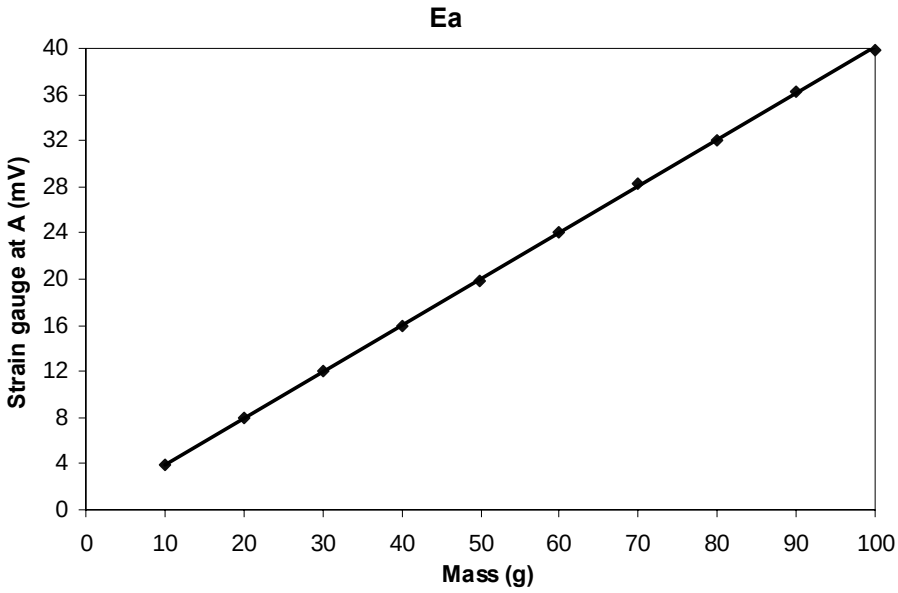

Figure 5.2 (Continued) First Step of the Balance Calibration

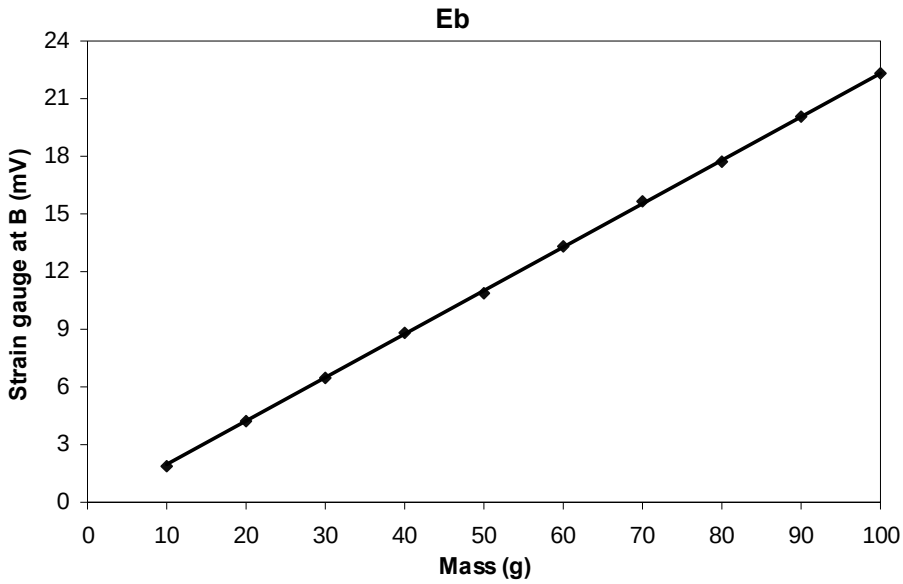

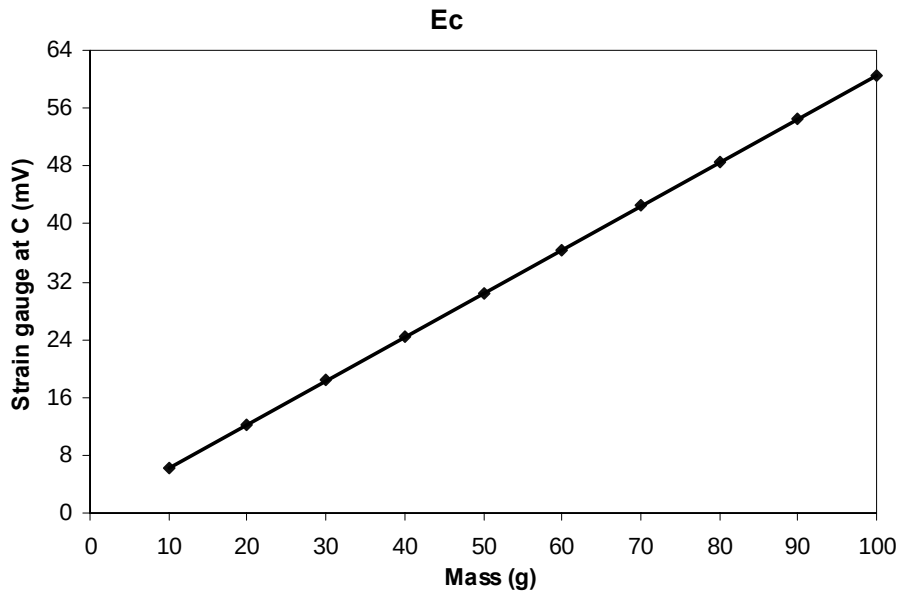

Figure 5.2 First Step of the Balance Calibration

In the second step, dead weight was applied from a distance that was far away from the moment axis to give N=W, M=W.d, and T=0 (Figure 5.3). Therefore, the coefficients b_1, b_2, b_3 were determined from Equations 5.1- 5.3 as;

$$b_1 = \frac{E_A - a_a \times W}{W \times d} \tag{5.10}$$

$$b_2 = \frac{E_B - a_2 \times W}{W \times d} \tag{5.11}$$

$$b_3 = \frac{E_C - a_3 \times W}{W \times d} \tag{5.12}$$

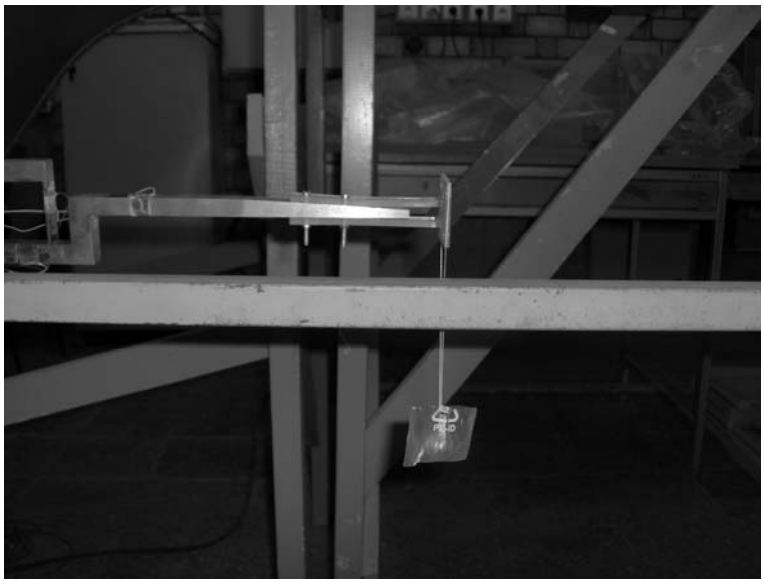

Figure 5.3 Calculation of Balance Coefficients b_1, b_2, b_3

The distance "d" which was selected according to the influence point of the drag force was 120 mm far from the moment axis. The calibration results were presented in a table and in figures below.

Table 5.2 Second Step of the Balance Calibration

Normal Force + Moment			
mass (g)	**E_A (mV)**	**E_B (mV)**	**E_C (mV)**
10	5.7	3.9	15.3
20	11.6	7.1	30.3
30	17.2	10.4	45.5
40	22.7	14.1	60.7
50	29.3	17.8	76.2
60	34.5	21.4	91.6
70	40.6	24.8	106.4
80	46.5	28.1	121.5
90	51.9	31.6	136.5
100	57.6	35.2	151.4

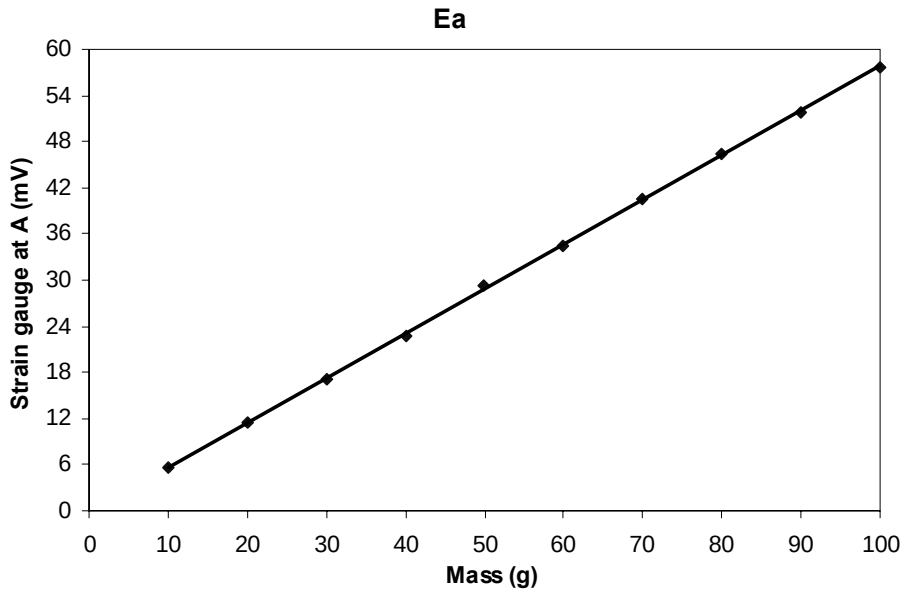

Figure 5.4 (Continued) Second Step of the Balance Calibration

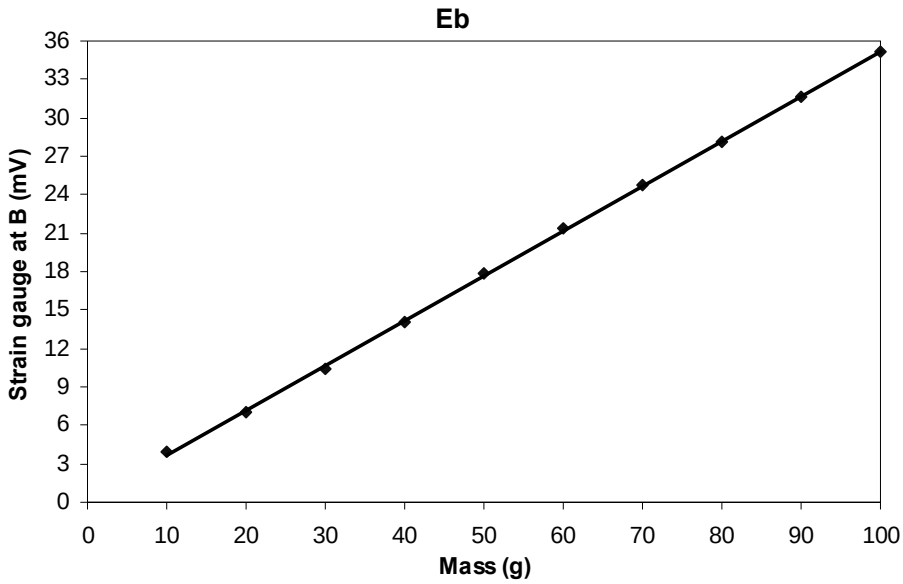

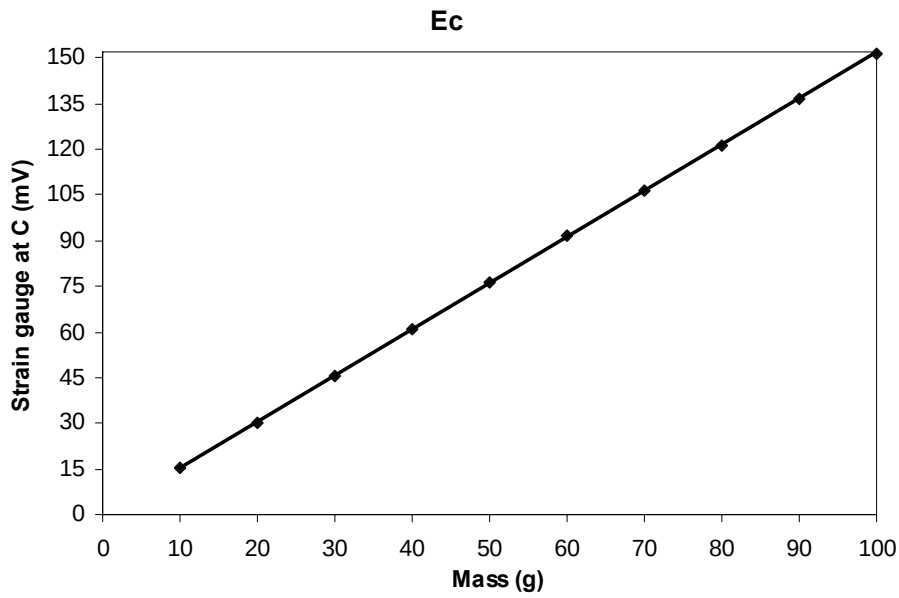

Figure 5.4 Second Step of the Balance Calibration

Finally, the balance was turned upside down and loading in such a manner gave that T=W, N=0, and M=0 (Figure 5.5). Therefore, by using Equations 5.1-5.3 the coefficients c_1, c_2, c_3 were determined as;

$$c_1 = \frac{E_A}{W} \tag{5.13}$$

$$c_2 = \frac{E_B}{W} \tag{5.14}$$

$$c_3 = \frac{E_C}{W} \tag{5.15}$$

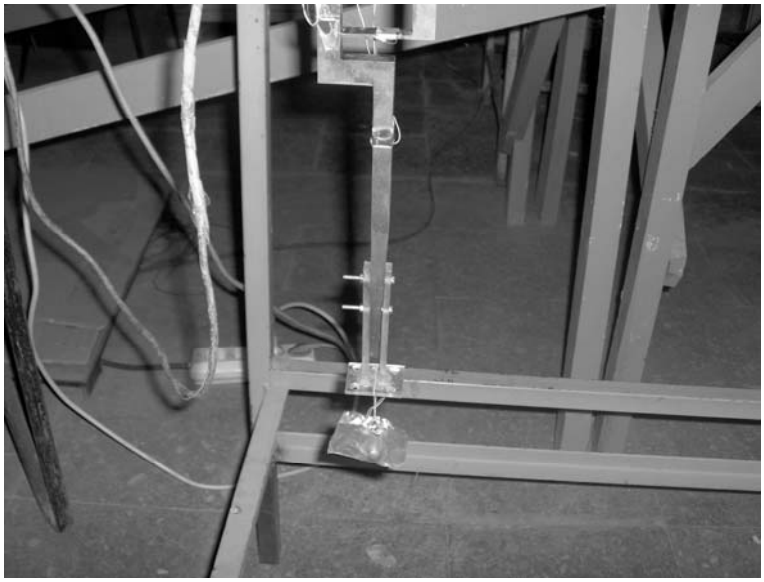

Figure 5.5 Calculation of Balance Coefficients c_1, c_2, c_3

Table 5.3 The Third Step of the Balance Calibration

Tangential Force			
mass (g)	**E_A (mV)**	**E_B (mV)**	**E_C (mV)**
10	0.6	3.7	0.7
20	1.3	7.1	1.5
30	1.8	10.3	2
40	2.5	14.1	2.7
50	3	17.5	3.5
60	3.5	20.9	4.1
70	4.3	24.3	4.9
80	4.8	27.9	5.4
90	5.5	31.5	6.2
100	6.1	35.2	7.2

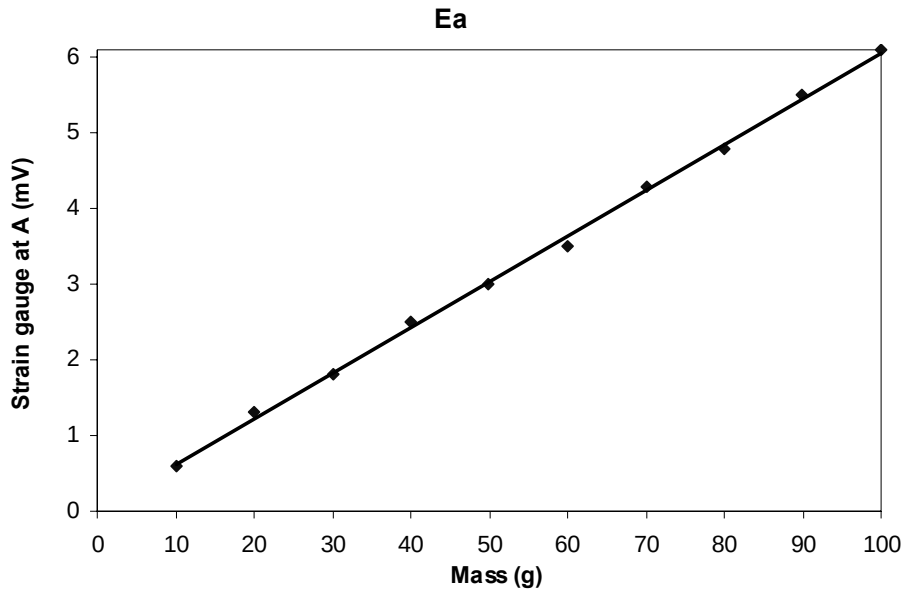

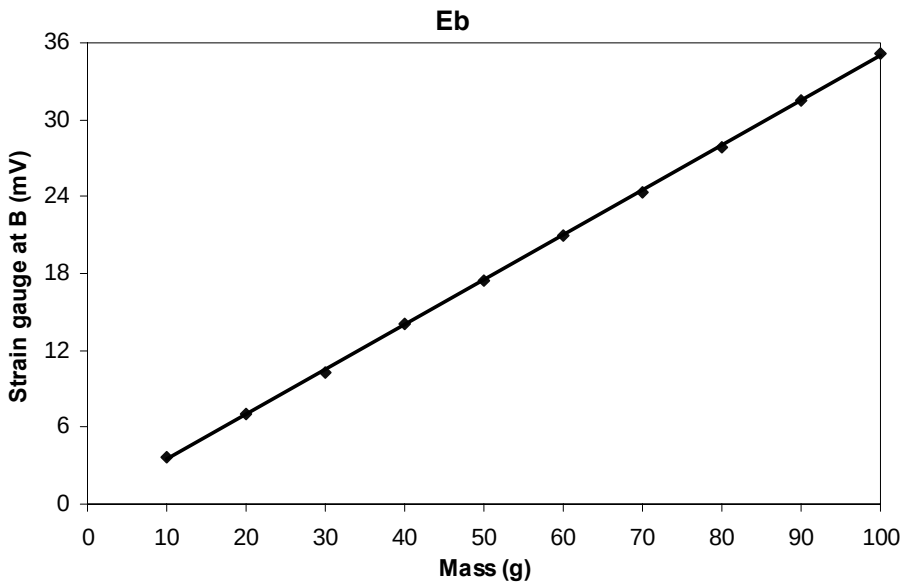

Figure 5.6 (Continued) Third Step of the Balance Calibration

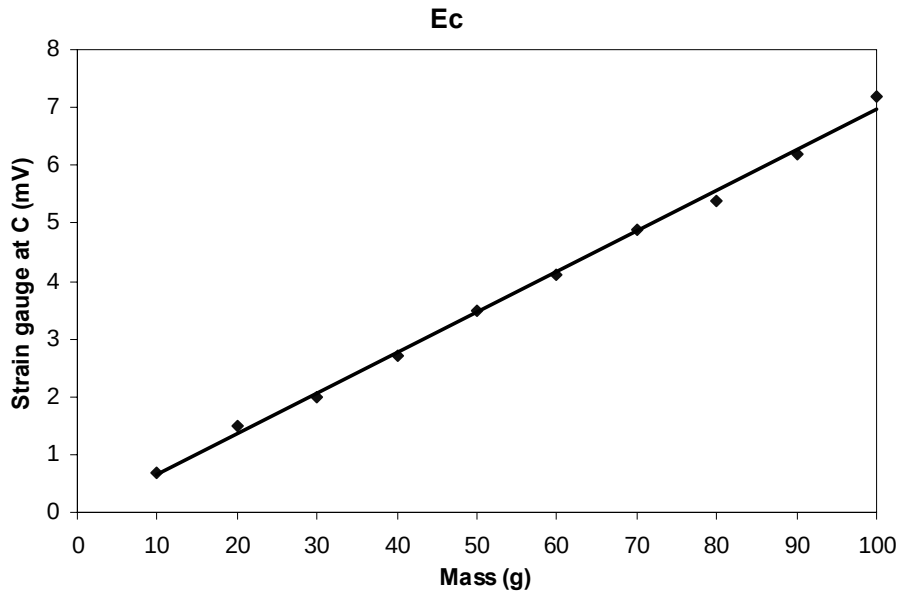

Figure 5.6 Third Step of the Balance Calibration

Therefore, the coefficient matrix can be found by considering the calibration curves. Equation 5.16 represents the determined balance coefficient matrix.

$$\begin{vmatrix} a_1 & b_1 & c_1 \\ a_2 & b_2 & c_2 \\ a_3 & b_3 & c_3 \end{vmatrix} = \begin{vmatrix} 40.8 & 142.3 & 6.4 \\ 22.4 & 150.8 & 35.9 \\ 62.2 & 771.2 & 6.9 \end{vmatrix} \tag{5.16}$$

For the connection between the balance and the Amplifier, there was only one original socket of the amplifier. For the remaining two pair of gauges, different sockets were adapted. Therefore, the balance, the amplifier and the oscilloscope were connected.

5.1.2 Setting the Freestream Speed

Before each experiment, room temperature was read from digital thermometer. Density of the air was calculated using the corresponding temperature value. Dynamic pressure was measured from the differential of the pressures of the Pitot

tube and the static pressure hole at the tunnel wall and it was shown on the Micromanometer. Since the experiments were aimed to conduct at a freestream velocity of 19 m/s, dynamic pressures were calculated using density of the air and that value of the freestream velocity. Thus, rpm of the fan was adjusted due to the dynamic pressure read from the digital screen of the Micromanometer.

5.1.3 Determination of Flow Uniformity

Flow uniformity in 4 distinct cross-section of the test section was determined by means of Pitot Static surveys. Measurements on velocity were made on 5 by 11 grids with uniform of 62.5 mm in z-direction and 50 mm in y-direction. The measurements were repeated at 4 streamwise (x) direction 250 mm apart between x = 0 to 750 mm from the leading edge of the ground plane. The results are shown in Figure 5.7. As seen from the results that the freestream velocity is not constant throughout the length of the test section, but increases slowly in the downstream direction. This is because a boundary layer exists on the walls of the test section as well as on both sides of the ground plane. The boundary layer growth reduces the cross sectional area for the flow. This reduction in area causes the freestream flow to accelerate in the downstream direction. Details of the boundary layer growth are described in Appendix D.

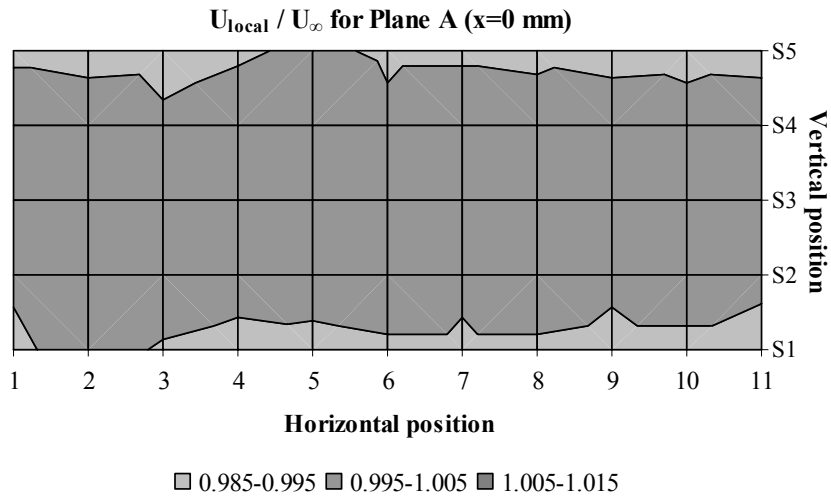

Figure 5.7 (Continued) Flow Uniformity in the Test Section

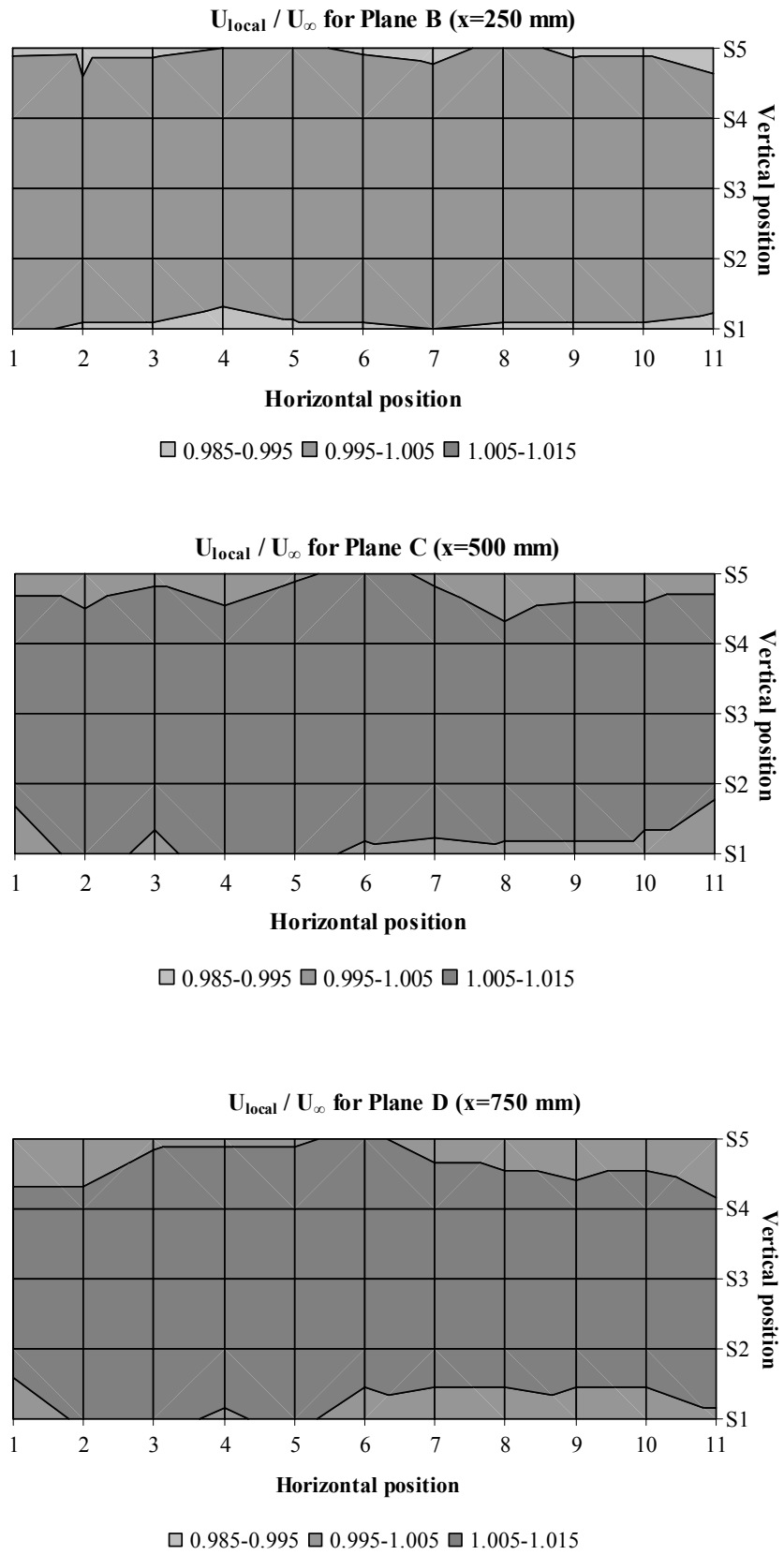

Figure 5.7 Flow Uniformity in the Test Section

5.1.4 Calibration of Hot-wire Anemometer

The basic principle of the operation of a hot-wire anemometer is the heat transfer from the heated wire to the cold surrounding fluid. Since the hotwire anemometer is a temperature sensitive device, firstly, its balancing was done prior to each experiment. Hot–wire anemometer was balanced as described in the user's manual [36].

In order to find the relationship between the fluid velocity and the electrical output of the heated wire, a calibration method should be applied. King's Law which is one of the fundamental equation of the hot-wire anemometry was used for the calibration. Since the Anemometer, used in the present study, is a Constant Temperature Hot-wire Anemometer, simplified form of the King's Law can be written in the form of

$$E^2 = A + B.U_{eff}^{1/2} \tag{5.17}$$

where, U_{eff} is the effective velocity, E is the bridge output voltage, A and B are the calibration constants [33].

The calibration constants, A and B, were determined with plotting the graph of E^2 against $U_{eff}^{1/2}$ and finding a best straight line. In order to read U_{eff}, dynamic pressure was measured from the reference Pitot tube and static hole at the wall of the test section. Rpm of the wind tunnel was increased from 350 to 1050 with the step of 50. Finally it was adjusted to 1060 rpm which gave the freestream velocity value of 19 m/s. At each rpm of the wind tunnel, voltages were recorded to the computer in an interval of 20 seconds. Meanwhile, the average dynamic pressures were also read from the Micromanometer and recorded to an Excel file in the computer. After the measurements were conducted, the average values of the voltages were calculated. Corresponding freestream velocities at each rpm were also calculated using the measured dynamic pressures. Table 5.4 shows the calibration results of the hot-wire anemometer.

Table 5.4 Calibration Results of the Hot-wire Anemometer

RPM	P (Pa)	U (m/s)	E (V)	$U_{eff}^{0.5}$	E^2
350	20	6.0	3.01	2.45	9.06
400	26	6.8	3.08	2.62	9.51
450	33	7.7	3.15	2.78	9.91
500	42	8.7	3.21	2.95	10.32
550	51	9.6	3.27	3.10	10.66
600	60	10.4	3.32	3.22	11.01
650	71	11.3	3.37	3.36	11.34
700	83	12.2	3.41	3.50	11.65
750	96	13.2	3.46	3.63	11.95
800	109	14.0	3.50	3.74	12.25
850	124	14.9	3.54	3.87	12.53
900	139	15.8	3.58	3.98	12.79
950	157	16.8	3.62	4.10	13.08
1000	174	17.7	3.65	4.21	13.35
1050	193	18.6	3.70	4.32	13.67
1060	200	19.0	3.71	4.36	13.74

The calibration curve (Figure 5.8) was plotted using $U_{eff}^{0.5}$ and E^2 values determined in Table 5.4.

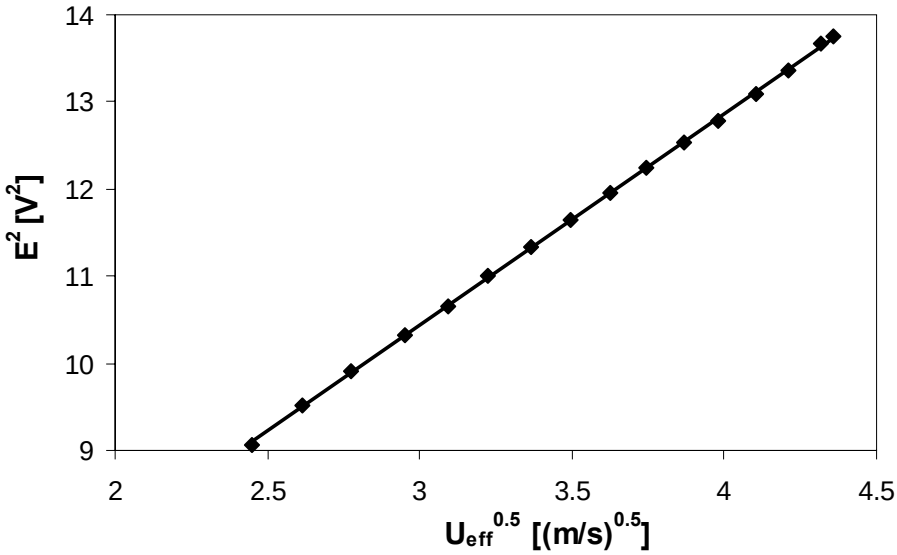

Figure 5.8 Calibration Curve of the Hot-wire Anemometer

From this graph, calibration equation was found as;

$$E^2 = 2.43U_{eff}^{1/2} + 3.15 \tag{5.18}$$

5.1.5 Determination of the Turbulence Intensity

The freestream turbulence level was required to be measured to obtain an acceptable time interval that gives a relatively steady state average value as well as an accurate account of unsteadiness of the signal. To determine this time, the velocities were measured with a hot-wire probe in intervals of 1 minutes, using data blocks of varying size and sampling time. The total number of blocks used for a particular set of data is the number needed to cover the entire 1 minute. It means that, e.g.; 60 numbers of data taken at 1 second were recorded and its average value was calculated. Likewise; 30 numbers of data taken at 2 seconds were recorded and its average value was calculated. The other data blocks were taken using the same procedure. The results are shown in Figure 5.9.

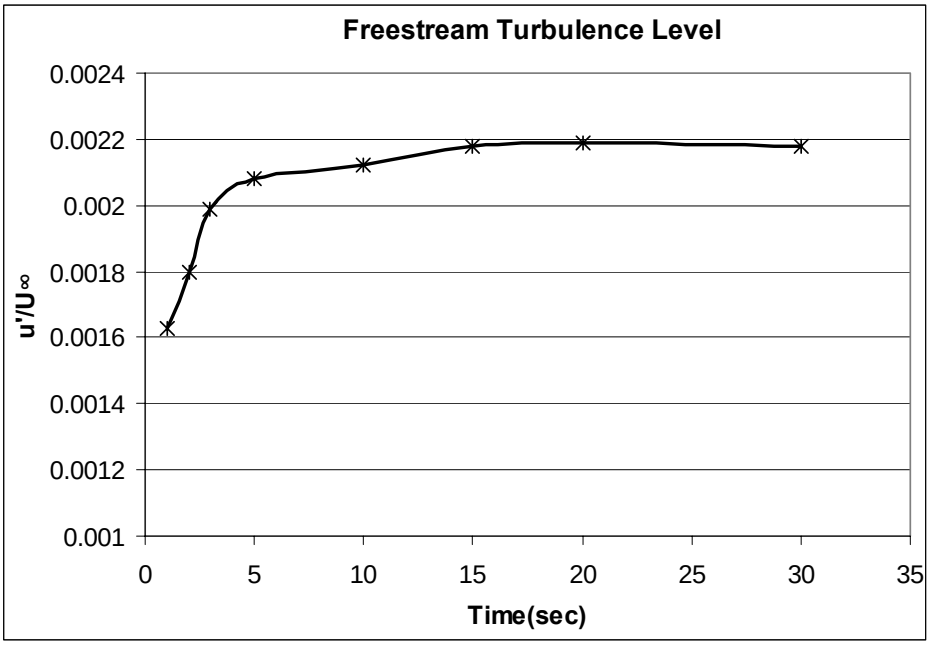

Figure 5.9 Freestream Turbulence Level in the Test Section

The results show that Turbulence level increases as the sampling time increases and reaches at a constant value of $u'/U_\infty = 0.0022$. This is the turbulence intensity in the test section, that can be written in a percentage form of $u'/U_\infty = 0.22$ %. It indicates that a minimum time of about 15 seconds is required to achieve steady state of the freestream.

5.2 Description of the Experiments

In the scope of the current study, drag measurements and surface pressure measurements of two different vehicle models were conducted for close following and passing situations of these models. Measurements were also made on each single model. In order to compare the results of these situations, experiments were conducted for each model with the titles of "*single vehicle measurements*", "*close-following measurements*" and "*overtaking measurements*".

Single vehicle drag measurements of each model were done at 3 different streamwise locations in order to observe the drag variations and to use them for drag coefficient ratios in close-following and passing situations.

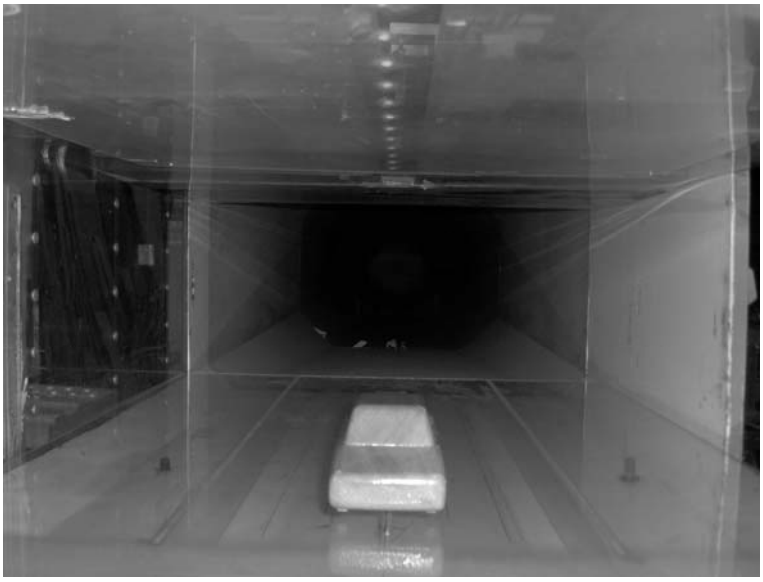

Figure 5.10 Single Vehicle Measurements of the MIRA Model

For both models, the first location was 150 mm and the second location was 430 mm from the leading edge of the ground plane. The third location of MIRA model was 730 mm from the leading edge of the ground plane. Since Ahmed Body is longer than MIRA model, the third location of single Ahmed Body was 800 mm. Models were placed at these locations carefully, according to the lines drawn on the ground plane. The experiments were repeated three times in each location for each model. The average value of drag coefficient was calculated using the determined drag coefficients from these three sets of experiments.

In one case, for both MIRA model and Ahmed Body have *tripping wires* to insure rapid transition to turbulent boundary layer flow. The tripping devices were copper wires. For MIRA model, the tripping wire had a 0.1 mm diameter and it was placed from 11 mm to the nose of the model. For Ahmed Body, the tripping wire which had a diameter of 0.2 mm was placed from 50 mm to the front end of the model. Determinations of the tripping wire's diameters and their locations are found using Flat plate Approximation explained in Reference [37]. Details of the Tripping technique are given in Appendix E.

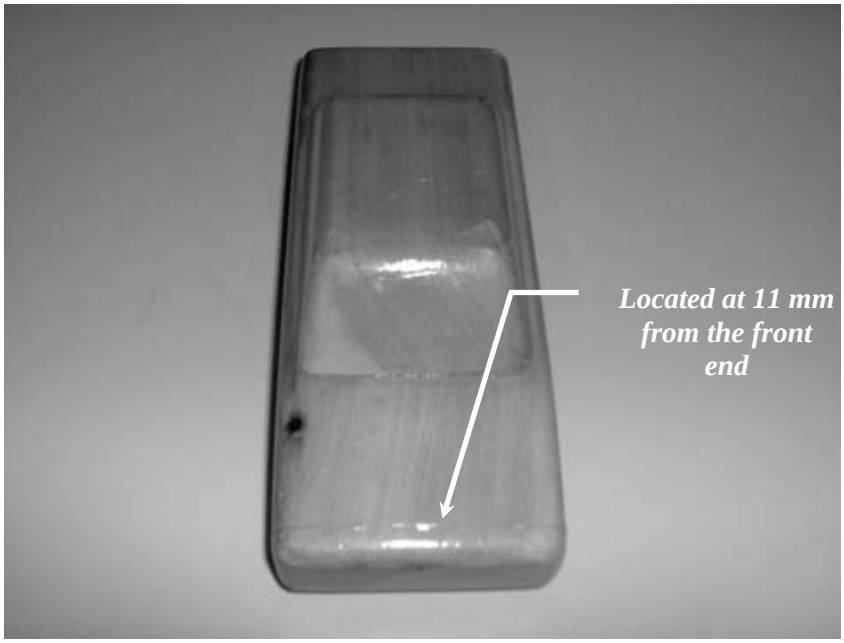

Figure 5.11 The Tripping Wire Used for the MIRA Model

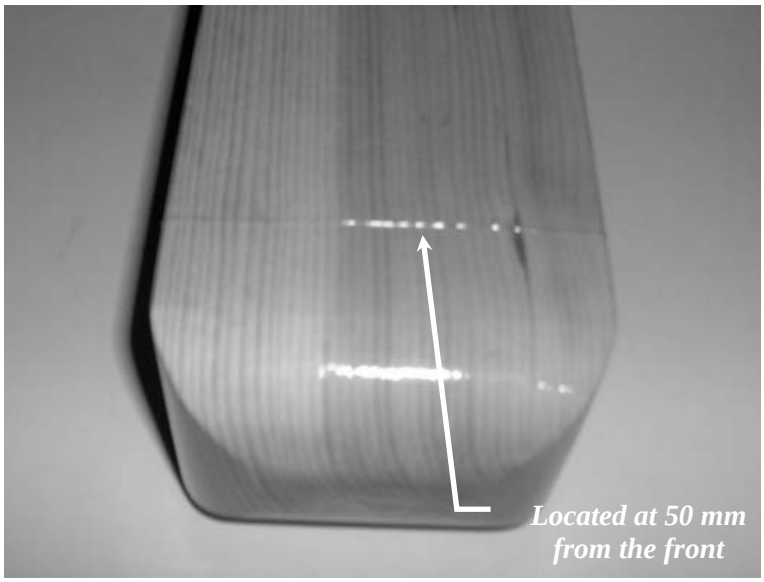

Figure 5.12 The Tripping Wire Used for the Ahmed Body Model

For close-following drag measurements, 10 different configurations were considered to observe the effect of the inter-vehicle spacings. Spacings between models were measured from the rear end of the leading vehicle to the front end of the trailing vehicle. The distances are normalized by the model length so the spacing "l" is the spacing of 1 car length.

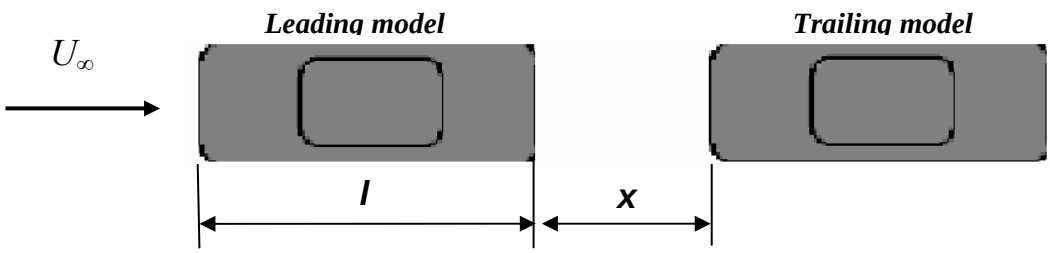

Figure 5.13 Schematic View of the Close-following Situation

where, x is the distance from rear end of the leading model to front end of the trailing model; l is the length of the model and U_∞ is the freestream velocity.

Before conducting the close-following experiments, leading model was fixed at 150 mm from the leading edge of the ground plane. The trailing model was elevated at the same height of the leading model by using four rubber materials attached to the legs of the model. These rubber materials attached to the ground plane by the help of electrical tapes to prevent the moving of the model from its place. Finally, the trailing model was placed on the ground plane, using the lines drawn, from x/l=0.1 to x/l=1 vehicle spacings.

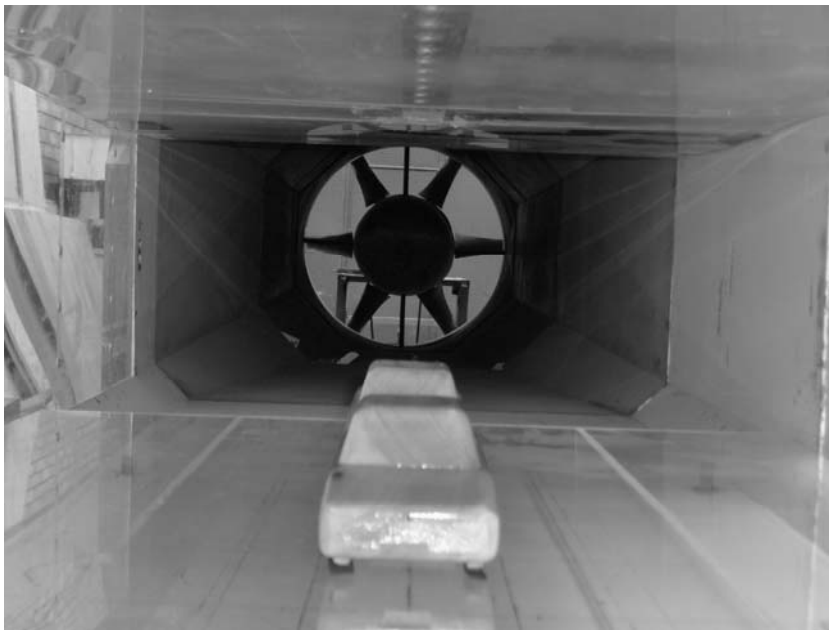

Figure 5.14 MIRA Model Close-following Situation in the Test Section

For MIRA model, the trailing model was placed at 730 mm from the leading edge of the ground plane. However, this location was at 800 mm from the leading edge of the ground plane for trailing model of the Ahmed Body. The leading model was placed in front of the trailing vehicle at 10 different locations using the same procedure.

In the overtaking measurements, besides the vehicle spacing, the lateral distance between models was also considered. Apart from close-following measurements, the longitudinal spacing was used as the distance from the front end of the leading model

to the front end of the trailing model for overtaking measurements. It was also normalized by the length of the model. The lateral distance between models was also normalized by the width of the model.

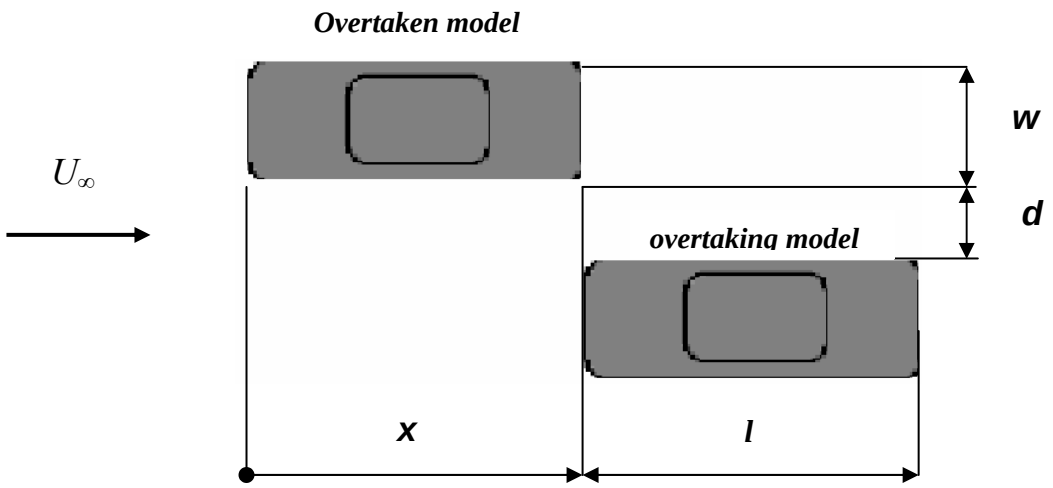

Figure 5.15 Schematic View of the Overtaking Situation

where, x is the distance from front end of the leading model to front end of the trailing model; l is the length of the model; d is the lateral spacing between models; w is the width of the model and U_∞ is the freestream velocity.

Overtaking measurements were conducted with two different lateral spacings in order to observe the effect of lateral distance. One of the models was fixed at 730 mm from leading edge of the ground plane. The other model was placed, firstly, to the left of the fixed model at 5 different longitudinal spacings; x/l = 1, 0.5, 0, -0.5 and -1. Then, the same model was placed to the right of the fixed model and measurements were done with the same longitudinal and lateral spacings.

Figure 5.16 Overtaking Situation for the Ahmed Body

After drag measurements, Continuity and Pressure Signature methods were applied to the determined drag coefficients for blockage corrections as explained in Chapter 3. For the application of the pressure signature method, firstly, difference in pressures between the tunnel empty and the tunnel containing the model were measured according to the readings from each static taps placed at the centerline of the wind tunnel ceiling. These differential pressures were also measured with Micromanometer. After the measurements, ΔC_P vs. location of taps graph was plotted. The maximum point at this graph was determined for finding the location of velocity to determine the local dynamic pressure based on the drag coefficient. For finding this local dynamic pressure, pressure differences between each static tap and reference were determined and pressure signature was determined according to the C_P vs. location of taps graph. At the location of maximum ΔC_P value, which was determined before, C_P value was found and this C_P value was used for the correction formula;

$$C_{Dcorrected} = C_D / (1 - C_P) \tag{5.19}$$

Surface pressure measurements were done for observations of the pressure distributions on all sides of the models (Figure 5.17). The variations of surface pressures have important effects on all forces and moments acting on the vehicle.

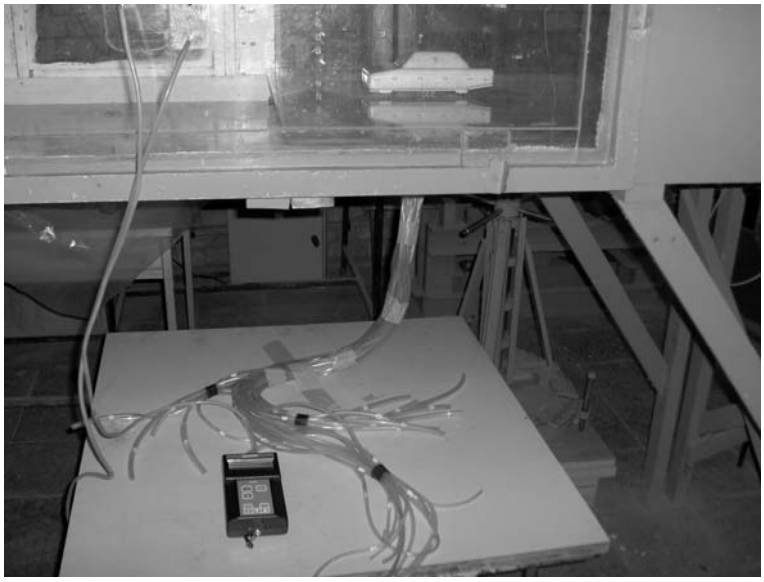

Figure 5.17 Surface Pressure Measurement Set-up

Before the surface pressure measurements, a slot was opened from the underside of the model. Then, 20 holes for Ahmed Body and 22 holes for MIRA model were drilled on the centerlines of the surfaces. Pressure tubes were placed from inside of the model to these holes. The hoses were attached to the tubes from inside of the model. These hoses were become together and they were taken out from the center of the underside of the model. A pasteboard which had same dimensions with the underside was placed to the model. Then, the hoses were marked according to the order on the surfaces. Finally, they were attached to the Micromanometer one by one.

Experiments of the surface pressure measurements were done as follows: Firstly, the motor drive of the wind tunnel was started up. It was adjusted to the required rpm

corresponded to the dynamic pressure that gave the freestream velocity of 19 m/s. It was waited about 1 minute to become steady state freestream. Then the dynamic pressure was recorded. The total pressure hose was pulled out from its place and static pressure of the test section was recorded. The next steps were recording the differential pressures. In order to measure these pressures, the hoses were attached to the positive port of the Micromanometer from the first to the last marked hoses. Before each measurement, it was waited again until the system reaches the steady state.

Figure 5.18 Surface Pressure Measurement for the Ahmed Body in Close-following Situation

The arrangements of the surface pressure experiments were same as the drag measurements. Single vehicle, close-following and overtaking measurements were done. But numbers of the experiments were less than drag force experiments. For close-following situation, experiments were conducted for the least vehicle spacing (x/l = 0.1) and the largest spacing (x/l = 1) between the leading and trailing models. Measurements were also done for x/l = 0.5 vehicle spacing.

In the passing situation, both 0.1 and 0.5 lateral spacings were considered. Experiments were only done for x/l = 1, x/l = 0 and x/l = -1 longitudinal spacings for MIRA model. However, for Ahmed Body, all longitudinal spacing configurations were considered in d/w = 0.1 configuration as the drag variations were observed sharply at this state. However, for d/w = 0.5 configuration, the longitudinal spacings were taken as the surface pressure experiments of the MIRA model.

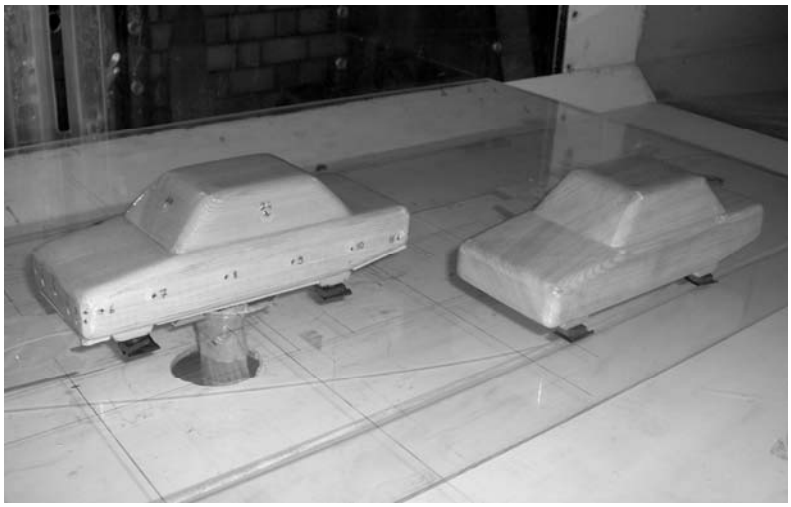

Figure 5.19 Surface Pressure Measurement for the MIRA Model in Overtaking Situation

Finally, the frequencies of periodic shedding vortices were measured for Ahmed Body model. According to the previous studies about wake survey of Ahmed Body explained briefly in Chapter 2, shear layers start where the model boundary layer separates from the body. Vortices shed until the shear layers from all sides coalesced at the free stagnation point. The vortices periodically continue to shed into the far wake from the free stagnation point. The periodic pumping causes interaction of the upper and lower portions of the ring vortex and results in periodic base fluctuations. In order to measure the shedding frequency, hot-wire probe was placed at a plane that was 45 mm distance from the model base. Measurement points on this plane are shown in Figure 5.20.

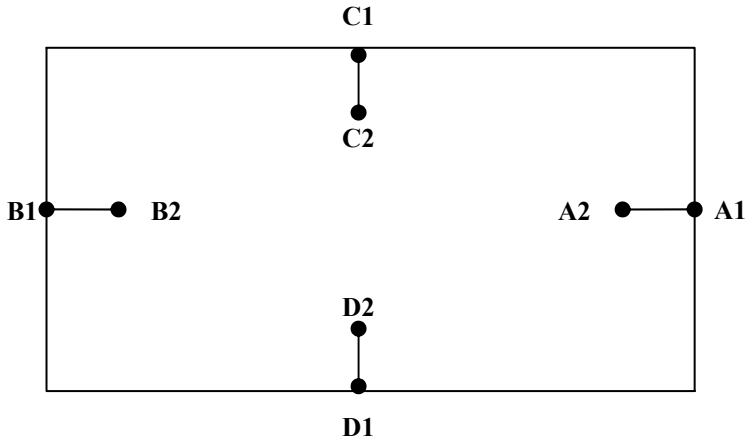

Figure 5.20 Schematic view of the measurement points behind Ahmed Body

The next step is recording some data in a definite time interval (Figure 5.21). This raw data is then transferred from voltage amplitude domain to frequency domain by the help of computer codes [38]. The found frequency values are used to find the related Strouhal numbers.

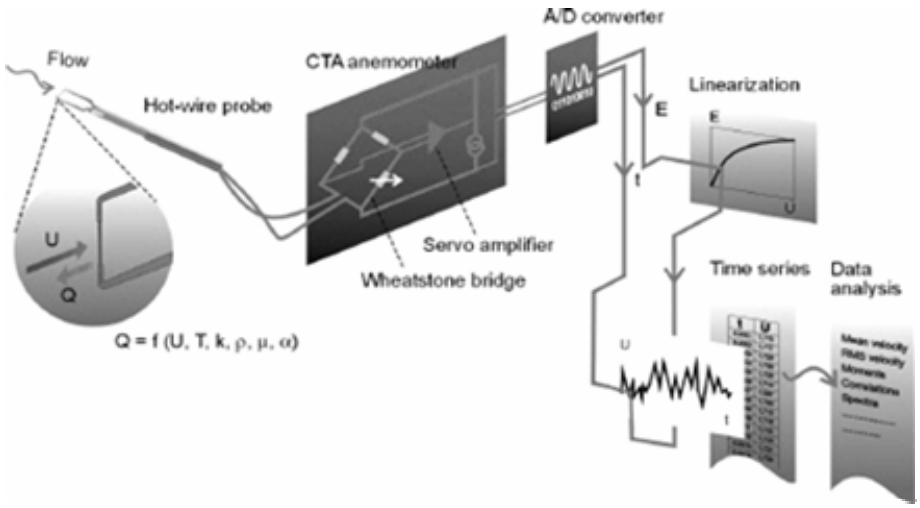

Figure 5.21 Data Acquisition with CTA Anemometer [39]

CHAPTER 6

RESULTS AND DISCUSSIONS

The experimental data obtained from single vehicle, close-following and overtaking measurements for MIRA and Ahmed Body models are presented in this chapter. For each situation, drag force and surface pressures were measured. Two different Blockage correction methods on the basis of drag coefficient results were applied. In addition to these, vortex shedding at the wake of the Ahmed Body was investigated. The results were discussed and compared with the results of the studies found in the literature.

6.1 Results of the MIRA Model

6.1.1 Single Vehicle Results

Before the correction methods were applied, the mean drag coefficient of MIRA model was measured as 0.329 with an uncertainty value of 0.015 or about 4.5%. Single vehicle drag measurements of the model were repeated at 3 different streamwise locations. It is obtained that there is a small increase in drag coefficient. But these slight increases are at the same order as the uncertainty values of the measurements.

Table 6.1 Average Uncorrected C_D values for the MIRA model

Location	Distance from leading edge (mm)	Uncorrected C_D
1	150	0.329
2	386	0.331
3	605	0.332

In the case of ground vehicles an additional effect is introduced by the presence of the road surface. According to the calculations explained in Appendix D, displacement thickness is approximately 2 mm at the end of the ground plane. Hucho and Sovran [1] suggest that the displacement thickness, δ^*, should be less than 10% of the model ground clearance for a passenger car model. Since the ground clearance is 13 mm for MIRA model, δ^*/h ratio is approximately 0.15. Therefore, the effect of ground plane boundary layer may be neglected.

Experiments were conducted at a Reynolds number of 2.9×10^5. Thus, the tests were conducted at Reynolds numbers about one order of magnitude lower when comparing with the full scale operation. In order to account for these differences, small roughness elements were utilized to artificially trip the boundary layer on the model. Tripping insures a turbulent boundary layer more nearly in character with a boundary layer at higher Reynolds number. Dryden H.L. used dimensional considerations to find an empirical law which gives the dependence of the position of completed transition x_{crit} both on the roughness height k and on the position of the roughness element x_k [37].

After the tripping was applied; drag coefficient was found as 0.325. The trip caused a slight decrease in drag and the change is the same order as the estimate of reliability in the experiments.

For the experiments conducted at METU Mechanical Engineering Fluid Mechanics Laboratory; the blockage ratio of 1/18 scale MIRA model is 2.6%. Continuity and simplified pressure signature were used as the blockage correction methods. When the continuity method was applied to the single vehicle measurements, corrected drag coefficients were found according to the equations 3.14 and 3.15. According to the equation 3.14, the ratio of the corrected and uncorrected dynamic pressures is found as 1.055.

When substituting this value to the equation 3.15, the corrected drag coefficients at different streamwise locations are found as in Table 6.2

Table 6.2 Average corrected C_D values for the MIRA model after Continuity Method

Position (mm)	C_{Dref}	C_{Dlocal}^*
150	0.329	0.312
386	0.331	0.314
605	0.332	0.315

In Table 6.2, C_{Dref} represents the uncorrected drag coefficient of single vehicle determined with using the reference dynamic pressure. C_{Dlocal}* is the corrected drag coefficient found by using the continuity correction method. The use of this model is justified in test conditions, where the model doesn't have a wake wider than the body. For the close-following and passing situations, wake blockage effect should be also considered. Thus, Pressure Signature method was used to obtain both solid and wake blockage effects.

As explained in Chapter 5, firstly, the graphs of ΔC_P (difference in C_P when the tunnel is empty and with a model present) with location of the static taps were plotted (Figure 6.1). The maximum point at this graph was obtained to determine the local dynamic pressure as the basis of the drag coefficient.

In order to find the local dynamic pressure, C_P value which is the pressure difference between each tap and the reference location divided by dynamic pressure at the reference location was determined (Figure 6.2).

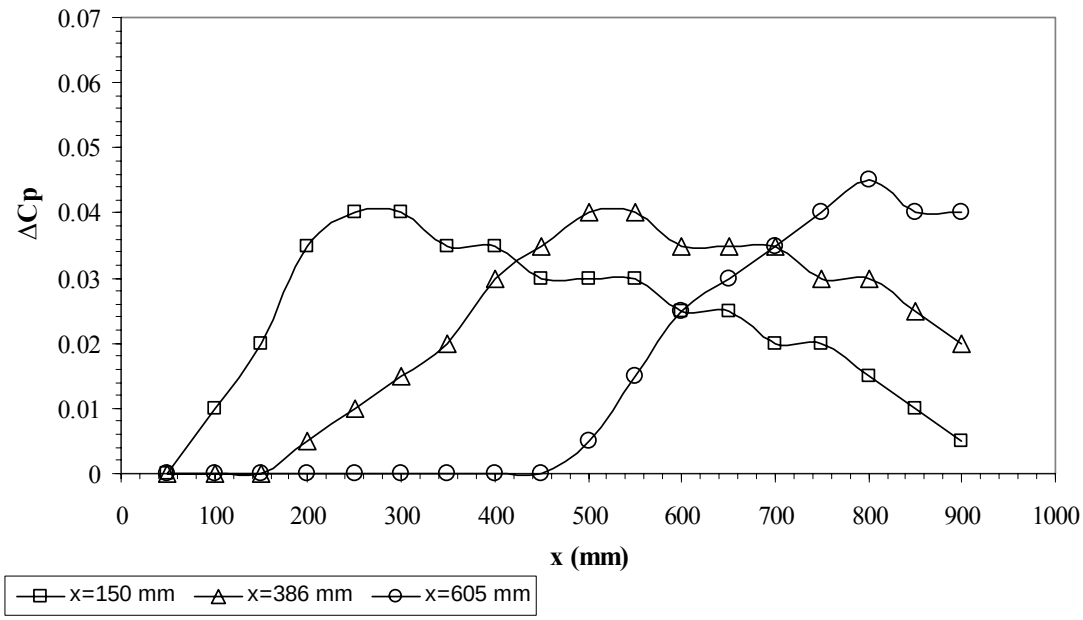

Figure 6.1 ΔC_P Distributions at Three Streamwise Locations for the MIRA Model

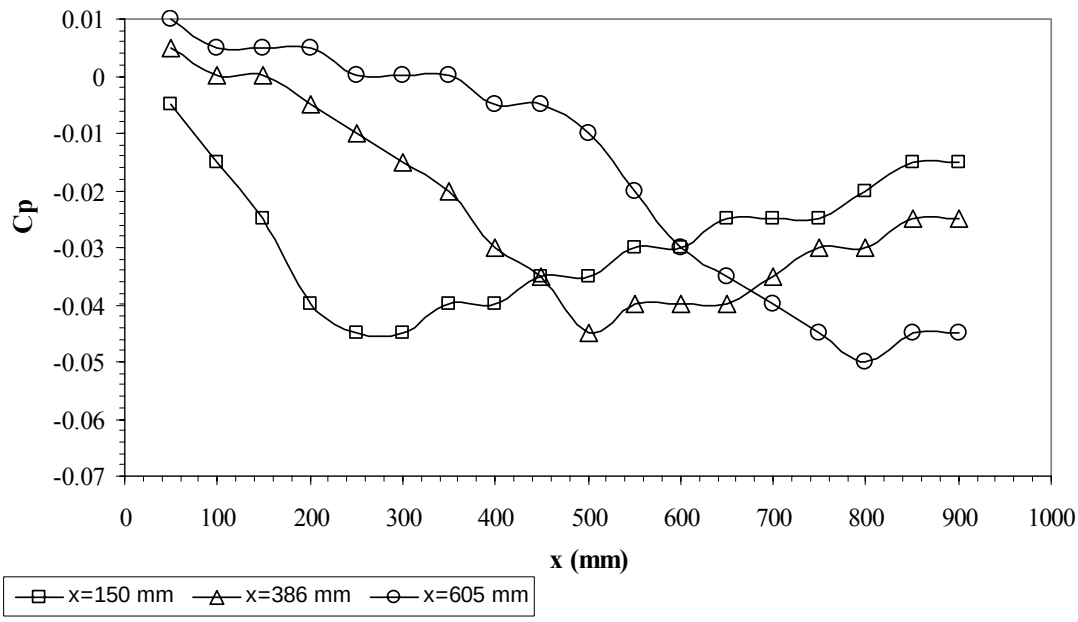

Figure 6.2 C_P Distributions at Three Streamwise Locations for the MIRA Model

C_P value was applied to the correction formula of $C_{Dcorrected} = C_D / (1- C_P)$ at the location of maximum ΔC_P. After the pressure signature method was utilized, corrected drag coefficients of MIRA were found as in Table 6.3.

Table 6.3 Average corrected C_D values for the MIRA Model after Pressure Signature Method

Position (mm)	ΔC_{Pmax}	C_{Plocal}	C_{Dref}	C_{Dlocal}^{**}
150	0.04	-0.045	0.329	0.315
386	0.04	-0.045	0.331	0.317
605	0.045	-0.05	0.332	0.316

In table 6.3, ΔC_{Pmax} is maximum value of difference in C_P when the tunnel is empty and with a model present. C_{Plocal} is found from the location of the ΔC_{Pmax}. Dynamic pressure at the reference location was determined with C_P which is pressure difference between each tap and the reference location divided by dynamic pressure at the reference. C_{Dref} is the uncorrected drag coefficient of single vehicle and C_{Dlocal}^{**} is the corrected drag coefficient found with the pressure signature method.

As seen from Table 6.3, blockage effect increases with respect to the measurement location from the leading edge of the ground plane. These values are very similar to the continuity correction results as the blockage ratios of the models are small. Continuity method results appear to provide better overall correction. But wake blockage effect should be also considered for close-following and passing situations. Thus, the pressure signature method was continued to be applied in order to obtain the wake blockage effect on the correction results.

The pressure coefficients measured from the centerlines of the right and left surfaces of the model is presented in Figure 6.3.

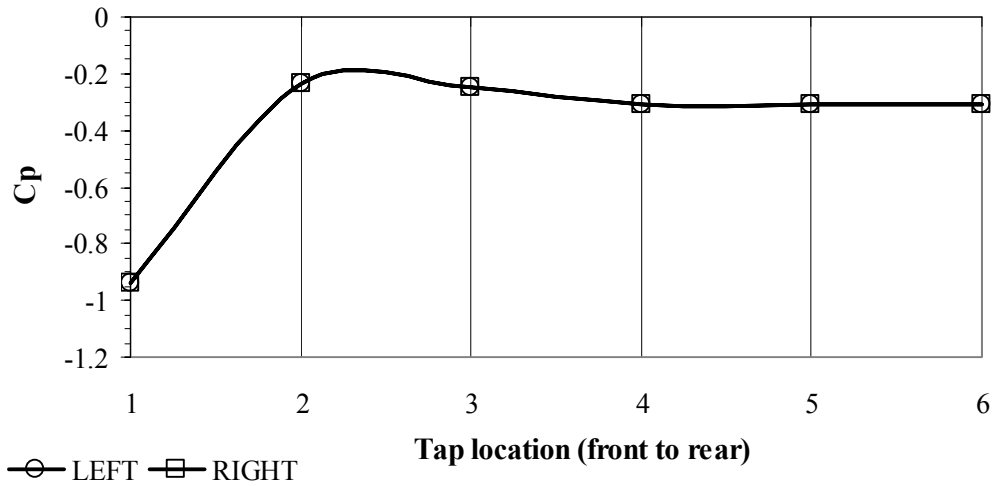

Figure 6.3 C_P Distributions at the centerlines of right and left surfaces of the MIRA Model

In Figure 6.3, the C_P values measured at left and right surfaces are same. It is expected as there is not a yaw angle or another model to cause an aerodynamic effect on it. If they were not the same, there would be a side force acting on the model. The C_P values at location 1 are lower than the others. Because it is very near to the edge between front and side edges. Air molecules slow down at that location and as a result, reduction in their speeds and increments in pressures occur.

Figure 6.4 represents the measurements from front and rear surfaces of the model. C_P values are positive at the front surface while they are negative at the rear. When the air molecules approach the front of the model, they begin to compress and in doing so they raise the air pressure in front of the model. Meanwhile, wake is caused by the hole left in the air as the model passes through it. A continuous vacuum in the rear of the model sucks in the opposite direction of the motion of the model. Thus, the pressure drop occurs at the rear end of the model.

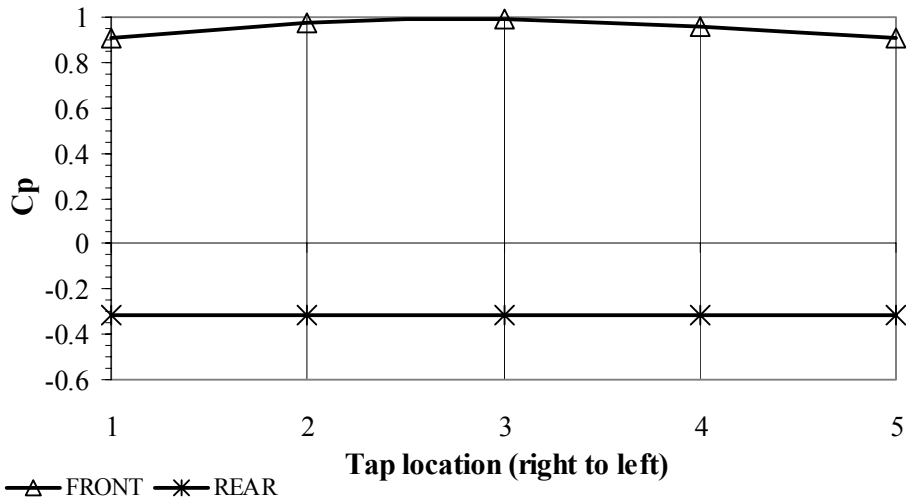

Figure 6.4 C_P Distributions at the centerlines of front and rear surfaces

6.1.2 Close-Following Results

Drag is measured on each of two models in tandem separately. The spacing between models is uniform and measured from the trailing edge of the forward vehicle to the leading edge of the rear vehicle. The distance is normalized by the model length, so that spacing *1* is a distance of 1 car-length. The data presented is averaged over at least three sets of independent measurements. All test results were shown within the error bounds established from the single vehicle measurements shown in the figures.

Figure 6.5 represents the data for close-following situation as a function of spacing between the vehicles. The forward vehicle is represented by the squares while the rear vehicle by triangles. Drag coefficient of each vehicle is divided by the single vehicle drag coefficient. This C_D ratio represents the change in drag resulting from the unique aerodynamics of both vehicles in close-following situation. The ratio is less sensitive to possible variations in C_D resulting from small differences between models, location in the wind tunnel, etc. Both leading and trailing model results were corrected with using the pressure signature method.

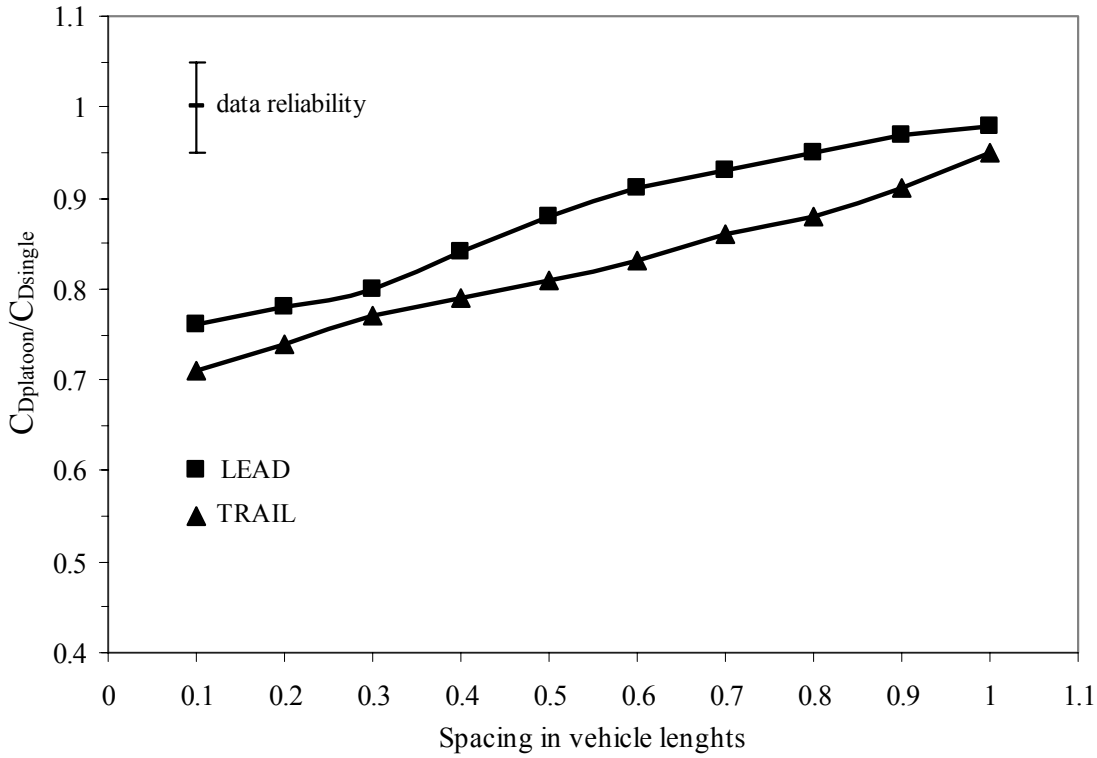

Figure 6.5 Drag Coefficient Ratios of the MIRA Models in Close-following Situation

The data shown in Figure 6.5 represents the average values of data taken over three sets of separate and identical experiments. In this figure, $C_{Dplatoon}$ is the drag coefficient of the model in the platoon and $C_{Dsingle}$ is the drag coefficient of the model in the single vehicle situation. The uncorrected data and pressure signature results are given in Appendix A.

As the spacing decreases, the lead model begins to feel the presence of the trail model. The drag coefficient of the lead vehicle drops to a value of about 0.88 $C_{Dsingle}$ when the spacing is half a model length. C_D for the trailing model drops to about 0.81 $C_{Dsingle}$ at spacing of 0.5 vehicle length. The trailing vehicle which is contained in the wake of the lead vehicle experience a decrease in drag as the spacing decreases. For the smallest vehicle spacing, drag coefficient of the trailing model drops to about 71 % of the single car value whereas the C_D of leading model is 76 % $C_{Dsingle}$.

Tripping cases were applied for x/L = 0.1 and x/L = 0.5 configurations in close-following situation of MIRA model. Slight decreases were found for both the lead and trail vehicles. The drag coefficient ratio C_D / $C_{Dsingle}$ changes are again the same order as the estimate of reliability. As a result, Tripping cases were not applied for the other platoon configurations. The uncorrected data obtained with and without trip cases for x/l = 0.1 and x/l = 0.5 are shown in Table 6.4 and Table 6.5.

Table 6.4 C_D Results of the MIRA Models with and without trip for x/l=0.1

Leading Vehicle			**Trailing Vehicle**		
Case	$C_{Dplatoon}$	$C_{Dplatoon}$ / $C_{Dsingle}$	**Case**	$C_{Dplatoon}$	$C_{Dplatoon}$ / $C_{Dsingle}$
Without Trip	0.250	0.76	Without Trip	0.236	0.71
With Trip	0.244	0.75	With Trip	0.229	0.69

Table 6.5 C_D Results of the MIRA Models with and without trip for x/l=0.5

Leading Vehicle			**Trailing Vehicle**		
Case	$C_{Dplatoon}$	$C_{Dplatoon}$ / $C_{Dsingle}$	**Case**	$C_{Dplatoon}$	$C_{Dplatoon}$ / $C_{Dsingle}$
Without Trip	0.290	0.88	Without Trip	0.269	0.81
With Trip	0.285	0.88	With Trip	0.263	0.79

It has been confirmed that, for a row of bluff bodies at close spacings, the flow separating from the front body can smoothly reattach to the corner of the downstream body [25],[40]. Gharib and Roshko [40] studied the relation between the flow oscillations in the cavity shear layer and the cavity drag. They concluded that when the flow traveled over a cut-out, a low-drag regime was always associated with the fact that the cavity shear layer attached at the downstream corner. When the shear layer impinged on the downstream wall that was below the corner, higher cavity drag was observed. Browand et al. [13] measured the drag force experienced by two

minivan models arranged in tandem. They found significant drag variations in both vehicles in the *strong interaction regime* and used the cavity flow analysis to explain their results.

As seen from Figure 6.5, the drag coefficients increase with the increasing spacing. This observation may be explained by the cavity analysis. It is more difficult for the flow to attach to the corner of the downstream model when the gap between the models is bigger. A higher cavity drag means a larger pressure on the downstream wall (front surface of the rear model) or lower pressure on the upstream wall (base surface of the front model).

How the rear and front pressures, and consequently the drag force of each vehicle, may change due to the variation of inter-vehicle spacing is shown from Figure 6.6 to Figure 6.11. In Figure 6.6, front and rear pressure distributions of the leading vehicle are given at the least vehicle spacing, x/l = 0.1.When it is compared with the single vehicle results, it is obtained that the C_P values are higher. They increase from the values of about -0.3 to -0.2.

Therefore, the surface pressures at the base are higher. The higher base pressure helps to reduce the drag force acting on it. It causes a lower cavity drag. Since the flow is shielded by the leading vehicle, C_P values at the front end of the trailing model decrease from about 1 to 0.7 (Figure 6.7). There is about 30 % pressure drop at the front end of the trailing vehicle. The rear end values are almost same.

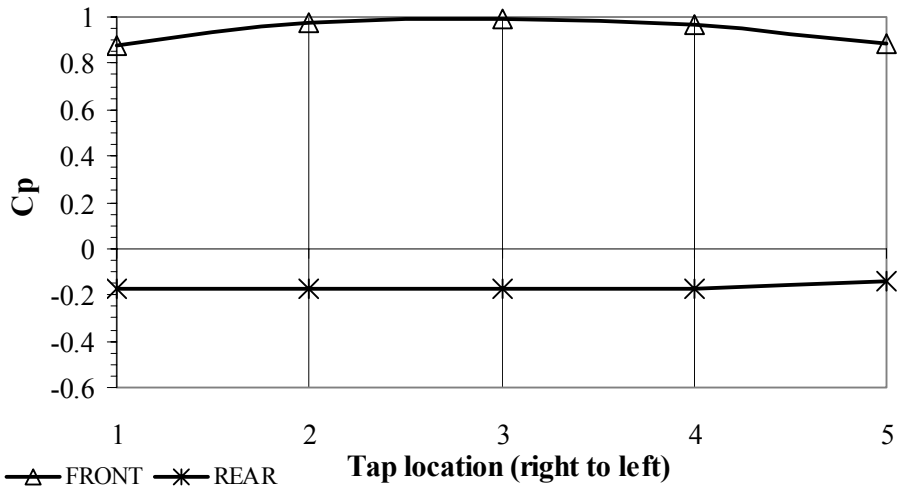

Figure 6.6 C_P Distribution at the front and rear end of the leading vehicle for x/l=0.1

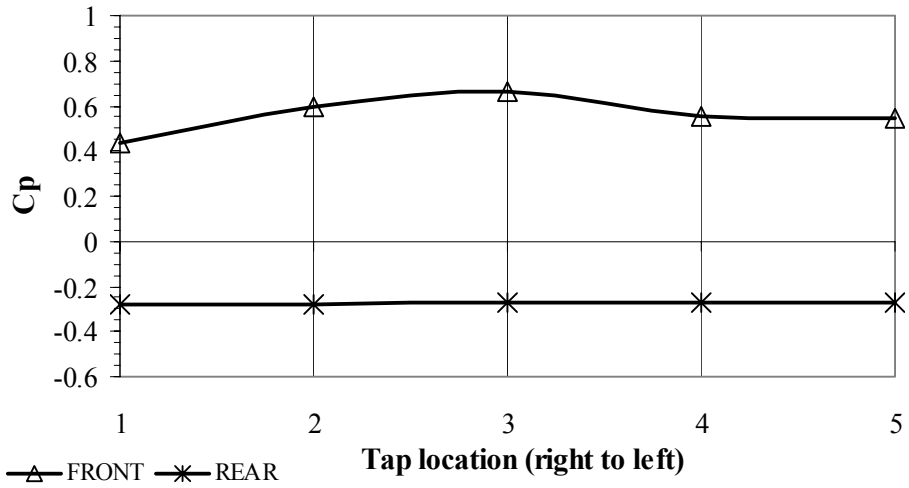

Figure 6.7 C_P Distribution at the front and rear end of the trailing vehicle for x/l=0.1

A higher cavity drag resulting from the larger gap between the models causes higher front pressure on the trailing vehicle and a lower base pressure on the leading vehicle. As shown in Figure 6.8, at the middle vehicle spacing (x/l = 0.5), front end pressures of the trailing vehicle increase when it is compared with the least vehicle spacing (x/l = 0.1). There is also a reduction at the rear end pressures of the leading model (Figure 6.9).

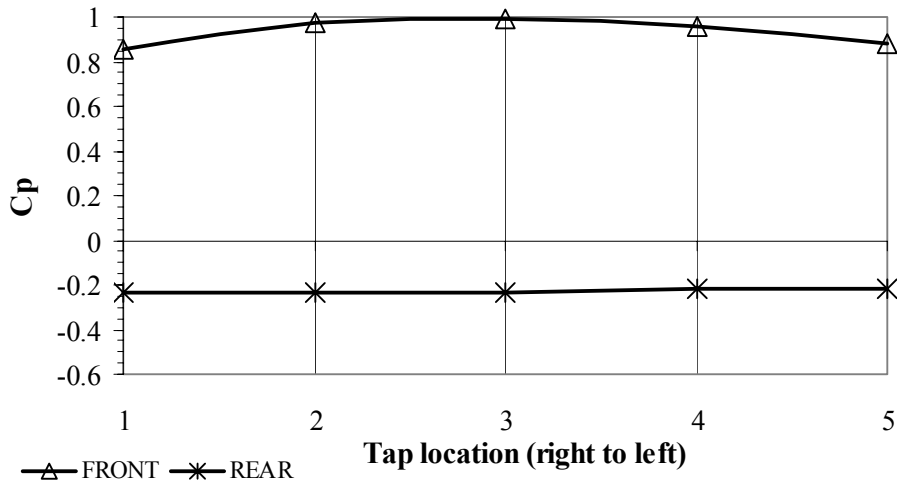

Figure 6.8 C_P Distribution at the front and rear end of the leading vehicle for x/l=0.5

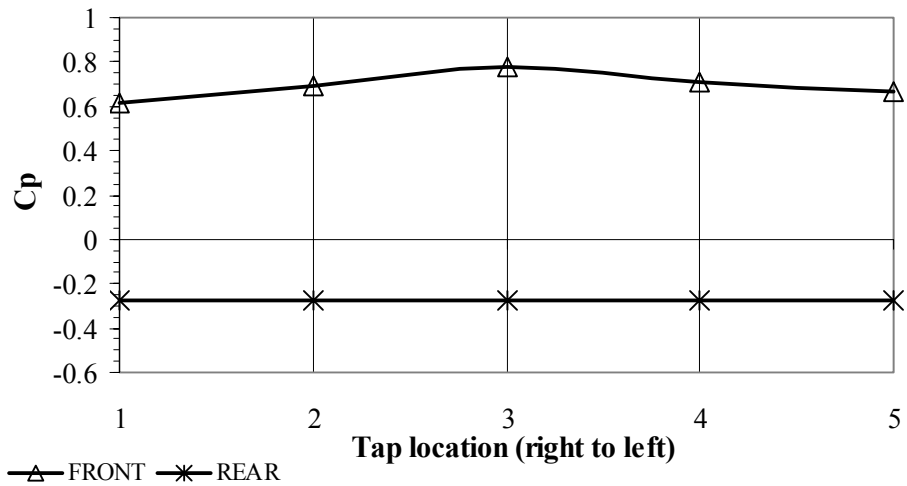

Figure 6.9 C_P Distribution at the front and rear end of the trailing vehicle for x/l=0.5

At the largest vehicle spacing (x/l = 1), front and rear pressures of the leading vehicle is almost same as the single vehicle values (Figure 6.10). The leading vehicle is not affected by the cavity drag at that position and therefore, the drag experienced by the leading vehicle is nearly unchanged when it is compared with the single vehicle. Thus, the drag coefficient ratio is almost unity as shown in Figure 6.5. For the trailing vehicle, the front pressures are lower than the single vehicle state (Figure 6.11).

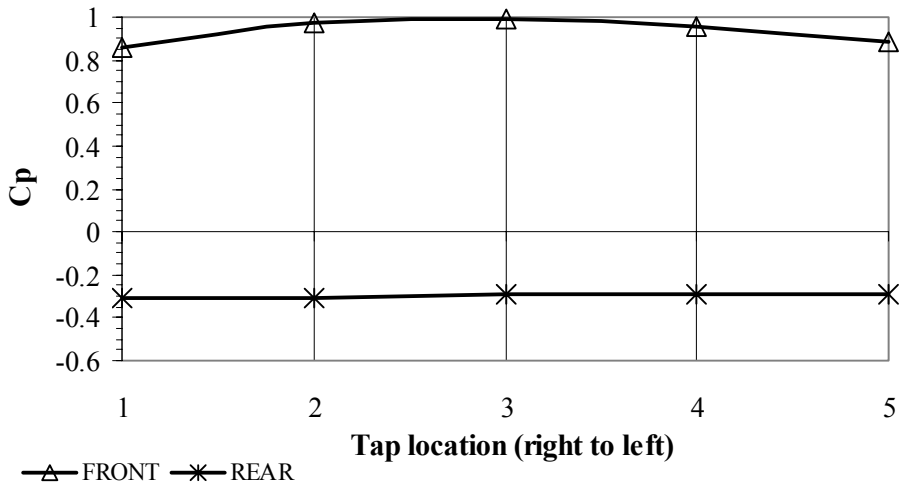

Figure 6.10 C_P Distribution at the front and rear end of the leading vehicle for x/l=1

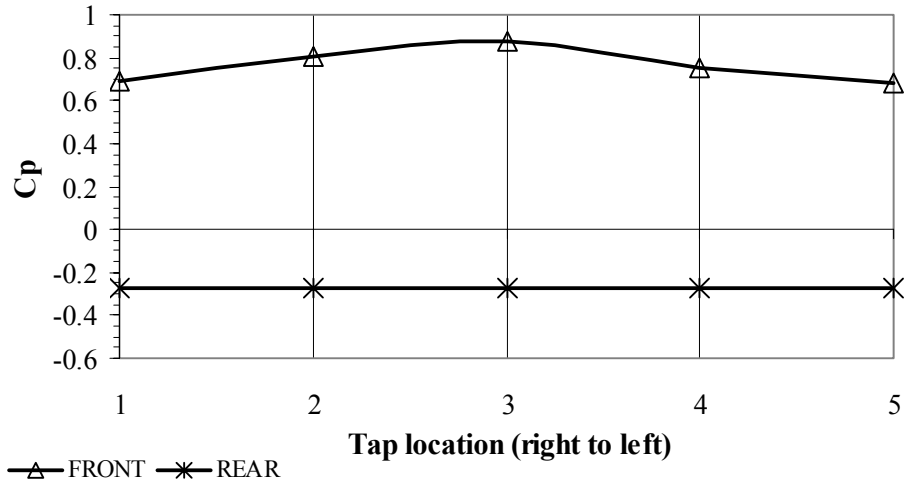

Figure 6.11 C_P Distribution at the front and rear end of the trailing vehicle for x/l=1

Average drag coefficient ratios of the models increase linearly as seen from Figure 6.12. The maximum drag reduction occurs at 0.1 vehicle spacing. An average drag coefficient ratio which was the overall measure of drag performance of the vehicles in close-following was defined by Zabat et al [10], [11]. In their study, they evaluate the aerodynamic performance of individual members of 2, 3 and 4-vehicle platoons. The details of these studies were mentioned in Chapter 2.

$$(C_{Dp})_{avg} / C_{Dsingle} = \left(\frac{1}{n}\right)\sum_{i=1}^{n}(C_{Di} / C_{Dsingle}) \quad (6.1)$$

Where *i* represents the *i*th platoon member and n is the number of vehicles in the platoon.

The authors stated that average drag coefficient ratios of vehicles in a platoon possessed much smoother behavior than the drags of individual vehicles. An extrapolation to larger platoon size may be obtained with using the equation 6.1.

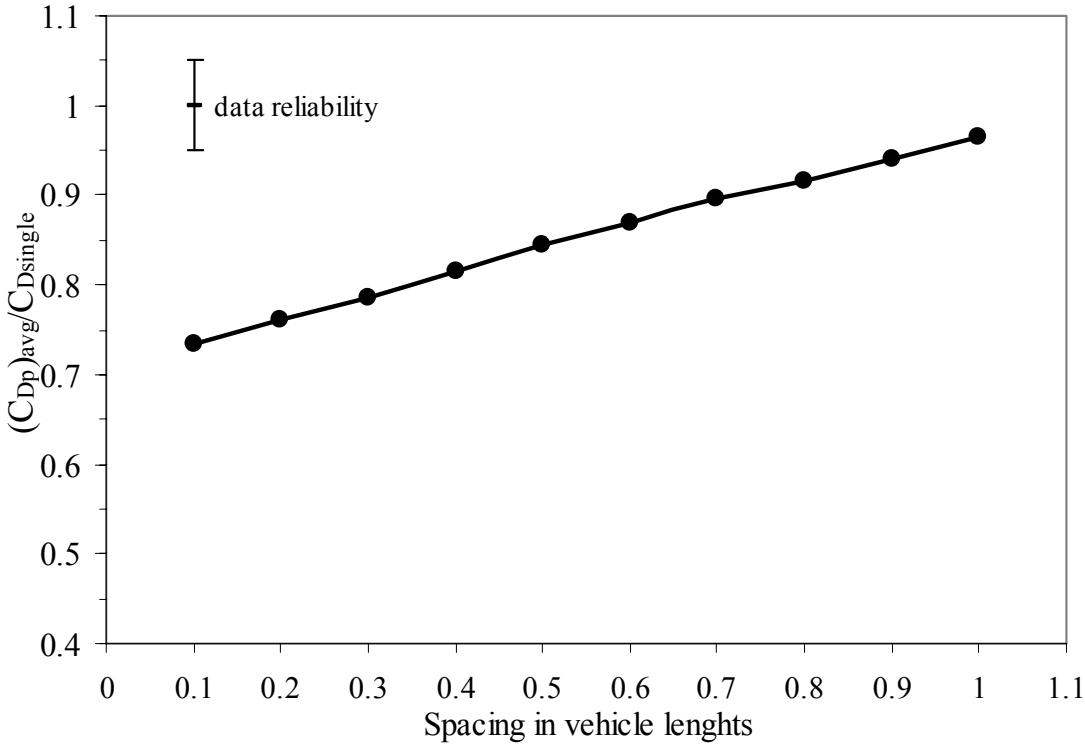

Figure 6.12 Average Drag Coefficient Ratios of the MIRA Models in Close-following Situation

6.1.3 Overtaking Results

In overtaking measurements, drag was measured on each of two models side by side with two different lateral spacings. The lateral distance between models was normalized by the width of the model. Experiments were conducted at d/w = 0.1 and d/w = 0.5 for the effect of the lateral spacings. The longitudinal spacing was used as the distance from the front end of the leading model to the front end of the trailing model for overtaking measurements. It was also normalized by the length of the model.

Figure 6.13 and Figure 6.14 represent the data for overtaking situations as a function of vehicle spacing between the vehicles. The overtaken vehicle is represented by the stars while the overtaking vehicle by triangles. Drag coefficient of each vehicle is divided by the single vehicle drag coefficient. The data shown in Figure 6.13 and Figure 6.14 are the average values of data taken over three sets of separate and identical experiments. These average values results were corrected with using pressure signature method. The uncorrected data and pressure signature results are given in Appendix A. Also, surface pressure results are given in Appendix B.

For the closer situation (d/w = 0.1), the drag coefficients of both vehicles decrease at x/l = 1 (Figure 6.13). When the longitudinal spacing begins to decrease, the overtaken vehicle's drag coefficient increase substantially and at x/l = 0.5, C_D becomes greater than the single vehicle's value. C_D of overtaken vehicle continues to increase and reaches at the maximum when both vehicles are side by side. After that location, C_D of overtaken vehicle begins to decrease and becomes about 0.94 of single vehicle's C_D value. It continues to decrease gradually and reaches at the minimum at x/l = -1. Meanwhile, the overtaking vehicle's C_D value is almost not to change when its longitudinal position comes from 1 to 0.5. C_D of overtaking vehicle decreases linearly between 0 to -1 and becomes smaller than the single vehicle's value at x/l = -1

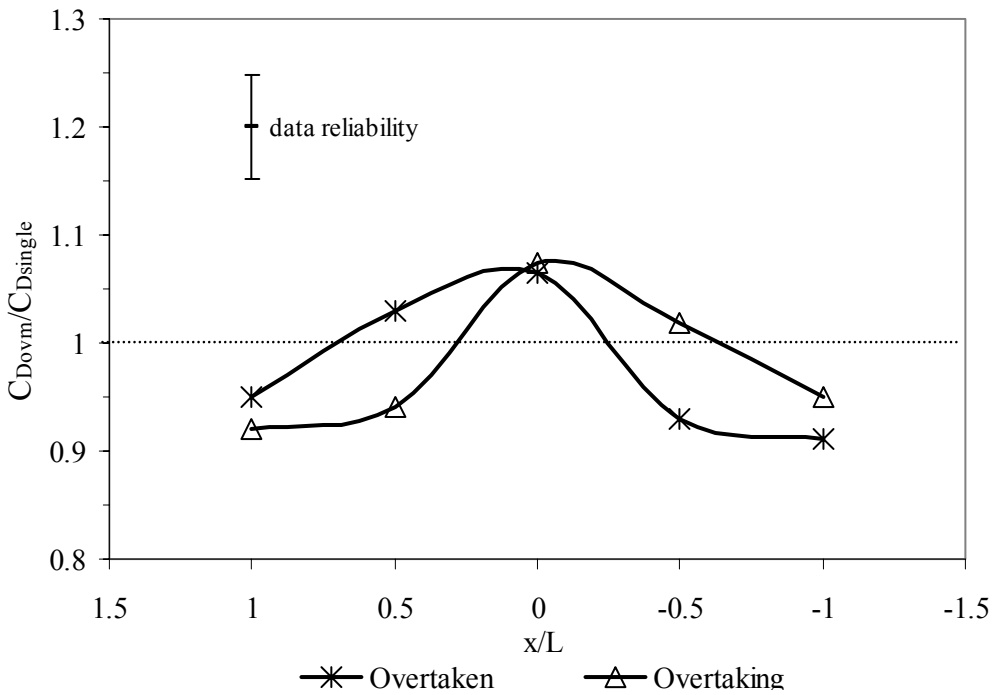

Figure 6.13 Drag Coefficient Ratios of the MIRA Models in Overtaking Situation (d/w = 0.1)

As seen from Figure 6.13, drag coefficient of both vehicles change about 10% of their single vehicle's value. Their C_D values are smaller than the $C_{Dsingle}$ when the longitudinal spacing is 1. Their first minimum is initially reached when the high pressure field at front of the overtaking vehicle tends to increase the base pressure of the overtaken vehicle. Similarly, the low pressure field at the base of the overtaken vehicle tends to decrease the front pressure of the overtaking vehicle. At x/l = 0.5, increased base pressure of the overtaken vehicle begins to decrease and reduced by the low pressure at the base of the overtaking vehicle. At the same time, the front pressure of the overtaking does not change substantially. High pressure at the front ends and low pressure at the rear ends of the both vehicle effect each other and therefore, they reach their maximum at x/l = 0. Front and base pressures of the overtaking vehicle tends to become single vehicle's values at x/l = -0.5. Due to the low base pressures of the overtaking vehicle, its front pressures decrease. Thus, C_D value also decreases and reaches its second minimum when spacing is -1. The front

pressures of overtaken vehicle almost do not change between -0.5 and -1, its drag coefficient does not change considerably.

Figure 6.14 and Figure 6.15 represent the results of left and right surface pressure distributions of the overtaken and overtaking vehicles

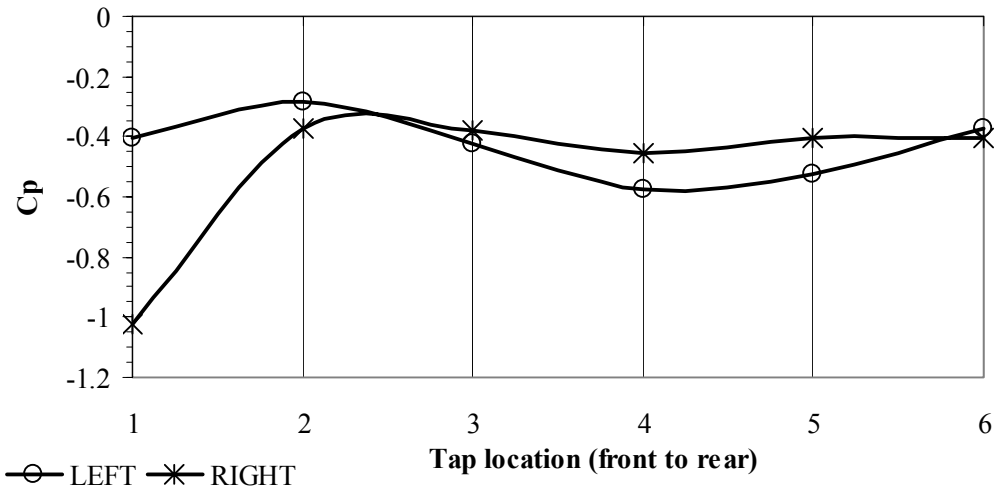

Figure 6.14 C_P Distributions at the right and left sides of the overtaken vehicle at x/l=0

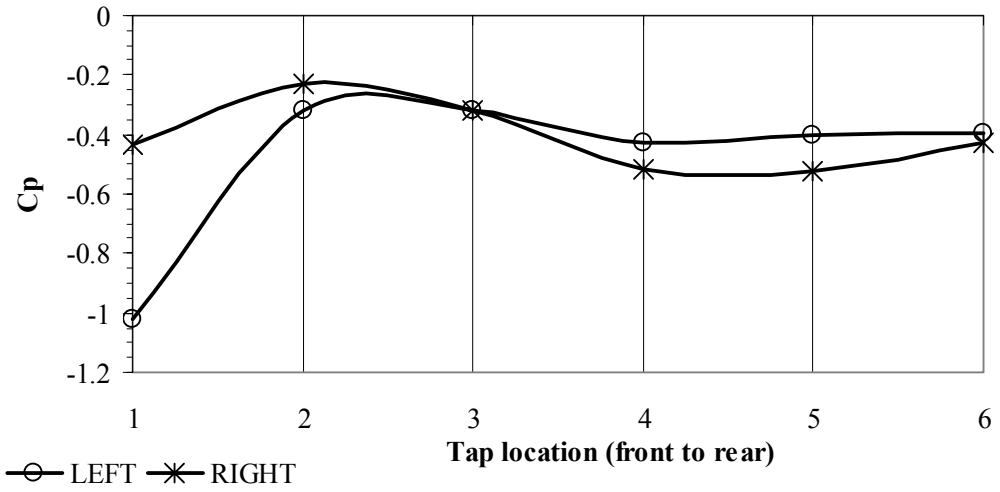

Figure 6.15 C_P Distributions at the right and left sides of the overtaking vehicle at x/l=0

In Figure 6.14, left surface pressures are higher than right surface pressures for the overtaken vehicle. There is a side force from left to right for the overtaken vehicle. For the overtaking vehicle's results shown in Figure 6.15, right surface pressures are higher than left ones at all positions. Therefore, side force occurs from right to left. As a result, both vehicles push each other to the other sides at the side by side position because of the side forces influence on them.

In Figure 6.16, the further situation (d/w = 0.5) is shown. Like the closer situation, pressure interactions between the vehicles are observed for it. But these interactions are not influential as the d/w = 0.1 situation. Therefore, drag coefficient of both vehicles change about 5 % of their single vehicle's value. For d/w = 0.5, drag coefficient ratio of both vehicles according to the longitudinal spacing trends are similar to the closer situation.

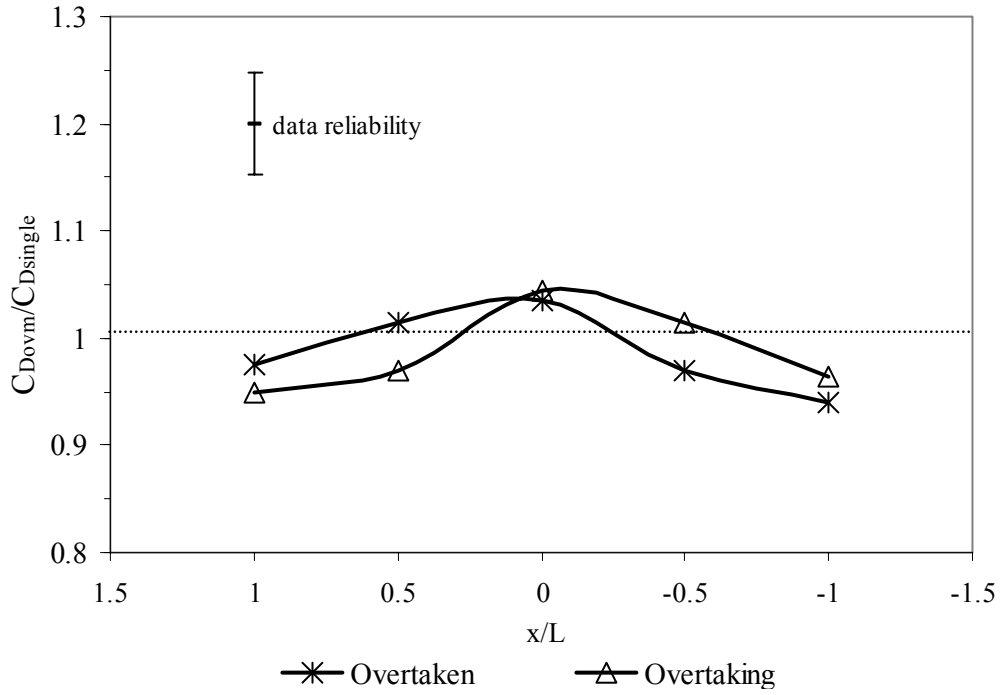

Figure 6.16 Drag Coefficient Ratios of the MIRA Models in Overtaking Situation (d/w=0.5)

6.2 Results of the Ahmed Body Model

6.2.1 Single Vehicle Results

The mean uncorrected drag coefficient of Ahmed Body model was measured as 0.296 with an uncertainty value of 0.013 or about 4.4 %. Single vehicle drag measurements of the model were repeated at 3 different streamwise locations as applied in MIRA model single vehicle. The slight increments in drag coefficients are the same order as the uncertainty values of the measurements.

Table 6.6 Average Uncorrected C_D values for the Ahmed Body

Location	Distance from leading edge (mm)	Uncorrected C_D
1	150	0.296
2	370	0.298
3	672	0.302

Experiments were conducted at a Reynolds number of 3.3×10^5 for Ahmed Body. Tripping wire was utilized to artificially trip the boundary layer on the model. With using the procedure explained in Appendix E, Tripping was applied to obtain a turbulent boundary layer on the model. After the tripping was applied; C_D was found as 0.292 for Ahmed Body single vehicle.

For 1/4 scale Ahmed Body, the blockage ratio is 3.1%. Continuity and simplified pressure signature were used as the blockage correction methods. For the continuity method, the ratio of the corrected and uncorrected dynamic pressures is found as 1.065. When substituting this value to the equation 3.15, the corrected drag coefficients at different streamwise locations are found as in Table 6.2

Table 6.7 Average corrected C_D values for the Ahmed Body after Continuity Method

Position (mm)	C_{Dref}	C_{Dlocal}*
150	0.296	0.278
370	0.298	0.280
672	0.302	0.283

In Table 6.5, C_{Dref} represents the uncorrected drag coefficient of single vehicle determined with using the reference dynamic pressure. C_{Dlocal}* is the corrected dynamic pressure found with using the continuity correction method.

Similar to the corrections of MIRA model, pressure signature method was also applied for the correction of drag coefficient. In Figure 6.17, the graphs of ΔC_P (difference in C_P when the tunnel is empty and with a model present) with location of the static taps are shown for 3 different streamwise locations which represent the positions of the model fixed to the three component balance.

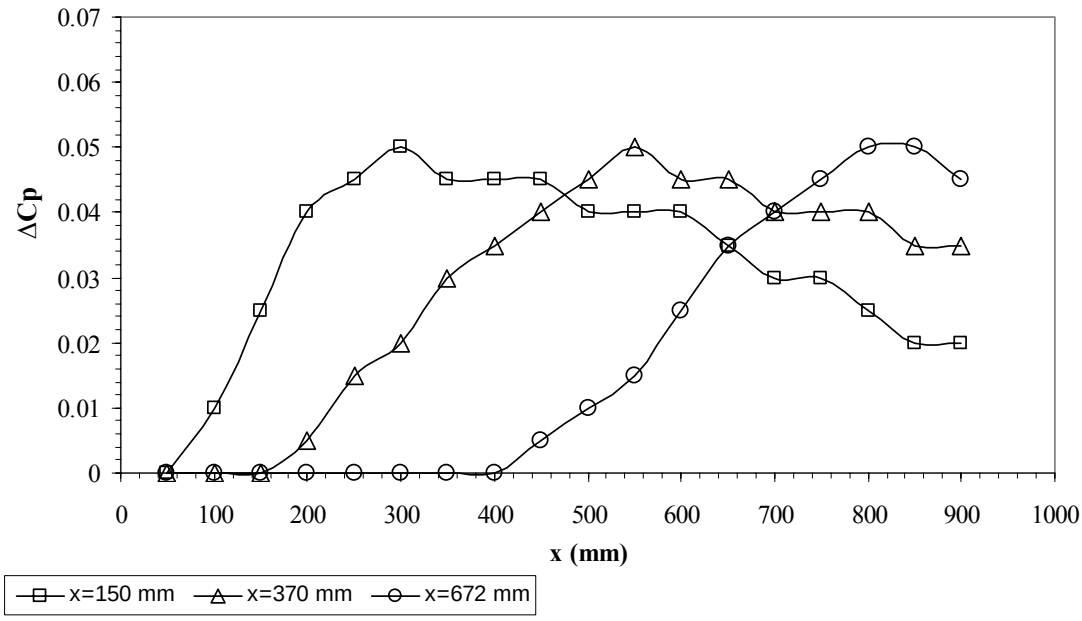

Figure 6.17 ΔC_P Distributions at Three Streamwise Locations for the Ahmed Body Model

In Figure 6.18, C_P values which are the pressure difference between each tap and the reference location divided by dynamic pressure at the reference location are shown.

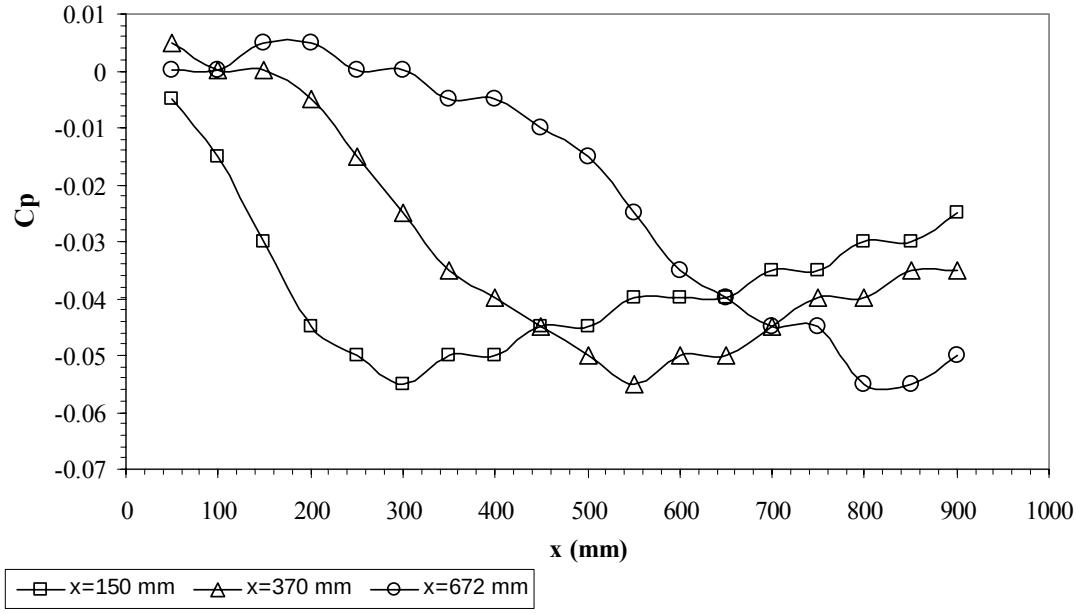

Figure 6.18 C_P Distributions at Three Streamwise Locations for the Ahmed Body Model

The corrected drag coefficients of Ahmed Body model were found as in Table 6.6 with using the pressure signature method.

Table 6.8 Average corrected C_D values for the Ahmed Body after Pressure Signature Method

Position (mm)	ΔC_{Pmax}	C_{Plocal}	C_{Dref}	C_{Dlocal}**
150	0.045	-0.05	0.296	0.282
370	0.045	-0.055	0.298	0.283
672	0.05	-0.06	0.302	0.285

The pressure signature correction results are very similar to continuity correction results as the MIRA model's case. Continuity method results appear to provide better overall correction again. But Ahmed Body has a more blunt shape and sharp edges and also it has a rectangular base with a 0° slant angle. These parameters affect the wake of the Ahmed Body considerably. Thus, the pressure signature method was applied in close-following and passing situations in order to obtain the wake blockage effect.

The pressure coefficients measured from the centerlines of the right and left surfaces of the model is presented in Figure 6.19. They have both the same values as expected.

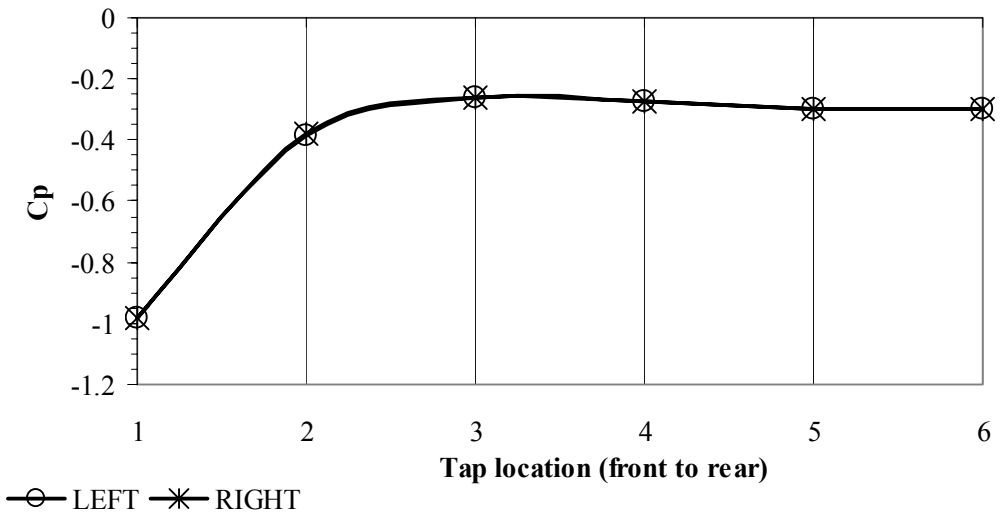

Figure 6.19 C_P Distributions at the of right and left surfaces of the Ahmed Body Model

C_P value of left and right surfaces is -1 at the first tap location. They increase to a value of -0.4 at the second location. They become almost constant value of -0.3 after the third tap location.

Figure 6.20 represents the measurements at the front and rear surfaces of the model. There are three tap locations at front of the Ahmed Body. These taps were located at

the centerline of the flat part of the front surface. There are five tap locations at the rear centerline as the experiments of MIRA model. The pressures are constant at the rear surface for single vehicle state as seen from Figure 6.20. For the front surface, C_P values are about 0.8 at the second and fourth tap location whereas it is 1 at the middle. This location is the stagnation point. It means that the static pressure read from this tap is equal to the total pressure in the wind tunnel.

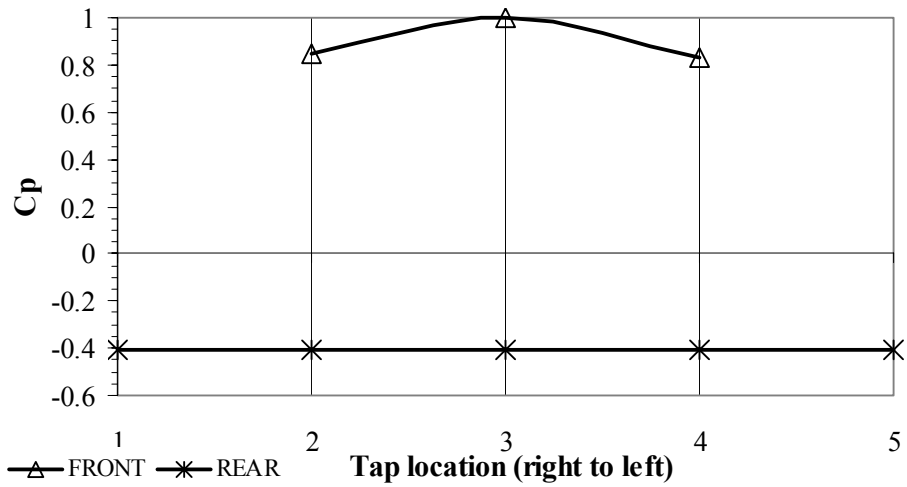

Figure 6.20 C_P Distributions at the of front and rear surfaces of the Ahmed Body Model

6.2.2 Close-Following Results

Figure 6.21 represents the data for close-following situation as a function of vehicle spacing between the vehicles. The data presented is averaged over at least three sets of independent measurements. All test results are shown within the error bounds established from the single vehicle measurements shown in the figures. The forward vehicle is represented by the squares while the rear vehicle by triangles. Longitudinal spacing is measured on the centerline from the rear end of the leading model to the front end of the trailing model and is normalized with model length. Results were corrected by using the pressure signature method.

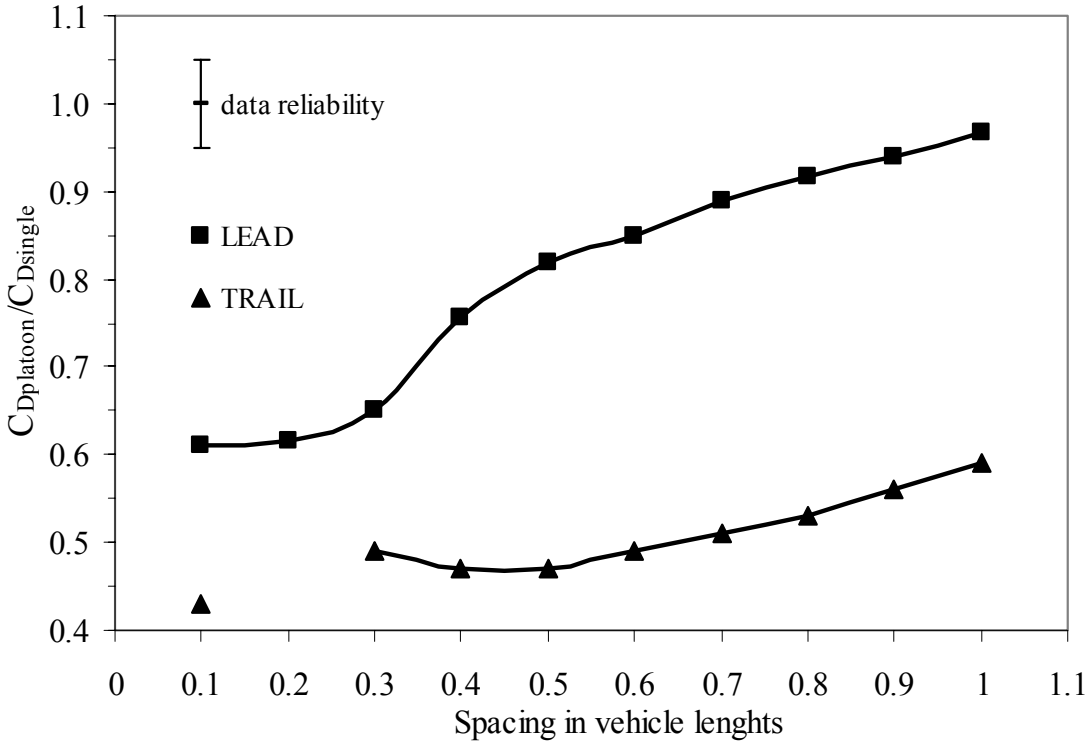

Figure 6.21 Drag Coefficient Ratios of the Ahmed Body Models in Close-following Situation

Because of the their more blunt shapes and sharp edges, the leading and trailing Ahmed Body models feel the presence of the aerodynamic interactions substantially. The drag coefficient of the lead vehicle drops linearly when the spacing decreases from one to half of the model. At half spacing, C_D of the leading vehicle is about 0.82 $C_{Dsingle}$. Between 0.2 and 0.5 vehicle spacing, the influence of the aerodynamic interactions on the leading vehicle increases and therefore C_D decreases from 0.82 $C_{Dsingle}$ to 0.62 $C_{Dsingle}$. It seems to be almost constant between 0.1 and 0.2 vehicle spacings. On the other hand, drag coefficient of the trailing vehicle decreases importantly. It decreases from 0.59 to 0.46 $C_{Dsingle}$ when the vehicle spacing decreases from one to half vehicle spacing. Then, it begins to increase between 0.3 and 0.5 spacings. It reaches to minimum at 0.1 vehicle spacing with a value of 0.42 $C_{Dsingle}$. Drag force could not be measured at 0.2 vehicle spacing due to the high aerodynamic effects of the leading vehicle's wake. A *flow induced vibration problem* was observed at this vehicle spacing.

For x/L = 0.1 and 0.5 configurations, Tripping cases were applied to Ahmed Body models. According to the results, reductions in drag are more observable for Ahmed Body Trip cases but C_D / $C_{Dsingle}$ changes are not higher than their uncertainty values. Thus, they were not used for the Ahmed Body experiments. The uncorrected data obtained with and without trip cases for x/l = 0.1 and x/l = 0.5 are shown in Table 6.9 and Table 6.10, respectively.

Table 6.9 C_D Results of the Ahmed Body with and without trip for x/l=0.1 situation

Leading Vehicle			**Trailing Vehicle**		
Case	**$C_{Dplatoon}$**	**$C_{Dplatoon}$ / $C_{Dsingle}$**	**Case**	**$C_{Dplatoon}$**	**$C_{Dplatoon}$ / $C_{Dsingle}$**
Without Trip	0.182	0.61	Without Trip	0.127	0.43
With Trip	0.175	0.60	With Trip	0.118	0.40

Table 6.10 C_D Results of the Ahmed Body with and without trip for x/l=0.5 situation

Leading Vehicle			**Trailing Vehicle**		
Case	**$C_{Dplatoon}$**	**$C_{Dplatoon}$ / $C_{Dsingle}$**	**Case**	**$C_{Dplatoon}$**	**$C_{Dplatoon}$ / $C_{Dsingle}$**
Without Trip	0.244	0.82	Without Trip	0.140	0.47
With Trip	0.238	0.82	With Trip	0.132	0.45

Because of the *strong interaction regime* between the vehicles, cavity drag changes are more observable for Ahmed Body model. Figures 6.22-6.26 represent the rear and front surface pressure distributions. General trends are same as the MIRA model. But, because of the larger wake of the Ahmed Body, higher reductions and increments are observed.

In Figure 6.22, front and rear pressure distributions of the leading vehicle are given for the least vehicle spacing, x/l = 0.1. It is obtained that the C_P values are not

constant at the rear base of the leading vehicle. C_P increases from -0.4 to -0.2 at the second tap. Then it decreases to the value about -0.3. It reaches its maximum at the fourth location and finally decreases again to the value of -0.4. Higher base pressures cause lower cavity drag. On the other hand, there are big reductions in the front pressures of the trailing vehicle as a result of the lower cavity drag (Figure 6.23). The increment in the rear base pressures is the other effect of the drag reduction at that position.

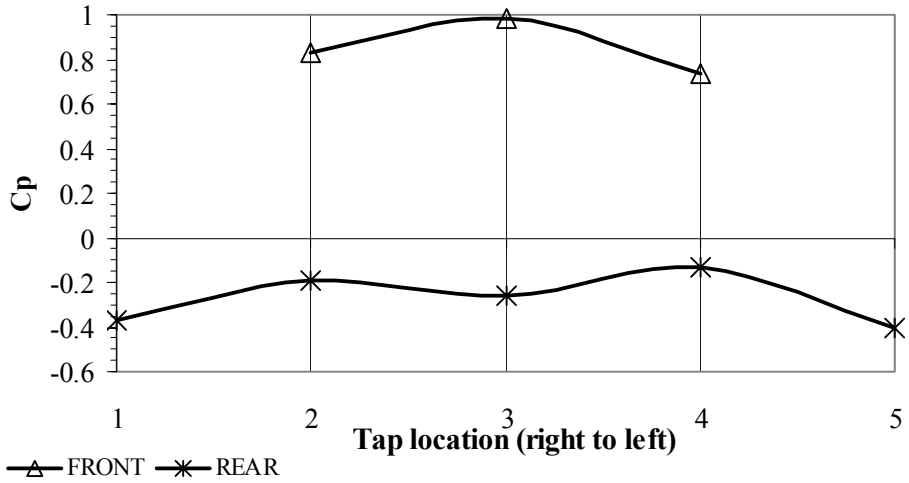

Figure 6.22 C_P Distribution at the front and rear end of the leading vehicle for x/l=0.1

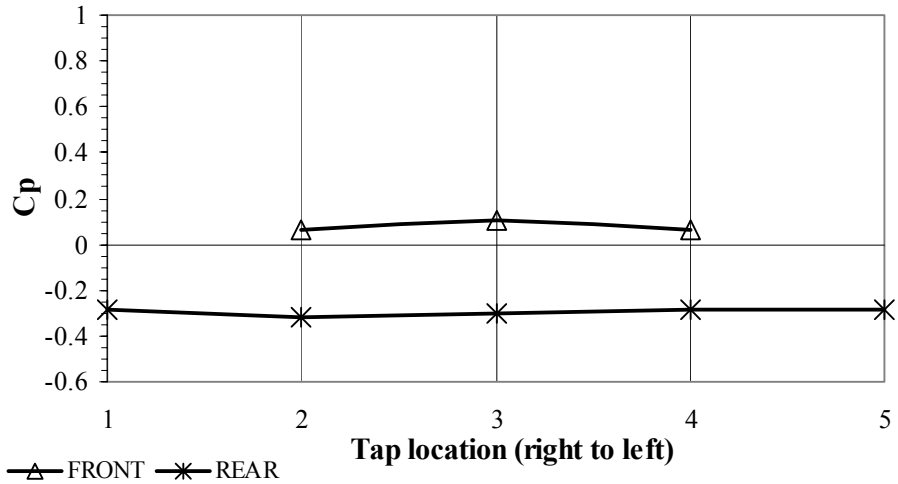

Figure 6.23 C_P Distribution at the front and rear end of the trailing vehicle for x/l=0.1

When it is compared with the MIRA model, front pressures of the trailing Ahmed Body increase suddenly with the increment of the spacings. Meanwhile, rear base pressures of the leading vehicle decrease for the higher gaps. C_P Distribution at the front and rear end of trailing model for half and one vehicle lengths are given in Appendix B.

Average drag coefficient ratios of the models decrease linearly between one vehicle length and half vehicle length as seen from Figure 6.24. When the gap decreases from 0.5 to 0.3 spacings, drag reduction increases. As the trailing vehicle could not be measured, drag coefficient is unknown for 0.2 vehicle spacing. Finally, the minimum value of drag coefficient occurs at 0.1 vehicle spacing. The average drag coefficient of both vehicles drops to almost half of the single vehicle's value.

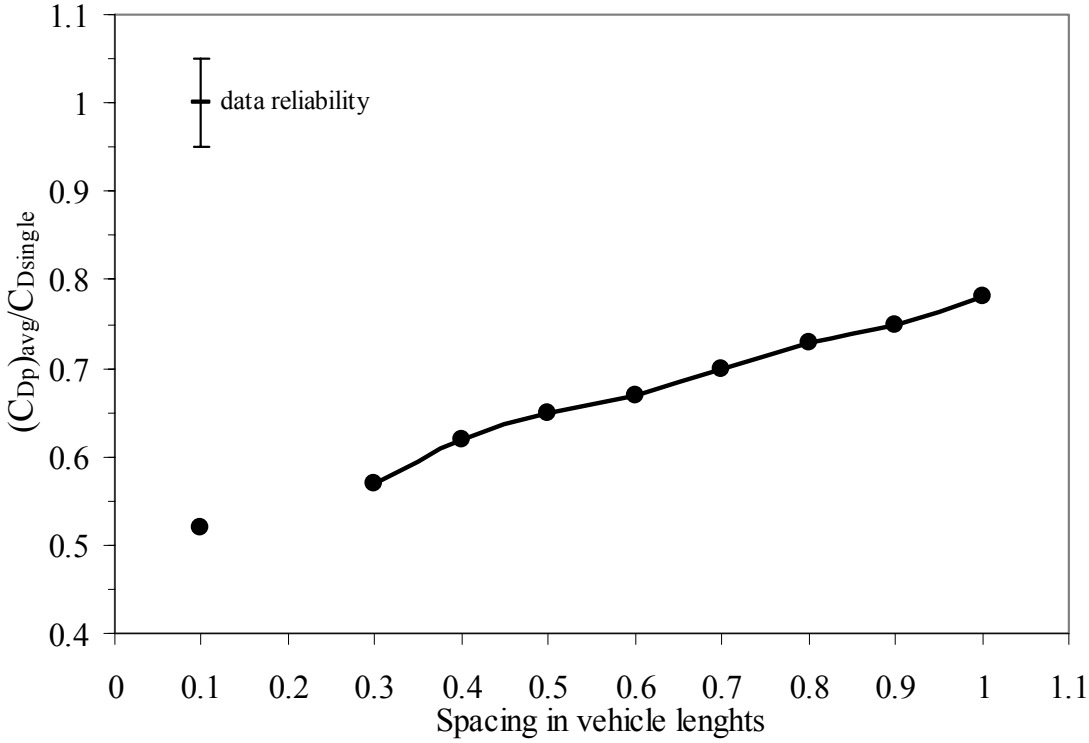

Figure 6.24 Average Drag Coefficient Ratios of the Ahmed Body in Close-following Situation

As explained in Chapter 2, there are some studies about close-following or platoon operations in which different type of vehicles were used. In Figure 6.25 and Figure 6.26, C_D ratio with respect to the vehicle spacing results of the Ahmed Body and MIRA models are compared with the other models used in the platoon operations. GM Chevrolet Lumina APV minivan models in the study of Zabat et al [10], [11] and racing car models in the study of Romberg et al. [41] were used for comparison. In these studies, the drag coefficients are also normalized by the coefficient of a single vehicle model in isolation. In Figure 6.25, the leading models of different type of vehicles in platoon operations are compared. Squares for MIRA model, triangles for Ahmed Body, stars for Lumina and circles for Race car were used as the representative symbols.

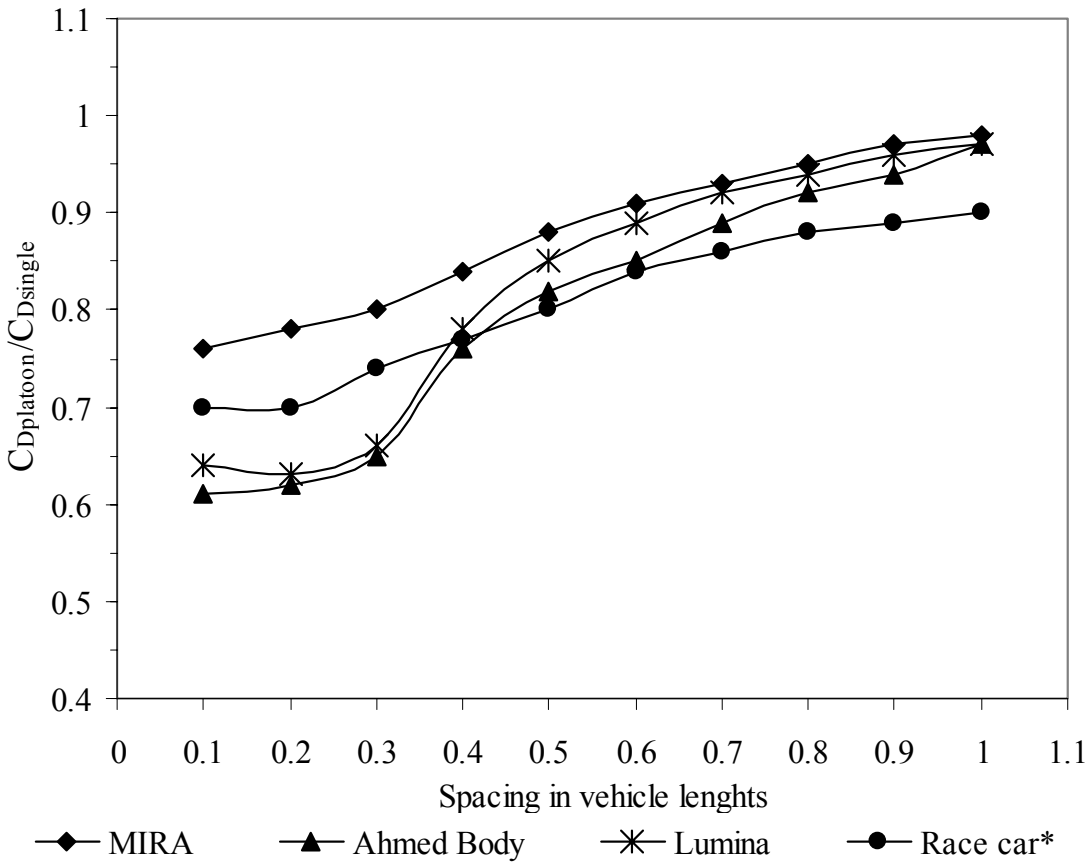

Figure 6.25 Drag variations with inter-vehicle spacing of different types of models for the leading vehicle in Close-following Situation

Because of different geometries of the vehicles used for comparison, general trend of drag variations are different as seen from Figure 6.25. MIRA model, which is a sedan type, has the least drag reductions at all spacings. The highest drag reductions are observed in Ahmed Body for the spacings smaller than 0.5 vehicle length. For larger spacings, race car has big reductions in drag. It is probably due to the rear base geometry of this vehicle. Lumina and Ahmed Body drag coefficients increase slowly between 0.1 and 0.3 vehicle lengths. Their drag coefficients increase substantially above 0.3 vehicle length. Because of their larger rear bases, pressure variations on the rear surface change suddenly for these vehicles. It affects the cavity drag between the trailing and leading vehicles importantly and causes higher drag coefficients at the larger spacings.

The trailing vehicle experiences lower drag than the leading one because it is shielded by the leading vehicle. The highest reduction in drag is observed on the Ahmed Body as shown in Figure 6.26. Above 50 % drag reduction occurs for Ahmed Body at spacings smaller than 0.5 vehicle length. Although drag coefficient of the Ahmed Body increase with the increments of spacings larger than 0.5 vehicle length, the least C_D ratios can be still observed on it. The highest C_D ratios are observed on the MIRA model. But C_D ratios of Lumina van model are smaller than MIRA at 0.1 and 0.2 vehicle lengths. It decreases between 0.3 and 0.5 vehicle spacings and then begins to increase again after that position. But these increments are slightly and there is only 5 % drag change between half and one vehicle length for Lumina model.

The least changes are observed on the racing car model as shown with circle symbols in Figure 6.26. Only 8 % increment in drag coefficient occurs from 0.1 to 1 vehicle lengths. It can be concluded that, there are strong aerodynamic interactions between the leading and trailing racing car models because of its aerodynamic shape. As a result of larger wake, the trailing racing car has lower front pressures and it causes reductions in drag forces.

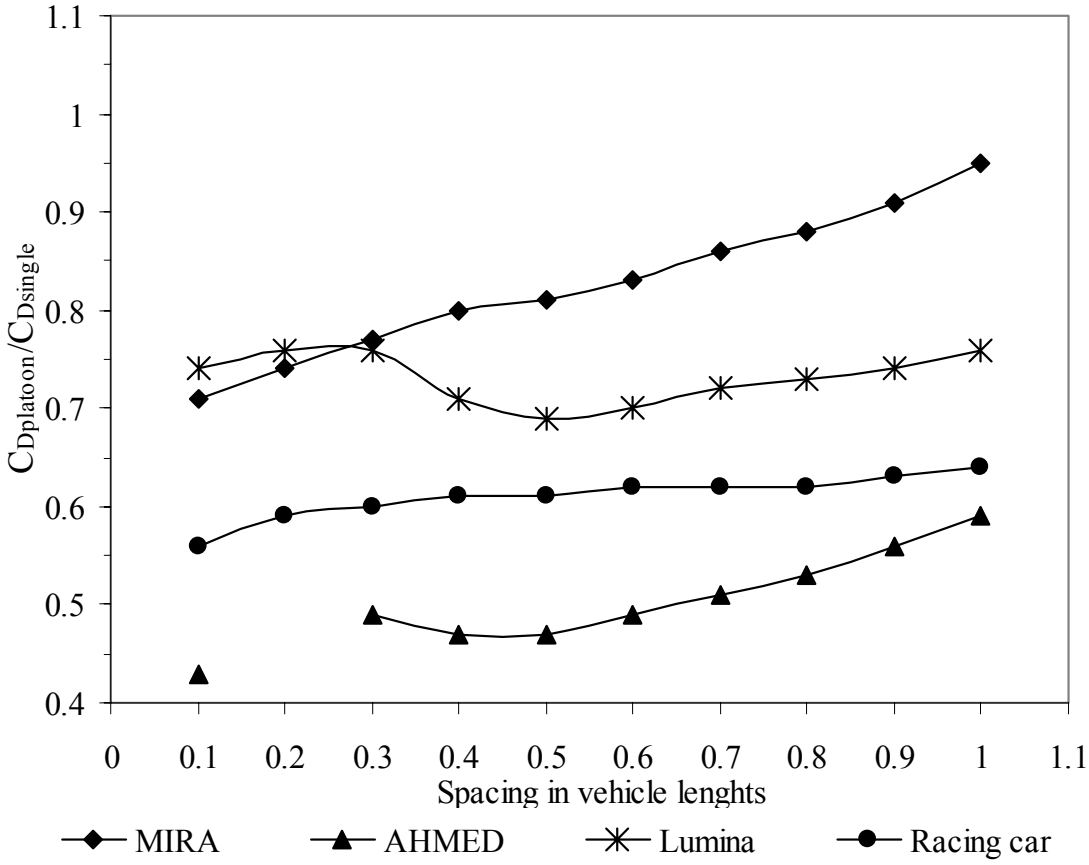

Figure 6.26 Drag variations with inter-vehicle spacing of different types of models for the trailing vehicle in Close-following Situation

It is observed from Figure 6.25 and Figure 6.26 that there is a critical spacing about 0.3 vehicle length for Ahmed Body and Lumina van models. For these models, drag coefficients of the leading vehicles increase suddenly larger than 0.3 vehicle length. For smaller spacings, C_D of the leading Ahmed Body and Lumina models change slowly. This is also correct for the Lumina trailing vehicle. It begins to decrease from this critical spacing of 0.3 to half vehicle length. For the larger spacings, it increases again. The C_D of the trailing Ahmed Body also decreases at the spacings from 0.3 to 0.4. It becomes constant between 0.4 and 0.5 vehicle lengths and at the larger spacings, it increases faster than the Lumina model. As the C_D of the trailing Ahmed Body could not be measured, the trend of it is unclear. The factors that are involved in these chaotic drag behaviors are discussed in the following pages.

In the study carried out by Koenig and Roshko [25], drag and flow field of two separated bluff bodies were investigated. In that study, several flow regimes depending on the gap/diameter parameters were identified. They concluded that the shear layers were thicker and the level of velocity fluctuation and of Reynolds stress was much higher for *the medium drag regime* than in l*ow drag Regime.* This indicated that there was a large-scale oscillation involving the whole cavity. Its coupling with the vortex structure in the shear layer could account for the high Reynolds stress there. This large scale cavity oscillation may be regarded as the beginning of a wake mode of the forebody, strongly influenced by the presence of the rear body.

When considering the Ahmed Body case again, the flow structure between the models is the most important reason of the vibration problem that should be investigated. Also, the flow structure at the wake of the trailing model is important. The main part of the unsteady loads on the trailing vehicle is due to the shedding vortices in the shear layers. For the 0.2 vehicle spacing, the oscillations in drag become much larger in amplitude because of these unsteady loads. Therefore, frequencies of the vortices shed from the front and rear bodies should be considered. In addition to these, natural frequency of the structure should be measured. When the frequency of the shedding vortices is very close to the natural frequency exhibited by the three component balance, the vibration occurs on the balance. These investigations are recommended for the further works.

At the end of the current study, it was decided to determine the frequencies of the shedding vortices behind single model for comparing the results with the past works and showing a way for the further works about this flow induced vibration problem. The shedding frequency is presented as a non-dimensional frequency or Strouhal number.

$$St = \frac{f_V . D_e}{U_\infty} \tag{6.2}$$

where, f_v is the characteristic frequency of vortex shedding; D_e is the effective diameter based on the height or width of the model base and U_∞ is the freestream

velocity. The shedding frequencies found at the measurement points at the wake plane of single Ahmed Body model are shown in Figure 6.27.

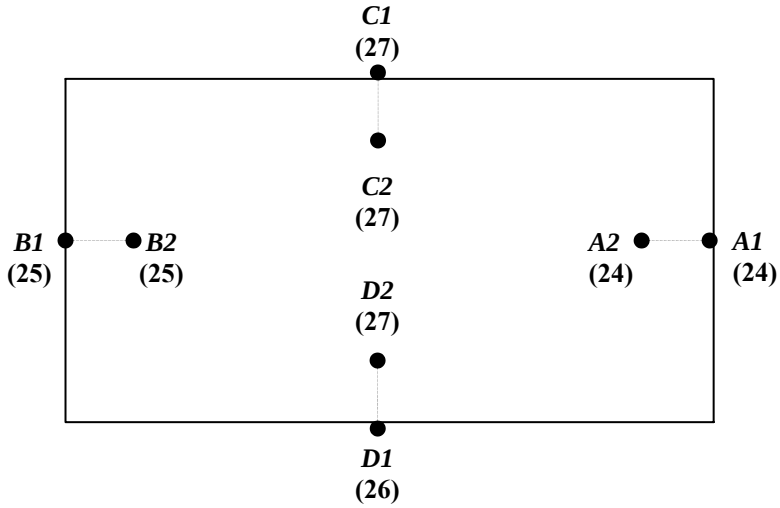

Figure 6.27 Shedding Frequencies at the measurement points of the wake plane behind single Ahmed Body Model

In the Literature, the vortex shedding occurs from the sides of the model at a Strouhal number between St ≈ 0.1 and St ≈ 0.2 for different scales and types of Squareback geometries [4], [5], [6]. According to the results shown in Figure 6.27, Strouhal number was obtained as St ≈ 0.10 for the characteristic frequency of the shedding vortices around 27 Hz, the base height of 0.072 m and freestream velocity of 19 m/s. The peak frequencies obtained from power spectral density estimates at the right and left sides of the Ahmed Body model were obtained around 25 Hz. For the base width of 0.096 m, this corresponds to a Strouhal number of St ≈ 0.12.

In Figure 6.28, X and Y represent A1 and A2, respectively. XY is the cross-correlation of the power spectral densities of these two points. The peak frequency is 24 Hz for both A1 and A2. From the cross correlation of the power spectral densities of A1 and A2, the peak frequency is obtained as 24 Hz again. The Power Spectral Estimates of the points on other sides of the wake plane are shown in Appendix C.

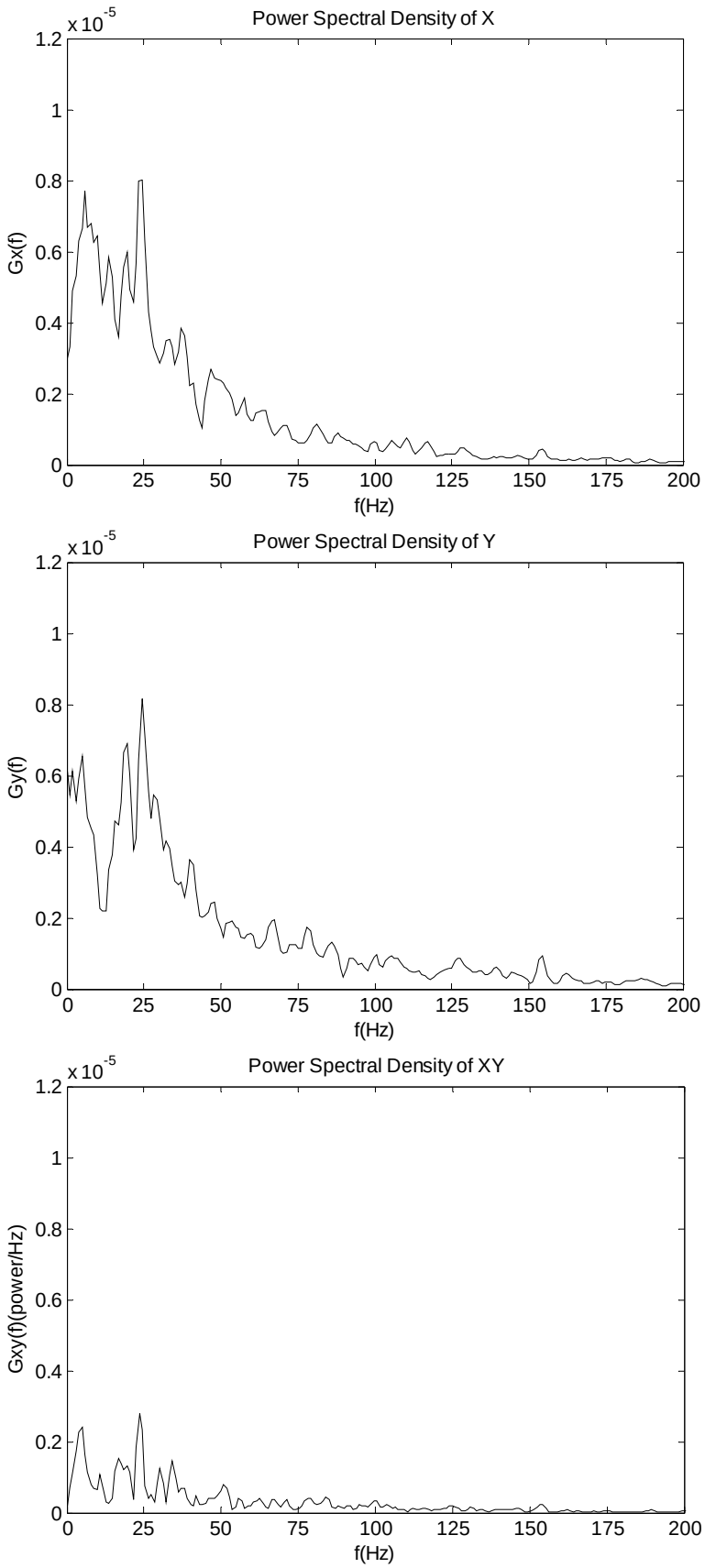

Figure 6.28 Power Spectral Density Estimates for the Points at the Right Side

In the previous study [35], Re-St relations were investigated for circular, rectangular and triangular cylinders. It was found that Strouhal number had a constant value along a wide range of Reynolds number. Peak frequencies at points A1 and A2 were obtained to consider the Re-St variations. Experiments were conducted from 600 to 1070 rpm for six different freestream velocities. The results are shown in Table 6.11. Re vs. St graph is given in Figure 6.29.

Table 6.11 Peak frequencies and St numbers with respect to the freestream velocities

ω (rpm)	U∞ (m/s)	Re	f (Hz)	St
600	10.3	179220	13	0.122
700	12.1	210540	15	0.120
800	13.9	241860	17	0.119
900	15.7	273180	19	0.117
1000	17.5	304500	22	0.122
1070	19	330600	24	0.123

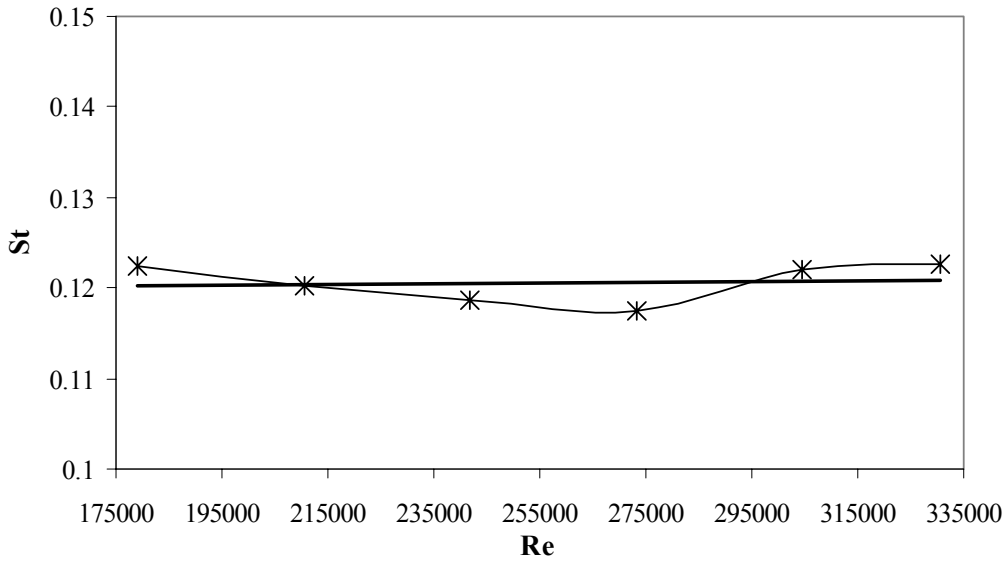

Figure 6.29 Re vs. St Graph for the Points at the Right Side

6.2.3 Overtaking Results

Similar to the MIRA model, overtaking experiments were conducted at d/w = 0.1 and d/w = 0.5 for Ahmed Body. The longitudinal spacing was used as the distance from

the front end of the leading model to the front end of the trailing model. Figure 6.30 and Figure 6.32 represent the data for overtaking situations as a function of vehicle spacing between the vehicles. The overtaken vehicle is represented by stars while the overtaking vehicle by triangles. Drag coefficient of each vehicle is divided by the single vehicle drag coefficient. In Figure 6.31, overtaking maneuver results are shown for the closer lateral spacing (d/w = 0.1). Since there are strong interactions between Ahmed Body models, big amount of changes are observed at all positions when compared to the MIRA model. Drag coefficients of both overtaking and overtaken vehicles are smaller than single state at x/l = 1. C_D of overtaken becomes greater than the single vehicle's value at x/l = 0.5. When both vehicles are side by side position, the increment is about 17 % of the single vehicle's value. Then, it begins to decrease and becomes about 0.85 $C_{Dsingle}$. It continues to decrease gradually and reaches the minimum at x/l = -1. Because of the largest drag reduction of overtaken vehicle occurred between x/l = 0 and x/l = -0.5, detailed measurements were done for this range as shown in Figure 6.31.

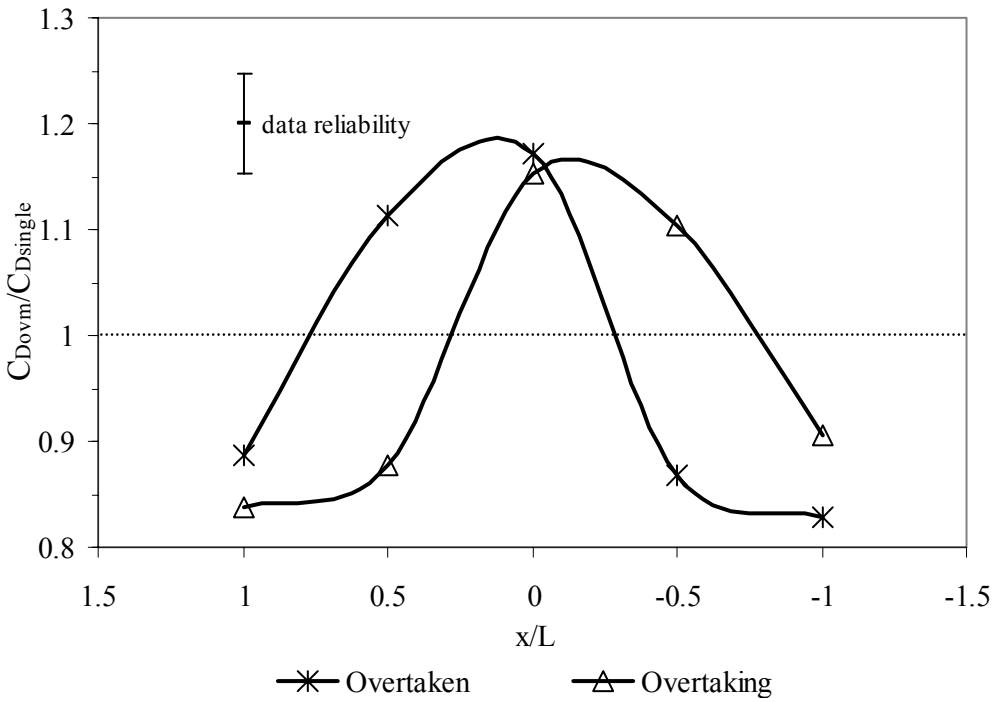

Figure 6.30 Drag Coefficient Ratios of the Ahmed Body in Overtaking Situation (d/w=0.1)

Figure 6.31 shows the C_D ratios with respect to spacings between 0 to -0.5 vehicle spacings with a step of 0.1. Reductions in drag with respect to the spacings have linear behaviors as seen in the figure. When the longitudinal spacing is x/l = -0.25, the drag coefficient of the model becomes equal to the $C_{Dsingle}$.

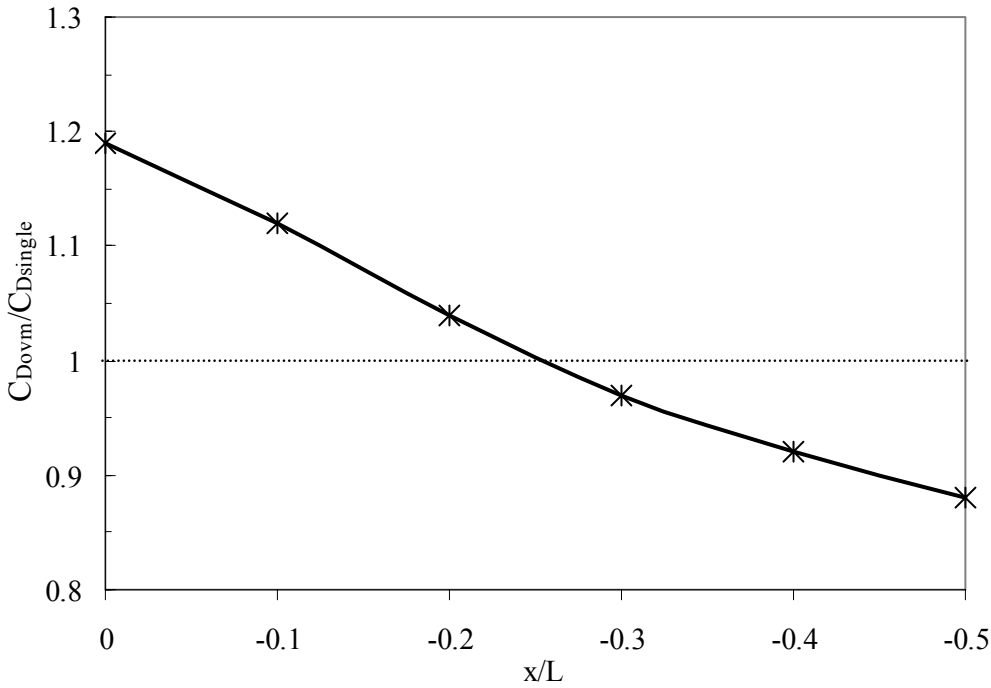

Figure 6.31 Drag variations with vehicle spacing between x/l=0 and x/l=-0.5 for the Ahmed Body in Overtaking Situation (d/w=0.1)

The reduction of C_D is at the maximum value when the longitudinal spacing is one vehicle length. C_D increases to about 0.88 $C_{Dsingle}$ at x/l = 0.5. C_D reaches the maximum at side by side location similar with the overtaken vehicle. Then, the descent of the C_D begins after side by side location and it becomes 1.1 $C_{Dsingle}$ when x/l = -0.5. Finally, a larger descent occurs between -0.5 and -1 spacings and C_D of overtaking vehicle reaches the second minimum with a reduction of 10 % with respect to drag coefficient of single vehicle.

Pressure variations of the front and rear surfaces that cause drag changes are same as explained in MIRA model's overtaking case. Because of these variations are larger than the MIRA cases, amount of the descents and increments are also larger for Ahmed Body. High pressures at front of the overtaking vehicle tend to increase the base pressure of the overtaken vehicle. Similarly, the low pressure field at the base of the overtaken vehicle tends to decrease the front pressure of the overtaking vehicle. These aerodynamic interactions between vehicles occur at all positions as explained in MIRA case. But they are more powerful rather than the interactions between MIRA models.

When the vehicles are side by side (x/l = 0) position, left and right surface pressure distributions are as shown in Figure 6.32 and 6.33. For the overtaken vehicle, pressures at front of the left surface are higher than the right surface (Figure 6.32). It means that there is a side force from left to right side.

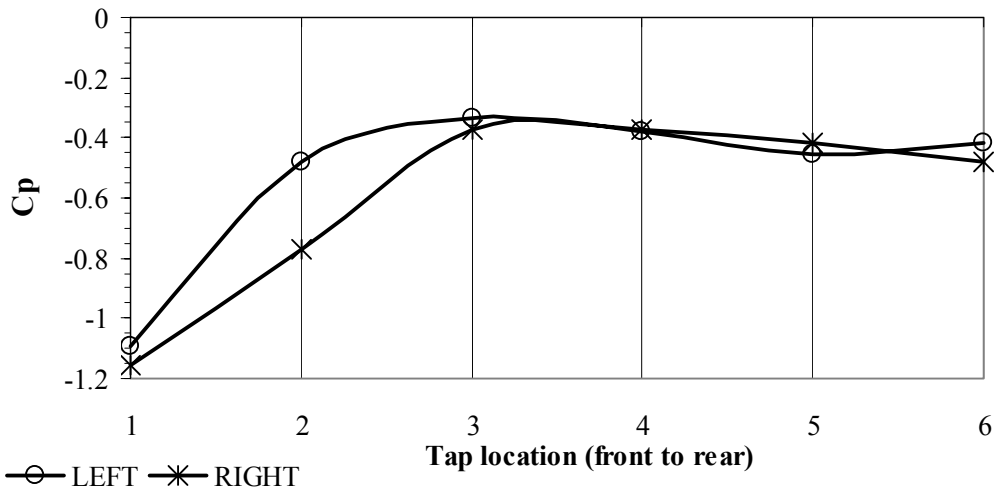

Figure 6.32 C_P Distributions at the right and left sides of the Ahmed Body overtaken vehicle at x/l=0 position

Left and right pressure distributions are given in Figure 6.33 for the overtaking vehicle at side by side position. Right surface pressures are higher than the left ones especially from the first to third tap locations. Likewise, these pressure differences cause side force from right to left for the overtaking vehicle.

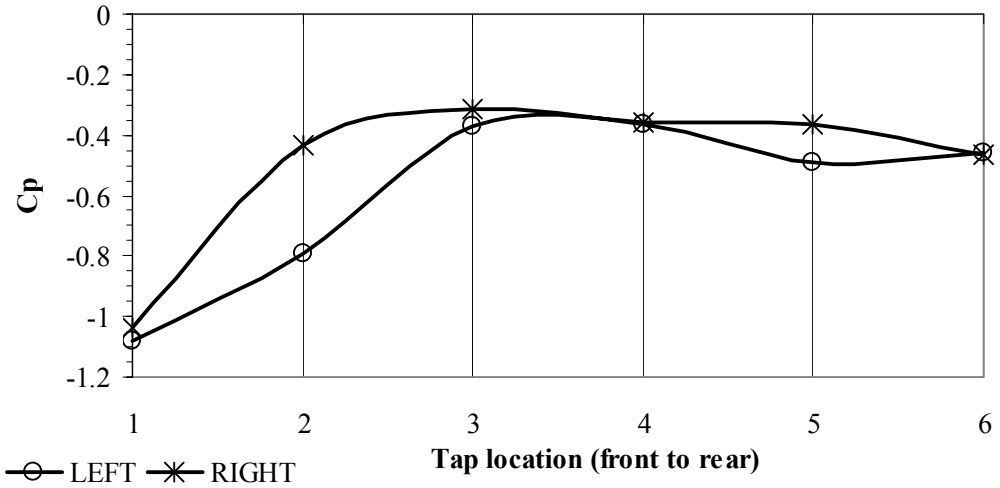

Figure 6.33 C_P Distributions at the right and left sides of the Ahmed Body overtaking vehicle at x/l=0 position

It can be concluded from the results of the pressure distributions at the side surfaces; both vehicles push each other similar with the MIRA model's case. Therefore, when the vehicles are at side by side position, they tend to push each other to the opposite sides.

In the further situation (d/w = 0.5) shown in Figure 6.34, aerodynamic interactions are not so strong as the closer situation for Ahmed Body models. Variations of drag coefficients are similar with the closer situation. But the magnitudes of these changes are much lower than observed in the closer situation.

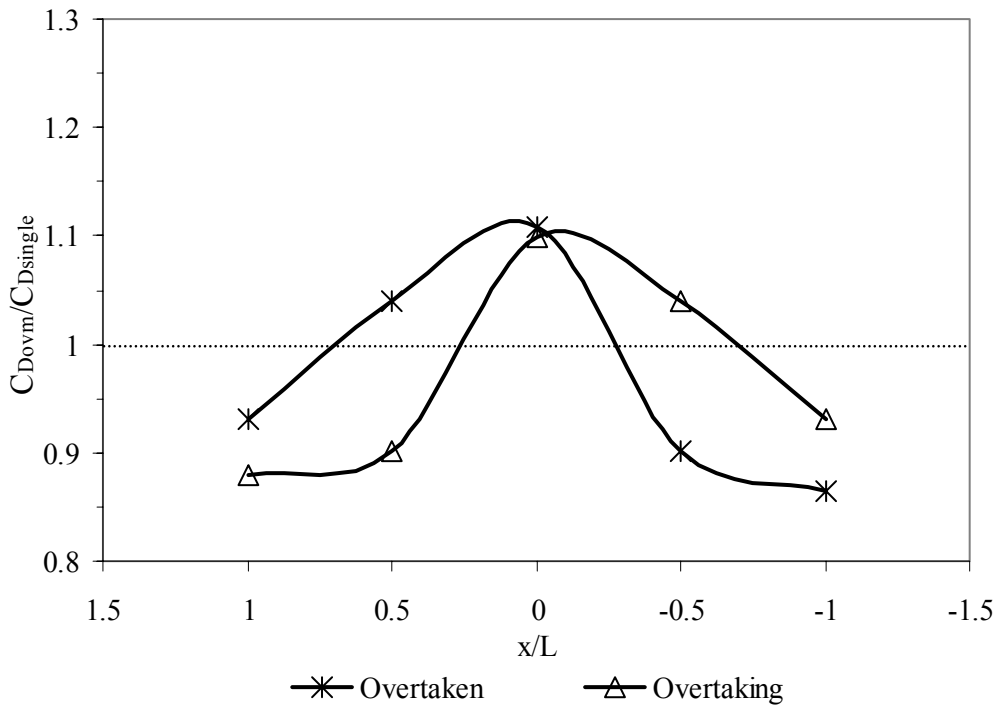

Figure 6.34 Drag Coefficient Ratios of the Ahmed Body in Overtaking Situation (d/w=0.5)

CHAPTER 7

CONCLUSIONS AND RECOMMENDATIONS

In this chapter, the major conclusions of the results from wind tunnel experiments are discussed. Some final comments on possible extensions of this study are also presented.

7.1 Conclusions

In the scope of the current study, aerodynamic interactions of two different types of vehicles were investigated when they were in close-following and passing situations. Drag forces and surface pressures of the models at each situation were measured according to this aim. Two different Blockage correction methods on the basis of drag coefficient results were applied. For each vehicle model, the results were categorized due to the single vehicle, close-following and overtaking situations. The results were discussed and compared with the results of the studies found in the literature.

The uncorrected mean drag coefficient of MIRA model was measured as 0.329 with an uncertainty value of 0.015 or about 4.5 %. For Ahmed Body it was measured 0.296 with an uncertainty value of 0.013 or about 4.4 %. Single vehicle drag measurements of the models were repeated at 3 different streamwise locations. It was obtained that there are small increments in drag coefficient for both vehicles. But these slight increments were at the same order as the uncertainty values of the measurements.

Experiments were conducted at a Reynolds number of 2.9×10^5 for MIRA and 3.3×10^5 for Ahmed Body. Thus, the tests were conducted at Reynolds numbers about one order of magnitude lower when comparing with the full scale operation. In order to account these differences, small roughness elements were utilized to artificially trip the boundary layer on the model. After the tripping was applied; drag coefficient of MIRA was found as 0.325. For Ahmed Body, it was measured as 0.292. The trip caused slight decreases in drags and the changes are the same order as the estimate of reliability in the experiments.

For the experiments conducted at METU Mechanical Engineering Fluid Mechanics Laboratory; the blockage ratio of 1/18 scale MIRA model is 2.6 %. For 1/4 scale Ahmed Body, the blockage ratio is 3.1 %. Continuity and simplified pressure signature were used as the blockage correction methods. Drag coefficients at all streamwise locations were corrected with an amount of 5.5 % for MIRA and 6.5 % for Ahmed Body due to the continuity method. Pressure signature results are very similar to continuity correction results since the blockage ratios of the models are small. Continuity method results appear to provide better overall correction. But wake blockage effect should also be considered for close-following and passing situations. Thus, Pressure Signature method was used to obtain both solid and wake blockage effects.

For the close-following situations of the vehicles, drag is measured on each of two models in tandem separately. The distance between the vehicles is normalized by the model length, so that spacing 1 is a distance of 1 car-length. For MIRA model, linear increments are observed for both leading and trailing models. Because of their more blunt shapes and sharp edges, the leading and trailing Ahmed Body models feel the presence of the aerodynamic interactions substantially. The important reduction in drag occurs at the least vehicle spacing for both vehicle types. About 29% drag reduction occurs for trailing vehicle whereas the leading model drops to 24% of its single vehicle value for MIRA model. The drag coefficient values sharply reduce for both trailing and leading models of Ahmed Body. At that location, the leading vehicle has a drag reduction with an amount of 39 % whereas a maximum drag reduction of 58 % is achieved for the trailing vehicle.

When the flow travels over a cut-out, a low-drag regime is always associated with the fact that the cavity shear layer attached at the downstream corner. When the shear layer impinged on the downstream wall that is below the corner, higher cavity drag is observed [39]. At the least spacing between vehicles, surface pressures at the rear base of the leading model are obtained higher. The higher base pressure helps to reduce the drag force acting on it. Therefore, it causes a lower cavity drag.

For MIRA model, about 30 % pressure drop occurred at the front end of the trailing vehicle. A higher cavity drag resulting from the larger gap between the models causes higher front pressure on the trailing vehicle and a lower base pressure on the leading vehicle. At the middle vehicle spacing (x/l = 0.5), front end pressures of the trailing vehicle increase when it is compared with the least vehicle spacing (x/l = 0.1). Also, there is a reduction at the rear end pressures of the leading model. For the largest vehicle spacing (x/l = 1), front and rear pressures of the leading vehicle is almost same as the single vehicle. The leading vehicle is not affected by the cavity drag at that position and therefore, the drag experienced by the leading vehicle is nearly unchanged when it is compared with the single vehicle. Thus, the drag coefficient ratio is almost unity. For the trailing vehicle, the front pressures are lower than the single vehicle and therefore, they cause a drag reduction on it.

Because of the strong interaction regime between the vehicles, cavity drag changes are more observable for Ahmed Body model. General trends are same as the close-following situation of the MIRA model. But, because of the larger wake of the Ahmed Body, higher reduction in front pressures and higher increments in rear pressures occur.

When comparing the results for a platoon of MIRA models and Ahmed Body models with the results of the other types of vehicle models used in the literature, aerodynamic interactions are heavily due to the shape and size of the vehicles. MIRA model which is a sedan type has the least drag reductions at all spacings. The highest drag reductions are observed in Ahmed Body for the spacings smaller than 0.5 vehicle length. For larger spacings, race car has big reductions in drag. It is probably due to the rear base geometry of this vehicle. Lumina and Ahmed Body drag

coefficients increase slowly between 0.1 and 0.3 vehicle lengths. Then, their drag coefficients increase substantially above 0.3 vehicle length. Because of their larger rear bases, pressure variations on the rear surface change suddenly. They produce larger and more turbulent wakes with their more blunt shape and sharp corners. It affects the cavity drag between the trailing and leading vehicles importantly and causes higher drag coefficients at the larger spacings. The more streamlined shape of the cars results in smaller changes in the force coefficients. There is a critical spacing about 0.3 vehicle length for Ahmed Body and Lumina van models. For these models, drag coefficients of the leading vehicles increase suddenly larger than 0.3 vehicle length. For smaller spacings, C_D of the leading Ahmed Body and Lumina models change slowly. This is also correct for the Lumina trailing vehicle. It begins to decrease from this critical spacing of 0.3 to half vehicle length. For the larger spacings, it increases again. The C_D of the trailing Ahmed Body also decreases at the spacings from 0.3 to 0.4. It becomes constant between 0.4 and 0.5 vehicle lengths and at the larger spacings, it increases faster than the Lumina model. As the C_D of the trailing Ahmed Body could not be measured, the trend of it is unclear. Thus, it was decided to investigate the factors that are involved in chaotic drag behaviors.

For the spacing of 0.2 vehicle length, the force balance exhibits several significant modes of oscillation. Since there is a little natural damping in the system, strong resonances are observed. The main part of the unsteady loads on the trailing vehicle is due to the shedding vortices in the shear layers. At this spacing, the oscillations in drag become much larger in amplitude because of these unsteady loads. Therefore, frequencies of the vortices shed from the front and rear bodies should be considered. In addition to these, natural frequency of the structure should be measured. When the frequency of the shedding vortices is very close to the natural frequency exhibited by the three component balance, the vibration occurs on the balance. These investigations are recommended for the further works. The shedding frequency is presented as a non-dimensional frequency or Strouhal number. At the end of the current study, it was decided to the frequencies of the shedding vortices behind single model for comparing the results with the past works and showing a way for the further works about this flow induced vibration problem. The vortex shedding occurs from the left and right sides of the model with a Strouhal number of $St \approx 0.12$.

For the upper and down sides, vortex shedding occurs with St ≈ 0.10 at the wake of the Ahmed Body model.
Drag was measured on each of two models side by side with a two different lateral spacings for the overtaking situations. The lateral distance between models was normalized by the width of the model. Experiments were conducted at d/w = 0.1 and d/w = 0.5 to determine the effect lateral spacings.

For MIRA model, first minimum is initially reached when the high pressure field at front end of the overtaking vehicle tends to increase the base pressure of the overtaken vehicle. High pressure at the front ends and low pressure at the rear ends of the both vehicle effect each other and therefore, they reach their maximum when they are at side by side position. They reach their second minimum when the rear end of the overtaking vehicle is aligned with the front end of the overtaken vehicle. Because of the pressure differences between left and right surfaces, side forces influence on both vehicles. As a result, they push each other to the opposite sides. For the further situation (d/w = 0.5), interactions are not influential as the d/w = 0.1 situation. Therefore, drag coefficient of both vehicles do not change considerably.

Like the close-following situation, there are strong interactions between Ahmed Body models for the overtaking situation. When it is compared with the MIRA model, big amount of changes are observed at all positions. Because of the pressure variations are larger than the MIRA cases, amount of the descents and increments are also larger for Ahmed Body. When both vehicles are side by side position, the increment is about 17 % of the single vehicle's value. It can be concluded from the results of the pressure distributions at the side surfaces; both vehicles push each other similar with the MIRA model's case.

7.2 Future Work Recommendations

As a future work, the following recommendations can be taken into consideration.

Besides the drag force, other forces and moments acting on the vehicle can be measured and investigated for the aerodynamic interactions of vehicles in close-

following and passing situations. For these investigations, a new test set-up can be designed and constructed.

An internal balance may be designed and constructed to reduce the uncertainties that influence the drag force and/or other forces and moments. Because of the slight values of the side forces, this should be useful for their measurements. But if the present balance is wanted to be used, some improvements should be done on it. Especially, for the vehicles with more blunt shapes, vibrations due to the unsteady loads may occur on the balance. Some precautions should be done to eliminate these effects.

The detailed investigations of the vibration of the balance may be considered for the flow induced vibration problems. The natural frequency of the balance can be measured and compared with the shedding frequencies. The effects of the characteristic frequencies of the vortices with respect to the spacing between vehicles can be investigated. Besides the shedding frequency, the effects of the pumping frequencies may be considered for their effects on the leading vehicles in close-following situations.

The aerodynamic interactions of mixed vehicles will result in forces of different magnitudes. For example, a small vehicle in the wake of a larger vehicle will produce different forces compared to the case of a large vehicle in the wake of a smaller vehicle. The experiments may be extended to the many cases of different shapes and sizes of vehicles.

Results of the current study may be extended to the more general case of transient flow around bluff bodies. Experiments can be planned on basic shapes such as cylinders, boxes and spheres and other simplified scale vehicles.

Visualization of the flow and velocity field measurements will provide a better understanding of the flow dynamics. Particle image velocimetry (PIV) measurements may provide velocity fields at cross-sections in the flow and some visualization.

REFERENCES

[1] Hucho W.H., Sovran G., "Aerodynamics of Road Vehicles", Annual Reviews of Fluid Mechanics, 485-537, (1993)

[2] Tsuei J.L., Savaş Ö. and Hedrick J.K. "Transient Platoon Aerodynamics during Passing Maneuvers and In-Line Oscillations", California PATH Research Report, UCB-ITS-PRR-2000-26, University of California, (2000)

[3] Ahmed, S.R., Ramm, G. and Faltin, G., "Some salient features of the time-averaged ground vehicle wake" SAE Transactions, Volume 93, Part 2, 473-503, (1984).

[4] Sims-Williams D.B. and Dominy R.G., "Experimental Investigation into Unsteadiness and Instability in Passenger Car Aerodynamics", SAE Transactions, SAE Paper 980391, (1998)

[5] Duell E.G., George A.R., "Experimental Study of a Ground Vehicle Body Unsteady Near Wake", SAE Transactions, Volume 108, 1589-1601, (1999)

[6] Berger E., Scholz D., Schumm M., "Coherent Vortex Structures in the Wake of a Sphere and Circular Disk at Rest and Under Forced Vibrations", Journal of Fluids and Structures", 231-257, (1990)

[7] Templin J.T. and Raimondo S., "Experimental Evaluation of Test Section Boundary Interference Effects in Road Vehicle Tests in Wind Tunnels", Journal of Wind Engineering and Industrial Aerodynamics, Volume 22, 129-148, (1986)

[8] Williams J., Wallis S., Hoffman J., Martindale B., Arnette S., "Effect of Test Section Configuration on Aerodynamic Drag Measurements", SAE Transactions, Volume 110, Part 1, 680-694, (2001)

[9] Mercker E.,"A Blockage Correction for Automotive Testing in a Wind Tunnel with Closed Test Section", Journal of Wind Engineering and Industrial Aerodynamics, Volume 22, 149-167, (1986)

[10] Zabat M, Frascaroli S, Browand F. "Drag Measurements on a Platoon of Vehicles", California PATH Research Report, UCB-ITS-PRR-93-27, University of California, (1994)

[11] Zabat M, Stabile N, Frascaroli S, Browand F. "The Aerodynamics performance of Platoons: Final Report", California PATH Research Report, UCB-ITS-PRR-95-35, University of California, (1995)

[12] Chen A.L., Savaş Ö., Hedrick K., "Transient Vehicle Aerodynamics in Four Car Platoons", California PATH Research Report, UCB-ITS-PRR-97-50, University of California, (1997)

[13] Browand F., Hong P., Marcu B., Tucker A., "Drag Forces Experienced by Two Full Scale Vehicles at Close Spacing ", California PATH Research Report, UCB-ITS-PRR-98-5, University of California, (1998)

[14] Browand F., Michaelian M., "Field Experiments Demonstrate Fuel Savings for Close-Following", California PATH Research Report, UCB-ITS-PRR-2000-14, University of California, (2000)

[15] Browand F., McArthur J., Radovich C. "Fuel Saving Achieved in the Field Test of Two Tandem Trucks", California PATH Research Report, UCB-ITS-PRR-2004-20, University of California, (2004)

[16] Kobayashi N. and Sasaki Y., "Aerodynamics effects of an overtaking articulated heavy goods vehicle on car-trailer - an analysis to improve controllability", SAE Transactions, SAE Paper 871919, (1987)

[17] Telionis P., Fahrner C. J., and Jones G. S., "An experimental study of highway aerodynamic interferences", Journal of Wind Engineering and Industrial Aerodynamics, Volume 17, 267-293, (1984)

[18] Azim A. F. A., "An experimental study of the aerodynamic interference between road vehicles", SAE Transactions, SAE Paper 940422, (1994)

[19] Heffley R. K., "Aerodynamics of passenger vehicles in close proximity to trucks and buses", SAE Transactions, SAE Paper 730235, (1973)

[20] Shiraishi N., Matsumoto M. and Shirato H., "On aerodynamic instabilities of tandem structures", Journal of Wind Engineering and Industrial Aerodynamics, Volume 23, 437 447, (1986)

[21] Ota T. and Nishiyama H., "Flow around two elliptic cylinders in tandem arrangement", Transactions of the ASME Journal of Fluids Engineering, Volume 108, 98-103, (1986)

[22] Morel T. and Bohn M., "Flow over two circular disks in tandem", Transactions of the ASME Journal of Fluids Engineering, Volume 102, 104-111, (1980)

[23] Alan J. W., "Aerodynamic drag and pressure measurements on a simplified tractor trailer model", Journal of Wind Engineering and Industrial Aerodynamics, Volume 9, 125-136, (1981)

[24] Howell J., "Catastrophic lift forces on racing cars", Journal of Wind Engineering and Industrial Aerodynamics, Volume 9, 145-154, (1981)

[25] Koenig K. and Roshko A., "An experimental study of geometrical effects of the drag and flow field of two bluff bodies separated by a gap", Journal of Fluid Mechanics, Volume 156, 167-204, (1985)

[26] Zdravkovich M. M., "Review of flow interference between two circular cylinders in various arrangements", Transactions of the ASME Journal of Fluids Engineering, 618-633, (1977)

[27] Fox R.W., McDonald A.T., Introduction to Fluid Mechanics, John Wiley & Sons, New York, (1994)

[28] Hucho W.H., Aerodynamics of Road Vehicles: from fluid mechanics to vehicle engineering, Butterworths, London, (1986)

[29] Tiainen J.S., "Use of CFD to Design a Future CFD/Experimental Wind Tunnel Program to Investigate the Blockage Effects of Bluff Bodies with Significant Upwash", MSc Thesis, Cranfield University, September, (2002)

[30] Carr G. W., Stapleford W. R., "Blockage effects in Automotive Wind Tunnel Testing", SAE Transactions 860093, (1986)

[31] "Design, Construction and Calibration of an Aerodynamic Balance", ME 483 Experimental Techniques in Fluid Mechanics Report, January, (1997)

[32] Alnor AXD 540 Micromanometer Owner's Manual, Alnor TSI Incorporated

[33] Ayaz Y., "Three Dimensional Velocity Measurement Behind an Axial Flow Fan", MSc Thesis, METU, June, (1988)

[34] Şahin C.F., Sukas S., "Aerodynamic Studies on Flow Induced Vibrations in a Wind Tunnel", ME 483 Experimental Techniques in Fluid Mechanics Report, January, (2004).

[35] Gümüşlüol Ü., Örselli E., "Aerodynamic Studies on Flow Induce Vibrations in a Wind Tunnel", ME 483 Experimental Techniques in Fluid Mechanics Report, January, (2005)

[36] Dantec DISA Type 56C17 CTA Bridge Instruction Manual, Dantec Documentation Department, Scientific Research Equipment Division

[37] Schlichting H., "Boundary Layer Theory", Springer, New York, (1999)

[38] Kayılı S., "Flow Induced Vibrations at the wake of 3D Object", ME 520 Analysis and Measurement Techniques for Random Vibrations and Noise" Report, January, (2006)

[39] Jorgensen F.E., "How to Measure Turbulence with Hot-wire Anemometers (a practical guide)", http://www.dantecdynamics.com/cta/Princip/Index.html, Dantec Dynamics, (2002)

[40] Gharib M. and Roshko A., "The Effect of Flow Oscillations on Cavity Drag", Journal of Fluid Mechanics, Volume 177, 501-530, (1987)

[41] Romberg G.F., Chianese J.F., Lajoie L.G., "Aerodynamics of Race Cars in Drafting and Passing Situations", SAE Paper 710213, (1971)

[42] Munson R. B., Young D. F., Okiishi T.H., Fundamentals of Fluid Mechanics, John Wiley & Sons, New York, (1998)

APPENDIX A

DRAG COEFFICIENT RESULTS OBTAINED IN THE CLOSE FOLLOWING AND PASSING SITUATIONS

The results obtained from uncorrected data and after the application of pressure signature correction method are presented in the tables. The graphs of ΔC_P (difference in C_P when the tunnel is empty and with a model present) with location of the static taps are plotted. C_P graphs are shown for finding the location of velocity to determine the local dynamic pressure as the basis of the drag coefficient.

A.1 Results of the MIRA Model

A.1.1 Close-Following Results

Table A.1 Uncorrected Drag Coefficient Results of the MIRA Model for Close following Situation

x/L	$C_{Dref\,1}$	$C_{Dref\,2}$	$C_{Dref\,1} / C_{D\infty}$	$C_{Dref\,2} / C_{D\infty}$
0.1	0.250	0.236	0.76	0.71
0.2	0.257	0.246	0.78	0.74
0.3	0.263	0.256	0.8	0.77
0.4	0.276	0.262	0.84	0.79
0.5	0.290	0.269	0.88	0.81
0.6	0.299	0.276	0.91	0.83
0.7	0.306	0.286	0.93	0.86
0.8	0.313	0.292	0.95	0.88
0.9	0.319	0.302	0.97	0.91
1	0.322	0.315	0.98	0.95

Table A.2 Pressure Signature Corrected Results of the MIRA Model for the Close following Situation

x/L	$\Delta C_{Pmax\ 1}$	$\Delta C_{Pmax\ 2}$	$C_{Plocal\ 1}$	$C_{Plocal\ 2}$	$C_{Dlocal\ 1}$	$C_{Dlocal\ 2}$	$C_{Dlocal\ 1}$ / $C_{D\infty}$	$C_{Dlocal\ 2}$ / $C_{D\infty}$
0.1	0.04	0.05	-0.045	-0.055	0.239	0.223	0.76	0.71
0.2	0.04	0.05	-0.045	-0.055	0.246	0.233	0.78	0.74
0.3	0.04	0.05	-0.045	-0.055	0.252	0.242	0.80	0.77
0.4	0.04	0.05	-0.045	-0.055	0.264	0.249	0.84	0.79
0.5	0.04	0.045	-0.045	-0.055	0.277	0.255	0.88	0.81
0.6	0.04	0.045	-0.045	-0.050	0.286	0.262	0.91	0.83
0.7	0.04	0.045	-0.045	-0.050	0.293	0.272	0.93	0.86
0.8	0.04	0.04	-0.045	-0.045	0.299	0.280	0.95	0.88
0.9	0.04	0.04	-0.045	-0.045	0.305	0.289	0.97	0.91
1	0.04	0.04	-0.045	-0.05	0.309	0.300	0.98	0.95

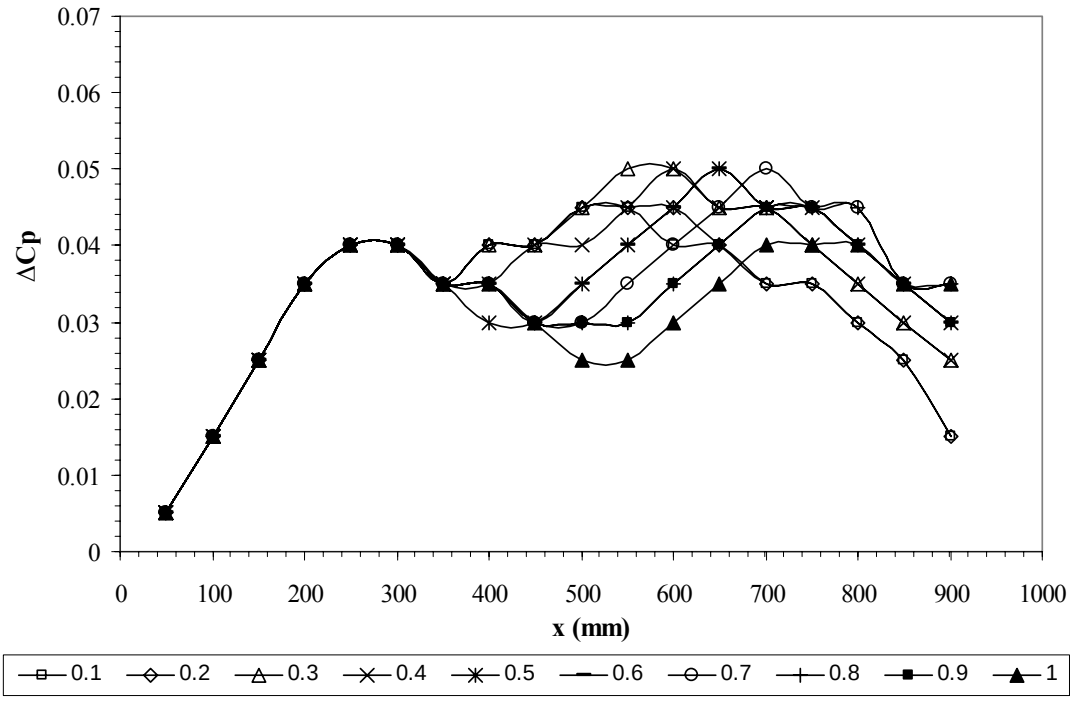

Figure A.1 ΔC_P Distributions of the MIRA Leading Vehicle in Close Following Situations

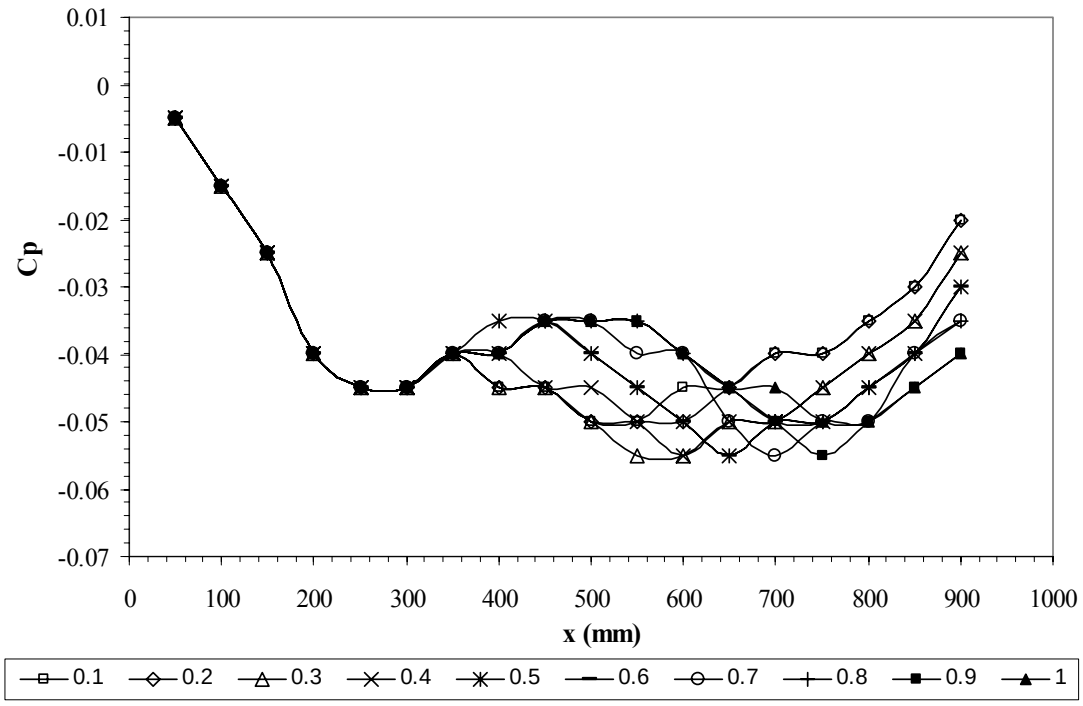

Figure A.2 C_P Distributions of the MIRA Leading Vehicle in Close Following Situations

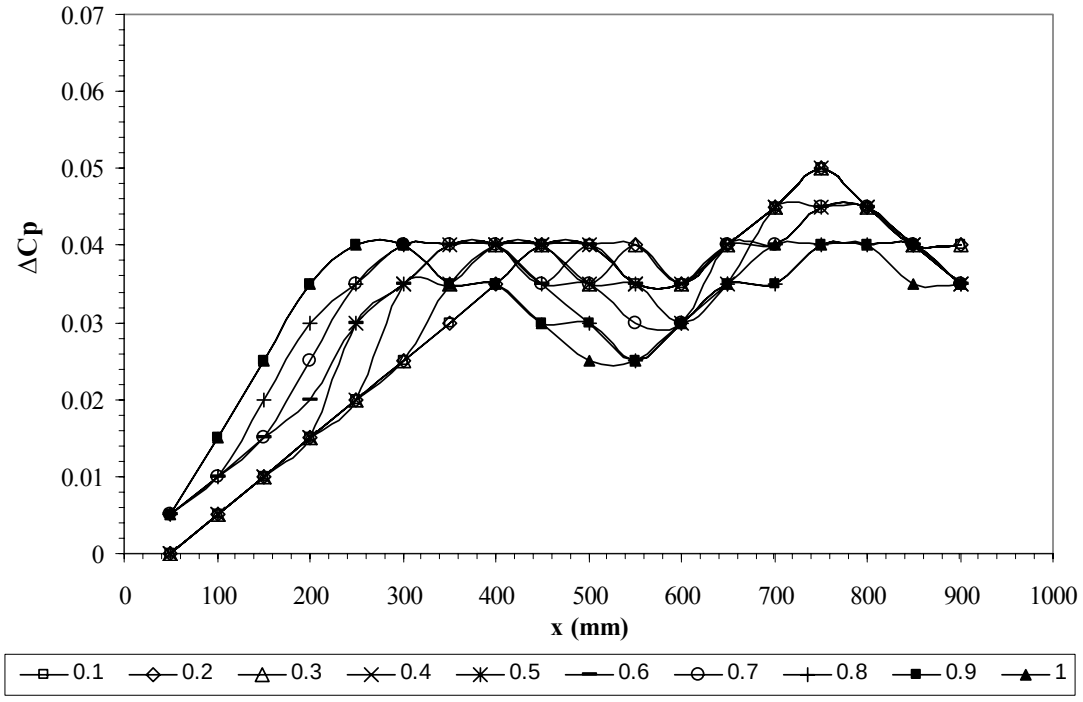

Figure A.3 ΔC_P Distributions of the MIRA Trailing Vehicle in Close Following Situations

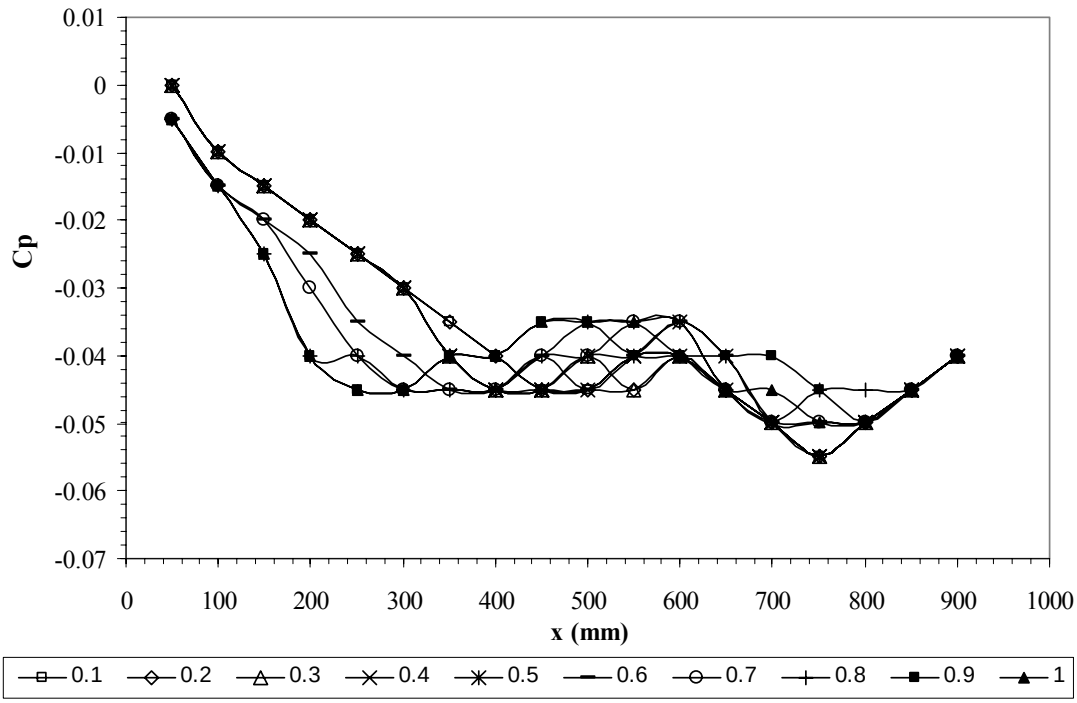

Figure A.4 C_P Distributions of the MIRA Trailing Vehicle in Close Following Situations

A.1.2 Overtaking Results

A.1.2.1 The Closer Situation (d/w=0.1)

Table A.3 Uncorrected Drag Coefficient Results of the MIRA Model for the Closer Overtaking Situation (d/w=0.1)

x/L	$C_{Dref\,1}$	$C_{Dref\,2}$	$C_{Dref\,1}$ / $C_{D\infty}$	$C_{Dref\,2}$ / $C_{D\infty}$
-1	0.318	0.305	0.96	0.92
-0.5	0.341	0.311	1.03	0.94
0	0.357	0.354	1.08	1.07
0.5	0.314	0.344	0.95	1.04
1	0.308	0.318	0.93	0.96

Table A.4 Pressure Signature Corrected Results of the MIRA Model for the Closer Overtaking Situation (d/w=0.1)

x/L	$\Delta C_{Pmax\ 1}$	$\Delta C_{Pmax\ 2}$	$C_{Plocal\ 1}$	$C_{Plocal\ 2}$	$C_{Dlocal\ 1}$	$C_{Dlocal\ 2}$	$C_{Dlocal\ 1}$ / $C_{D\infty}$	$C_{Dlocal\ 2}$ / $C_{D\infty}$
-1	0.05	0.05	-0.055	-0.055	0.301	0.289	0.95	0.91
-0.5	0.05	0.05	-0.055	-0.055	0.323	0.295	1.02	0.93
0	0.045	0.045	-0.05	-0.05	0.340	0.337	1.07	1.06
0.5	0.05	0.05	-0.055	-0.055	0.298	0.326	0.94	1.03
1	0.05	0.05	-0.055	-0.055	0.292	0.301	0.92	0.95

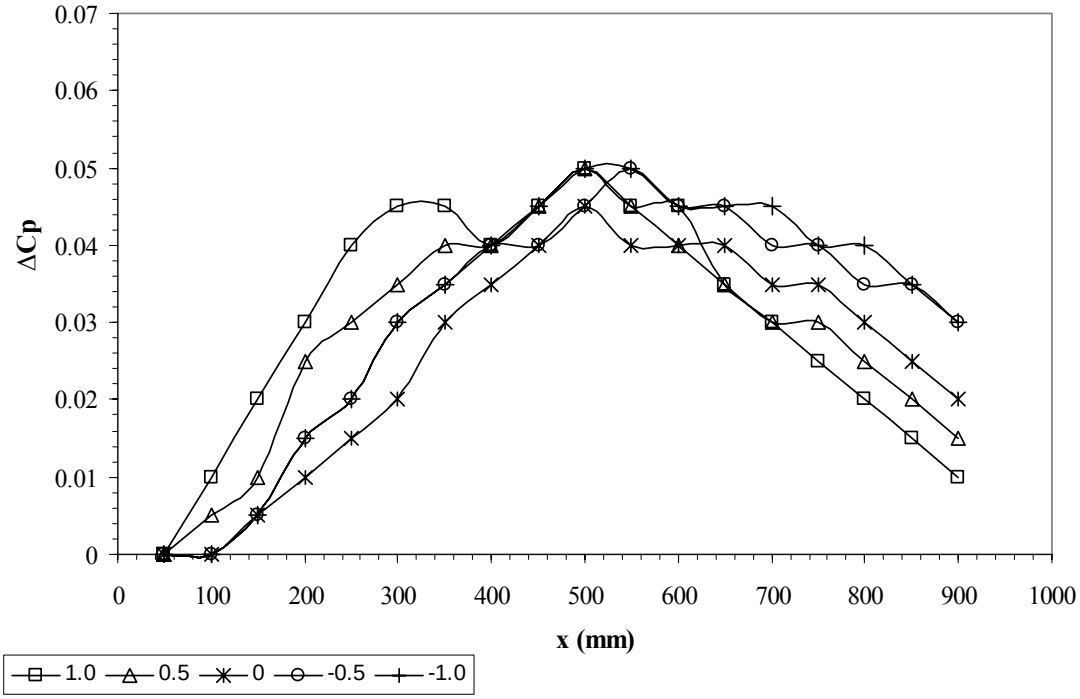

Figure A.5 ΔC_P Distributions of the MIRA Overtaking Vehicle for the Closer Overtaking Situations (d/w=0.1)

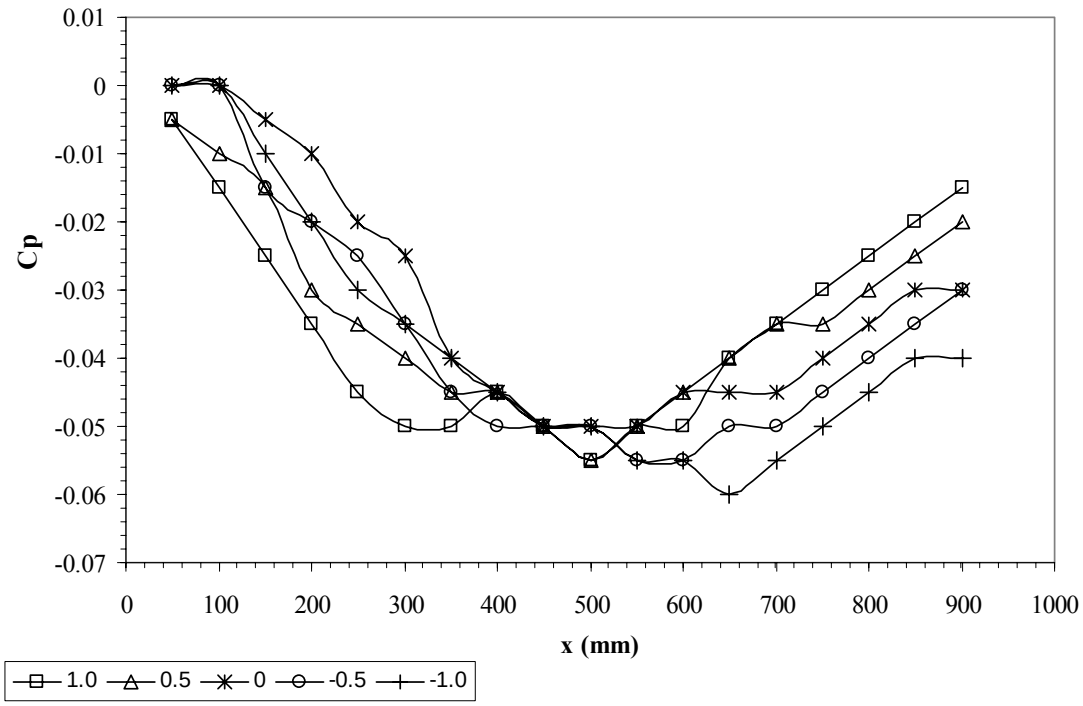

Figure A.6 C_P Distributions of the MIRA Overtaking Vehicle for the Closer Overtaking Situations (d/w=0.1)

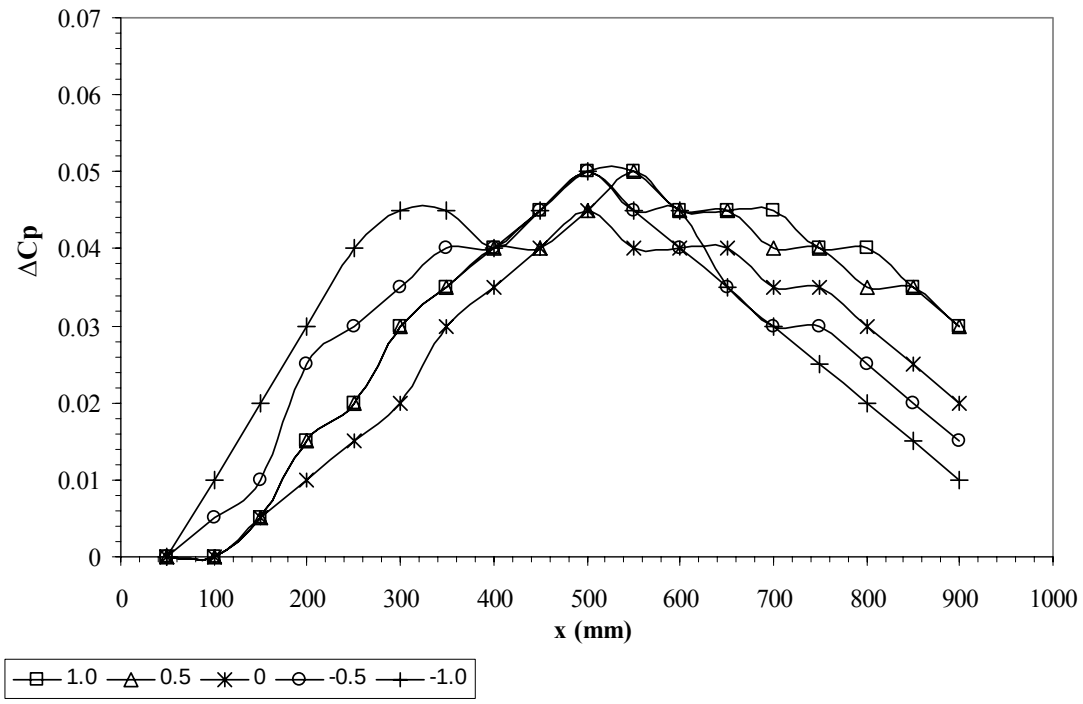

Figure A.7 ΔC_P Distributions of the MIRA Overtaken Vehicle for the Closer Overtaking Situations (d/w=0.1)

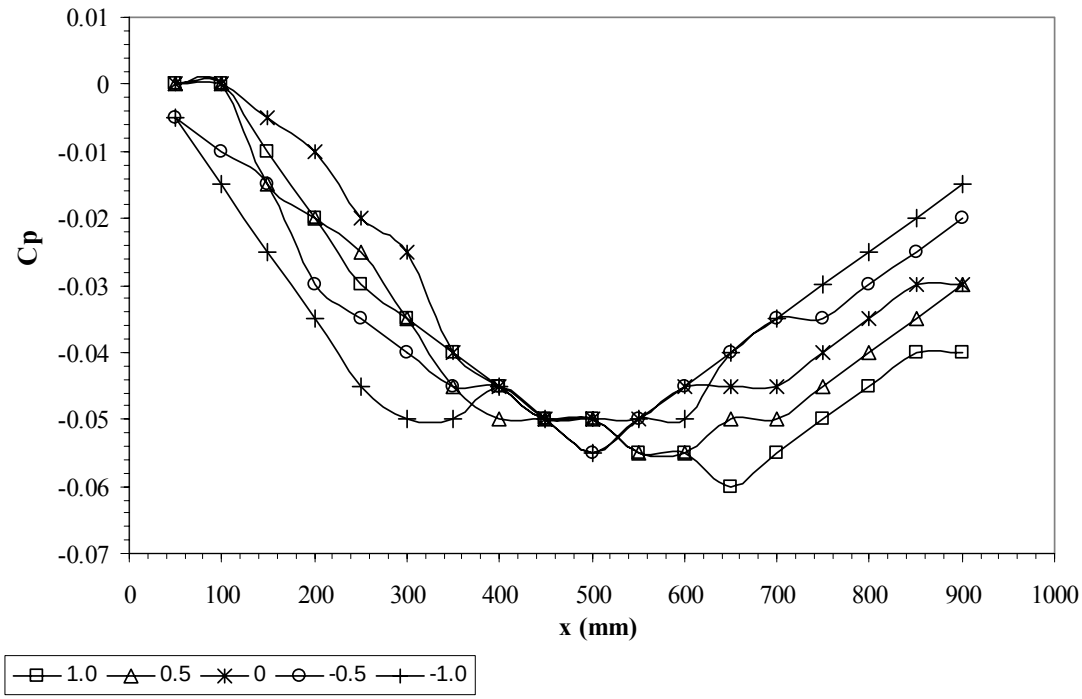

Figure A.8 C_P Distributions of the MIRA Overtaken Vehicle for the Closer Overtaking Situations (d/w=0.1)

A.1.2.1 The Further Situation (d/w=0.5)

Table A.5 Uncorrected Drag Coefficient Results of the MIRA Model for the Further Overtaking Situation (d/w=0.5)

x/L	$C_{Dref\,1}$	$C_{Dref\,2}$	$C_{Dref\,1}$ / $C_{D\infty}$	$C_{Dref\,2}$ / $C_{D\infty}$
-1	0.321	0.311	0.97	0.94
-0.5	0.338	0.321	1.02	0.97
0	0.348	0.344	1.05	1.04
0.5	0.321	0.338	0.97	1.02
1	0.314	0.324	0.95	0.98

Table A.6 Pressure Signature Corrected Results of the MIRA Model for the Further Overtaking Situation (d/w=0.5)

x/L	$\Delta C_{Pmax\ 1}$	$\Delta C_{Pmax\ 2}$	$C_{Plocal\ 1}$	$C_{Plocal\ 2}$	$C_{Dlocal\ 1}$	$C_{Dlocal\ 2}$	$C_{Dlocal\ 1}$ / $C_{D\infty}$	$C_{Dlocal\ 2}$ / $C_{D\infty}$
-1	0.045	0.04	-0.05	-0.045	0.306	0.298	0.96	0.94
-0.5	0.045	0.04	-0.05	-0.045	0.322	0.307	1.01	0.97
0	0.045	0.045	-0.05	-0.05	0.331	0.328	1.04	1.03
0.5	0.04	0.045	-0.045	-0.05	0.307	0.322	0.97	1.01
1	0.04	0.045	-0.045	-0.05	0.301	0.309	0.95	0.97

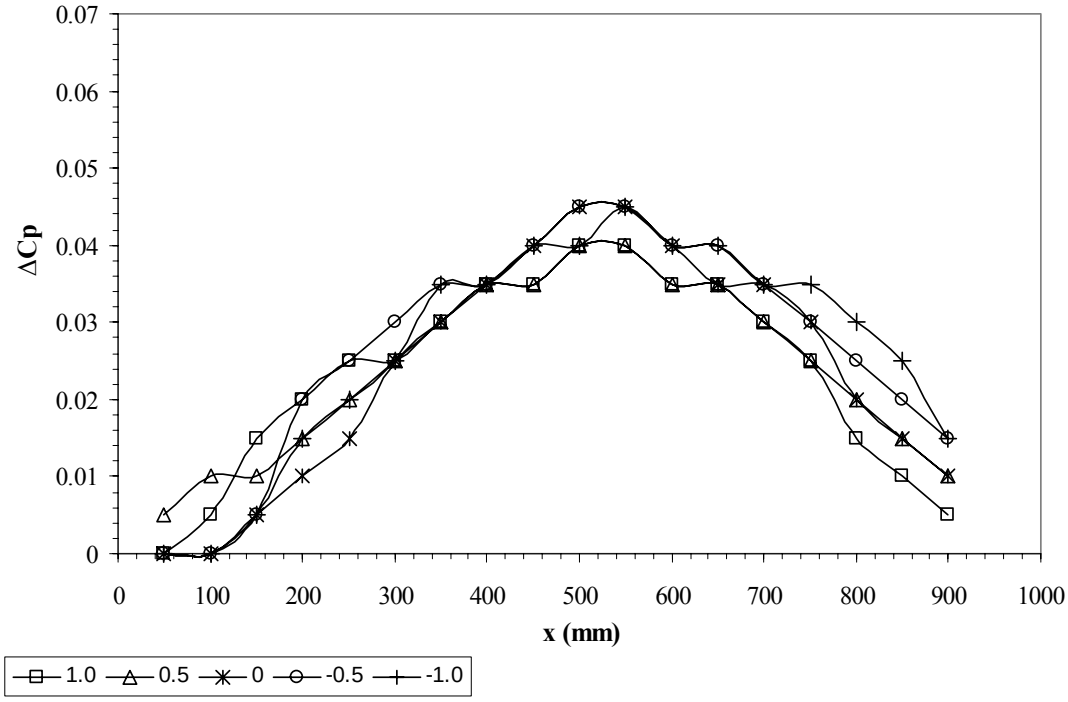

Figure A.9 ΔC_P Distributions of the MIRA Overtaking Vehicle for the Further Overtaking Situations (d/w=0.5)

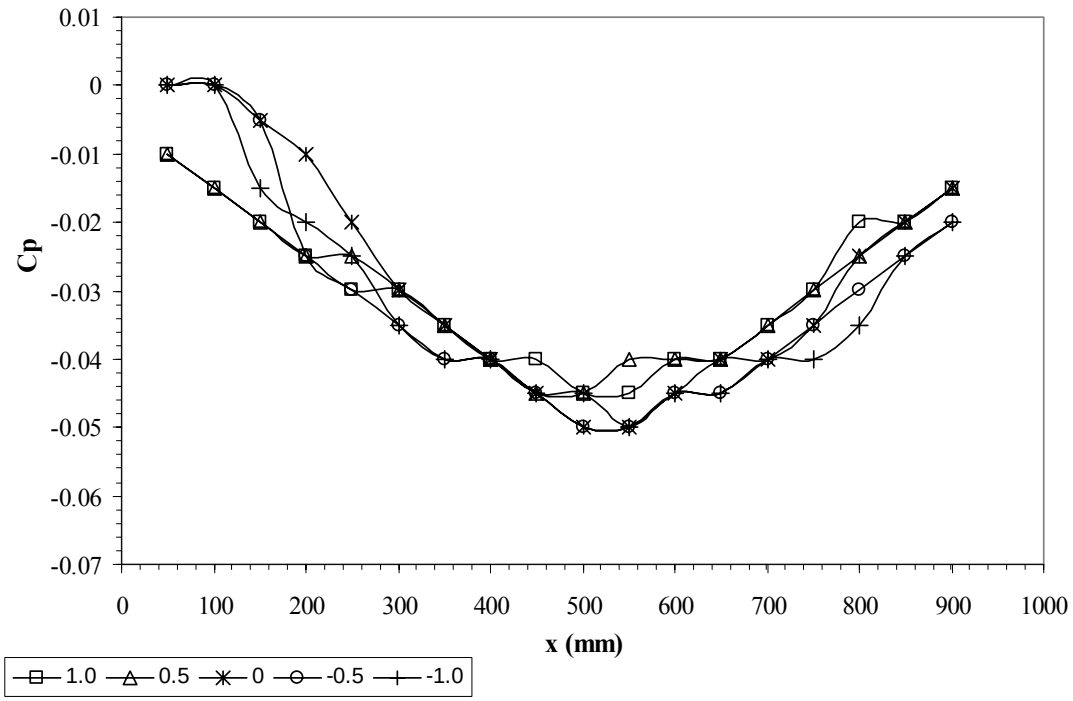

Figure A.10 C_P Distributions of the MIRA Overtaking Vehicle for the Further Overtaking Situations (d/w=0.5)

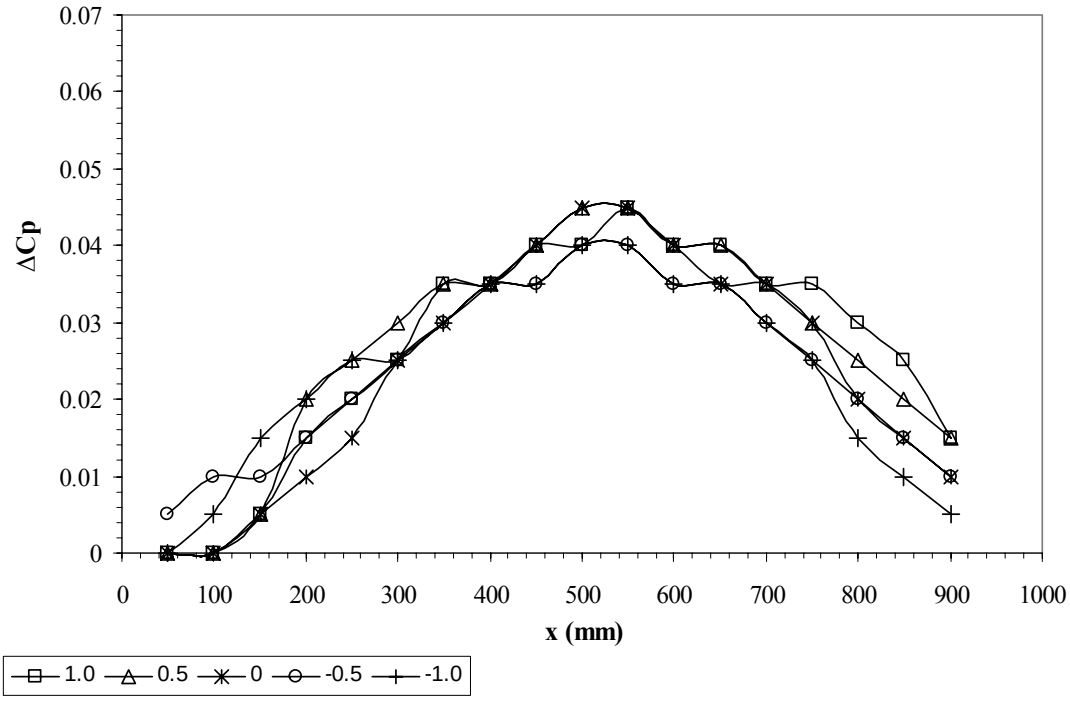

Figure A.11 ΔC_P Distributions of the MIRA Overtaken Vehicle for the Further Overtaking Situations (d/w=0.5)

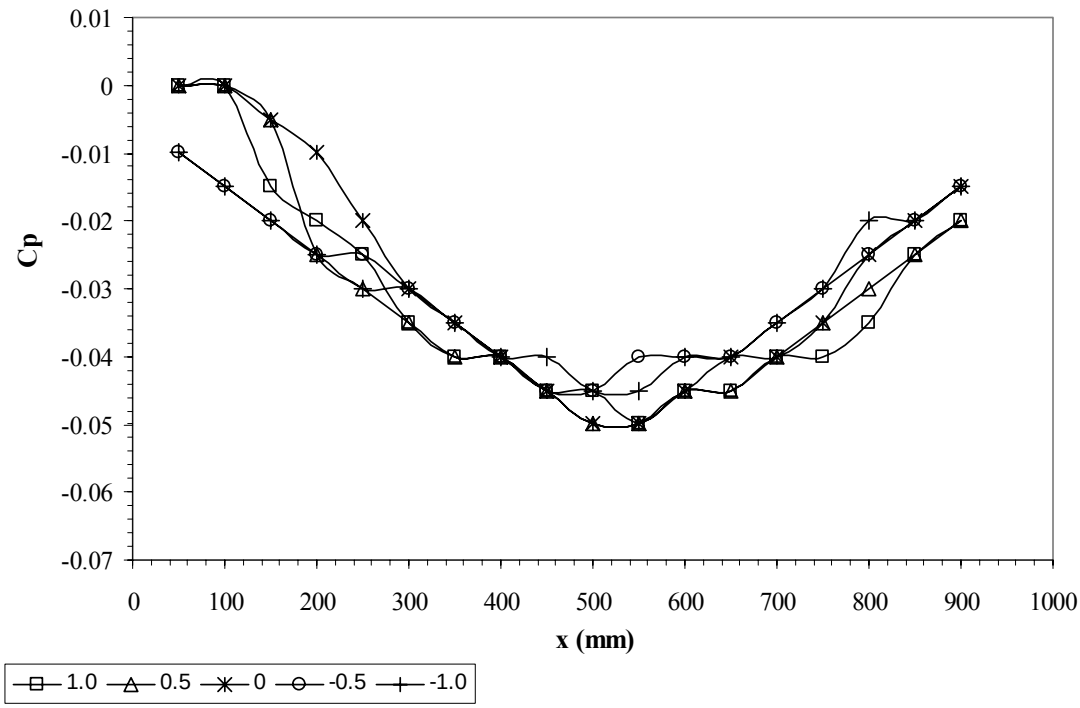

Figure A.12 C_P Distributions of the MIRA Overtaken Vehicle for the Further Overtaking Situations (d/w=0.5)

A.2 Ahmed Body Results

A.2.1 Close-Following Results

Table A.7 Uncorrected Drag Coefficient Results for the Ahmed Body Model in Close following Situation

x/L	$C_{Dref\,1}$	$C_{Dref\,2}$	$C_{Dref\,1}$ / $C_{D\infty}$	$C_{Dref\,2}$ / $C_{D\infty}$
0.1	0.182	0.127	0.61	0.43
0.2	0.183	NA	0.62	NA
0.3	0.192	0.146	0.65	0.49
0.4	0.224	0.139	0.76	0.47
0.5	0.244	0.14	0.82	0.47
0.6	0.252	0.146	0.85	0.49
0.7	0.262	0.152	0.89	0.51
0.8	0.271	0.156	0.92	0.53
0.9	0.279	0.167	0.94	0.56
1	0.286	0.176	0.97	0.59

Table A.8 Pressure Signature Corrected Results of the Ahmed Body Model for the Close following Situation

x/L	$\Delta C_{Pmax\ 1}$	$\Delta C_{Pmax\ 2}$	$C_{Plocal\ 1}$	$C_{Plocal\ 2}$	$C_{Dlocal\ 1}$	$C_{Dlocal\ 2}$	$C_{Dlocal\ 1}$ / $C_{D\infty}$	$C_{Dlocal\ 2}$ / $C_{D\infty}$
0.1	0.05	0.06	-0.055	-0.065	0.173	0.119	0.61	0.42
0.2	0.05	NA	-0.055	NA	0.173	NA	0.62	NA
0.3	0.05	0.06	-0.055	-0.065	0.182	0.137	0.65	0.48
0.4	0.05	0.06	-0.055	-0.065	0.212	0.131	0.75	0.46
0.5	0.05	0.055	-0.055	-0.060	0.231	0.132	0.82	0.46
0.6	0.05	0.055	-0.055	-0.060	0.239	0.138	0.85	0.48
0.7	0.05	0.055	-0.055	-0.060	0.248	0.143	0.88	0.50
0.8	0.05	0.055	-0.055	-0.060	0.257	0.147	0.91	0.52
0.9	0.05	0.05	-0.055	-0.055	0.264	0.158	0.94	0.56
1	0.05	0.05	-0.055	-0.055	0.271	0.167	0.96	0.59

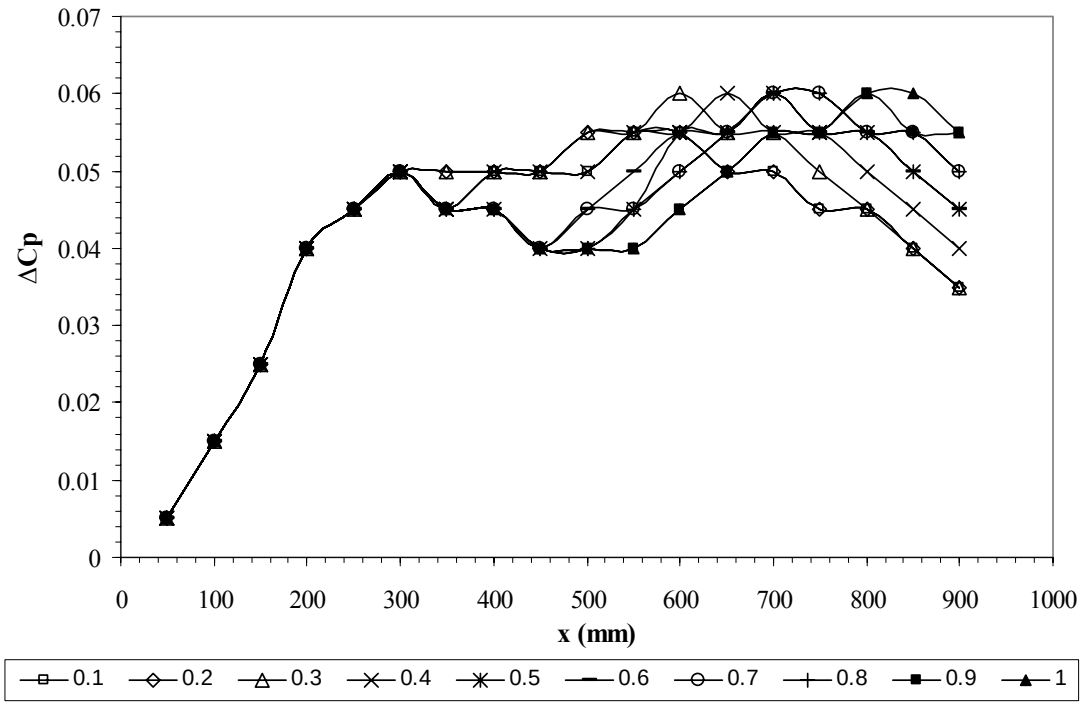

Figure A.13 ΔC_P Distributions of the Ahmed Body Leading Vehicle in Close Following Situations

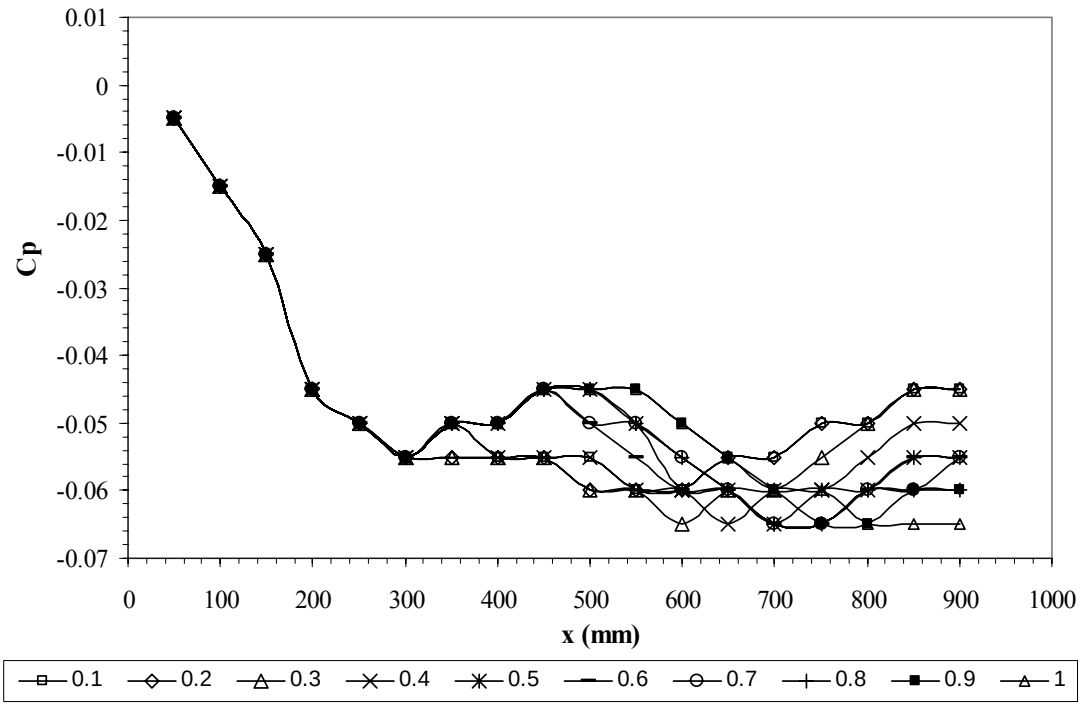

Figure A.14 C_P Distributions of the Ahmed Body Leading Vehicle in Close Following Situations

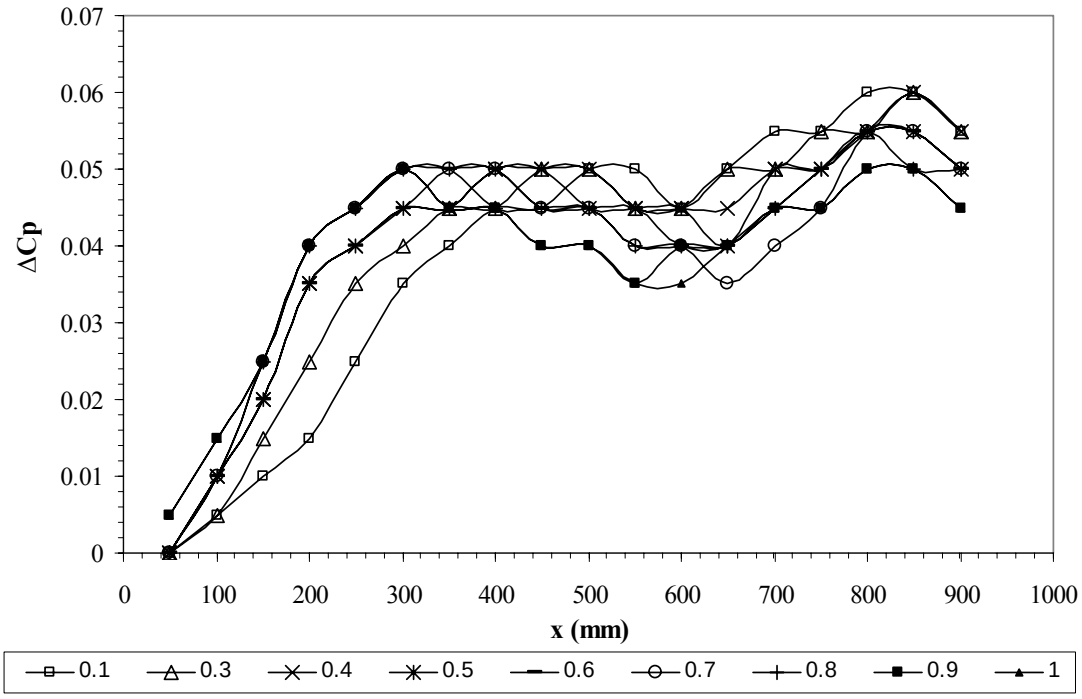

Figure A.15 ΔC_P Distributions of the Ahmed Body Trailing Vehicle in Close Following Situations

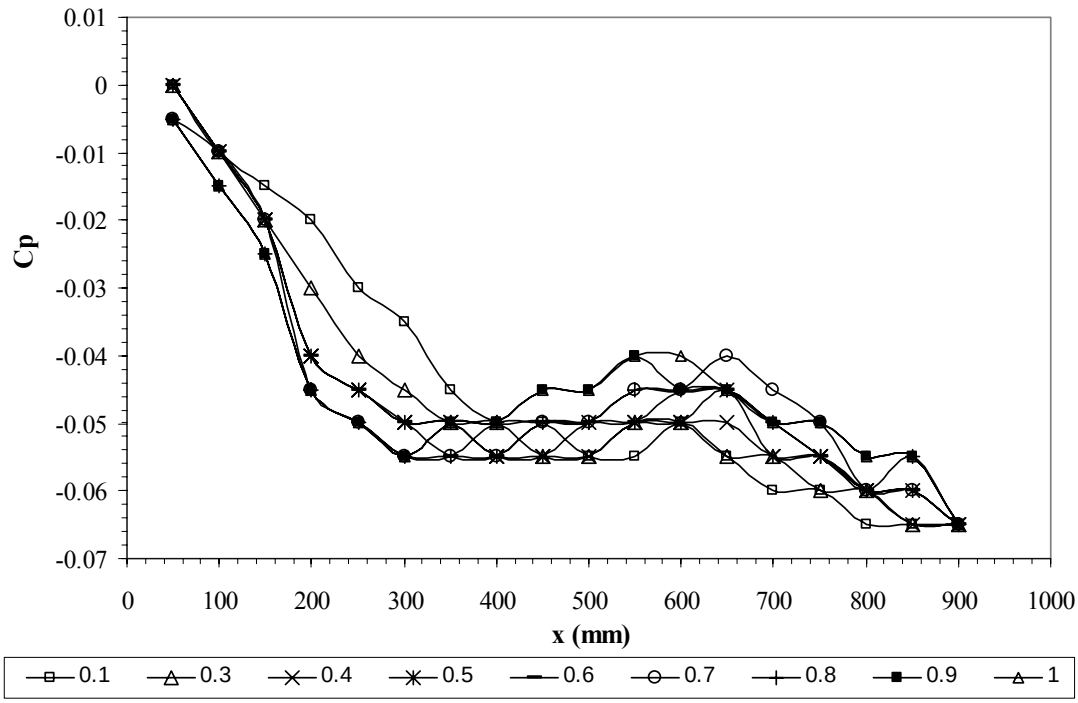

Figure A.16 C_P Distributions of the Ahmed Body Trailing Vehicle in Close Following Situations

A.2.2 Overtaking Results

A.2.2.1 The Closer Situation (d/w=0.1)

Table A.9 Uncorrected Drag Coefficient Results of the Ahmed Body Model for the Closer Overtaking Situation (d/w=0.1)

x/L	$C_{Dref\,1}$	$C_{Dref\,2}$	$C_{Dref\,1}$ / $C_{D\infty}$	$C_{Dref\,2}$ / $C_{D\infty}$
1	0.253	0.268	0.85	0.9
0.5	0.265	0.337	0.89	1.13
0	0.349	0.355	1.17	1.19
-0.5	0.334	0.262	1.12	0.88
-1	0.274	0.250	0.92	0.84

Table A.10 Pressure Signature Corrected Results of the Ahmed Body Model for the Closer Overtaking Situation (d/w=0.1)

x/L	$\Delta C_{Pmax\ 1}$	$\Delta C_{Pmax\ 2}$	$C_{Plocal\ 1}$	$C_{Plocal\ 2}$	$C_{Dlocal\ 1}$	$C_{Dlocal\ 2}$	$C_{Dlocal\ 1}$ / $C_{D\infty}$	$C_{Dlocal\ 2}$ / $C_{D\infty}$
1	0.06	0.06	-0.065	-0.065	0.238	0.252	0.84	0.89
0.5	0.06	0.06	-0.065	-0.065	0.249	0.316	0.88	1.11
0	0.06	0.06	-0.065	-0.065	0.327	0.333	1.15	1.17
-0.5	0.06	0.06	-0.065	-0.065	0.313	0.246	1.10	0.87
-1	0.06	0.06	-0.065	-0.065	0.257	0.235	0.91	0.83

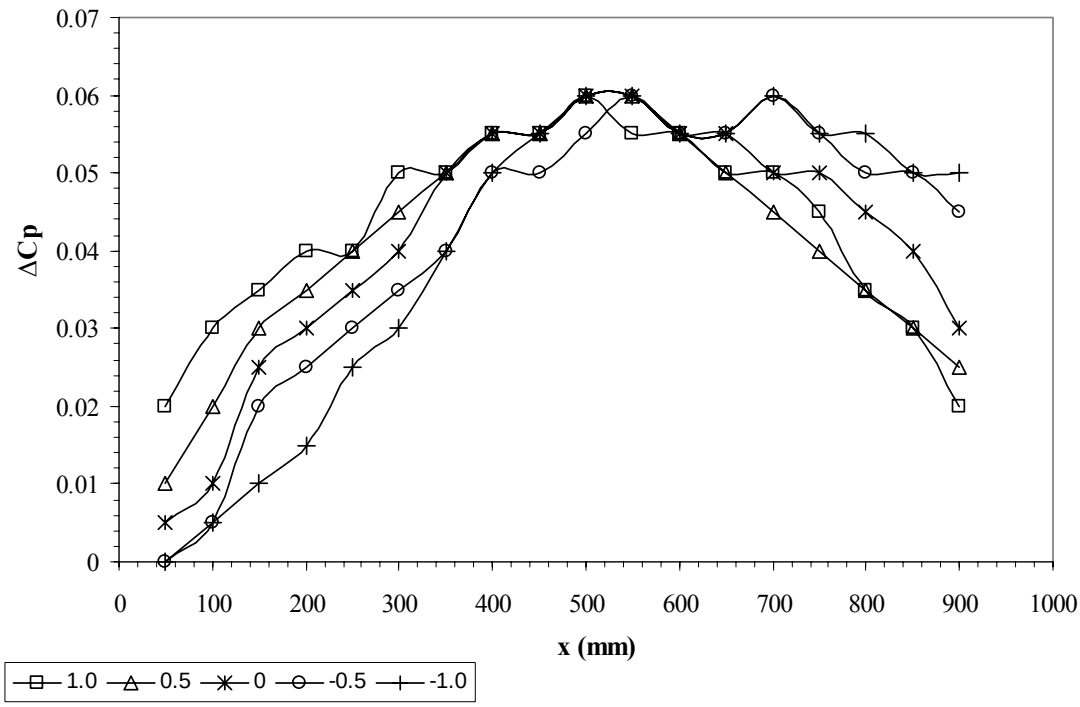

Figure A.17 ΔC_P Distributions of the Ahmed Body Overtaking Vehicle for the Closer Overtaking Situations (d/w=0.1)

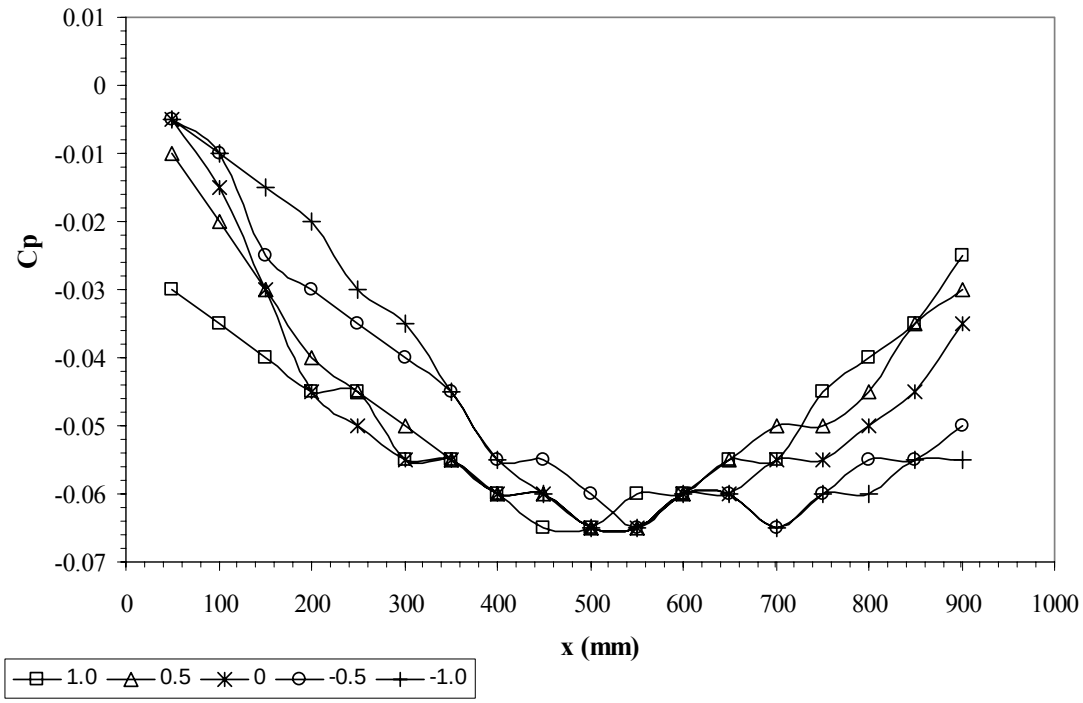

Figure A.18 C_P Distributions of the Ahmed Body Overtaking Vehicle for the Closer Overtaking Situations (d/w=0.1)

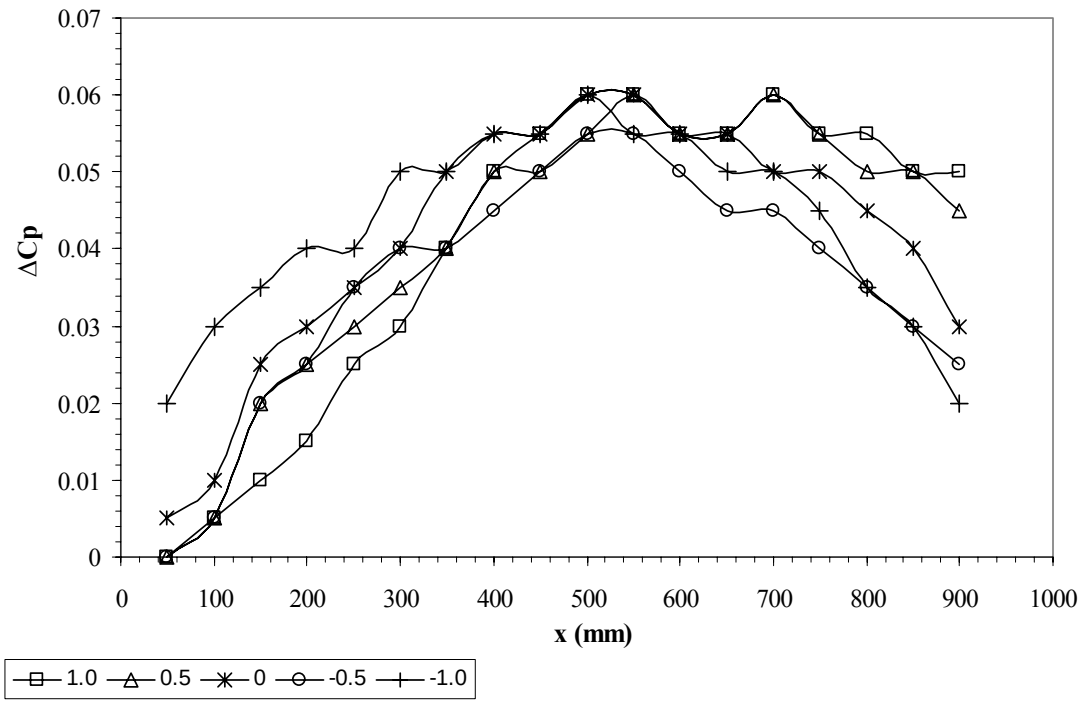

Figure A.19 ΔC_P Distributions of the Ahmed Body Overtaken Vehicle for the Closer Overtaking Situations (d/w=0.1)

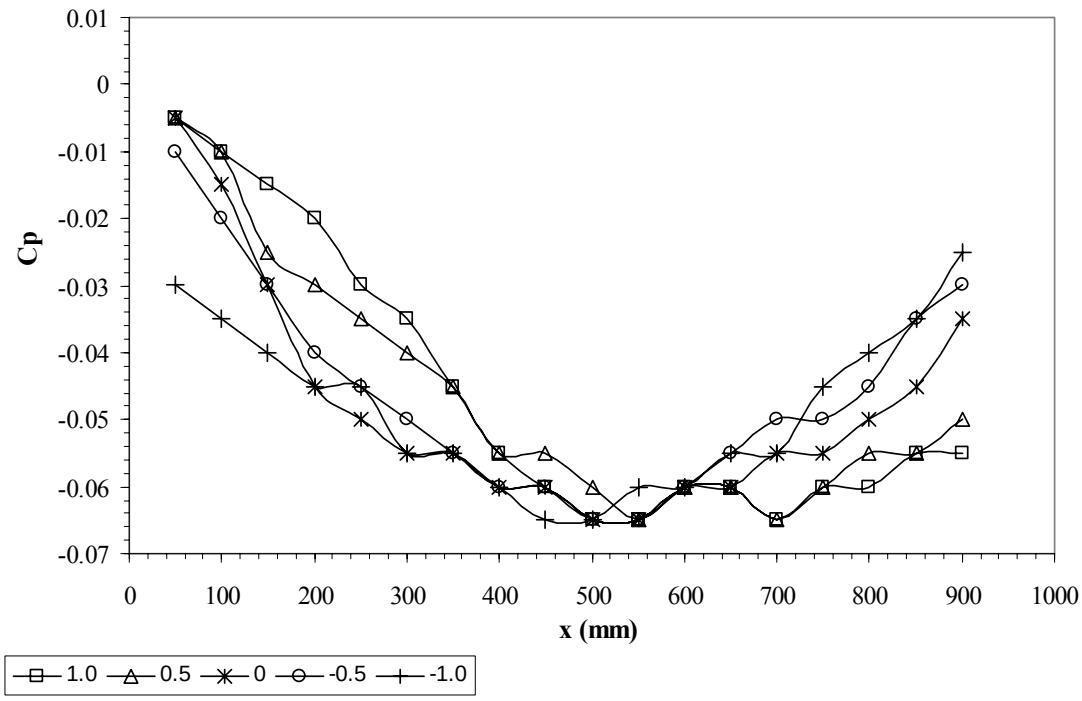

Figure A.20 C_P Distributions of the Ahmed Body Overtaken Vehicle for the Closer Overtaking Situations (d/w=0.1)

A.2.2.1 The Further Situation (d/w=0.5)

Table A.11 Uncorrected Drag Coefficient Results of the Ahmed Body Model for the Further Overtaking Situation (d/w=0.5)

x/L	$C_{Dref\,1}$	$C_{Dref\,2}$	$C_{Dref\,1}$ / $C_{D\infty}$	$C_{Dref\,2}$ / $C_{D\infty}$
1	0.262	0.280	0.88	0.94
0.5	0.271	0.313	0.91	1.05
0	0.331	0.334	1.11	1.12
-0.5	0.313	0.271	1.05	0.91
-1	0.280	0.259	0.94	0.87

Table A.12 Pressure Signature Corrected Results of the Ahmed Body Model for the Further Overtaking Situation (d/w=0.5)

x/L	$\Delta C_{Pmax\ 1}$	$\Delta C_{Pmax\ 2}$	$C_{Plocal\ 1}$	$C_{Plocal\ 2}$	$C_{Dlocal\ 1}$	$C_{Dlocal\ 2}$	$C_{Dlocal\ 1}$ / $C_{D\infty}$	$C_{Dlocal\ 2}$ / $C_{D\infty}$
1	0.05	0.055	-0.05	-0.060	0.250	0.264	0.88	0.93
0.5	0.055	0.055	-0.06	-0.060	0.256	0.295	0.90	1.04
0	0.055	0.055	-0.06	-0.060	0.312	0.315	1.10	1.11
-0.5	0.055	0.055	-0.06	-0.060	0.295	0.256	1.04	0.90
-1	0.055	0.05	-0.06	-0.055	0.264	0.246	0.93	0.87

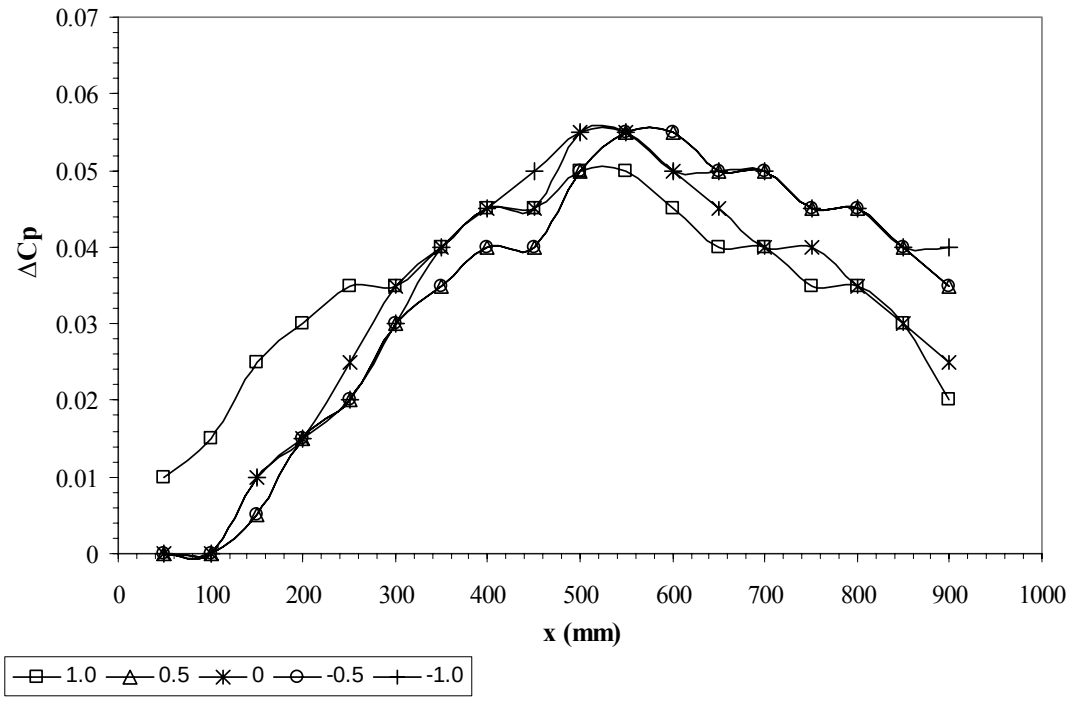

Figure A.21 ΔC_P Distributions of the Ahmed Body Overtaking Vehicle for the Further Overtaking Situations (d/w=0.5)

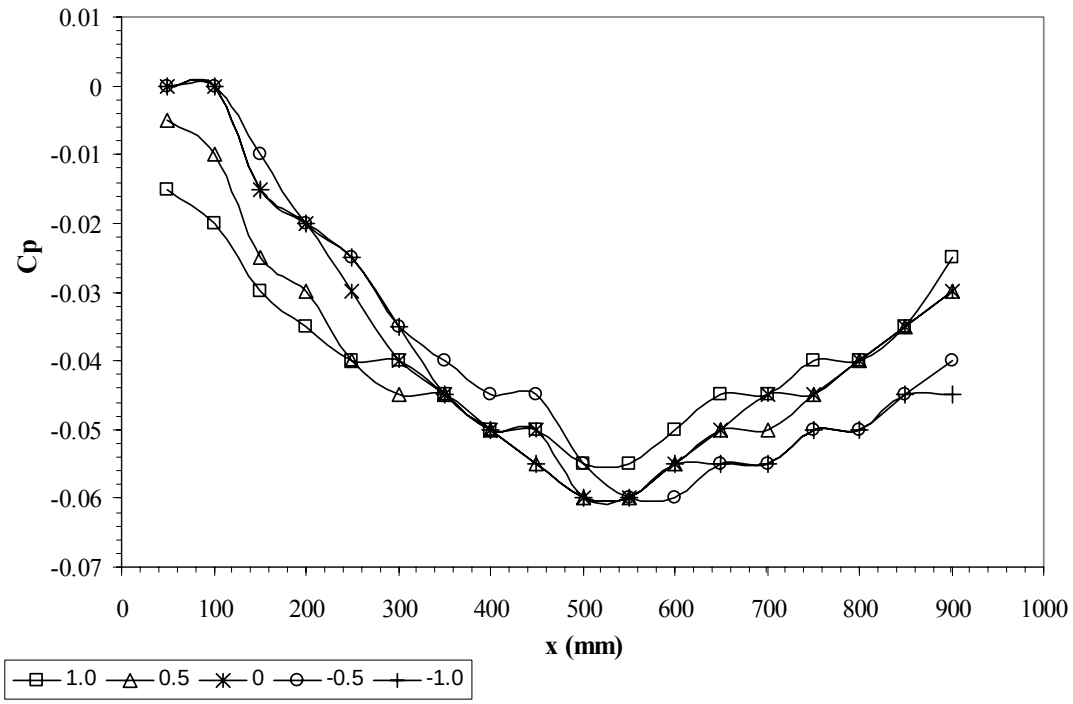

Figure A.22 C_P Distributions of the Ahmed Body Overtaking Vehicle for the Further Overtaking Situations (d/w=0.5)

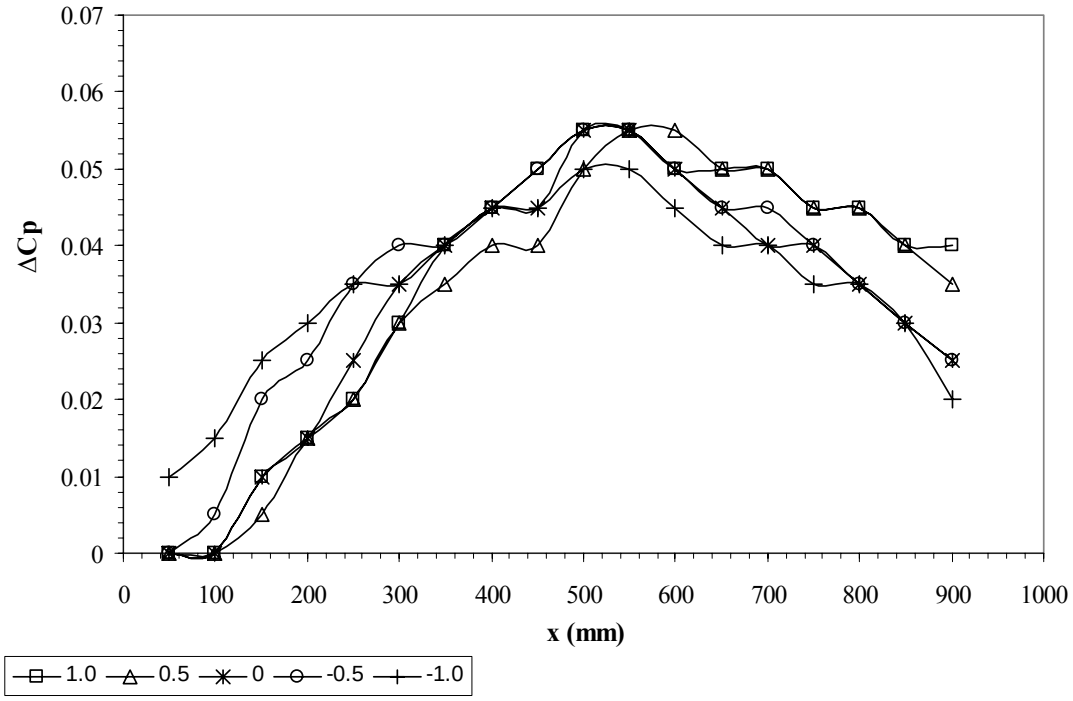

Figure A.23 ΔC_P Distributions of the Ahmed Body Overtaken Vehicle for the Further Overtaking Situations (d/w=0.5)

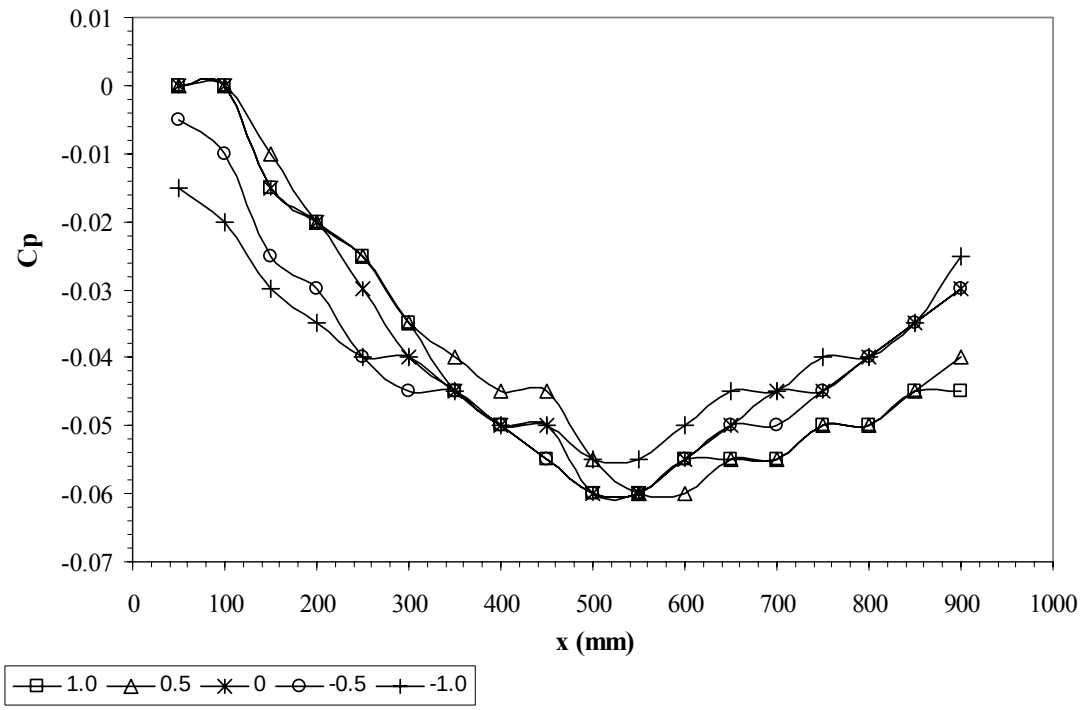

Figure A.24 C_P Distributions of the Ahmed Body Overtaken Vehicle for the Further Overtaking Situations (d/w=0.5)

APPENDIX B

SURFACE PRESSURE DISTRIBUTIONS IN CLOSE FOLLOWING AND PASSING SITUATIONS

Surface pressure distributions of the MIRA and Ahmed Body models are shown in this part. Firstly, pressure tap locations at right, left, front and rear surfaces are given from Figure B.1 to Figure B.4 for both vehicle models. Then, pressure distributions on the surfaces of the MIRA model are presented. Because the graphs for the close-following situations were given in Chapter 6, only overtaking situations results of the MIRA model is given from Figure B.5 to Figure B.10. The results include x/l = 1, x/l = 0 and x/l = -1 positions for the closer (d/w = 0.1) and the further (d/w = 0.5) overtaking situations. The first three Figures represent the closer overtaking situations while the rest is for the further situations.

For Ahmed Body model, the first two graphs represent the middle (x/l = 0.5) and the furthest (x/l = 1) spacing results for the close-following situations. Front and rear surface pressure distributions are given in Figure B.11 and Figure B.12 for the middle and the furthest situations, respectively. The smallest vehicle spacing situation (x/l = 0.1) was presented in Chapter 6. The overtaking situations are presented for the same positions with the MIRA model. As the left and right surface pressure distributions were given in Results and Discussion, the rear and front surface pressures are shown in Figure B.14

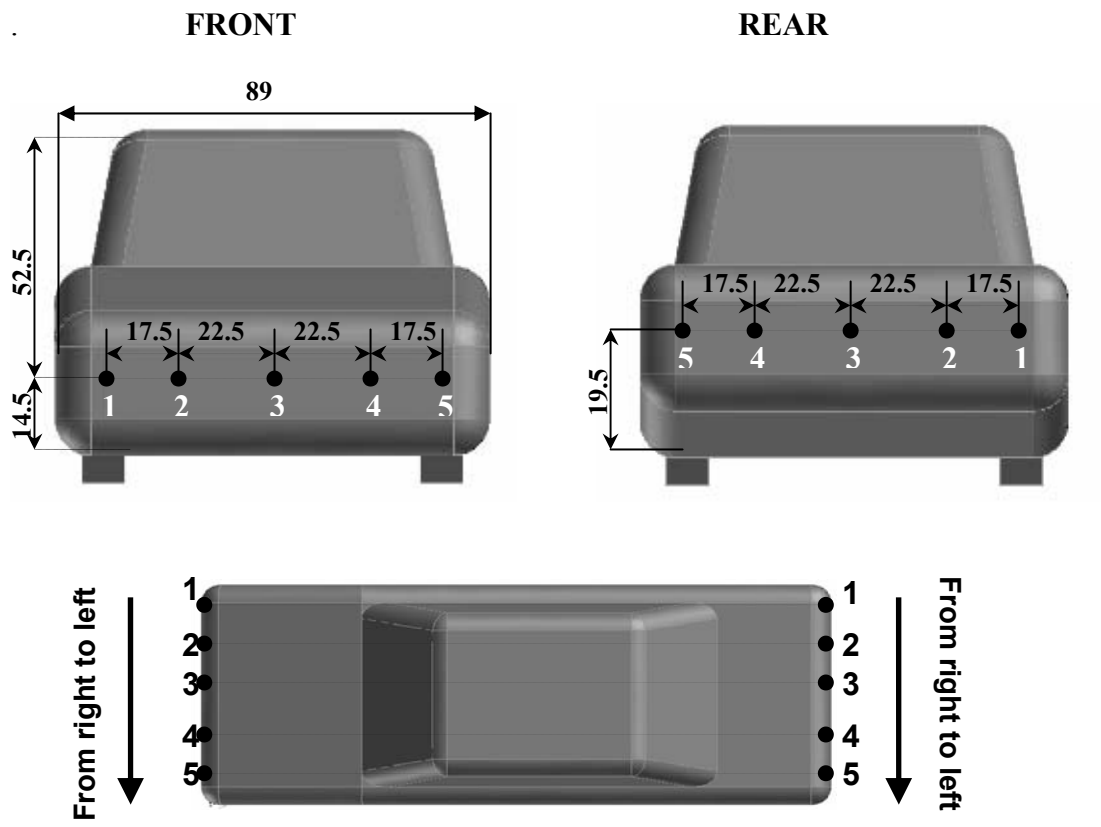

Figure B.1 Tap Locations at the front and rear surfaces of MIRA Model

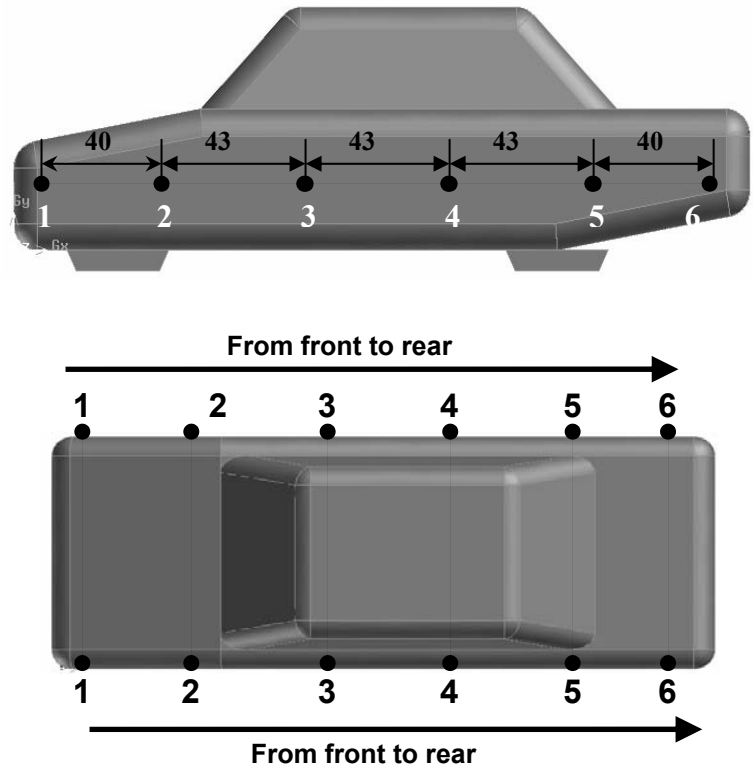

Figure B.2 Tap Locations at the right and left surfaces of MIRA Model

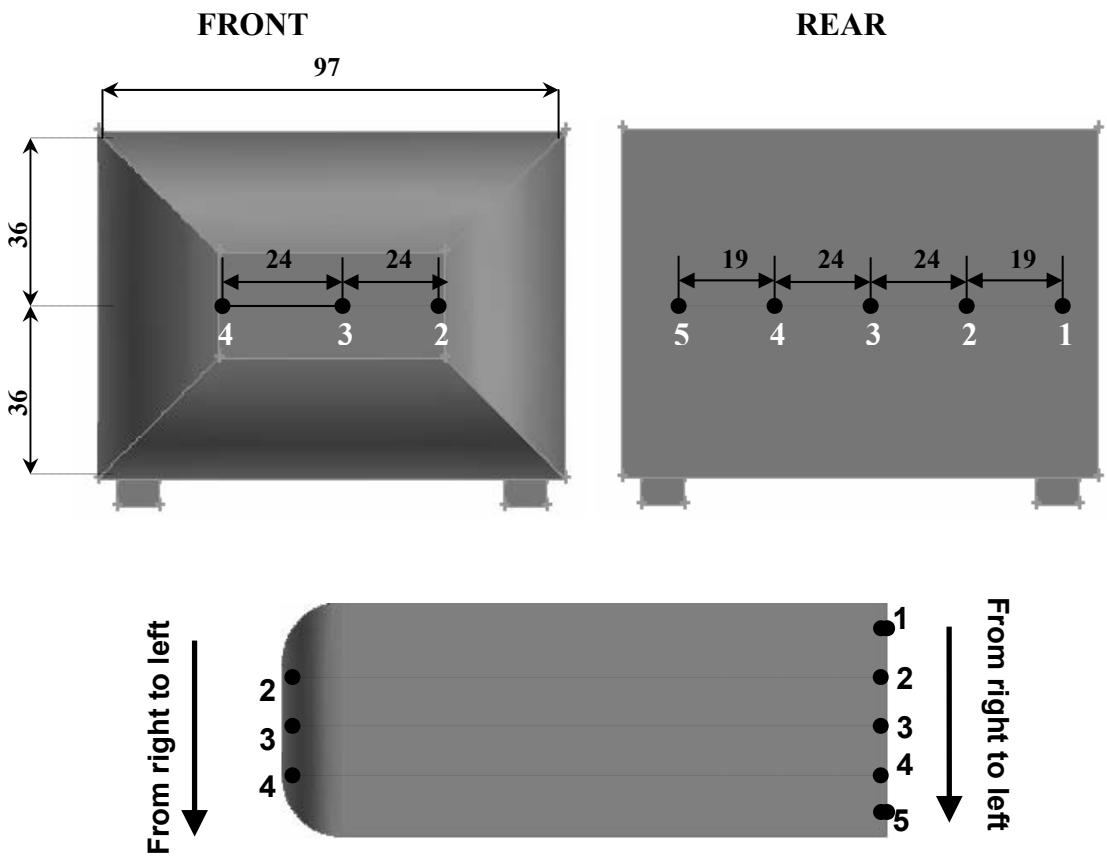

Figure B.3 Tap Locations at the front and rear surfaces of Ahmed Body Model

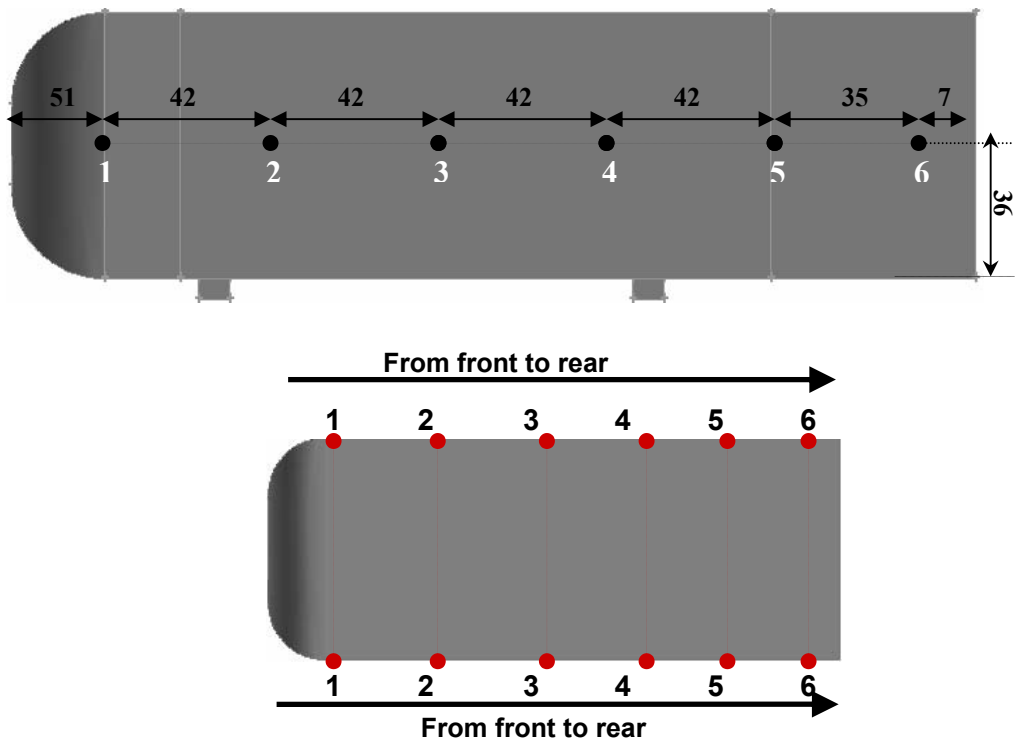

Figure B.4 Tap Locations at the right and left surfaces of Ahmed Body Model

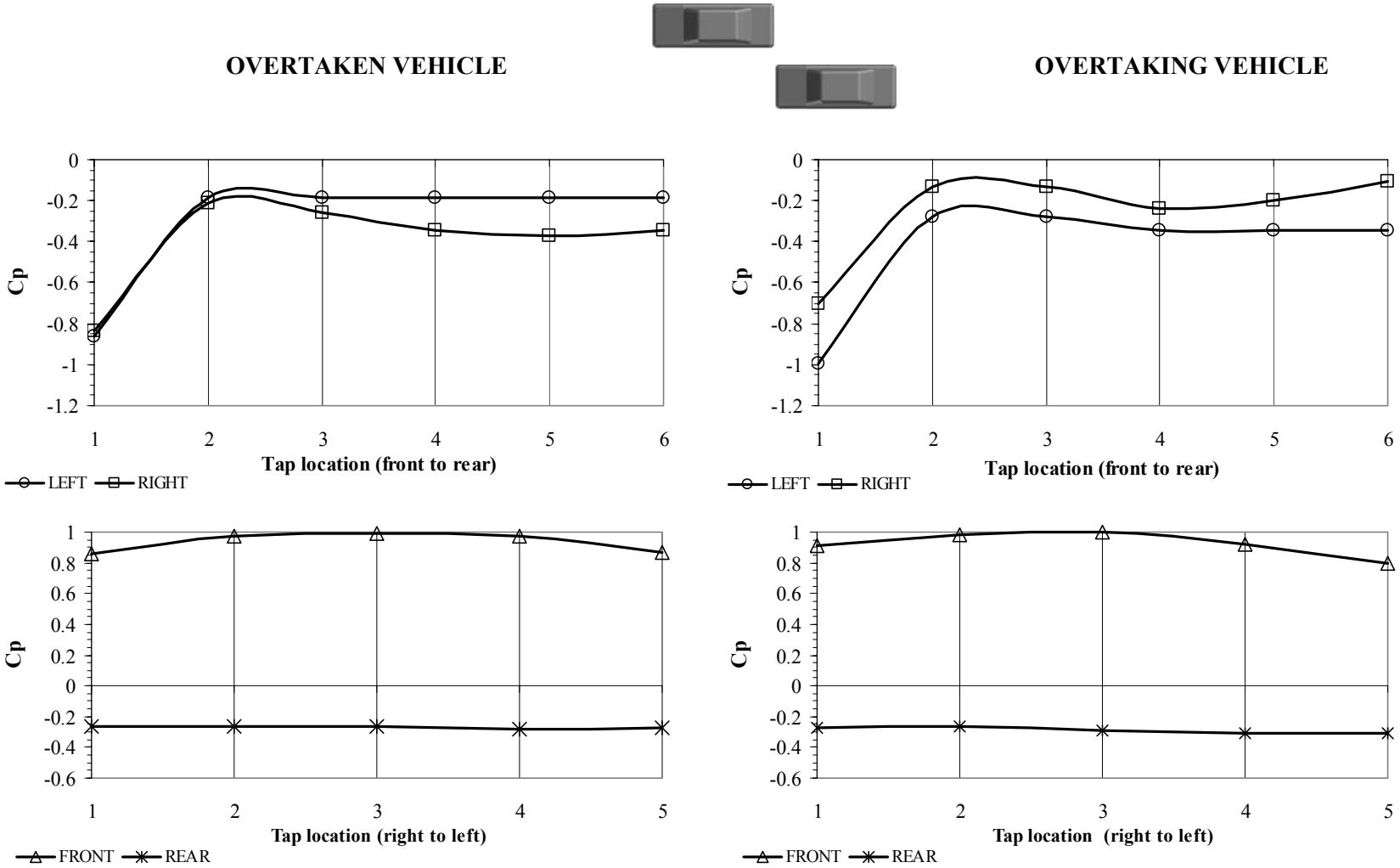

Figure B.5 Surface Pressure Distributions of the MIRA Model for the Closer Overtaking Situation when x/l= 1

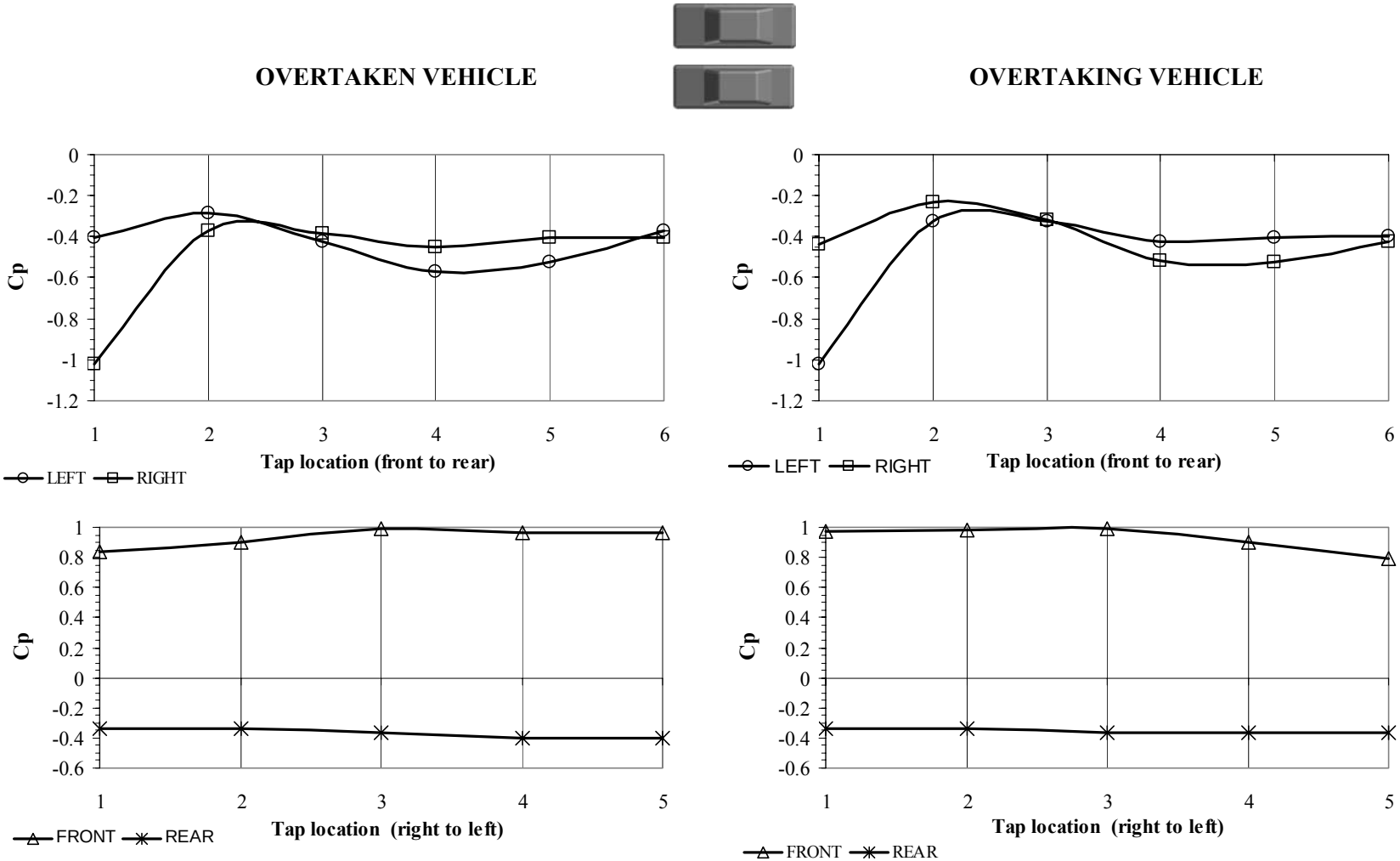

Figure B.6 Surface Pressure Distributions of the MIRA Model for the Closer Overtaking Situation when x/l= 0

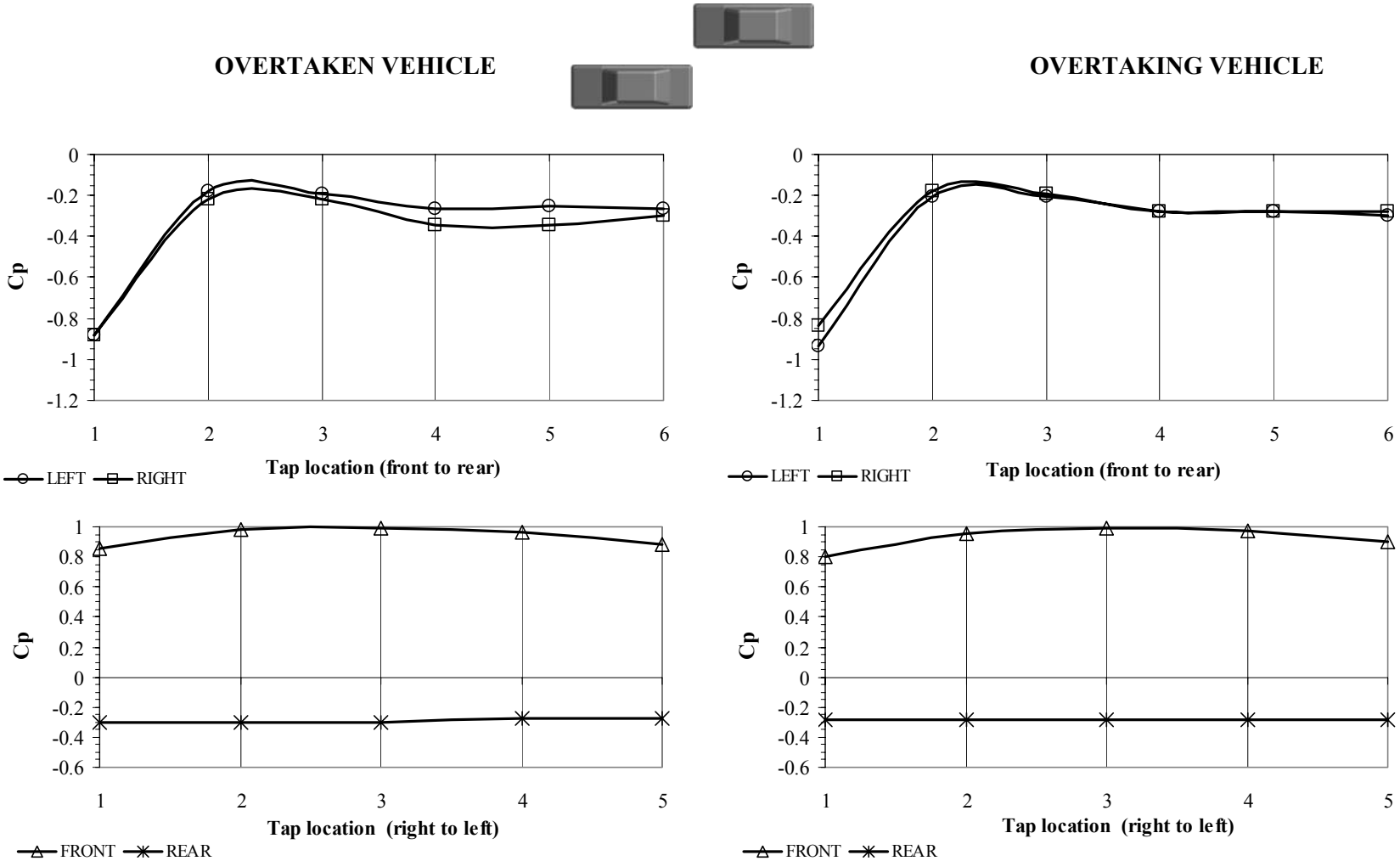

Figure B.7 Surface Pressure Distributions of the MIRA Model for the Closer Overtaking Situation when x/l= -1

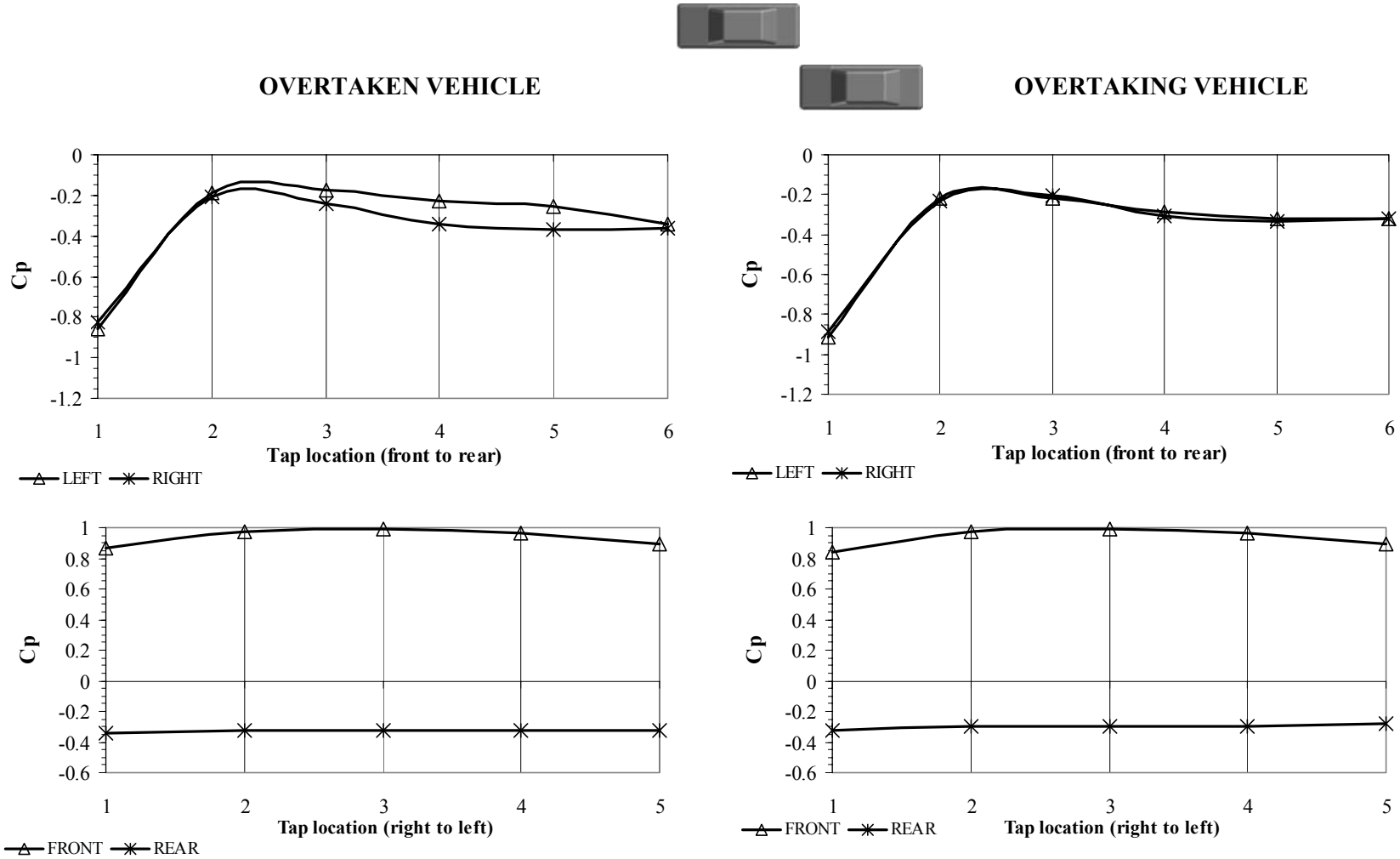

Figure B.8 Surface Pressure Distributions of the MIRA Model for the Further Overtaking Situation when x/l= 1

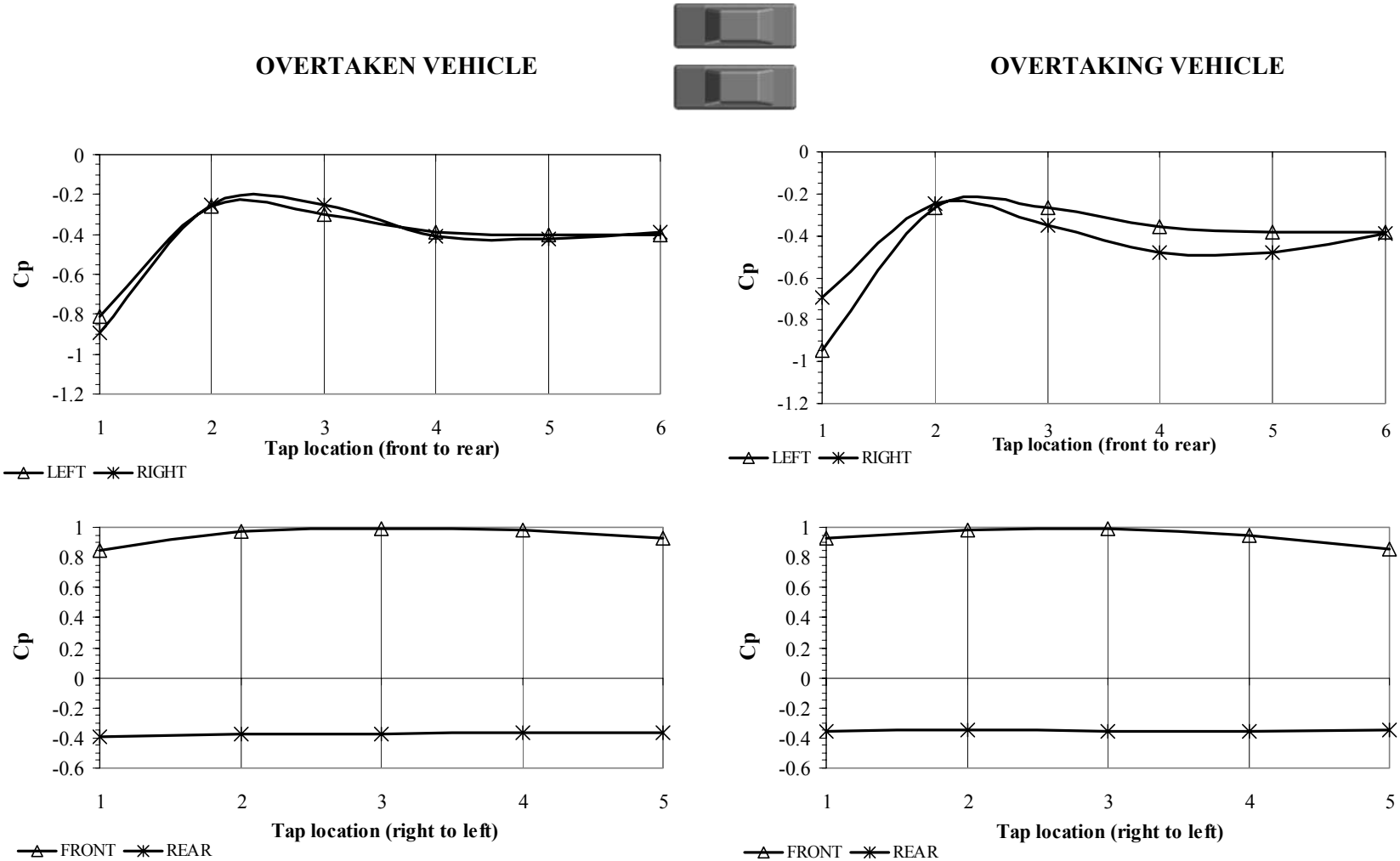

Figure B.9 Surface Pressure Distributions of the MIRA Model for the Further Overtaking Situation when x/l= 0

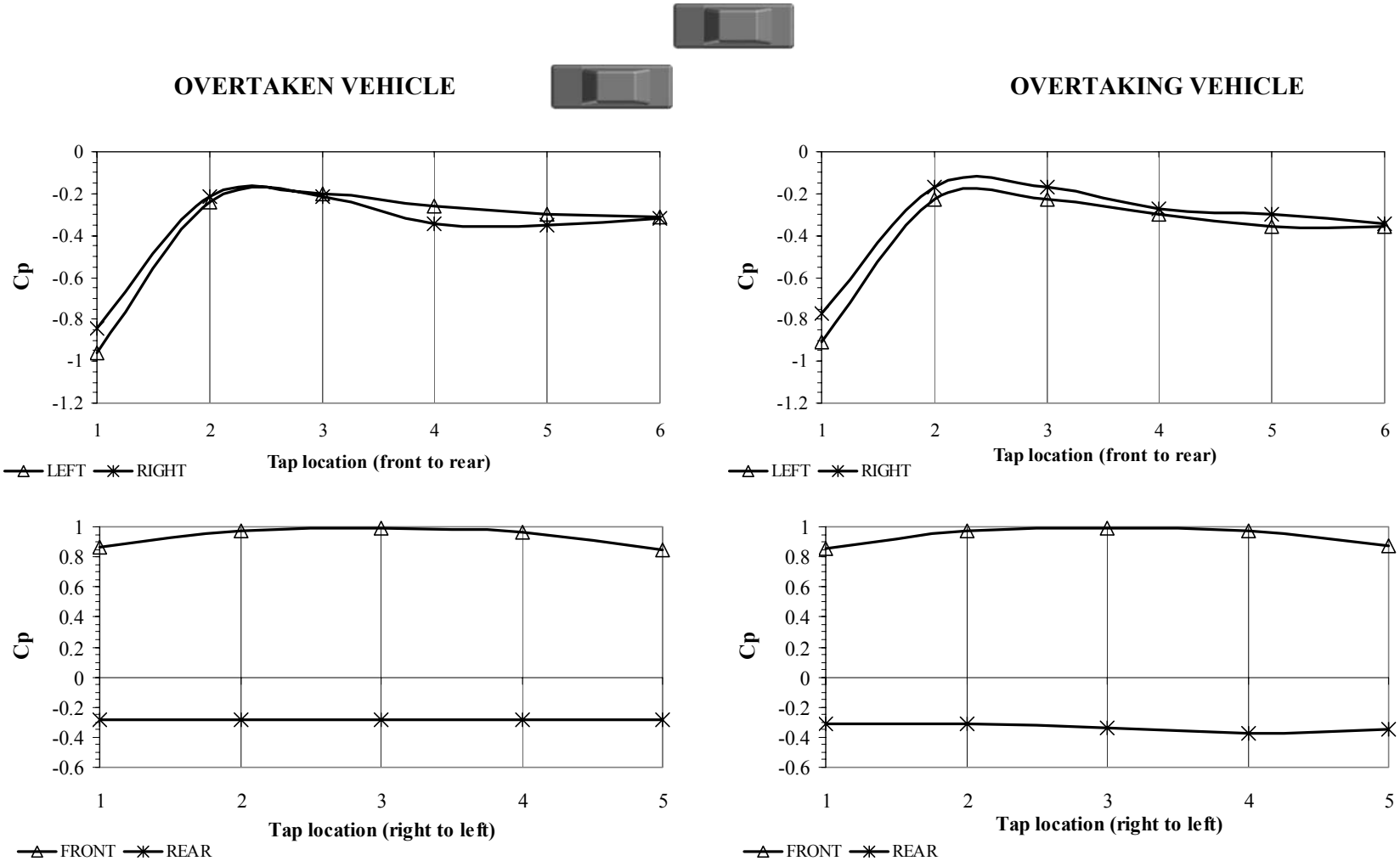

Figure B.10 Surface Pressure Distributions of the MIRA Model for the Further Overtaking Situation when x/l= -1

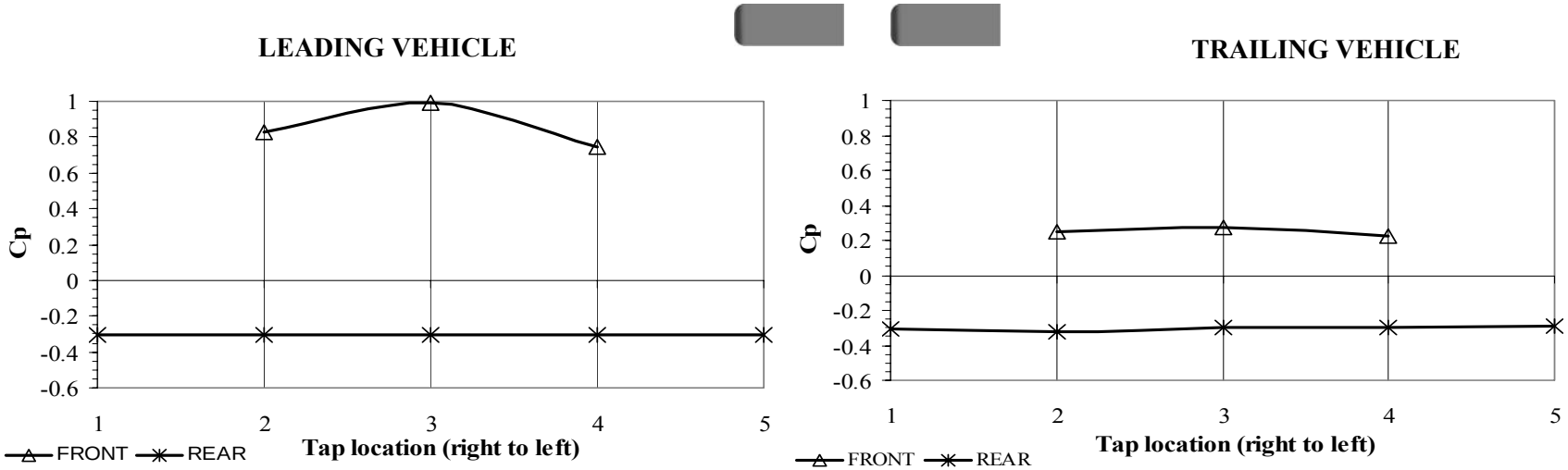

Figure B.11 Surface Pressure Distributions of the Ahmed Body Model for the Close Following Situation when x/l= 0.5

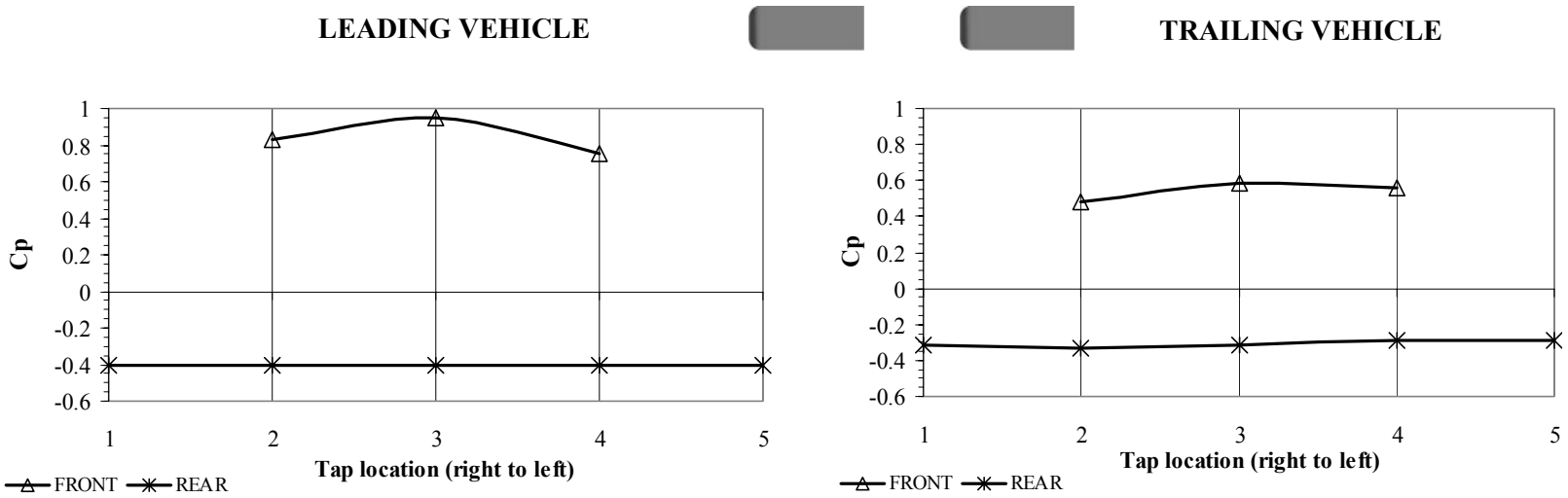

Figure B.12 Surface Pressure Distributions of the Ahmed Body Model for the Close Following Situation when x/l= 1

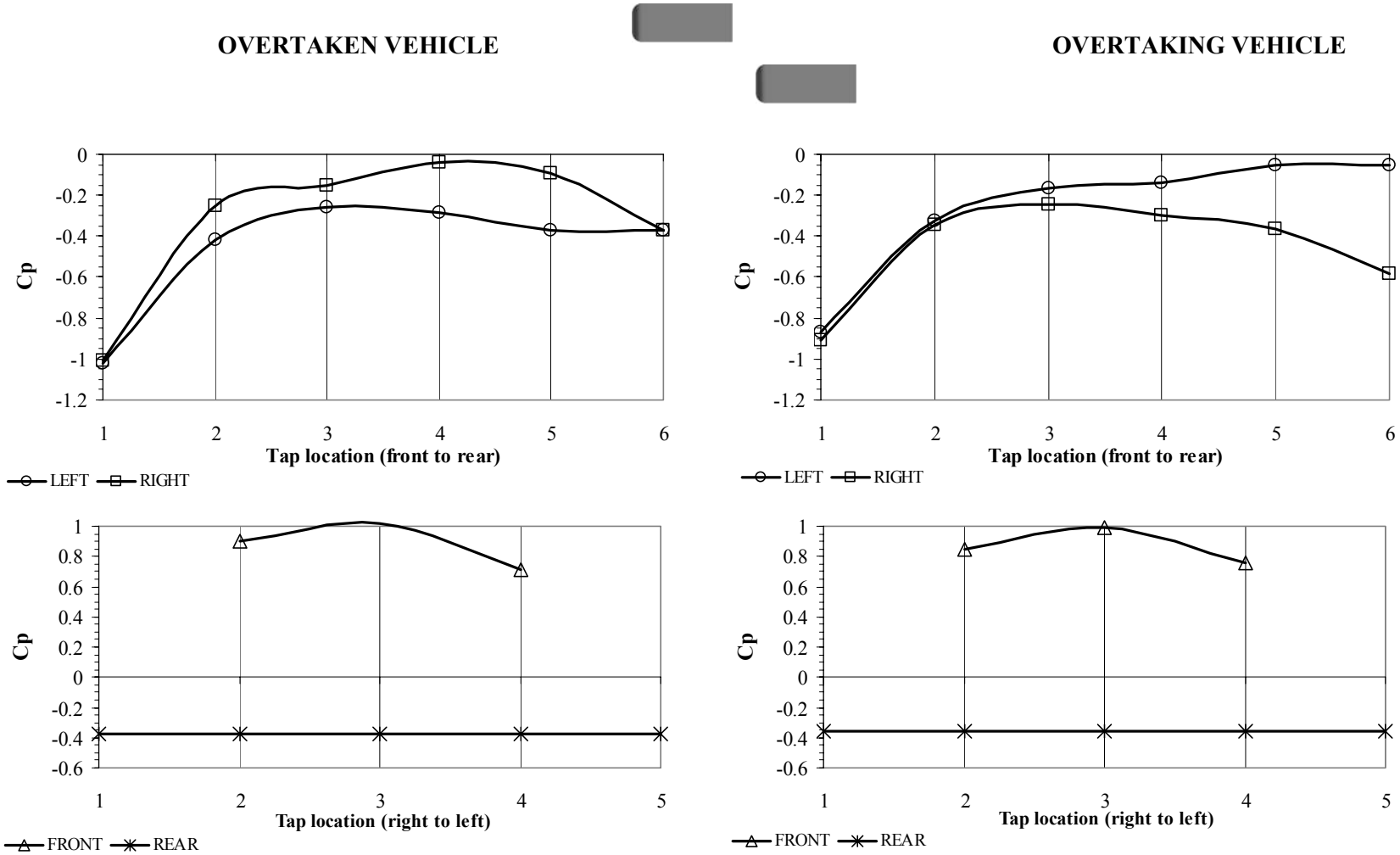

Figure B.13 Surface Pressure Distributions of the Ahmed Body Model for the Closer Overtaking Situation when x/l= 1

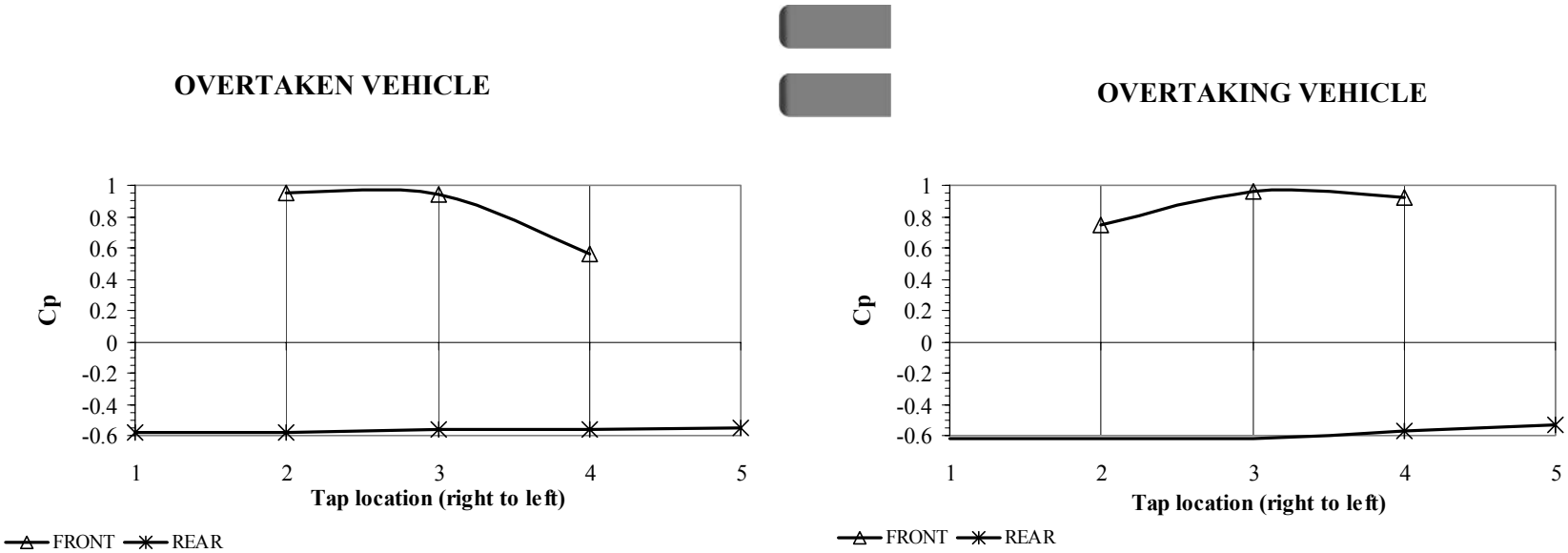

Figure B.14 Surface Pressure Distributions of the Ahmed Body Model for the Closer Overtaking Situation when x/l= 0

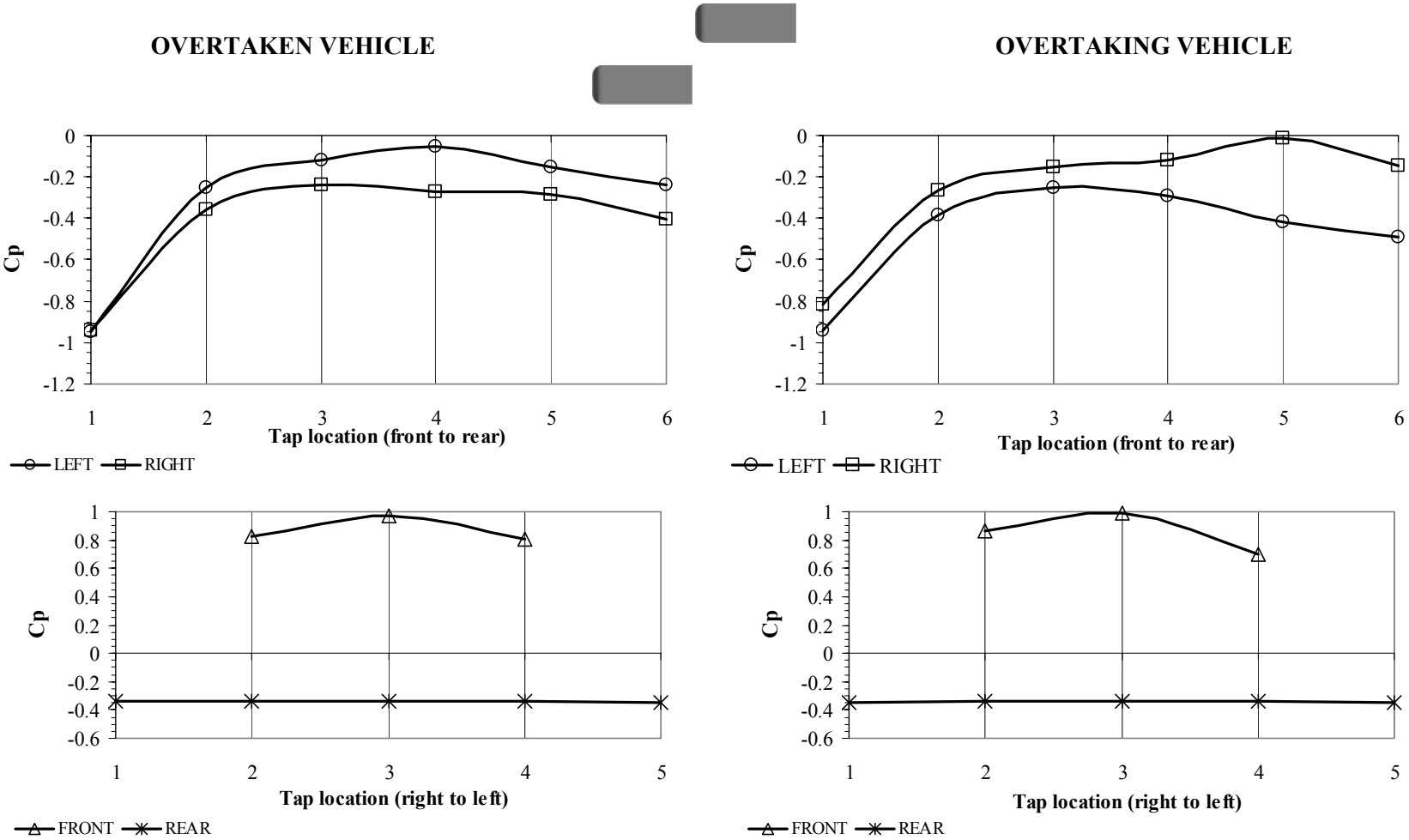

Figure B.15 Surface Pressure Distributions of the Ahmed Body Model for the Closer Overtaking Situation when x/l= -1

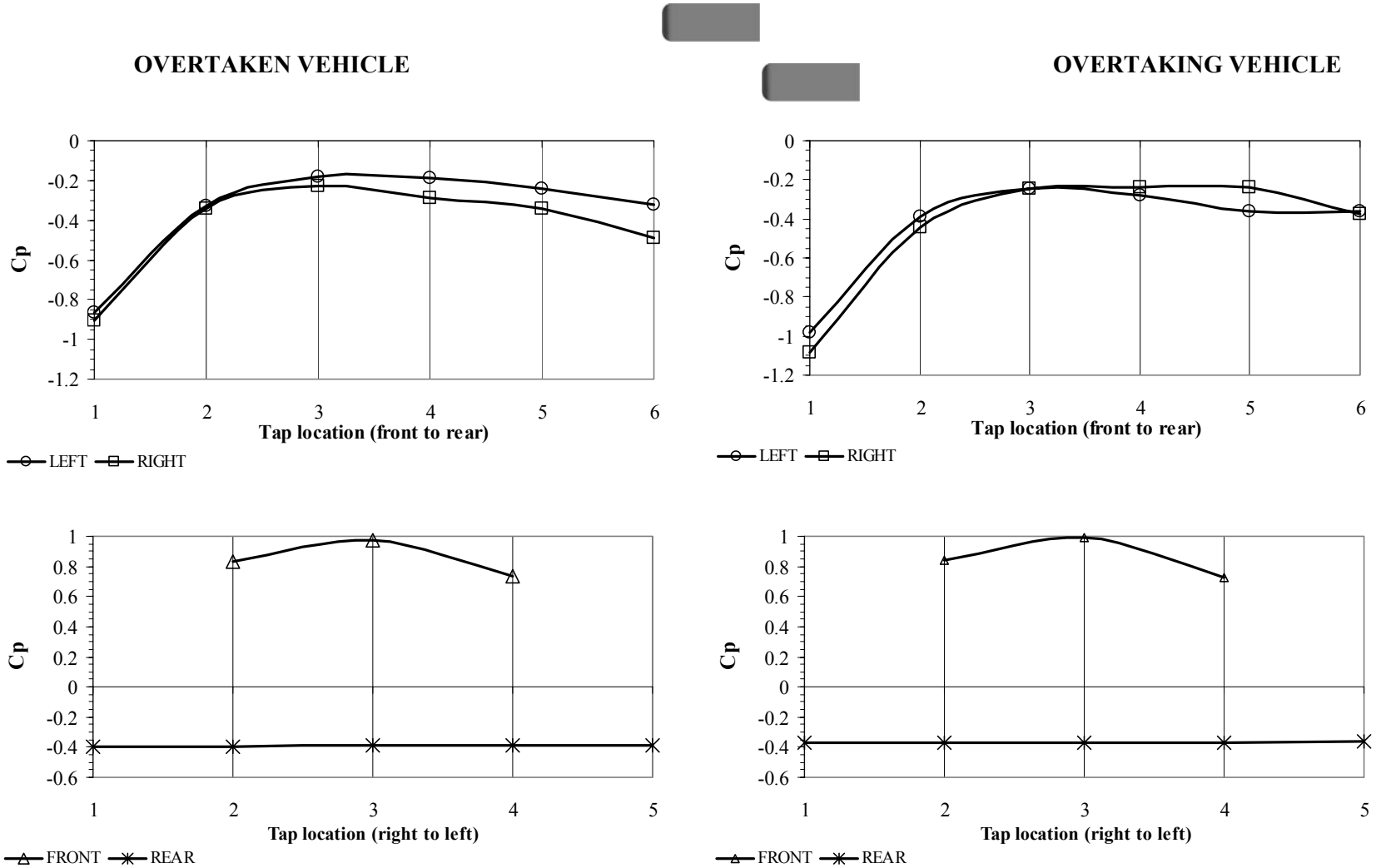

Figure B.16 Surface Pressure Distributions of the Ahmed Body Model for the Further Overtaking Situation when x/l= 1

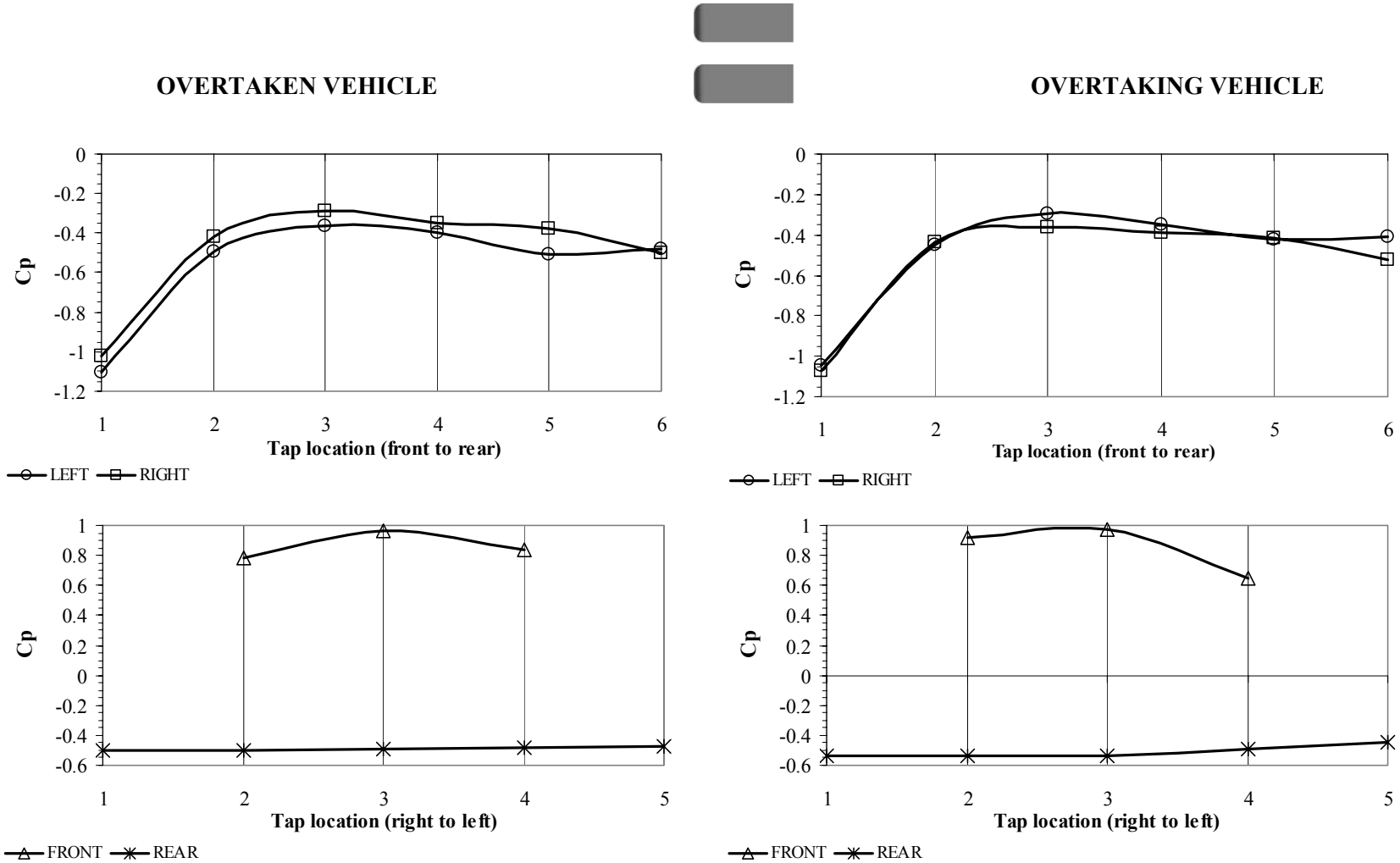

Figure B.17 Surface Pressure Distributions of the Ahmed Body Model for the Further Overtaking Situation when x/l= 0

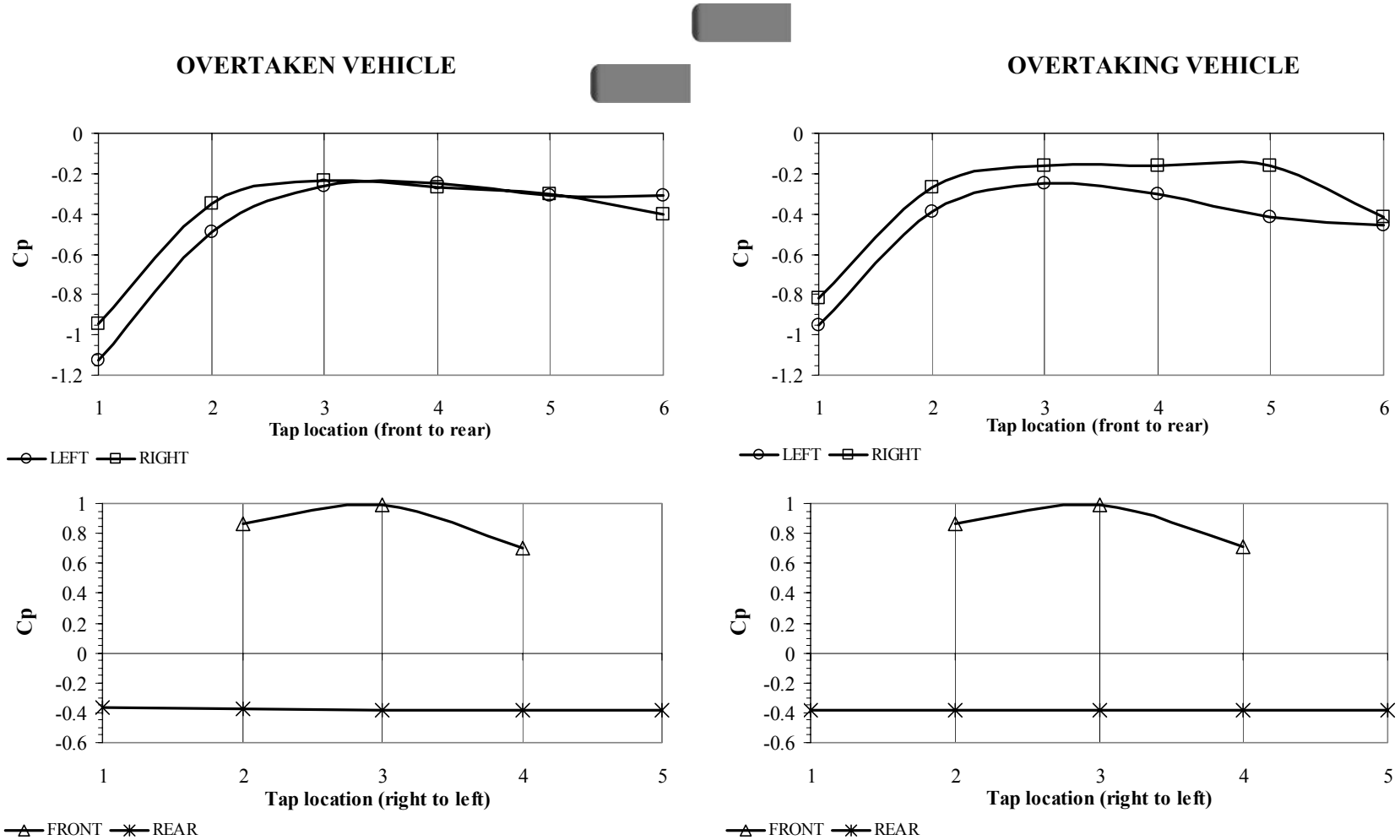

Figure B.18 Surface Pressure Distributions of the Ahmed Body Model for the Further Overtaking Situation when x/l= -1

APPENDIX C

POWER SPECTRAL ESTIMATES OF FREQUENCIES OF THE VORTICES BEHIND AHMED BODY MODEL

The obtained data and their spectral estimates are given with the graphical forms in the following pages. The data are compared with two positions at the same elevation level at the wake of the Ahmed Body. The obtained frequency values are listed in the Results and Discussion part and they are compared with the previous study obtained from the literature survey.

The Power Spectral Estimates of the points at the left, upper and down sides of the wake plane are shown from Figure C.1 to C3. The results for the points at the right side were given in Results and Discussion. In the Figures, X represents the point on the edge and Y represents the point from 1.8 cm inside the edge. XY is the cross-correlation of the power spectral densities of these two points.

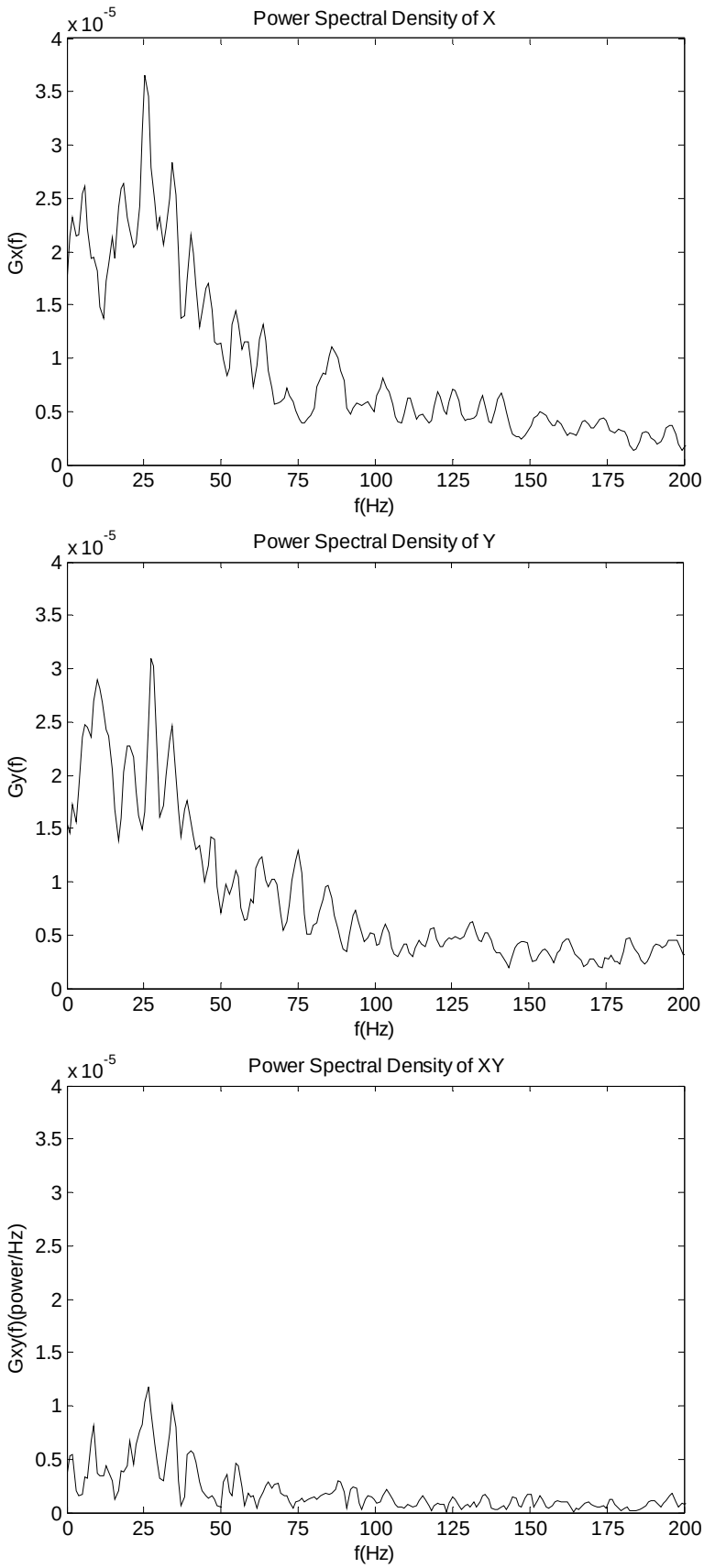

Figure C.1 Power Spectral Density Estimates for the points at the upper side

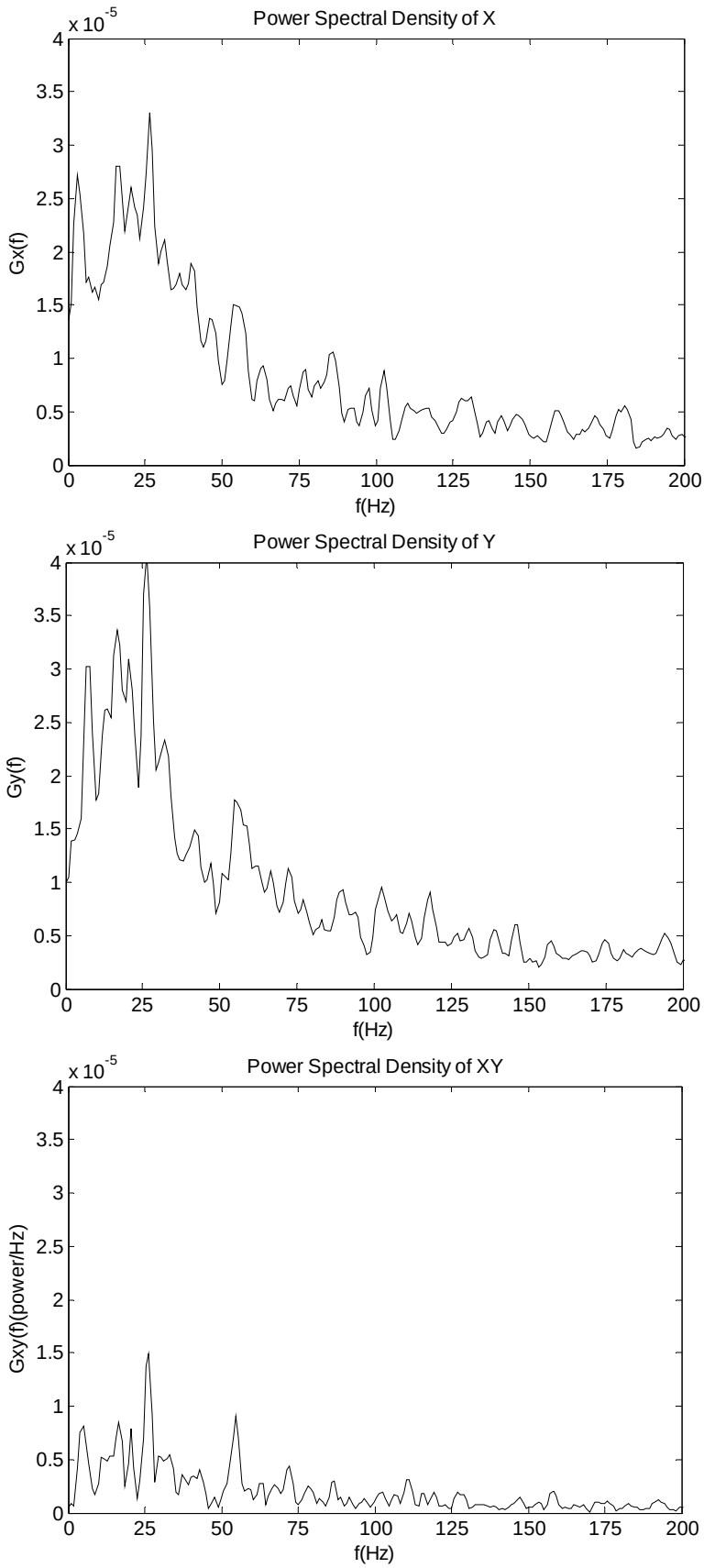

Figure C.2 Power Spectral Density Estimates for the points at the bottom side

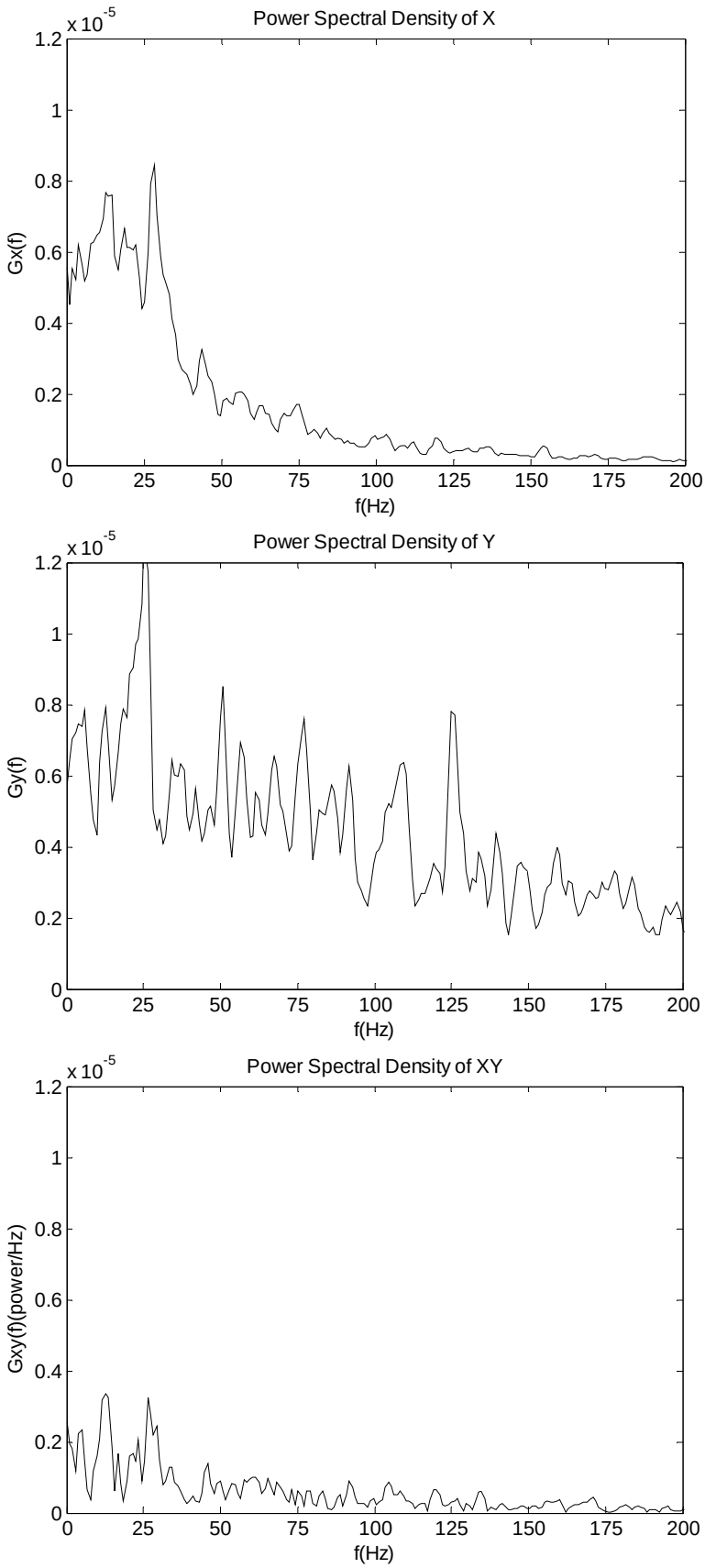

Figure C.3 Power Spectral Density Estimates for the points at the left side

APPENDIX D

EFFECT OF THE GROUND PLANE BOUNDARY LAYER ON DRAG MEASUREMENTS

In the case of ground vehicles, an additional effect is introduced by the presence of the road surface. If one uses a flat plate to model the road surface in a wind-tunnel, a layer of slow moving fluid (the ground plane boundary layer) grows continuously in the downstream direction. This layer does not exist on the actual road surface since it is the vehicle that is in motion and not the medium (air). It is necessary then to minimize the thickness of the ground plane boundary layer, δ, in wind-tunnel tests.

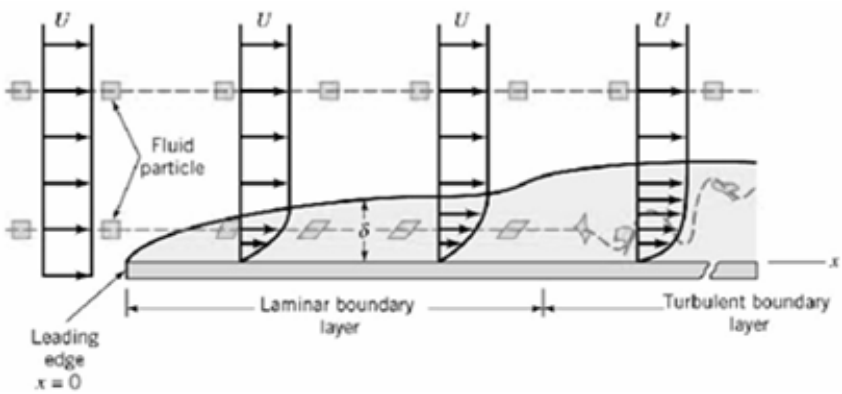

Figure D.1 Sketch of Boundary Layer Flow [42]

For incompressible flow over a smooth flat plate (zero pressure gradient), transition from laminar to turbulent flow in the boundary layer is considered to occur at Reynolds number ($Re_{crit} = U\, x_{crit} / \upsilon$) of 500,000. For air at standard conditions with

a freestream velocity of U = 19 m/s, this corresponds to length, x_{crit}, along the plate of x ≈ 395 mm. Thus, from the leading edge to x = 395 mm, boundary layer is laminar.

In 1908, Blasius found the solution for two dimensional, steady, incompressible flow with zero pressure gradient laminar boundary layer using the governing equations of motion. At the wall, velocity is zero as the distance from the surfaces approaches infinity. Continuity and momentum integral equations for laminar flow are:

$$\frac{\partial u}{\partial x} + \frac{\partial v}{\partial y} = 0 \tag{D.1}$$

$$u\frac{\partial u}{\partial x} + v\frac{\partial u}{\partial y} = \upsilon\frac{\partial^2 u}{\partial y^2} \tag{D.2}$$

By nondimensionalizing the equations with the boundary-layer thickness and velocity, Blasius was able to find a similarity free stream solution for the boundary conditions of no slip at the wall and asymptotic approach to free stream velocity away from the wall (Figure D.2). Evaluating the equations for *u/U= 0.99*, the following approximations for the boundary-layer thickness and displacement thickness can be found.

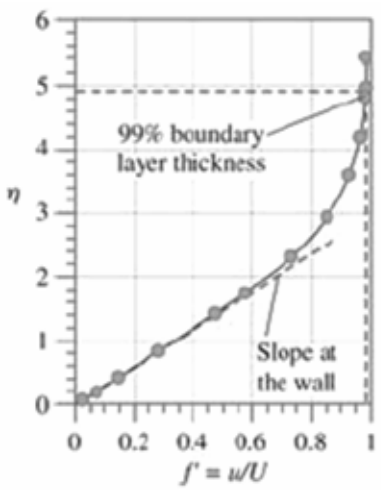

Figure D.2 Velocity Profile for the Laminar Boundary Layer along a Flat Plate at Zero Incidence

If $y = \delta$ when $u/U = 0.99$, numerical integration of the Blasius equation gives:

$$\delta \approx \frac{5.0}{\sqrt{U/\nu x}} = \frac{5.0x}{\sqrt{Re_x}} \tag{D.3}$$

The boundary layer thickness, δ, is indicated on the velocity profile plot of Figure D.2.

$$\delta^* = \int_0^{\delta}\left(1-\frac{u}{U}\right)dy = \left(\frac{\partial\eta}{\partial y}\right)^{-1}\int_0^{5.0}\left(1-\frac{df}{d\eta}\right)d\eta \tag{D.4}$$

$$\delta^*\left(\frac{\partial\eta}{\partial y}\right) = \frac{\delta^*}{x}\sqrt{\frac{Ux}{\nu}} = \left(5.0 - f\big|_{\eta=5.0}\right) = 5 - 3.279 \tag{D.5}$$

$$\frac{\delta^*}{x} = \frac{1.721}{\sqrt{Re_x}} \tag{D.6}$$

According to the Equation D.6, displacement thickness is found as $\delta^* \approx 0.9$ mm at x = 395 mm. For the platoon cases, δ^*/h ratio is 0.07 for MIRA leading model and 0.06 for Ahmed Body leading model. Both values are smaller than 0.1 and therefore there is not any problem about the interactions between ground plane and leading models.

After 395 mm transition occurs and then boundary layer becomes turbulent. Therefore, after this point, calculations are made according to the turbulent boundary layer.

There are no exact solutions for turbulent boundary layer flow. Since there is no precise expression for the shear stress in turbulent flow, solutions are not available for turbulent flow. However, considerable headway has been made in obtaining numerical solutions for turbulent flow by using approximate shear stress relationships. Approximate turbulent boundary layer results can also be obtained by use of the momentum integral equation [41].

Von Karman Momentum Integral Equation is solved using one-seventh law for velocity profile

$$\frac{u}{U} = \left(\frac{y}{\delta}\right)^{\frac{1}{7}} \tag{D.7}$$

However, this profile does not hold in the immediate vicinity of the wall, since at the wall it predicts *du/dy* = ∞. This profile can not be used in the definition of τ_w in terms of δ as done for laminar boundary layer flow. For turbulent boundary layer flow the expression is adapted to developed for pipe flow;

$$\tau w = 0.03325\rho\overline{V}^2\left[\frac{\nu}{R\overline{V}}\right]^{0.25} \tag{D.8}$$

For a 1/7 power profile in a pipe, this equation gives $\overline{V}/U = 0.817.$ Substituting $\overline{V} = 0.817U$ and $R = \delta$;

$$\tau w = 0.0233\rho U^2\left[\frac{\nu}{U\delta}\right]^{0.25} \tag{D.9}$$

Momentum integral equation is applied;

$$\tau w = \rho U^2 \frac{d\delta}{dx}\int_0^1 \frac{u}{U}\left(1-\frac{u}{U}\right)d\eta \tag{D.10}$$

Substituting for τ_w and u/U and integrating gives;

$$0.0233\left[\frac{\nu}{U\delta}\right]^{0.25} = \frac{d\delta}{dx}\int_0^1 \eta^{1/7}(1-\eta^{1/7})d\eta = \frac{7}{72}\frac{d\delta}{dx} \tag{D.11}$$

Thus a differential equation for δ is obtained;

$$\delta^{1/4} d\delta = 0.240\left(\frac{\nu}{U}\right)^{0.25} dx \tag{D.12}$$

Integrating gives;

$$\frac{4}{5}\delta^{5/4} = 0.240\left(\frac{\nu}{U}\right)^{0.25} x + c \tag{D.13}$$

$$\begin{aligned} &\delta = 0.0028 @ x = 0.395\text{m} \\ &\Rightarrow c = -0.0023 \end{aligned} \tag{D.14}$$

$$\delta^{5/4} = 0.3\left(\frac{\nu}{U}\right)^{0.25} x - 0.00288 \tag{D.15}$$

$$\Rightarrow \delta = \left[0.3\left(\frac{\nu}{U}\right)^{0.25} x - 0.00288\right]^{4/5} \tag{D.16}$$

According to this formula, boundary layer thickness is approximately 1.6 cm at the end of the ground plane. For turbulent boundary layers δ^* is approximately 1/8 of boundary layer thickness. [14]. Therefore, displacement thickness is approximately 2 mm at the end of the ground plane. As the Ground clearance is 13 mm for MIRA and 16 mm for Ahmed Body model, δ^*/h ratio is approximately 0.15 For MIRA model and 0.13 for Ahmed Body model. Hucho and Sovran [15] suggest that for a passenger car model affixed to a ground plane, the displacement thickness, δ^*, should be less than 10% of the model ground clearance. So, the effect of ground plane boundary layer may be neglected for single vehicle states. Wind tunnel testing by others indicates that having too thick a surface boundary layer retards the flow under the vehicle and generally leads to a decrease in the estimated drag coefficient. δ^*/h ratios at maximum distance from leading edge are also very small and do not retard the flow under the vehicle.

APPENDIX E

BOUNDARY LAYER TRIPPING TECHNIQUE

In one case, the model has a tripping wire to insure rapid transition to turbulent boundary layer flow. H.L. Dryden used dimensional considerations to find an empirical law which gives the dependence of the position of completed transition x_{crit} both on the roughness height k and on the position of the roughness element x_k. He found that, for incompressible flows, all experimental data where the position of completed transition is not directly dependent on the roughness element, and thus for which $x_{crit} > x_k$, lies pretty well along one curve, about $Uk / \upsilon \approx 900$. This occurs in the plot of the Reynolds number $Re_{l\ crit} = U\delta_{l\ crit} / \gamma$ formed with the displacement thickness of the boundary layer at the position of transition $\delta_{l\ crit}$ against $k / \delta_{l\ k}$ (Figure E.1), where $\delta_{l\ k}$ is the displacement thickness at the position of the roughness element. The second scale on the vertical axis is $Re_{x\ crit} = U\ x_{crit} / \gamma$. The relation between the two Reynolds numbers on the vertical axis is;

$$\mathrm{Re}_{\mathrm{lcrit}} = \frac{\mathrm{U}\delta_{\mathrm{lcrit}}}{\nu} = 1.72\sqrt{\frac{\mathrm{Ux}_{\mathrm{crit}}}{\nu}} = 1.72\sqrt{\mathrm{Re}_{\mathrm{x\ crit}}} \qquad \text{(E.1)}$$

With increasing k, x_{crit} shifts closer to the roughness element, so that as k increases, the straight lines in Figure E.1 run from left to right. As soon as the position of completed transition has reached the roughness element, $x_{crit} = x_k$, the experimental data deviate upwards from this curve.

a) b)

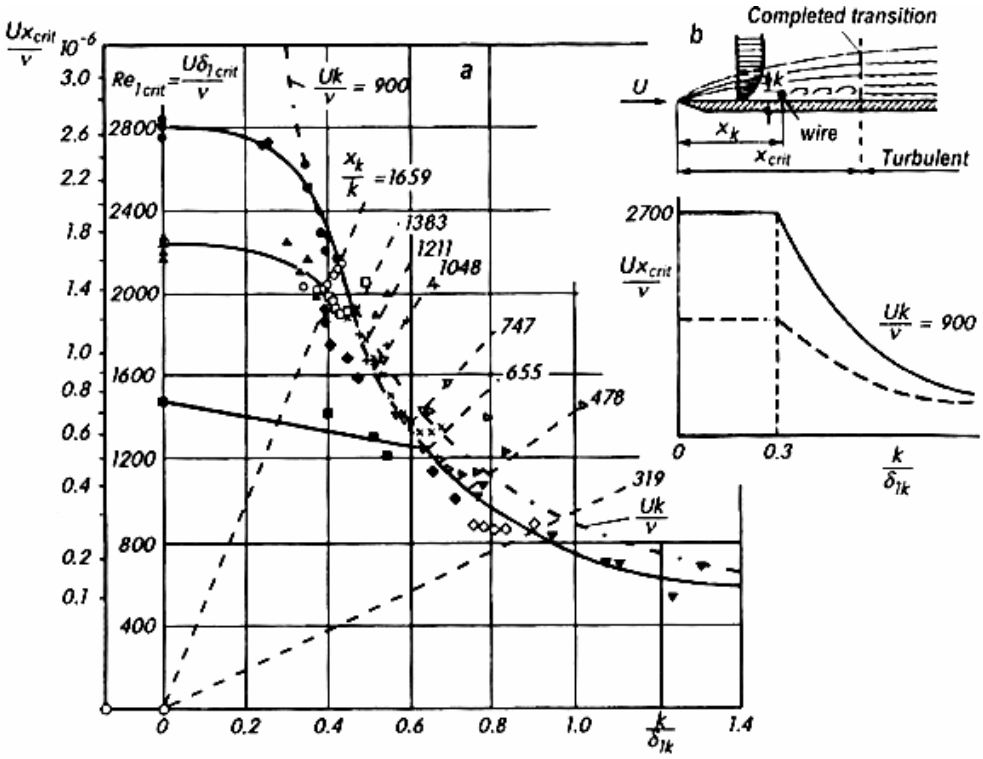

Figure E.1 Effect of Single Roughness Elements on Transition [37]

a) Dependence of the critical Reynolds number on the ratio of the roughness height k to displacement thickness of the boundary layer at the position of the roughness element $\delta_{l\,k}$, for two dimensional single roughness elements in incompressible flow. The index 0 implies the smooth plate.

- - - - - - - - Computed using Equation E.2 for $(Re_{l\ crit})_0 = 1.7\times10^6$; p = const. after Feindt E.G. (1956).

▲ $(Re_{l\ crit})_0 = 1.7\times10^6$; p = const. after Tani I.

● $(Re_{l\ crit})_0 = 1.7\times10^6$; p = const. after Tani I.

♦ $(Re_{l\ crit})_0 = 2.7\times10^6$; p = const. after Schubauer G.B., Skramstad H.K.

■ $(Re_{l\ crit})_0 = 6\times10^5$; p = const. after Tani I. et al.

b) Basic sketch of the laminar-turbulent transition with individual roughness element (wire) and effect of outer turbulence on the critical Reynolds number $Re_{x\ crit}$.

———— Without outer turbulence

- - - - - - - - - - - With outer turbulence

As the height k is increased, the position of the point of transition x_{crit} moves closer to the roughness element. The experimental points begin to deviate from this curve upwards as soon as the point of transition has reached the roughness element when $x_{crit} = x_k$. They then lie along the family of straight lines which contain x_k/k as a parameter and are given by;

$$\frac{U\delta_{l\,crit}}{\upsilon} = 3.0\frac{k}{\delta_{l\,k}}\frac{x_k}{k} \tag{E.2}$$

x_k/k and $k/\delta_{l\,k}$ are chosen from the Figure E.1 to obtain the Reynolds number at the transition point.

$x_k/k = 319$

$k/\delta_{l\,k} = 0.9$

These values are then substitute in Equation E.2.

$$Re_{l\,crit} = \frac{U\delta_{l\,crit}}{\upsilon} = 3.0 \times 0.9 \times 319 = 861 \tag{E.3}$$

For air at standard conditions with freestream velocity U = 19 m/s, displacement thickness at the transition point is found as $\delta_{l,crit}$ = 0.68 mm. using the relation between the Reynolds numbers in Equation E.1;

$$Re_{l,\,crit} = 1.72\sqrt{Re_{x,\,crit}}$$

$$Re_{x,\,crit} = \frac{(Re_{l,\,crit})^2}{1.72} = \frac{(861)^2}{1.72} = 2.5 \times 10^5$$

Then, the position of completed transition is found by using the Reynolds number at that position.

$$Re_{x,crit} = \frac{Ux,\,crit}{\upsilon} = 2.5 \times 10^5$$

$$\frac{19(x_{crit})}{1.5\times10^{-5}} = 2.5\times10^{5}$$

$$x_{crit} = 198\text{mm}$$

According to the similarity between models and prototypes, the position of the completed transition is obtained. Since the roughness elements are placed on the model to simulate the rapid transition to turbulent boundary layer, the positions of the roughness element and completed transition are same; $x_{crit,m} = x_k$. Critical roughness heights of the models are determined by using the ratio of, x_k / k = 319 chosen before.

For 1/18 scale MIRA model,

$$\frac{x_{crit,m}}{x_{crit,p}} = \frac{l_m}{l_p} = \frac{1}{18} \Rightarrow x_{crit,m} \approx 11\text{mm}$$

$$x_{crit,m} = x_k = 11\text{mm}$$

$$\frac{x_k}{k} = 319 \Rightarrow k = \frac{x_k}{319} = \frac{11}{319} \approx 0.04\text{mm}$$

For 1/4 scale Ahmed Body model;

$$\frac{x_{tr,m}}{x_{tr,p}} = \frac{l_m}{l_p} = \frac{1}{4} \Rightarrow x_{tr,m} \approx 50\text{mm}$$

$$x_{tr,m} = x_k = 50\text{mm}$$

$$\frac{x_k}{k} = 319 \Rightarrow k = \frac{x_k}{319} = \frac{50}{319} \approx 0.16\text{mm}$$

APPENDIX F

UNCERTAINTY ANALYSIS

This analysis is applied for indicating the uncertainties in the experimental measurements. The uncertainties in the calculations are estimated using the following procedure.

Let the result R is a function of the independent variables x_1, x_2,……., x_n as:

$$R = R(x_1, x_2, \ldots\ldots, x_n) \tag{F.1}$$

If the uncertainty in the result and the uncertainties in the independent variables are denoted as W_R and w_1, w_2,……., w_n, respectively, the uncertainty in the result may be expressed as:

$$W_R = \left[\left(\frac{\partial R}{\partial x_1} w_1 \right)^2 + \left(\frac{\partial R}{\partial x_2} w_2 \right)^2 + \left(\frac{\partial R}{\partial x_3} w_3 \right)^2 + \ldots\ldots\ldots\ldots\ldots + \left(\frac{\partial R}{\partial x_n} w_n \right)^2 \right]^{1/2} \tag{F.2}$$

As mentioned in Chapter 3, the aerodynamic behavior of road vehicles in close-following and passing situations, drag is the most important factor from the viewpoint of the fuel economy. The ratio of drag force with the dynamic head is called as *drag coefficient*.

$$C_D = \frac{D}{\frac{1}{2}\rho . V^2 . A} \tag{3.6}$$

In Equation 3.6, D is the drag force; ρ is the density of air; V is the freestream velocity and A is the frontal area exposed to the oncoming flow.

As seen in Equation (3.6), there are four parameters that affect the drag coefficient. For finding the uncertainty of drag coefficient, uncertainty of each parameter should be obtained.

F.1 Uncertainty in the drag force

Drag force experiments were conducted by using Three Component Balance as mentioned in Chapter 4 and Chapter 5. A 3x3 matrix was used to obtain the drag coefficient.

$$D = \frac{\begin{vmatrix} E_A & b_1 & c_1 \\ E_B & b_2 & c_2 \\ E_C & b_3 & c_3 \end{vmatrix}}{\begin{vmatrix} a_1 & b_1 & c_1 \\ a_2 & b_2 & c_2 \\ a_3 & b_3 & c_3 \end{vmatrix}} \tag{5.4}$$

Small letters in Equation 5.4 are balance coefficients. They are found from the calibration. During the tests, the strains E_A, E_B, E_C are measured and than they are substituted in to Equation 5.4. Thus, not only the measured strains but also the balance coefficients affect the drag force. Therefore, their uncertainties in the calibration should be obtained

.

$$W_D = \left[\left(\frac{\partial D}{\partial E_A} W_{EA}\right)^2 + \left(\frac{\partial D}{\partial E_B} W_{EB}\right)^2 + \left(\frac{\partial D}{\partial E_C} W_{EC}\right)^2 + \left(\frac{\partial D}{\partial a_1} W_{a1}\right)^2 + \left(\frac{\partial D}{\partial a_2} W_{a2}\right)^2 + \right.$$

$$+ \left(\frac{\partial D}{\partial a_3} W_{a3}\right)^2 + \left(\frac{\partial D}{\partial b_1} W_{b1}\right)^2 + \left(\frac{\partial D}{\partial b_2} W_{b2}\right)^2 + \left(\frac{\partial D}{\partial b_3} W_{b3}\right)^2 + \left(\frac{\partial D}{\partial c_1} W_{c1}\right)^2 +$$

$$\left. + \left(\frac{\partial D}{\partial c_2} W_{c2}\right)^2 + \left(\frac{\partial D}{\partial c_3} W_{c3}\right)^2 \right]^{1/2} \tag{F.3}$$

In order to find the uncertainties in each calibration coefficient, Equations 5.7-5.15 are used. Each uncertainty is found according to the Equation F.2. For a sample calculation, the uncertainty in the calibration coefficient a_1 can be estimated. Calibration coefficient, a_1, can be obtained with using the Equation 5.7.

$$a_1 = \frac{E_A}{W} \tag{5.7}$$

$$W_{a1} = \left[\left(\frac{\partial a_1}{\partial E_A} W_{EA} \right)^2 \right]^{1/2} \tag{F.4}$$

$$W_{a1} = \left[\left(\frac{1}{W} \times W_{EA} \right)^2 \right]^{1/2} \tag{F.5}$$

$$W_{a1} = \left[\left(\frac{1}{0.392} \times 0.1 \right)^2 \right]^{1/2} = 0.255$$

The other uncertainties in the calibration coefficients are obtained with the same procedure. On the other hand, uncertainties in the measurements of strains are obtained for each experiment. The obtained uncertainty values are then applied into the Equation F.3 for the result uncertainty in the drag force.

When the procedure of uncertainty analysis was applied for the single vehicle measurements, uncertainty in the drag force of MIRA model was obtained as ±0.01 N whereas it was ±0.012 N for Ahmed Body model.

F.2 Uncertainty in the density

Since density of air is a function of pressure and temperature, uncertainty in the density of air is the root-sum square combination of the effect of each of these measurement uncertainties.

The uncertainty in temperature is 0.5°C since the maximum thermometer scale is 1°C and the uncertainty in atmospheric pressure is 0.5mmHg since the minimum barometer scale is 1mmHg.

Uncertainty in density of air can be calculated by Equation F.6.

$$W\rho_{air} = \left[\left(\frac{\partial \rho_{air}}{\partial P} W_P \right)^2 + \left(\frac{\partial \rho_{air}}{\partial T} W_T \right)^2 \right]^{1/2} \tag{F.6}$$

Writing the ideal gas relation;

$$P = \rho_{air} RT \tag{F.7}$$

$$\rho_{air} = \frac{P}{RT} \tag{F.8}$$

For single vehicle measurement of the MIRA model, temperature was measured as 18 °C and atmospheric pressure was 673 mmHg. The ideal gas constant for air is 0.287 kJ/kg.K

$$P = 673\text{mmHg} = 89{,}726\text{kPa}$$

$$T = 18 + 273.15 = 291.15\text{K}$$

$$R = 0.287\text{kJ/kg.K}$$

$$\frac{\partial \rho_{air}}{\partial P} = \frac{1}{RT} = \frac{1}{0.287 \times 291.15} = 0.012$$

$$\frac{\partial \rho_{air}}{\partial T} = -\frac{P}{RT^2} = -\frac{89{,}726}{(0.287) \times (291.15)^2} \approx -0.004$$

Therefore, uncertainty in the density of air is;

$$W\rho_{air} = \left[(0.012 \times 0.5)^2 + (-0.004 \times 0.5)^2 \right]^{1/2} = \pm 6.3 \times 10^{-3}\,\text{kg/m}^3$$

F.3 Uncertainty in the freestream velocity

Uncertainty in the freestream velocity can be obtained with using the Equation of dynamic pressure (Equation F.9)

$$P_{dyn} = \rho_{air}.V^2 / 2 \tag{F.9}$$

As explained in Chapter 5, freestream velocity in the test section was measured with using the Micromanometer. Freestream velocities are determined from the read dynamic pressures according to the Equation F.10.

$$V = \left[\frac{2P_{dyn}}{\rho_{air}} \right]^{1/2} \tag{F.10}$$

Thus, uncertainty in the freestream velocity can be calculated by;

$$WV = \left[\left(\frac{\partial V}{\partial Pdyn} WPdyn \right)^2 + \left(\frac{\partial V}{\partial \rho air} W\rho air \right)^2 \right]^{1/2} \tag{F.11}$$

The uncertainty in the density of air is 6.3×10^{-3} kg/m^3 as determined in part F.2. The uncertainty in dynamic pressure is ±1 Pa.

$$\frac{\partial V}{\partial Pdyn} = \frac{1}{(\rho air)^{1/2} \times (Pdyn)^{1/2}} = \frac{1}{1.04 \times 13.67} = 0.07$$

$$\frac{\partial V}{\partial \rho air} = -\frac{(Pdyn)^{1/2}}{(\rho air)^{3/2}} = \frac{13.67}{1.12} = 12.22$$

Substituting the obtained values into Equation F.11 gives;

$$WV = \left[(0.07)^2 + \left(12.22 \times (6.3 \times 10^{-3})\right)^2 \right]^{1/2} = \pm 0.104 \text{ m/s}$$

F.4 Uncertainty in the Frontal Area

According to the consecutive measurements for the frontal areas of the models, the uncertainty values were found as $W_A \approx \pm\ 0.0002\ m^2$.

F.5 Uncertainty in the Drag Coefficient

Finally, uncertainty in the drag coefficient is obtained with using the found uncertainty values of parameters that affect the drag coefficient. It can be determined according to the Equation F.12.

$$W_{CD} = \left[\left(\frac{\partial C_D}{\partial D} W_D \right)^2 + \left(\frac{\partial C_D}{\partial V} W_V \right)^2 + \left(\frac{\partial C_D}{\partial \rho} W_\rho \right)^2 + \left(\frac{\partial C_D}{\partial A} W_A \right)^2 \right]^{1/2} \qquad \text{(F.12)}$$

The derivatives are found with using the Equation (3.6).

$$W_{CD} = \left[\left(\frac{1}{\frac{1}{2}\rho V^2 A} W_D \right)^2 + \left(\frac{-2D}{\frac{1}{2}\rho V^3 A} W_V \right)^2 + \left(\frac{-D}{\frac{1}{2}\rho^2 V^2 A} W_\rho \right)^2 + \left(\frac{-D}{\frac{1}{2}\rho V^2 A^2} W_A \right)^2 \right]^{1/2} \qquad \text{(F.13)}$$

For single vehicle measurement of the MIRA model;

D=0.364 N A = 0.0059 m^2
V = 18.63 m/s ρ = 1.077 kg/m^3

Finally, substituting these values and also the uncertainties in the parameters into Equation F.13 gives;

$$W_{CD} = \left[(0.009)^2 + (-0.004)^2 + (-0.002)^2 + (-0.011)^2 \right]^{1/2} = \pm 0.015$$

Therefore, the drag coefficient of MIRA model is 0.329 ± 0.015 or 0.329 ± 4.5 %

For single vehicle measurement of Ahmed Body model, the calculations explained above are applied with using the values in the experiment.

T= 17 °C V = 18.75 m/s

P_{dyn} =190 Pa ρ = 1.081 kg/m^3

D=0.394 N A = 0.007 m^2

After the calculations, the uncertainty in the drag coefficient of Ahmed Body model was obtained as ± 0.0013. Thus, the drag coefficient of Ahmed Body model is 0.296 ± 0.013 or 0.296 ± 4.4 %

F.6 Uncertainty in the Pressure Coefficient

For finding the uncertainty in the pressure coefficient (C_P), Equation 3.21 is used.

$$C_P = \frac{(P_{local} - P_\infty)}{(1/2\rho U_\infty^2)} \tag{3.21}$$

As explained in Chapter 4, P_{local} -P_∞ is read from the Micromanometer. If it is represented by ΔP, Equation 3.21 can be written as ΔP / ($1/2\rho V^2$). Thus, the uncertainty in the pressure coefficient can be obtained by the Equation F.14.

$$W_{Cp} = \left[\left(\frac{\partial C_p}{\partial P} W_P \right)^2 + \left(\frac{\partial C_P}{\partial V} W_V \right)^2 + \left(\frac{\partial C_P}{\partial \rho} W_\rho \right)^2 \right]^{1/2} \tag{F.14}$$

$$W_{Cp} = \left[\left(\frac{1}{\frac{1}{2}\rho V^2} W_P \right)^2 + \left(\frac{-2\Delta P}{\frac{1}{2}\rho V^3} W_V \right)^2 + \left(\frac{-\Delta P}{\frac{1}{2}\rho^2 V^2} W_\rho \right)^2 \right]^{1/2} \tag{F.15}$$

After the uncertainty analysis were done, maximum uncertainties in the magnitudes of the pressure coefficients were determined for each measurement sets. It was found that the maximum uncertainties in the pressure coefficients of MIRA and Ahmed Body models were less than 5% of their magnitudes submitted in Chapter 6 and Appendix B.